UNIVERSIDAD AUTÓNOMA DE MADRID

Science Faculty

Department of Applied Physics

New Atomic Force Spectroscopy methods for biomedical applications

A thesis submitted to the Universidad Autónoma de Madrid in accordance with the requirements of the degree of Doctor in Philosophy by:

Andra Cristina Dumitru

Supervised by

Prof. Ricardo García García

Instituto de Ciencia de Materiales de Madrid

Consejo Superior de Investigaciones Científicas

April 11th 2016

Abstract

Atomic Force Microscopy (AFM) is powerful tool in nanoscience, which stands out in the microscopy field due to the amazing observations of biological, physical and chemical processes at unprecedented resolutions and time scales. Although the AFM is an instrument designed to measure mechanical interactions between a sharp tip and a sample, it is more widely known for the remarkable images of atomic structures and individual molecules. The development of AFM-based force spectroscopy methods started more than two decades ago, by exploiting the capability of the instrument to measure forces in the piconewton range. Force spectroscopy methods contribute to our understanding of processes and problems for which an experimental approach was unthinkable. These methods have been applied to study the nanomechanics of a wide range of materials, biomolecules, chemical entities, cells and tissues. Undoubtedly, the force detection capabilities of AFM exhibit a high potential of being used both in fundamental studies and in applied fields.

Integrated force spectroscopy methods can enhance the development of advanced ultrasensitive bioanalytical devices and biosensors. However, current limitations of force spectroscopy methods need to be overcome first. For example, one limitation of force spectroscopy applied to the study of single molecules is the difficult and tedious work required to separate specific biomolecular recognition events from unspecific adhesion events. Another weak point of present force spectroscopy methods is that historically, they have been developed and tested on model or well-established systems or surfaces. Faster, cheaper and more reliable biomedical applications could really benefit from the development new AFM-based force spectroscopy methods and their applications to nonstandard systems.

In this context, this doctoral thesis addresses some of the problems and issues arising from the application of force spectroscopy to non-ideal systems found in

many biomedical applications. The thesis is divided into 7 chapters and has two major goals: 1) to develop reliable and robust methods for single-molecule and single-cell force spectroscopy; 2) to demonstrate the capabilities of force spectroscopy in several problems with biomedical relevance. Those scientific problems range from molecular level studies of the action of drug delivery systems, to electronic biosensors, to the nanoscale characterization of the biodegradability and biocompatibility of implantable materials.

In the first chapter, an overview of atomic force microscopy is presented. After a historic introduction to the technique, a basic description of the experimental setup, the calibration methods and the most common operating modes is provided.

In the second chapter, AFM-based single-molecule techniques are introduced, along with general information on tip functionalization approaches and the application to the exploration of the energy landscape of biomolecules. The chapter ends with a short review of the most relevant technical advances in SMFS throughout the last decade.

In the third chapter, SMFS is applied to study a small-interference RNA (siRNA) delivery system. This study provides relevant information for future dendrimer-based siRNA delivery systems aimed to transfection procedures in two ways: a) it identifies the range of unbinding forces which allow the dissociation of the siRNA from the dendriplex and an efficient transfection b) it validates experimentally, for the first time, the theoretical predictions made by molecular modeling on the binding energies between dendrimers and siRNA at the single molecule scale.

In the fourth chapter, a comparative single-molecule force spectroscopy *versus* electrolyte-gated field effect transistor study is described. This study meets the challenging task of correlating a mechanical nanoscale metrology that probes individual or a few antibody-antigen pairings with the electrical response of the electrolyte-gated field effect transistor, which involves a wide number of recognition events. A molecular perspective to the immune detection processes sensed in a real electrolyte-gated field effect transistor is provided by means of single-molecule force spectroscopy.

In the fifth chapter, a study of the adsorption of Immunoglobulin G (IgG) antibodies on graphene revealed the preservation of the antibody's secondary structure, strong anchoring to the hydrophobic substrate and retention of immunoactivity. Predominant vertical adsorption orientations of the IgG antibodies were observed, which, coupled with their bioactivity towards specific antigens, are key properties that could possibly enable the development of very sensitive graphene-based immunological biosensors in the future.

In the sixth chapter, a new AFM method for the *in situ* study of the degradation and nanomechanical properties of biocompatible polymeric scaffolds is presented. This research encompasses the analysis of the changes in morphological properties of polymeric structures and the correlation with the evolution of their mechanical properties (Young modulus). The experimental results were in good agreement with numerical simulations and provided valuable information for the elucidation of the dynamics of the polymer degradation during the first two weeks of immersion in biological buffer.

In the seventh chapter, an innovative approach to investigate the foreign body reaction mechanism is presented. The results hint at the molecular basis of this process, and clearly indicate that adhesion is a potential target to minimize the foreign body reaction against materials that are immunogenic *a priori*. A third generation tetracycline with anti-inflammatory properties, minocycline, was used to reduce the activation of mononuclear phagocytes towards foreign body reaction. This chapter shows how single-cell force spectroscopy coupled with the nanoscale analysis of materials properties and biomarkers profiling, can provide an effective tool to screen the immunogenic potential of materials and assess *in vitro* the efficacy of chemical or pharmacological treatments.

Resumen

La microscopia de fuerza atómica (AFM, por sus siglas en ingles) es una herramienta robusta utilizada en nanociencia, que se destaca en el campo de las microscopias gracias a sus extraordinarias observaciones de procesos biológicos, físicos y químicos, con resoluciones y a escalas temporales sin precedente. Aunque el microscopio de fuerza atómica es un instrumento diseñado para medir interacciones mecánicas entre una punta afilada y una muestra, es más conocido por las imágenes de alta resolución de estructuras atómicas y moléculas individuales. El desarrollo de métodos de espectroscopia de fuerzas basados en AFM empezó hace más de dos décadas, sacando provecho a la capacidad del instrumento para medir fuerzas en el rango de piconewtons. Los métodos de espectroscopia de fuerzas contribuyen a nuestro entendimiento de procesos y problemas para los cuales una manera experimental de abordarlos era impensable. Estos métodos se aplicaron al estudio nanomecánico de varias categorías de materiales, biomoléculas, entidades químicas, células y tejidos. Sin duda, la capacidad de detectar fuerzas del AFM lo hace un instrumento con gran potencial para ser empleado tanto en estudios fundamentales como en campos aplicados.

La integración de métodos de espectroscopia de fuerzas puede agilizar el desarrollo de dispositivos bioanalíticos y biosensores ultrasensibles. Sin embargo, el paso inicial consiste en superar las limitaciones actuales de los métodos de espectroscopia de fuerzas. Por ejemplo, una de las limitaciones al aplicar la espectroscopia de fuerzas al estudio de moléculas individuales es el trabajo difícil y tedioso que se requiere para separar los eventos biomoleculares de reconocimiento específicos de los eventos de adhesión no específica. Otro punto débil de los métodos de espectroscopia de fuerzas utilizados en el presente es el hecho de que, históricamente, se habían desarrollado y probado en sistemas o

superficies modelo bien establecidos. Aplicaciones biomédicas más rápidas, baratas y fiables se podrían desarrollar con nuevos métodos de espectroscopia de fuerzas basadas en AFM y con sus aplicaciones en sistemas no-estándar.

En este contexto, la presente tesis doctoral se dirige a los problemas y cuestiones que surgen de la aplicación de la espectroscopia de fuerzas en sistemas no-ideales encontrados en muchas aplicaciones biomédicas. La tesis esta dividida en 7 capítulos y tiene dos objetivos principales: 1) desarrollar métodos fiables y robustos para espectroscopia de fuerzas de moléculas y células individuales; 2) demonstrar las capacidades de la espectroscopia de fuerzas en varios problemas con relevancia en biomedicina. Estos problemas se extienden desde estudios a nivel molecular de la acción de sistemas de entrega de fármacos, a biosensores electrónicos, pasando por la caracterización a nanoescala de la biodegradación y biocompatibilidad de materiales implantables.

En el primer capítulo se presenta una visión de conjunto de la microscopia de fuerza atómica. Después de una introducción de la técnica desde el punto de vista histórico, se proporciona una descripción básica del montaje experimental, los métodos de calibración y los modos de operación más comunes.

En el segundo capítulo se introducen los métodos de estudio de moléculas individuales con el AFM, junto con información general sobre la funcionalización de la punta y la aplicación para explorar los estados energéticos de las biomoléculas. El capitulo termina con una pequeña revisión de los avances técnicos más relevante en microscopia de fuerzas de moléculas individuales de la última década.

En el tercer capítulo se presenta la aplicación de la microscopia de fuerzas de moléculas individuales al estudio de un sistema de entrega de RNA pequeño de interferencia (siRNA). El estudio proporciona información relevante para el diseño de futuros sistemas de entrega de siRNA basados en dendrímeros y dirigidos a procedimientos de transfección de dos maneras: a) identificando el rango de fuerzas de rotura que permiten la disociación de siRNA del dendriplejo y una transfección eficiente; b) validando experimentalmente, por primera vez, las

predicciones teóricas hechas por estudios de modelización molecular sobre las energías de enlazamiento de los dendrímeros y siRNA a escala de moléculas individuales.

En el cuarto capítulo se describe un estudio comparativo de espectroscopia de fuerza de moléculas individuales y transistores de efecto de campo con puerta electrolítica. El reto del estudio es correlacionar un método mecánico a nanoescala que mide entre uno y pocas pares de anticuerpo-antígeno, con la respuesta eléctrica de un transistor de efecto de campo con puerta electrolítica, que involucra la detección de un gran número de eventos de reconocimientos. El estudio presentado en este capítulo aporta una perspectiva molecular de los procesos de inmunodetección medidos por un transistor de efecto de campo con puerta electrolítica real.

En el quinto capítulo se presenta un estudio de la adsorción de anticuerpos Inmunoglobulina G (IgG) en grafeno, que revela la conservación de la estructura secundaria del anticuerpo, su fuerte anclaje al sustrato hidrofóbico y la retención de la inmunoactividad. Se observó que las orientaciones de adsorción predominantes de los anticuerpos IgG son las verticales, lo que junto con su bioactividad hacia antígenos específicos, son propiedades clave que podrían hacer posible el desarrollo de biosensores inmunológicos basados en grafeno en un futuro.

En el sexto capítulo se presenta un nuevo método basado en AFM para estudiar *in situ* la degradación y las propiedades nanomecánicas de andamios poliméricos biocompatibles. Esta investigación abarca el análisis de los cambios morfológicos de las estructuras poliméricas estudiadas y la correlación con la evolución de sus propiedades mecánicas (modulo de Young). Los resultados experimentales fueron en concordancia con las simulaciones numéricas y aportaron información valiosa a la hora de elucidar la dinámica de la degradación del polímero durante las primeras dos semanas después de la inmersión en una solución tampón.

En el séptimo capitulo se presenta una aproximación novedosa para investigar el mecanismo de la reacción del cuerpo extraño. Los resultados obtenidos

proporcionan pruebas indirectas sobre la base molecular del proceso e indican claramente que la adhesión es un factor potencial a tener en cuenta cuando se quiere minimizar la reacción de cuerpo extraño de los materiales que son inmunogénicos *a priori*. Se describe también la utilización de la minociclina, una tetraciclina de tercera generación con propiedades anti-inflamatorias, para reducir la activación de los fagocitos mononucleares hacia la activación de la reacción de cuerpo extraño. Este último capitulo muestra como la espectroscopia de fuerzas de células individuales acoplada con el análisis a nanoescala de las propiedades de los materiales estudiado y el biomarcaje, pueden constituir una herramienta efectiva para cribar el potencial inmunogénico de materiales y para evaluar la eficacia de los tratamientos químicos o farmacológicos *in vitro*.

List of symbols

F	General force term
k	Cantilever spring constant
d	Cantilever deflection
w	Width
t	Thickness
l	Length
E	Young modulus
G	Shear modulus
k_{tor}	Torsional spring constant
k_B	Boltzmann constant
T	Temperature
A_0	Free oscillation amplitude
A_{sp}	Set-point amplitude
z_c	Tip-sample distance
ϕ	Phase shift
F_0	Cantilever driving force
ω	Angular frequency
ω_0	Angular natural frequency
F_{ts}	Tip-sample interaction force
m	Total cantilever mass
Q	Quality factor
k_{off}	Dissociation rate
F_{unb}	Unbinding force of interaction
L_{unb}	Unbinding length
k_{on}	Affinity rate
τ	Characteristic lifetime of the complex
K_a	Association constant
K_d	Dissociation constant
v	Arrhenius pre-exponential factor
ΔG^*	Activation free energy
$\Delta G^*(F)$	Activation free energy under the application of a force F

$\Delta G^*(0)$	Activation free energy of the reaction at zero force
x_β	Reaction coordinate
$k_{off}(F)$	Force-dependent dissociation rate
$S(t)$	Survival probability
r	Loading rate
$P(F)$	Unbinding force probability distribution
F^*	Most probable unbinding force
$\Delta G_{unbinding}$	Free energy of the unbinding process
h	Planck's constant
k_{eff}	Effective force constant
k_{linker}	Polymer linker stiffness
r_{eff}	Effective loading rate
s	Tip pulling speed
l_k	Kuhn length
l_p	Persistence length
L_c	Contour length
$x(F)$	Molecular extension under force F
k_s	Polymer segment elasticity
Φ	Stiffness of a polymer chain
R	Tip radius
ΔG_m	Measured free energy of the unbinding process
σ	Standard deviation
ν	Poisson ratio
D	Diffusion coefficient
C	Normalized solvent concentration
F_{adh}	Adhesion force
z_p	Piezo-scanner displacement
δ	Indentation
V_{GS}	Gate-source voltage
V_{DS}	Drain-source voltage
R_S	Solution resistance
R_{CT}	Charge transfer resistance
C_d	Debye-Helmhotz capacitance
W	Warburg element

List of acronyms

STM	Scanning Tunneling Microscopy
SNOM	Scanning Near-field Optical Microscope
AFM	Atomic Force Microscopy
PID	Proportional, Integral and Differential controller
AM-AFM	Amplitude Modulation Atomic Force Microscopy
HOPG	Highly Ordered Pyrolytic Graphite
DNA	Deoxyribonucleic Acid
RNA	Ribonucleic Acid
SPR	Surface Plasmon Resonance
NMR	Nuclear Magnetic Resonance
SMFS	Single-molecule Force Spectroscopy
EG	Ethylene Glycol
NTA	Nitrilotriacetic Acid
APTES	3-aminopropyl triethoxysilane
PEG	Polyethylene Glycol
NHS-ester	N-Hydroxysuccinimide ester
Mal	Maleimide
SATA	N-succinimidyl S-acetylthioacetate
FJC	Freely Jointed Chain model
WLC	Worm-Like Chain model
TREC	Topography and Recognition Imaging
HS-AFM	High-Sped Atomic Force Microscopy
HS-FS	High-Speed Force Spectroscopy
RNAi	interference RNA
mRNA	microRNA
siRNA	short interfering RNA
dsRNA	double-stranded RNA
RISC	RNA-induced silencing complex
AGO2	Argonaute 2
NP	Nanoparticle
PAMAM	Polyamidoamine

TGD-G1	TRANSGENEN Generation 1
PBS	Phosphate Buffered Solution
HEPES	4-(2-hydroxyethyl)-1-piperazineethanesulfonic acid
DMSO	dimethyl sulfoxide
DEPC	Diethylpyrocarbamate
1D	One-dimensional
2D	Two-dimensional
USP	United States Pharmacopeia
IgG	Immunoglobulin G
ELISA	Enzyme-Linked ImmunoSorbent Assay
QCM	Quartz Crystal Microbalance
EGOFET	Electrolyte-Gated Organic Field Effect Transistor
IL4	Interleukin 4
HSC_6NH_2	6-aminohexanethiol
PG	Protein G
His	Histidine
Fab	Antigen binding fragment
Fc	Crystallisable fragment
SB	Specific Binding
SUPD	Specific Unbinding Probability Density
SUP	Specific Unbinding Probability
GO	Graphite Oxide
MD	Molecular Dynamics
SMD	Steered-Molecular-Dynamics
BSA	Bovine Serum Albumin
BMP2	Bone Morphogenetic Protein 2
PLGA	Poly(lactic-*co*-glycolic) acid
FBR	Foreign Body Reaction
MP	Mononuclear Phagocytes
CNS	Central Nervous System
FBGC	Foreign-Body Giant Cell
SCFS	Single-cell force spectroscopy
PDMS	Poly-dimethylsiloxane
PS	Polystyrene

Contents

BMDM	Bone Marrow-Derived Mononuclear phagocyte
DMEM	Dulbecco's Modified Eagle's Medium
M-CSF	Macrophage Colony-Stimulating Factor
FBS	Fetal Bovine Serum
LPS	Lipopolysaccharide
FDA	Food and Drug Administration

Chapter 1

Introduction to Atomic Force Microscopy

1.1. History of Atomic Force Microscopy

In his lecture delivered to an American Physical Society meeting at the California Institute of Technology on the 29th of December 1959, physicist Richard Feynman asked the following question “What would happen if we could arrange the atoms one by one the way we want them?”. It had only been six years since Watson and Crick had elucidated the double-helix structure of DNA, Silicon Valley and the laser were still at the beginning and it would take decades for scanning probe microscopes and carbon nanotubes to be developed. Although his talk went unnoticed initially, many of the breakthroughs he was stressing that would be possible if scientists were able to “just look at the thing”, would soon set the bases of a new emerging field: nanotechnology. Following the invention of the scanning tunneling microscope (STM) by Binnig, Rohrer, Gerber and Weibel in 1981[1, 2] and culminating with the remarkable work of Eigler and Schweizer[3] of positioning individual atoms with STM, Feynman´s lecture started to be considered as the birth date of nanotechnology.

In STM, a very sharp conductive tip is held at a fixed position very close to the sample surface. As the tip is scanning the sample at a distance equivalent to the diameter of an atom, electrons of the last atom on the tip apex are transmitted by the tunneling effect to the neighboring atoms of the sample and vice versa. An electrical current is generated, which is directly related to the tip-sample distance, the applied voltage and the local density of states of the sample. Since the tunneling probability depends exponentially on the distance, changes in the surface topography can be mapped by keeping the current constant and recording the tip height. True atomic resolution images can be recorded with this technique[4, 5]. The major drawback of this technique is the fact that STM works best when conducting materials are employed, although it has been proved that organic molecules can be fixed on a conductive surface and studied[6, 7].

The invention of the STM was actually laying the foundation of a new series of scanning probe microscopes. The scanning near-field optical microscope (SNOM) [8, 9] was developed in parallel with the STM and went below the far field resolution limit by exploiting the properties of evanescent waves. Within this series of scanning probe techniques having the STM as a starting point, the atomic force microscope (AFM), developed by Binnig, Gerber and Quate in 1986[10], stands out as an excellent tool to obtain high resolution images and quantitative information of a wide range of samples. The AFM was developed in order to overcome the inherent limitations of STM and it was introduced in 1986, the same year Binnig and Rohrer received the Nobel Prize in Physics for the discovery of the STM. The invention of the AFM was a great advance with respect to STM, since it no longer relied on the tunneling current between the tip and the sample. Moreover, its spatial resolution is not limited by the diffraction limit, as in competing optical microscopy techniques. In AFM, the topography of both conducting and insulating samples can be imaged and in certain conditions atomic resolution can be obtained[11, 12]. The instrument has evolved through several generations and nowadays it can be used to measure samples in a variety of environmental conditions, from ultrahigh vacuum to air to liquid in a broad range of temperatures. Moreover, it is no longer limited to measuring the surface topography, but can be employed to quantify sample properties at or close to the surface.

The operating principle of AFM is based on the mechanical interactions between a scanning probe (tip) mounted at the end of a flexible cantilever spring and the sample surface. While scanning, as the probe approaches the sample, it enters an attractive regime governed by Van der Waals forces. The probe is weakly attracted towards the sample surface, which causes the bending of the cantilever. As the probe-sample distance becomes smaller, the probe enters a repulsive regime in terms of Lennard-Jones potential[13] and becomes strongly repelled from the surface. The attractive or repulsive forces that reflect the interaction between the probe and the surface can be measured by monitoring the cantilever deflection. The sample topography is obtained by plotting either the cantilever deflection or the height in each pixel of the image.

1.2. Basic principles

The instrumental setup of an AFM consists of three main components: a cantilever with a sharp tip, a piezoelectric transducer onto which the sample is mounted and a detection system.

Typical cantilevers used in AFM have a sharp probe attached to their free end and are made of silicon or silicon nitride by standard microfabrication techniques[14, 15]. They can be designed either as rectangular or V-shaped cantilevers and their dimensions vary from 10-200 μm in length, 5-30 μm in width and 0.2-2 μm in thickness. As for the tip, it can be made of silicon, silicon nitride or diamond, with a radius of curvature at the tip apex of 2-30 nm. AFM cantilevers with polymeric colloidal tips of 0.1-6 μm in diameter have also been developed for nanomechanical measurements. To enhance the reflectance of the laser beam on the cantilever backside, either a thin gold or an aluminum layer can be deposited on both sides of the cantilever[16]. Cantilever parameters, such as force constant and resonance frequency, can vary from 0.01 to 100 N/m and 2 kHz to the MHz range. Given the wide variety of cantilevers available nowadays, special attention must be paid to the cantilever choice according to the operation mode and environment. For example, contact mode AFM measurements in liquid medium require cantilevers with force constants of 0.02-1 N/m and resonance frequencies of 2-100 kHz.

If we consider the cantilever acting as a Hookean spring with a spring constant k, the bending of the cantilever, d, gives the direct measurement of the force, F :

$$F = -k \cdot d \qquad (1.1)$$

Cantilever deflections range between 1 ångström and several micrometers. This can be translated into a force sensitivity of 10^{-12} to 10^{-5} N.

Figure 1.1 depicts a scanning electron microscopy image of a rectangular silicon nitride cantilever along with a magnification of the tip area. The width, w, thickness, t, and length, l, can be measured with high precision from this kind of image. The force constant of the cantilever depends on its dimensions and the material it is made of

(Young modulus, E). Hence, the theoretical force constant of the cantilever spring k can be determined with the Equation 1.2 [17, 18]:

$$k = E\frac{w}{4}\left(\frac{t}{l}\right)^3 \qquad (1.2)$$

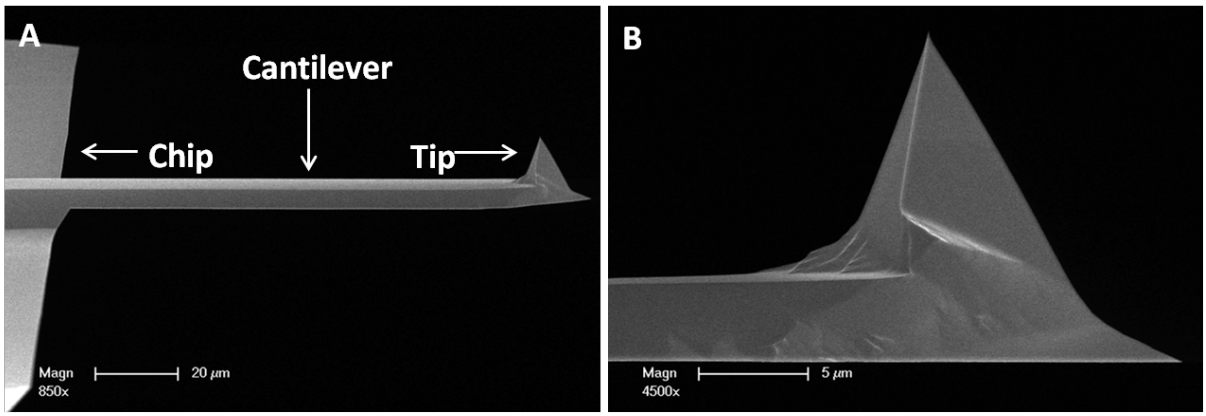

Figure 1.1. A: Scanning electron microscopy image of a typical commercial rectangular cantilever. B. Zoom of the pyramidal tip attached to the cantilever.

The lateral forces experienced by the tip while scanning the sample surface cause the torsion of the cantilever, which depends on the tip height h and the shear modulus G of the cantilever material. The torsional spring constant k_{tor} can be calculated with Equation 1.3[18]:

$$k_{tor} = \frac{G}{3}\frac{wt^3}{lh^2} \qquad (1.3)$$

However, this method for the estimation of the cantilever spring constant is both time-consuming and expensive, so other approaches for the accurate determination of k will be presented in Section 1.3.3 of this chapter.

The precise detection of the cantilever deflection is a key factor when performing AFM measurements, since the sensitivity of the detection system is directly correlated with the accurate estimation of the tip-sample interaction forces. A number of methods have been developed, but today nearly all AFM instruments use the Laser Beam Deflection scheme depicted in Figure 1.2. The cantilever bending and torsion can be detected by means of this scheme. The method uses a focused laser beam irradiated on the backside of the cantilever, which is then reflected to a mirror

and directed to a four-quadrant position sensitive photodiode, where the deflection and torsion of the cantilever are read out separately. When the cantilever is at equilibrium, the laser spot is adjusted so that the upper and lower sections of the photodiode show the same intensity. Small variations in the cantilever deflection generate changes in the incident angle of the laser beam irradiated on the backside of the cantilever and consequently in the direction of the reflected laser beam. The signal difference between the upper and lower sections of the photodiode gives the magnitude of the cantilever deflection. Several research groups have focused on improving the sensitivity of the Laser Beam Deflection system. Some chose to improve the components directly related to the electronic noise[19-21], whereas others focused on alternative techniques such as interferometry[22-24].

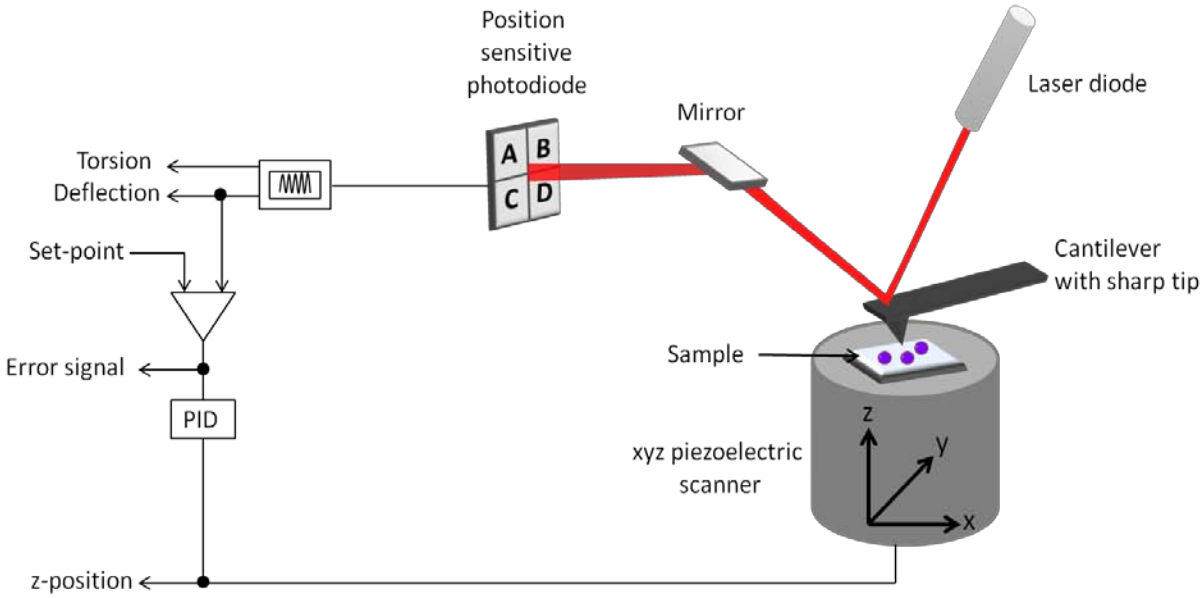

Figure 1.2. AFM setup with a Laser Beam Deflection system for the detection of the cantilever bending and torsion. As the tip scans the sample in the x-y direction, normal and friction forces between the tip and the sample are quantified simultaneously. This is done by measuring the vertical and lateral deflection of the laser beam, which is irradiated to the backside of the cantilever, reflected into a mirror and directed to a position sensitive photodiode. In the four-quadrant photodiode, the signal (A+B)-(C+D) corresponds to the measured cantilever deflection, while (A+C)-(B+D) is a measure of the cantilever torsion. The operation of the feedback system is represented by solid lines and arrows. The deflection signal measured by the photodiode is compared with a set-point deflection previously chosen by the operator. The difference between the real deflection signal and the set-point is translated into an error signal. A PID controller receives the error signal and minimizes it by moving the z-position of the scanner.

While scanning the sample surface, the cantilever deflection is maintained constant by means of a feedback system (Figure 1.2), which controls the scanner movement in the vertical axis. When the cantilever is deflected as a result of the tip-sample interaction forces, the photodiode records the lateral and vertical changes in the laser spot position. The photodiode current signal is transferred to the proportional, integral and differential controller (PID) and compared with a set-point value previously chosen by the operator. The feedback system adjusts the z-position of the piezoelectric scanner to minimize the difference between the set-point and the real deflection signal. As a result, the tip-sample interaction force is maintained constant for an optimal setup of the PID parameters.

To record an AFM topography image, the piezoelectric scanner moves the cantilever in the x-y plane over the sample surface. The z-position of the scanner is recorded as a function of the x-y position with sub-ångstrom precision. This generates a topography map of the sample surface, which can be further visualized and analyzed by computer processing.

1.3. Calibration

The calibration of several parameters is a matter of utmost importance for a proper use of the AFM instrument and reliable quantitative measurements.

1.3.1. Piezoelectric scanners

The piezoelectric transducers sensitivity depends on how much the material is expanded or contracted for each applied volt and is a characteristic parameter of the piezoelectric scanner. The displacement of the piezoelectric scanner as a function of the applied voltage should be carefully calibrated regularly (every 6-12 months). This allows for reliable quantitative information on the topography of the studied sample to be obtained. A variety of procedures were developed to calibrate the x-y-z displacement of the piezoelectric scanners, among them optical interferometry[25] and the more widely employed calibration specimens imaging[26, 27].

1.3.2. Photodiode sensitivity

In order to obtain reliable quantitative data from AFM measurements, an accurate estimation of the applied forces is necessary. The calibration of the photodiode sensitivity is required to correlate the change of the laser beam in volts with the displacement of the piezo-actuator in nanometers.

The photodiode sensitivity is usually calibrated by recording a deflection *versus* piezo-displacement curve in contact mode. In such a curve, the dependence of the cantilever deflection as a function of the piezo-displacement is recorded by performing repeated extend and retract cycles in the vertical axis (Figure 1.3).

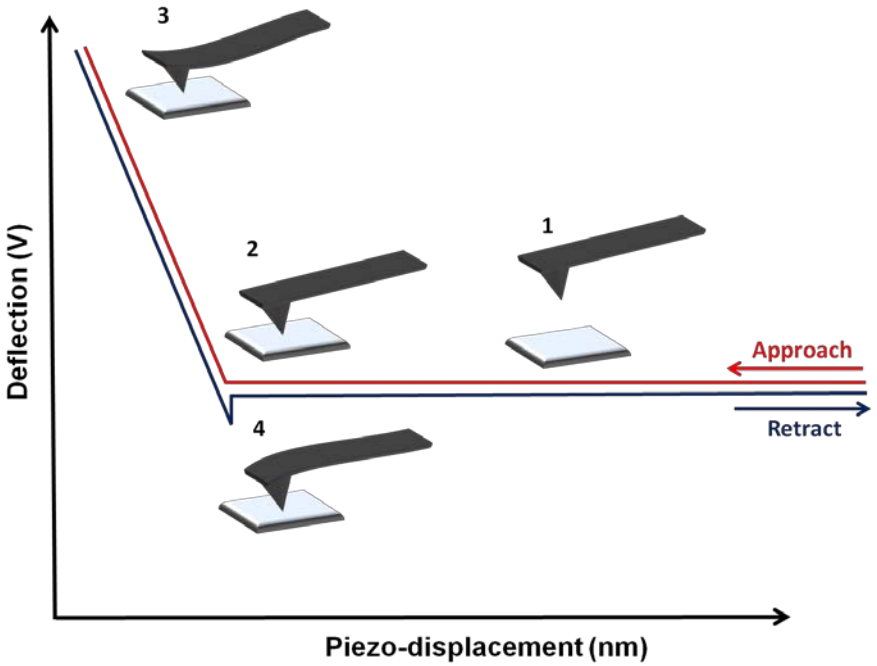

Figure 1.3. During the initial approach of the cantilever towards the sample, the deflection signal remains constant, indicating that there is no force acting on the cantilever (Step 1). Once the tip reaches the surface (Step 2), the cantilever is deflected until a preset value (Step 3). This leads to a linear increase of the deflection signal. The subsequent retraction of the tip results in a linear decrease of the deflection signal. Adhesion forces between the tip and the sample cause the cantilever to bend downwards during the piezo retraction (Step 4). This generates negative deflection values, which are also called adhesion peaks. The cantilever is further retracted until its initial position away for the sample (Step 1).

If the employed sample is a hard non-deformable material, the relationship between the piezo-displacement (nm) and the cantilever deflection (V) can be obtained from the slope of the curve in the repulsive contact region. This value is characteristic for each cantilever type and depends on the position of the laser spot on the backside of the cantilever. One needs to take into account the fact that since a repulsive interaction between the tip and the sample is involved, the tip will be damaged after the procedure is finished. This is why the photodiode sensitivity calibration should be performed at the end of the experiment.

This method for the calibration of the photodiode sensitivity is the most widely used in AFM experiments, however other less invasive methods have been developed through the years[28, 29].

1.3.3. Cantilever force constant

The theoretical force constant of a cantilever is given by Equation 1.2 [18]. While the Young modulus of the material is usually known with enough precision for each cantilever type and the length and width can be measured with an optical microscope, important errors can arise from the estimation of the cantilever thickness. This could lead to significant deviations of up to 50% of the real force constant from the nominal one provided by the manufacturer. Hence, this is a strong reason why every cantilever should be calibrated for each set of AFM measurements.

There are several methods that can be employed to transform the measured cantilever deflection from nanometers to force values. The most commonly used methods are the following:

1) The calibration method of Sader[16] consists of calculating the force constant, k, from the equation below:

$$k = \frac{\pi}{16}\rho w^2 l Q \omega^2{}_R \Gamma''(\omega_R) \qquad (1.4)$$

where $\Gamma''(\omega_R)$ is the imaginary part of the (dimensionless) hydrodynamic function evaluated at the resonance frequency in a medium of density ρ. Thus, the force constant can be estimated by measuring the cantilever's width w and length l on one

hand and by fitting the resonance curve of the cantilever in air to a Lorenzian and obtaining ω_R, the radial resonant frequency and Q, the quality factor of the fundamental flexural mode. The method was initially developed for rectangular cantilevers and has been further modified so that it can be applied for triangular cantilevers as well[30].

2) The thermal noise method [31, 32] is the most widely employed, since it can be used *in situ* and it is valid for both rectangular and triangular cantilevers. It is based on the equipartition theorem, which states that the kinetic energy stored in a system at a momentum coordinate, which is the deflection of a cantilever from its equilibrium position, is equal to one half of the thermal energy of the system[33].

$$\frac{1}{2}k\left\langle z^2\right\rangle = \frac{1}{2}k_B T \qquad (1.5)$$

Here $\left\langle z^2\right\rangle$ is the mean square deflection of the cantilever caused by thermal vibrations, k_B is the Boltzmann constant and T the temperature. The thermal noise spectrum plots the cantilever oscillations induced by Brownian motion as a function of the Fourier transform of the cantilever´s free oscillation frequencies recorded over a preset time. The force constant of the cantilever bears a direct correlation with the amplitude of the fluctuations, hence the thermal resonance curve can be fitted to a Lorentz function and the force constant can be extracted.

1.4. Setting up an AFM experiment

First, the cantilever is mounted on a special holder and the laser spot is focused on its backside. The laser spot position should be chosen so that the signal of the reflected beam is as high as possible and the signal-to-noise ratio is maximized. A detailed study of the optimal laser spot position along the cantilever backside is given by Schaffer and Fuchs[34].

The next step is the sample preparation. The sample to be analyzed is mounted on a sample holder, which in most systems is a metallic surface attached to the piezoelectric scanner through a magnet. The sample is usually immobilized onto the

sample holder by using double-sided tape, silver paint or glue. For biological samples, the substrate needs to be properly cleaned before sample deposition. It is recommendable to prepare a fresh sample for each experiment. Biomolecules are usually physisorbed onto flat surfaces like muscovite mica, highly ordered pyrolytic graphite (HOPG) or Au(111). Repulsive electrostatic forces between the biological sample and the flat surface should be minimized by properly adjusting the electrolyte concentration and pH conditions.

1.5. Operating modes

1.5.1. Contact mode

To this day, a wide range of AFM imaging modes has been developed. The oldest one from the historical point of view is contact mode AFM, also called static mode to distinguish it from the dynamic modes, which will be introduced later.

In contact mode the cantilever tip is in constant physical contact with the sample while scanning it in a raster-like manner. In other words, the tip is pressed against the sample surface until a repulsive force is detected by the cantilever. As the tip is scanning the sample in the x-y plane, the variations in the surface topography or material composition lead to changes in the tip-sample interaction forces, which in turn, make the cantilever bend. The detection system measures the topography induced bending of the cantilever at each position in the x-y plane. The instrument is equipped with a feedback loop system, which maintains the tip-sample contact through the voltage signal output applied to the z-piezo. The feedback loop makes the z-piezo adjust the sample height relative to the tip in such manner that the deflection remains constant or equal to a previously chosen set-point value. In constant force mode, this will provide quantitative information about the height of the measured sample. By correlating the height information with the lateral x-y position in each pixel, a topographical map of the sample surface can be obtained.

Due to its straightforwardness, contact mode AFM is easy to use and it can be employed to obtain high-resolution images of a wide variety of samples. Another advantage is the fact that it can be used to measure not only the deflection of the cantilever, but the torsion as well. It was shown as soon as 1987 by Mate *et al*.[35] that

the lateral force can be directly correlated with the friction between the tip and the sample, thus setting the bases of *friction force microscopy*.

However, contact mode AFM has several drawbacks as well. Measurements are affected by thermal drift and electronic noise. Also, the lateral resolution is limited by the contact radius, which is several nanometers when in physical contact with the sample. Since the tip is in constant contact with the sample, this can cause tip contamination issues, as well as irreversible damage to soft biological samples like DNA, cells, proteins etc. Lateral shear forces applied to the sample, which can be of the order of nN, can deform, destroy or sweep physisorbed molecules.

Still, there are groups who have managed to overcome the difficulties exposed before when using contact mode and to obtain true atomic or sub-nanometric resolution. True atomic resolution in water medium was obtained by Onhesorge and Binnig[11] using silicon cantilevers with a force constant of 0.2 N/m, a nominal radius of 10 nm and by applying forces between 10 to 60 pN (Figure 1.4.A). Muller *et al*.[36] imaged purple membrane and showed submolecular details of single bacteriorhodopsin molecules imaged in buffer solution (Figure 1.4.B).

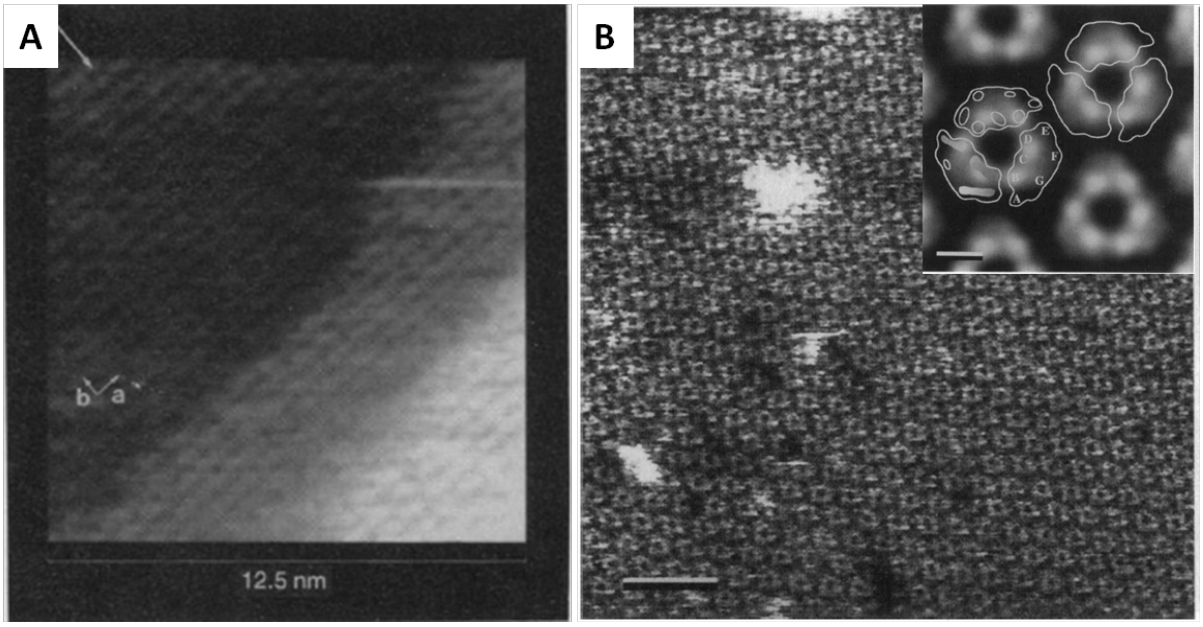

Figure 1.4. High-resolution AFM topography images obtained in contact mode AFM. A: Atomic resolution on a calcite sample in liquid medium. Adapted from Ref.36; B: Sub-nanometer resolution image of purple membrane and a zoom of averaged bacteriorhodopsin trimers. Adapted from Ref. 11.

1.5.2. Dynamic imaging modes

It was not late until the limitations of contact mode images were understood by the AFM community and new less invasive imaging modes were developed. To avoid high lateral forces between the tip and the sample, in dynamic force microscopy, the cantilever is oscillated in the vertical direction at a fixed excitation frequency exactly or very close to the cantilever's resonance[37-41]. Different detection schemes measuring either the phase shift or the change of the oscillation amplitude were proposed for this driving mechanism. However, throughout the years, amplitude modulation AFM (AM-AFM) or tapping mode, where the oscillation amplitude is used as a measure of the tip-sample distance, became the most widely employed technique for imaging in ambient conditions and liquid environment. In AM-AFM the tip is in intermittent contact with the sample and the applied lateral forces are often negligible[42-44].

The two observables, the oscillation amplitude and phase shift, are influenced by the tip-sample interaction forces and can be used as feedback channels. When the cantilever is oscillating far from the sample, such that the interaction force with the sample is zero, the amplitude at resonance is equal to the free oscillation amplitude, A_0, and the phase shift at resonance is 90°**.** To start the image acquisition, the tip is brought closer to the sample, so that it will oscillate at an average tip-sample distance z_c while the oscillation amplitude will be reduced to a set-point amplitude, A_{sp}. During scanning, if the cantilever reaches an area with differences in height or physical properties, the oscillation will change, so as a consequence the amplitude will be reduced to A' and the phase will change to ϕ' (Figure 1.5). At this point, the feedback loop will adjust the average tip-sample distance z_c such as to minimize the difference between A_{sp} and A'. Thus, a topography image is obtained from the parameters recorded by the scanner movement, while simultaneous images can also be collected in the phase channel ϕ. The phase image can be used to extract information about the physical properties of the sample[45]. Several studies have shown that the phase contrast and the energy dissipated in the tip-sample interaction are closely related[46-48].

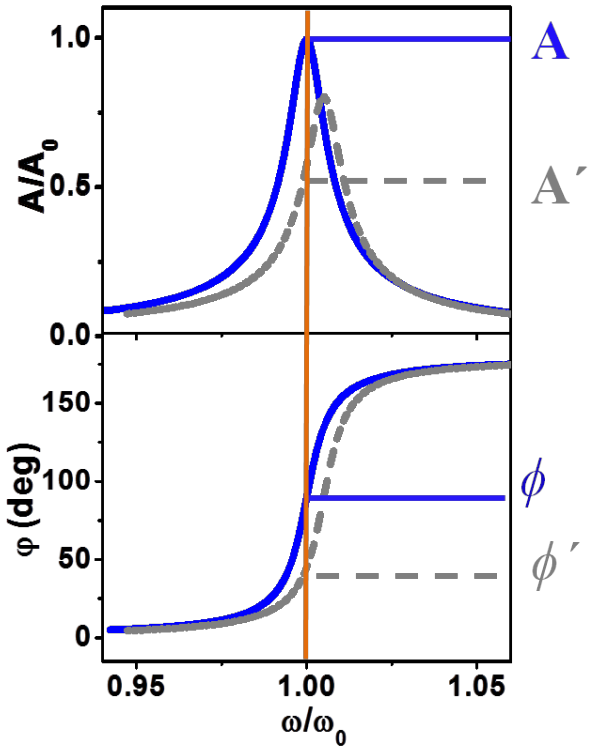

Figure 1.5. Cantilever resonance curve. While the cantilever scans the sample, changes in tip-sample interaction forces will change the oscillation, so as a consequence the amplitude will be reduced to *A'* and the phase will change to ϕ'.

The motion of the cantilever-tip system in AM-AFM can be approximated by a point-mass spring driven by an external force in the presence of tip-surface interaction forces[45]. The relevant equation of motion used o model dynamic AFM is a nonlinear second-order differential equation:

$$m\ddot{z} = -kz - \frac{m\omega_0}{Q}\dot{z} + F_0 \cos\omega t + F_{ts}(d) \qquad (1.6)$$

Where F_0 is the cantilever driving force, ω the angular frequency, m the effective mass, Q the quality factor, ω_0 the angular natural frequency, k the force constant of the cantilever and F_{ts} the tip-sample interaction force. The relationship between the effective mass m and the total cantilever mass m_c is $m \approx 0.25 m_c$. The parameters Q, ω_0 and k describe the properties of the first resonance mode.

It has been demonstrated that AM-AFM can be successfully used to obtain high-resolution images in both air and liquid medium. Figure 1.6 shows individual IgG antibodies measured in air with 2 nm lateral resolution[49] and IgM antibodies imaged in water[50].

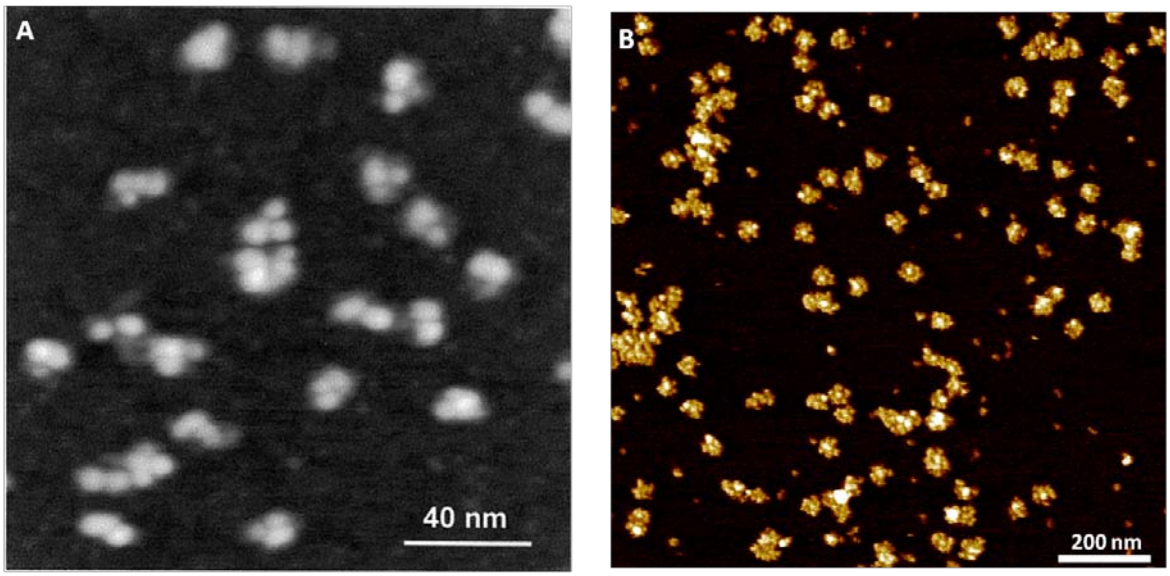

Figure 1.6. AM-AFM images of individual biomolecules adsorbed on mica. A: IgG antibodies in air medium. Adapted from Ref. 49; B: IgM antibodies measured in water. Adapted from Ref. 50.

1.6. References

1. G. Binnig, H. Rohrer, C. Gerber and E. Weibel, *Applied Physics Letters*, 1982, **40**, 178-180.
2. G. Binnig, H. Rohrer, C. Gerber and E. Weibel, *Physical Review Letters*, 1982, **49**, 57-61.
3. D. M. Eigler and E. K. Schweizer, *Nature*, 1990, **344**, 524-526.
4. G. Binnig, H. Rohrer, C. Gerber and E. Weibel, *Physical Review Letters*, 1983, **50**, 120-123.
5. M. Herz, F. J. Giessibl and J. Mannhart, *Physical Review B*, 2003, **68**, 045301.
6. J. Repp, G. Meyer, S. M. Stojković, A. Gourdon and C. Joachim, *Physical Review Letters*, 2005, **94**, 026803.
7. F. Rosei, M. Schunack, P. Jiang, A. Gourdon, E. Lægsgaard, I. Stensgaard, C. Joachim and F. Besenbacher, *Science*, 2002, **296**, 328-331.
8. U. Dürig, D. W. Pohl and F. Rohner, *Journal of Applied Physics*, 1986, **59**, 3318-3327.
9. A. Lewis, M. Isaacson, A. Harootunian and A. Muray, *Ultramicroscopy*, 1984, **13**, 227-231.
10. G. Binnig, C. F. Quate and C. Gerber, *Physical Review Letters*, 1986, **56**, 930-933.
11. F. Ohnesorge and G. Binnig, *Science*, 1993, **260**, 1451-1455.
12. S. Hembacher, F. J. Giessibl and J. Mannhart, *Science*, 2004, **305**, 380-383.
13. K. A. Dill and S. Bromberg, *Molecular Driving Forces: Statistical Thermodynamics in Chemistry and Biology* Garland Science, New York, 2003.
14. G. Binnig, G. Ch, E. Stoll, T. R. Albrecht and C. F. Quate, *EPL (Europhysics Letters)*, 1987, **3**, 1281.
15. O. Wolter, T. Bayer and J. Greschner, *Journal of Vacuum Science & Technology B*, 1991, **9**, 1353-1357.
16. J. E. Sader, I. Larson, P. Mulvaney and L. R. White, *Review of Scientific Instruments*, 1995, **66**, 3789-3798.
17. E. S. Tilman, *Nanotechnology*, 2005, **16**, 664.
18. E. Meyer, H. J. Hug and R. Bennewitz, *Scanning Probe Microscopy - The Lab on a Tip*, Springer-Verlag Berlin Heidelberg, 2004.
19. T. Fukuma, M. Kimura, K. Kobayashi, K. Matsushige and H. Yamada, *Review of Scientific Instruments*, 2005, **76**, 053704.
20. K. Kobayashi, H. Yamada, H. Itoh, T. Horiuchi and K. Matsushige, *Review of Scientific Instruments*, 2001, **72**, 4383-4387.
21. B. W. Hoogenboom, P. L. T. M. Frederix, D. Fotiadis, H. J. Hug and A. Engel, *Nanotechnology*, 2008, **19**, 384019.
22. R. Erlandsson, G. M. McClelland, C. M. Mate and S. Chiang, *Journal of Vacuum Science & Technology A*, 1988, **6**, 266-270.
23. D. Rugar, H. J. Mamin and P. Guethner, *Applied Physics Letters*, 1989, **55**, 2588-2590.
24. S. Jeffery, P. M. Hoffmann, J. B. Pethica, C. Ramanujan, H. Ö. Özer and A. Oral, *Physical Review B*, 2004, **70**, 054114.
25. E. Riis, H. Simonsen, T. Worm, U. Nielsen and F. Besenbacher, *Applied Physics Letters*, 1989, **54**, 2530-2531.
26. S. Pal and S. Banerjee, *Review of Scientific Instruments*, 2000, **71**, 589-590.
27. D. Alliata, C. Cecconi and C. Nicolini, *Review of Scientific Instruments*, 1996, **67**, 748-751.
28. M. J. Higgins, R. Proksch, J. E. Sader, M. Polcik, S. Mc Endoo, J. P. Cleveland and S. P. Jarvis, *Review of Scientific Instruments*, 2006, **77**, 013701.
29. P. Attard, T. Pettersson and M. W. Rutland, *Review of Scientific Instruments*, 2006, **77**, 116110.
30. J. E. Sader, J. A. Sanelli, B. D. Adamson, J. P. Monty, X. Wei, S. A. Crawford, J. R. Friend, I. Marusic, P. Mulvaney and E. J. Bieske, *Review of Scientific Instruments*, 2012, **83**, 103705.
31. H. J. Butt and M. Jaschke, *Nanotechnology*, 1995, **6**, 1.
32. J. L. Hutter and J. Bechhoefer, *Review of Scientific Instruments*, 1993, **64**, 1868-1873.

33. S. M. Cook, T. E. Schäffer, K. M. Chynoweth, M. Wigton, R. W. Simmonds and K. M. Lang, *Nanotechnology*, 2006, **17**, 2135.
34. T. E. Schäffer and H. Fuchs, *Journal of Applied Physics*, 2005, **97**, 083524.
35. C. M. Mate, G. M. McClelland, R. Erlandsson and S. Chiang, *Physical Review Letters*, 1987, **59**, 1942-1945.
36. D. J. Müller, F. A. Schabert, G. Büldt and A. Engel, *Biophysical journal*, 1995, **68**, 1681-1686.
37. Y. Martin and H. K. Wickramasinghe, *Applied Physics Letters*, 1987, **50**, 1455-1457.
38. Y. Martin, C. C. Williams and H. K. Wickramasinghe, *Journal of Applied Physics*, 1987, **61**, 4723-4729.
39. Q. Zhong, D. Inniss, K. Kjoller and V. B. Elings, *Surface Science*, 1993, **290**, L688-L692.
40. C. A. J. Putman, K. O. Van der Werf, B. G. De Grooth, N. F. Van Hulst and J. Greve, *Applied Physics Letters*, 1994, **64**, 2454-2456.
41. P. K. Hansma, J. P. Cleveland, M. Radmacher, D. A. Walters, P. E. Hillner, M. Bezanilla, M. Fritz, D. Vie, H. G. Hansma, C. B. Prater, J. Massie, L. Fukunaga, J. Gurley and V. Elings, *Applied Physics Letters*, 1994, **64**, 1738-1740.
42. H. G. Hansma, R. L. Sinsheimer, J. Groppe, T. C. Bruice, V. Elings, G. Gurley, M. Bezanilla, I. A. Mastrangelo, P. V. C. Hough and P. K. Hansma, *Scanning*, 1993, **15**, 296-299.
43. C. Möller, M. Allen, V. Elings, A. Engel and D. J. Müller, *Biophysical journal*, 1999, **77**, 1150-1158.
44. C. A. Putman, K. O. van der Werf, B. G. de Grooth, N. F. van Hulst and J. Greve, *Biophysical journal*, 1994, **67**, 1749-1753.
45. R. Garcia, *Amplitude Modulation Atomic Force Microscopy*, Wiley-VCH, Weinheim, Germany, 2010.
46. J. P. Cleveland, B. Anczykowski, A. E. Schmid and V. B. Elings, *Applied Physics Letters*, 1998, **72**, 2613-2615.
47. J. Tamayo and R. García, *Applied Physics Letters*, 1998, **73**, 2926-2928.
48. R. Garcia, C. J. Gómez, N. F. Martinez, S. Patil, C. Dietz and R. Magerle, *Physical Review Letters*, 2006, **97**, 016103.
49. A. San Paulo and R. García, *Biophysical journal*, 2000, **78**, 1599-1605.
50. A. P. Perrino and R. Garcia, *Nanoscale*, 2016, DOI: 10.1039/C5NR07957H.

Chapter 2

Biomolecular recognition at the single-molecule level

2.1. Emergence of single-molecule force spectroscopy

Molecular recognition processes play a fundamental role in numerous cellular functions and processes. They give rise to associations that span over a wide range of complexities and strengths. Figure 2.1 shows the typical dissociation rate k_{off} values for some representative biological complexes. Biological molecules possess the unique ability to recognize one another through processes that are governed by non-covalent molecular interactions (i.e. hydrogen and ionic bonds, Van der Waals forces, hydrophobic effects, π-π stacking). The nature of the interaction determines the stability and lifetime of the complex.

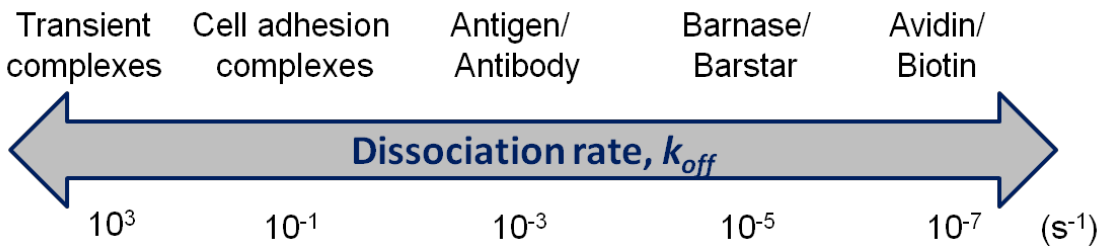

Figure 2.1. Typical k_{off} values for some representative biological complexes. Adapted from Ref 1.

Scientists have studied the kinetics and thermodynamics of biomolecular complexes by making use of standard biochemistry techniques. These studies involved the analysis of biomolecules immobilized onto a support or floating free in solution. Some of the used techniques include optical spectroscopy, surface plasmon resonance (SPR), nuclear magnetic resonance (NMR) and diferential

scanning calorimetry [2-4]. Bulk measurements performed with these techniques can only provide averaged results and do not have the capability to elucidate aspects which are only characteristic to individual molecules, such as population heterogeneity, hidden intermediates, multiple pathways, aggregation behaviour or rare events.

In the last two decades, single-molecule techniques have undergone major advances in terms of the complexity, time scales, and resolution. The fast growth of both force-based and fluorescence-based single-molecule techniques, has allowed scientists to approach and solve entirely new types of biological problems[5]. Among these techniques, AFM-based force spectroscopy stands out as an ideal tool for measuring intra- and intermolecular forces with high force and displacement sensitivity, in physiological conditions and with no need for previous labelling. Moreover, the small probe-sample contact areas in the range of several nm^2, allow the study of only one or few molecules at a time.

Single-molecule force spectroscopy (SMFS) was first introduced by the groups of Gaub and Colton in 1994 to probe the recognition mechanism and dissociation pathways of the streptavidin-biotin complex[6, 7]. Since then, it has been successfully applied to provide insights into molecular recognition processes such as the interaction between complementary DNA strands[8], ligands and receptors[9, 10] and antibody-antigen complexes[11-13]. SMFS measurements also unraveled details of protein folding and unfolding[14-16], DNA mechanics[17], the interaction between carbohydrates[18, 19] and cell adhesion processes[20, 21].

SMFS was one of the pioneering techniques to make possible the tackling of the protein folding problem, which emerged when the first atomic-resolution protein structures were introduced, around 1960. The protein folding problem consists of three problems[22, 23]:

(1) The thermodynamic question of what balance of inter-atomic forces dictates the structure of the protein, for a given amino acid sequence;

(2) The computational problem of how to predict a protein's native structure from its amino acid sequence;

(3) The kinetics question of what routes or pathways some proteins use to fold so quickly.

The first protein unfolding measurements involved the stretching of individual titin molecules and were carried out by Rief *et al.*[14]. The mechanical properties of this giant sarcomeric protein of strain muscle were measured by applying a mechanical pulling force at both ends of the titin molecule (Figure 2.2). The applied force was recorded as a function of the elongation, which resulted in a characteristic sawtooth pattern consistent with the sequential unfolding of individual titin domains.

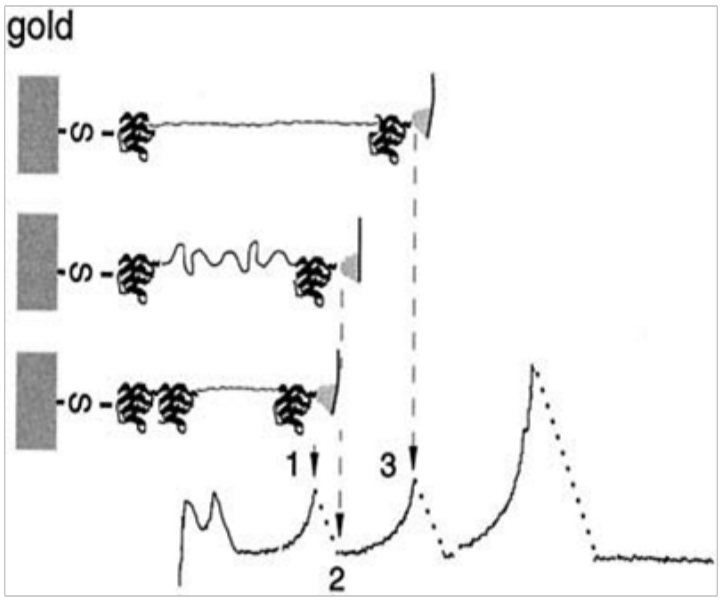

Figure 2.2. Sequential unfolding of individual titin Ig domains. Adapted from Ref.13

2.2. Single-molecule force spectroscopy experiments

To perform a single-molecule study of the molecular recognition between two interacting biomolecules, one partner is bound to the AFM tip apex, while the other is immobilized on the sample surface. Biomolecules are often covalently tethered either to the tip or the sample surface by means of flexible cross-linkers. The cross-linking of a polymeric linker with a biomolecule of interest followed by their anchoring to the AFM tip was first introduced by Hinterdorfer *et al*. and has been widely employed in SMFS studies ever since[11, 13, 24, 25]. In a typical SMFS experiment, a functionalized AFM tip is brought into contact with

the biomolecules immobilized on the sample substrate and then retracted back to its initial position. A molecular recognition event may occur if both biomolecular partners have enough orientational freedom to assume the appropriate configuration for binding. The adhesion force is then measured directly as the bending of the cantilever upon retraction.

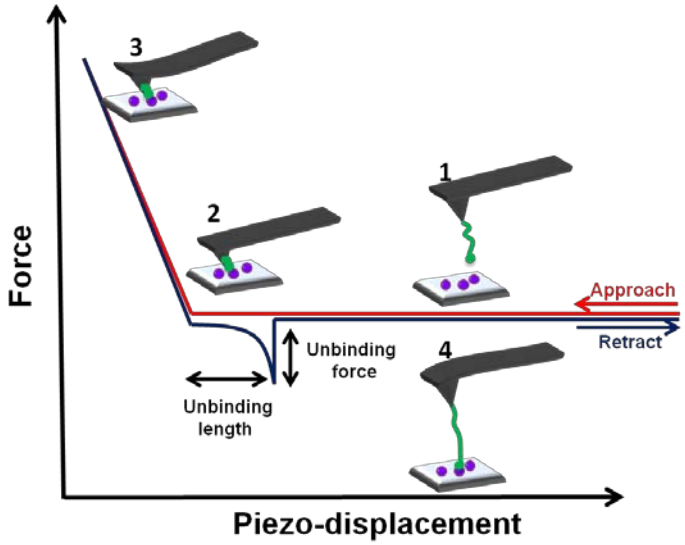

Figure 2.3. Schematic description of the main regions of an ideal force curve recorded in a single-molecule force spectroscopy experiment: 1. Tip far from the surface. 2. Initial tip-surface contact (approaching). 3. Tip-surface repulsive region. 4. Molecular recognition force.

Figure 2.3 shows a scheme of an ideal force-distance plot (force curve) where a molecular recognition event takes place. The force curve has four different steps. In step 1, the tip is far from the sample surface and the interaction force non-existent; step 2 illustrates the contact between the tip and the deposited molecules; step 3 depicts the repulsive forces between the tip and the sample when the tip is pushed toward the surface while in contact. In step 4, the tip is retracted (blue line) and the presence of an adhesion force will bend the tip downwards. When the magnitude of the interaction force between the two biomolecular partners exceeds that of the cantilever force constant, the tip will jump out of contact to its initial position. The adhesion force can be the result of a specific molecular recognition event or unspecific electrostatic interactions. Figure 2.3 depicts the particular case of a specific event. The unbinding force of interaction (F_{unb}) between the studied biomolecules is calculated from the vertical difference between the baseline and the minimum force at retraction.

The unbinding length (L_{unb}) is the difference between the tip-sample distance where the unbinding event occurs and the contact point.

2.3. Anchoring biomolecules to the AFM tip

In SMFS experiments, the biomolecules to be studied are immobilized on the sample or tip surfaces directly or via polymeric cross-linkers. When choosing an immobilization strategy, one should take into account that it should meet certain requirements[26]:

1) The biomolecules should be firmly anchored to the tip and sample surfaces by means of stronger bonds than the ones holding together the biomolecular complex to be studied. Covalent bonding strategies are usually exploited;
2) The immobilized biomolecules should retain their functionality and native structure. More importantly, the binding regions of the biomolecules should not be affected by the immobilization on a solid support;
3) To increase the probability of complex formation, the biomolecules should preserve their mobility and orientational freedom;
4) The functionalization conditions (density and orientation of biomolecules on the surface, pH, ionic strength) should be adjusted in such a manner as to promote the interaction of a single biomolecular complex at a time.

Gold or silanized surfaces are usually exploited as supports in SMFS studies and a wide variety of polymeric cross-linkers are available nowadays[1].

2.3.1 Functionalization of gold substrates

Gold is an attractive substrate, since gold-coated AFM probes are commercially available or can be fabricated making use of standard deposition techniques. The molecules to be bound to the gold substrate should bear a thiol (also called sulfhydryl) functional group or a thiol-functionalized cross-linker can be used as an intermediate. The strong covalent bond formed between metallic gold and sulphur ensures a firm attachment of the biomolecule to the substrate. Commercially available alkanethiols are some of the most common compounds used for the functionalization of gold tips[27-29]. Figure 2.4 illustrates an example of alkanethiols tethered to gold AFM probes[30].

Despite the straightforwardness of this functionalization strategy, a major drawback is the fact that gold coating increases the tip radius, making it duller, thus raising the probability of multiple interactions with the sample surface. Additionally, acidic or basic experimental environments can degrade the gold coating, which results in an irreversible tip damage.

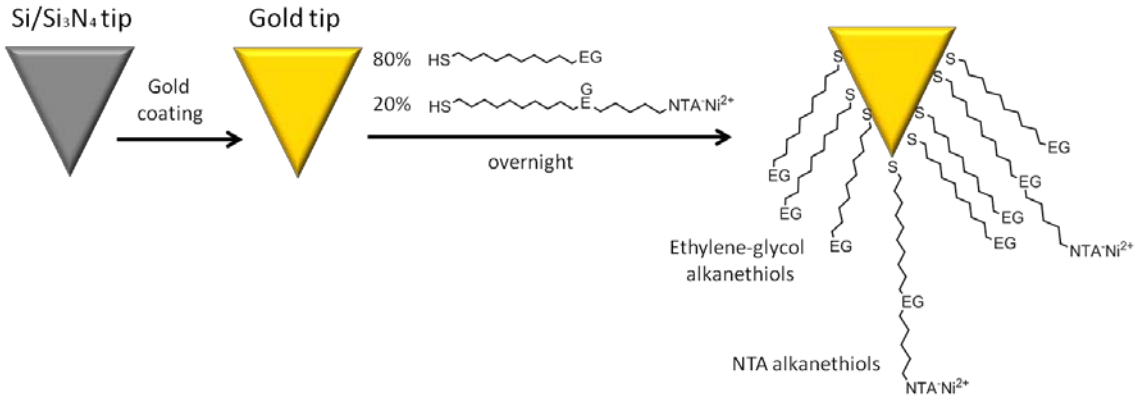

Figure 2.4. Scheme of the surface chemistry used to functionalize AFM tips with NTA/EG3-terminated alkanethiols. Adapted from Ref.30.

2.3.2. Functionalization of silicon substrates

Silanol surfaces are usually obtained by oxidizing a silicon or silicon nitride surface. Most AFM tips are made of these materials. The silanol groups (≡Si ─ OH) concentration can be increased by cleaning the substrate in acidic or basic solutions. One of the most common silanol functionalization procedures involves the reaction with aminosilanes. The resulting aminofunctionaized surface can then be easily functionalized with biomolecules. The chemical compound *(3-aminopropyl)triethoxysilane* (APTES) is one of the most employed reagents for the functionalization of substrates with amino- groups[31-33].

The main difficulty in using APTES to aminofunctionalize the AFM tip surface is the fact that the monolayer formation is competing with the polymerization of APTES molecules and subsequent formation of covalent APTES aggregates on the substrates[1]. Polymerized silane chains can interact with the sample surface and produce spurious unbinding events which might be mistakenly evaluated as specific.

The aminofunctionalization of an AFM tip with APTES, followed by the anchoring of a flexible *NHS-PEG$_{24}$-Mal* heterobifunctional linker (PEG) and of a protein is are schematized in Figures 2.5 and 2.6. The PEG linker bears a *maleimide* (Mal-) and an *N-Hydroxysuccinimide ester* (NHS-ester) functionality. On one hand, the NHS-ester reacts with the amine functional groups exposed on AFM tip surface, thus forming a covalent amide bond (Figure 2.5). On the other hand, the *maleimide* functional group reacts with thiolated molecules with the formation of a covalent carbon-sulfur bond (see Figure 2.6B). If the objective is the cross-linking of a protein to the PEG linker, the natural occurrence of Cysteine residues can be exploited, or their number can be incremented by using sulfhydryl-addition reagents (Figure 2.6A), such as *N-succinimidyl S-acetylthioacetate* (SATA) or *2-Iminothiolane* (Traut's Reagent)[34]. The resulting protein-PEG-functionalized AFM probe is depicted in figure 2.7.

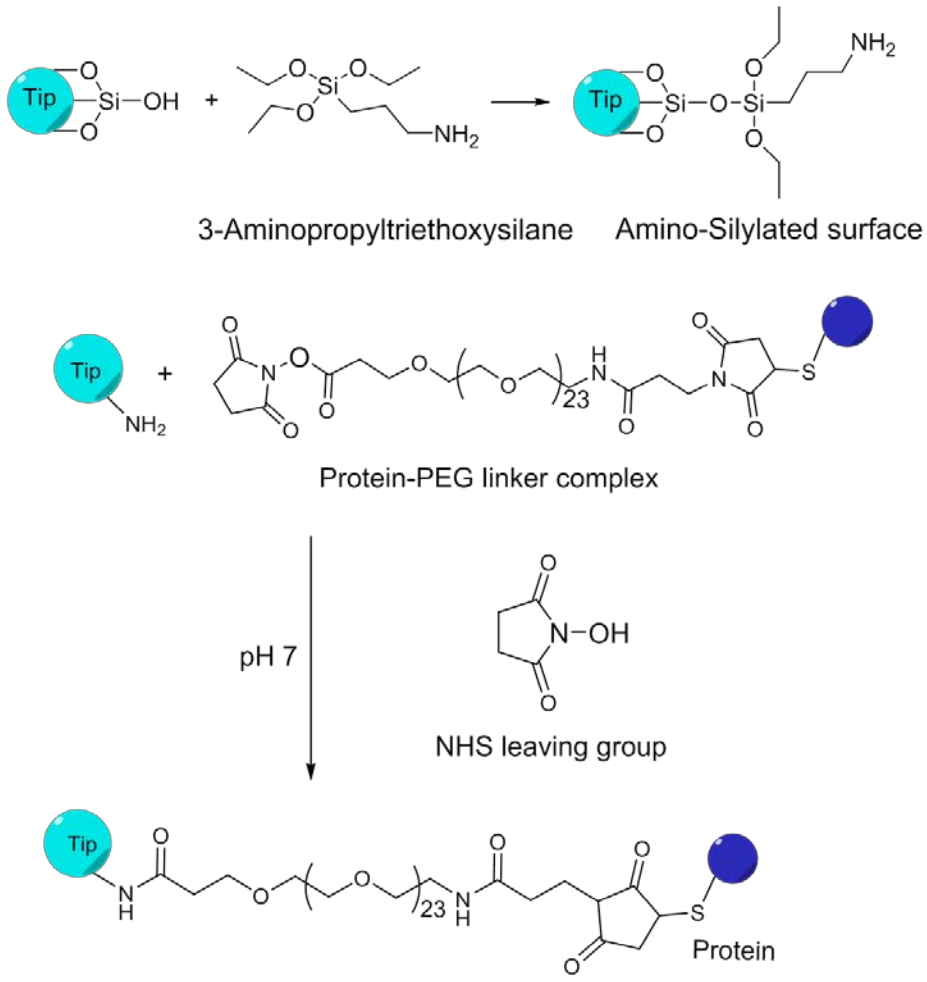

Figure 2.5. Scheme of the functionalization of a silicon tip with a protein-PEG complex.

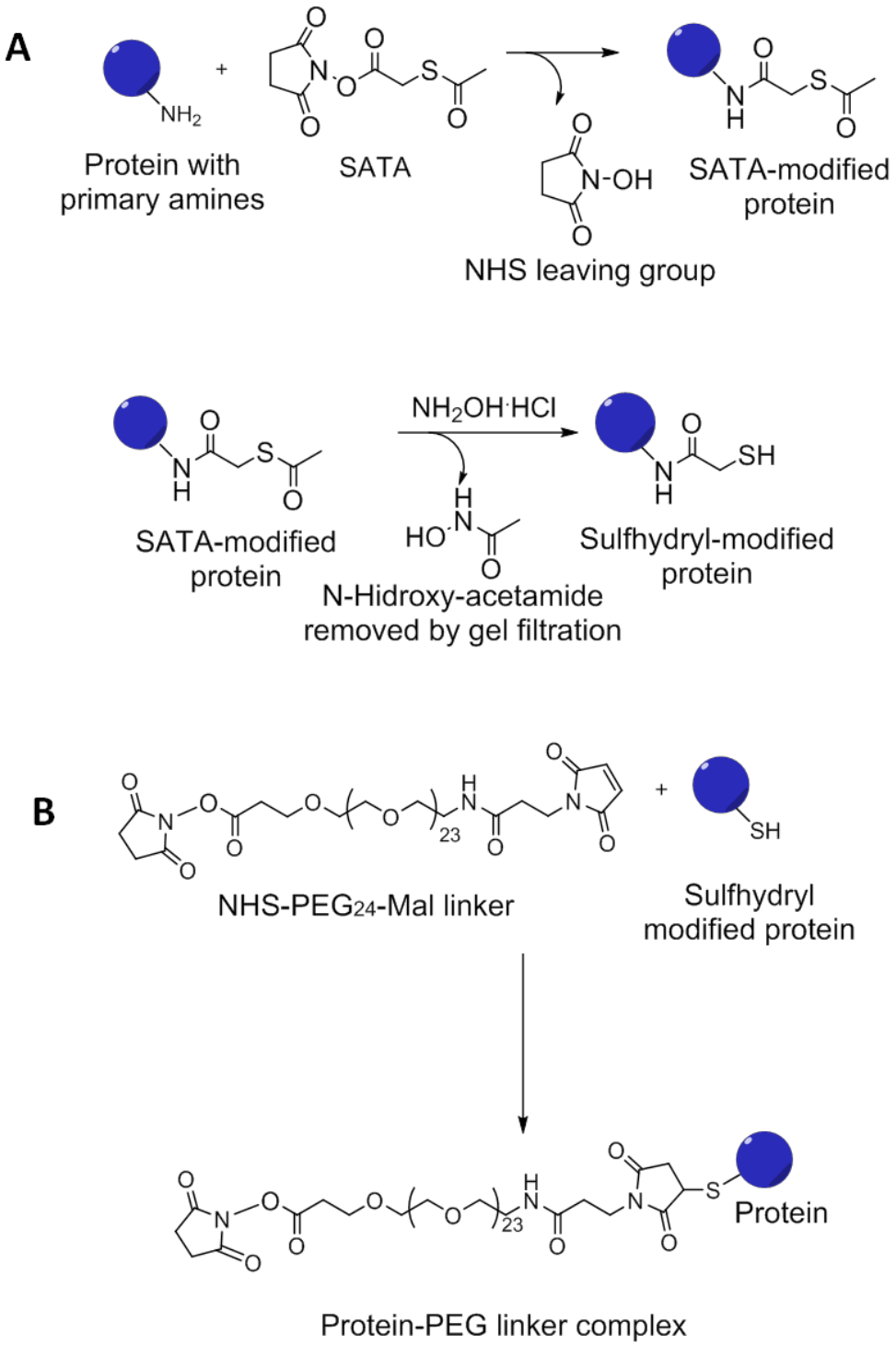

Figure 2.6. Scheme of the sulfhydryl modification of a protein and its subsequent cross-linking to a heterobifunctional PEG linker.

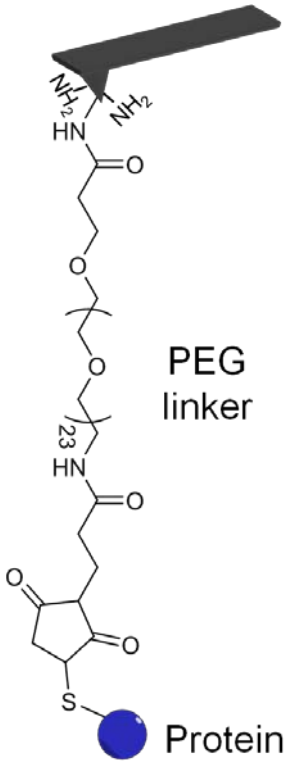

Figure 2.7. AFM tip functionalized with a PEG-protein complex

2.4. Energy landscape of biorecognition processes

The unbinding forces measured in SMFS experiments are in a way meaningless and difficult to compare when changing the experimental set-up. The reason is that force is not a thermodynamic parameter like entropy, enthalpy or free energy, so it is not a constant of the system. Therefore, one of the key issues in SMFS is how to connect the rupture forces to fundamental and kinetic parameters of a single bond.

The interaction between two molecular species A and B that form a complex AB is depicted in Figure 2.7. If the bound and the unbound states are separated by one transition state characterized by a single energy barrier, the reaction can be described as follows:

$$A + B \underset{k_{off}}{\overset{k_{on}}{\rightleftharpoons}} AB \qquad (2.1)$$

where k_{on} and k_{off} are the affinity and dissociation rates of the formed complex. The affinity rate, k_{on}, describes the diffusive properties of the molecules. The dissociation rate, k_{off}, being the inverse of the characteristic lifetime of the complex, τ_0 ($\tau_0 = k_{off}^{-1}$), defines the specificity of the interaction. The association AB satisfies the time-dependent equation:

$$\frac{d[AB]}{dt} = k_{on}[A][B] - k_{off}[AB] \qquad (2.2)$$

where [AB], [A] and [B] are the molar concentrations of the molecular complex AB and of the isolated molecules A and B. At equilibrium,

$$\frac{d[AB]}{dt} = 0 \qquad (2.3)$$

and according to the law of mass action

$$\frac{[AB]}{[A][B]} = \frac{k_{on}}{k_{off}} = K_a = \frac{1}{K_d} \qquad (2.4)$$

where K_a and K_d are the association and dissociation constants.

According to the reaction rate theory[35, 36], the dissociation constant k_{off} for a reaction in which the bound and the unbound states are separated by a single energy barrier is described by the Eyring equation[37], which is an Arrhenius-like expression:

$$k_{off} = \nu \cdot e^{\left(\frac{-\Delta G^*}{k_B T}\right)} \qquad (2.5)$$

The pre-exponential factor ν is a constant which expresses the fraction of reactant molecules with enough kinetic energy to react. The units of the pre-exponential factor depend on the reaction order as follows: for first-order (unimolecular) reactions the units are s^{-1}, while for second-order (bimolecular) reactions the units are $s^{-1}cm^{-3}$. The activation free energy of the reaction ΔG^* is the height of the energy barrier between the bound and the transition state of highest energy to which the system has to be raised before dissociation can occur, k_B is the Boltzmann constant and T is the absolute temperature.

2.4.1. The Bell-Evans model

Starting from the reaction rate theory, Bell was the first to introduce a phenomenological description of how an external force pulling on a bond reduces the activation energy barrier towards dissociation[38]. According to him, the presence of an external force helps the system overcome the potential barrier by thermal fluctuations and breaks the bond, thus reducing the lifetime of the bond. This in turn leads to processes occurring at shorter time scales than in the absence of force, which enables the study of slow dissociation processes by SMFS, otherwise inaccessible by other techniques.

In his model, Bell predicted that the presence of an external force applied in the direction favouring the unbound state, changes the activation free energy of the system as follows:

$$\Delta G^{*}(F) = \Delta G^{*}(0) - Fx_{\beta} \qquad (2.6)$$

Where $\Delta G^{*}(F)$ is the activation free energy under the application of a force F and the activation free energy of the reaction at zero force $\Delta G^{*}(0)$ decreases by a factor proportional to the applied force *F*. The reaction coordinate x_{β} corresponds to the distance between the bound and the transition state along the direction of the applied force (Figure 2.8). The model assumes that x_{β} remains constant under the external force, such that the force-dependent dissociation rate $k_{off}(F)$ can be written as:

$$k_{off}(F) = k_{off}(0) \cdot \exp\left(\frac{Fx_{\beta}}{k_B T}\right) \qquad (2.7)$$

where $k_{off}(0)$ is the dissociation rate in the absence of force. However, SMFS experiments do not provide a direct measurement of the reaction rates and the actual unbinding times might follow a broad statistical distribution. Moreover, the applied external forces are not constant in time, but they grow linearly with their retraction distance due to the Hookean stretching behaviour of the AFM cantilevers.

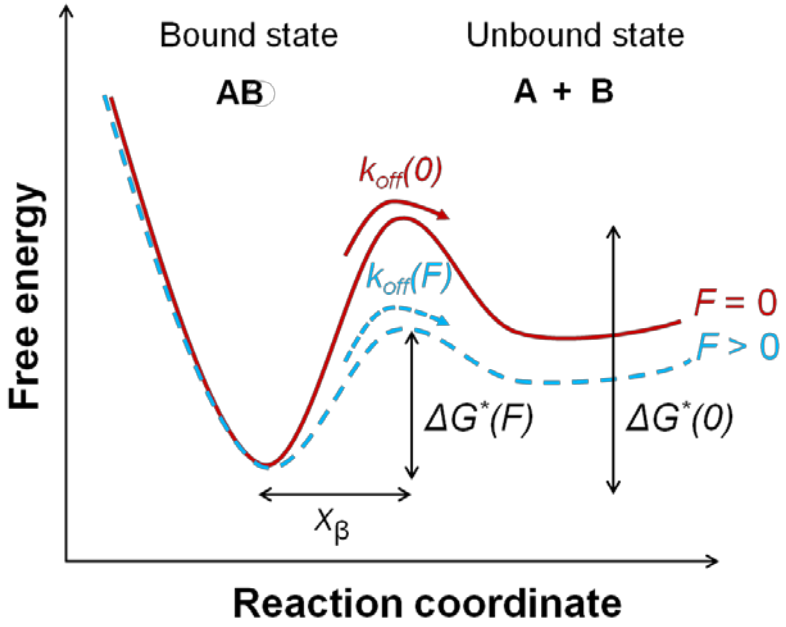

Figure 2.8. Energy landscape of an equilibrium biomolecular dissociation (continuous red line) and under the application of an external force, F (dashed blue line). The bound and unbound states are separated by an energy barrier, ΔG^*. The distance between the bound and the unbound states is called reaction coordinate, x_β, while the dissociation constant in the absence of force is $k_{off}(0)$ and in the presence of force is $k_{off}(F)$.

Starting from the Bell model, Evans and Ritchie assumed an external force, $F(t)$, that increases linearly in time and derived the survival probability $S(t)$ of the process[39-41] (i.e. the probability that the system is still in the bound state at the time t):

$$\frac{dF}{dt} = r \qquad (2.8)$$

$$\frac{dS(t)}{dt} = -k_{off}\left(F(t)\right)\cdot S(t) \qquad (2.9)$$

and thus

$$S(t) = \exp\left[-\int_0^t k_{off}(t')dt'\right] \qquad (2.10)$$

where r is the loading rate and $k_{off}(F(t))$ is the time-dependent dissociation rate. The survival probability, $S(t)$, is related to the unbinding force probability distribution $P(F)$ as follows:

$$P(F)dF = -\dot{S}(\tau)d\tau \qquad (2.11)$$

where τ is the lifetime of the complex. This results in a probability distribution equal to:

$$P(F) = \frac{k_{off}(F)}{r}\exp\left[-\int_0^F \frac{k_{off}(F')}{r(F')}dF'\right] \qquad (2.12)$$

which by carrying on the integration becomes

$$P(F) = \frac{k_{off}(F)}{r}\exp\left[\frac{Fx_\beta}{k_BT} + \frac{k_{off}\cdot k_BT}{x_\beta \cdot r}\left(1-\exp\left(\frac{Fx_\beta}{k_BT}\right)\right)\right] \qquad (2.13)$$

Finally, by calculating the maximum of the probability distribution function, $P(F)$, the most probable unbinding force, F^*, for a certain loading rate, r, is given by the following equation:

$$F^*(r) = \frac{k_BT}{x_\beta}\ln\left(\frac{x_\beta r}{k_{off}(0)k_BT}\right) \qquad (2.14)$$

According to Equation 2.14, the most probable unbinding force, F^*, will depend linearly on the logarithm of the loading rate, as illustrated in figure 2.9[42]. In addition to that, Equation 2.14 relates the forces measured in SMFS experiments with the dissociation rate in the absence of force, $k_{off}(0)$, and the position of the energy barrier along the reaction coordinate, x_β. By plotting F^* *vs.* $\ln(r)$ and doing a linear fit, x_β can be extracted from the slope of the fit, while $k_{off}(0)$ can be calculated from the intercept.

Once k_{off} is estimated using the Bell-Evans model, Equation 2.15, developed by Eyring[37] in the frame of the transition state theory, can be used to extract the free energy of the unbinding process $\Delta G_{unbinding}$:

$$\Delta G_{unbinding} = -k_B T \ln\left(\frac{k_{off}(0)\cdot h}{k_B T}\right) \qquad (2.15)$$

where *h* is Planck's constant.

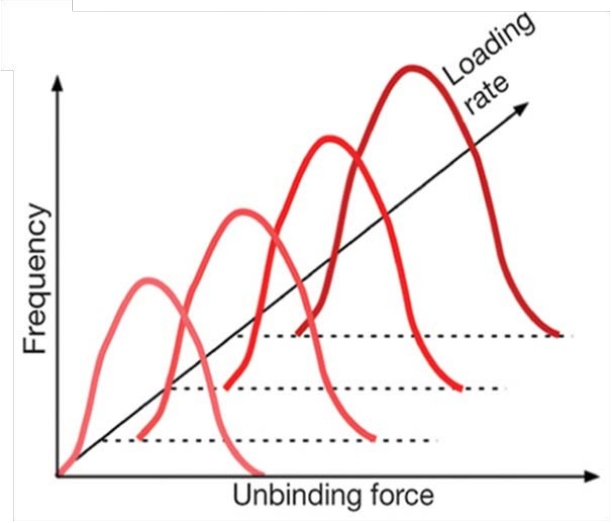

Figure 2.9. Dependence of the unbinding forces distribution with the loading rate, as predicted by the Bell-Evans model. Adapted from Ref. 42.

2.4.2. The effective loading rate

While theoretical models consider the cantilever stiffness as the defining factor in shaping the reaction potential, the use of polymer tethers as part of the AFM tip functionalization procedure lead to the introduction of the effective force constant k_{eff}, as the combination between the cantilever stiffness or force constant, k, and the polymer linker stiffness, k_{linker} (Figure 2.10). The effective force constant is equivalent to the force constant of two springs in series:

$$k_{eff} = \left(k^{-1} + k_{linker}^{-1}\right)^{-1} \qquad (2.16)$$

A practical approach used for the determination of the effective force constant is from the slope of the retraction curve before the jump-off to surface[43]. The effective loading rate, r_{eff}, is then obtained by multiplying the tip pulling speed, s, with the effective force constant of the cantilever-linker system:

$$r_{eff} = k_{eff} \cdot s \qquad (2.17)$$

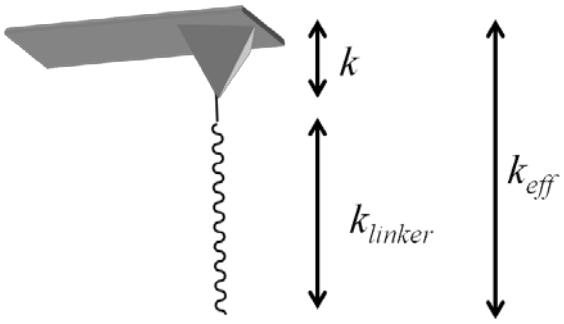

Figure 2.10. The effective force constant k_{eff} is the combination of the cantilever stiffness k and the stiffness k_{linker} of the PEG linker.

2.4.3. Polymer stretching under force

Flexible polymer chains are moving continuously at room temperature due to Brownian motion. They tend towards an equilibrium state of maximum entropy, the random coil configuration, which implies a large number of possible configurations. Since all these configurations cannot be described explicitly, a statistical mechanics approach is used to derive mean values describing the mean properties of the system. The mechanical properties of nucleic acids, proteins and polymers have been extensively studied by SMFS [14, 16, 44]. These studies provided insights on the elasticity of the molecules, but also on the energy barriers between the folded and unfolded states. Several models were developed to describe the behaviour of polymers upon stretching and the most proeminent are the freely jointed chain (FJC) model and the worm-like chain (WLC) model and their extensions. These models are used to fit the non-linear force-extension data measured by stretching polymers tethered to AFM tips [13, 25, 28].

The freely jointed chain model (also called the randomly jointed chain model) describes a single flexible polymer chain consisting of a series of n rigid segments of Kuhn length l_k connected by freely-rotating joints (Figure 2.11A)[44, 45]. The FJC model assumes that in the absence of force there is (1) no directional preference of bond angles, so the polymer chain follows a random walk in space; (2) no excluded volume effects due to long-range interactions between monomers; (3) free rotation at bond junctions. Upon the application of a tensile force F along the z direction of the freely jointed chain, the randomly

oriented segments align along the direction of the applied force, the configurational entropy is reduced, which reduces the number of possible chain configurations and the chain uncoils. The fully extended chain length is called contour length L_c

$$L_C = n \cdot l_K \qquad (2.18)$$

The extension of the polymer chain as a function of the pulling force is described by Equation 2.19:

$$x(F) = L_C \left[\coth\left(\frac{Fl_K}{k_B T}\right) - \frac{k_B T}{Fl_K} \right] \qquad (2.19)$$

where $x(F)$ is the molecular extension under the applied force F, L_c the contour length, l_K the Kuhn length, T the temperature and k_B the Boltzmann constant.

The FJC model was used to describe the elastic behaviour of a large number of macromolecules, such as polyethylene glycol in hexadecane, poly(methacrylic acid) and polydimethilsiloxane[44, 46, 47]

Deviations from the predictions of the FJC model at high stretching forces, led to the introduction of the extended freely jointed chain (eFJC) model[48, 49]. While the FJC model assumes an entropic dependence of force upon extension up to a maximum extension given by the contour length, the eFJC model hypothesizes that at high stretching forces, the molecular response becomes increasingly enthalpic and a molecule may be overstretched beyond its contour length. This is explained by the fact that before a chemical bond reaches its breaking point, the stretching of covalent bonds and the deformation of bond angles under force result in an increase in the effective the segment length. As depicted in figure 2.11B, the eFJC introduces an additional segment elasticity parameter k_s to account for the elasticity of individual segments when stretched:

$$x(F) = L_C \left[\coth\left(\frac{Fl_K}{k_B T}\right) - \frac{k_B T}{Fl_K} \right] \left(1 + \frac{F}{k_s l_K} \right) \qquad (2.20)$$

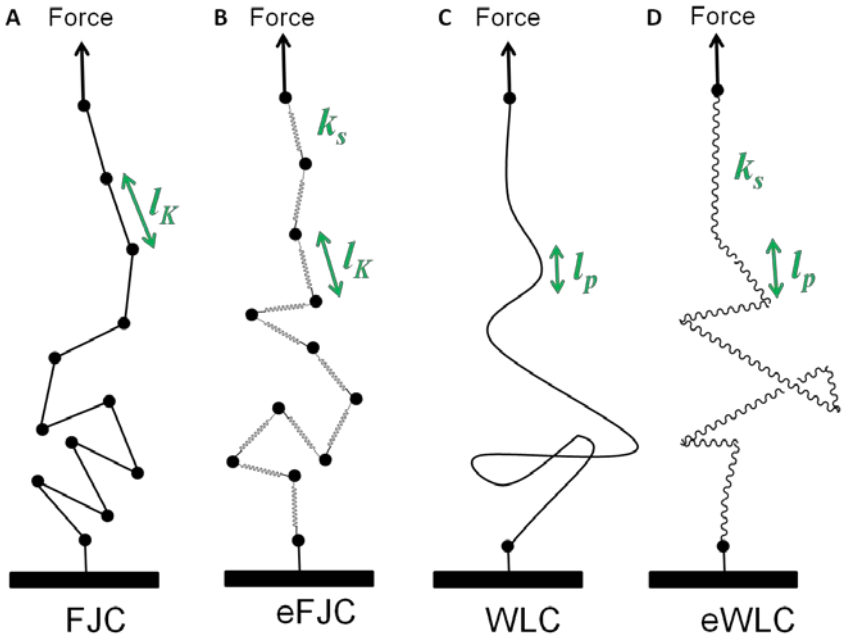

Figure 2.11. Polymer elasticity models commonly used in single-molecule force spectroscopy. A: The freely jointed chain (FJC) model considers a flexible polymer chain consisting of *n* rigid segments of characteristic length l_K (Kuhn length) connected in linear succession by freely rotating joints. B: The extended freely jointed chain (eFJC) model accounts for the enthalpic deformability of chain segments of length l_K by modeling them as elastic springs with a characteristic segment elasticity k_s. C: The worm-like chain (WLC) model does not consider any discrete structure along the polymer chain and describes it as a flexible rod with stiffness determined by the persistence length l_p. D: The extended worm-like chain (eWLC) model takes into the account the enthalpic deformability of the polymer chain in a similar fashion as the eFJC model.

The worm-like chain model (also called the Kratky-Porod model) does not consider any discrete structure along the polymer chain and it can be considered as a limit of the freely rotating chain when $l_K \rightarrow 0$ and $n \rightarrow \infty$ simultaneously [50, 51]. The polymer is treated as a homogenous elastic rod characterized by its contour length Lc and persistence length lp (Figure 2.11C). The persistence length is a measure of the distance over which two segments remain directionally correlated and it is related to the local bending stiffness of the polymer. In the frame of the WLC model, the force F versus extension x is given by Equation 2.21:

$$F(x) = \frac{k_B T}{l_p}\left(\frac{1}{4\left(1-\frac{x}{Lc}\right)^2} - \frac{1}{4} + \frac{x}{L_c}\right) \quad (2.21)$$

The assumptions of the WLC model were found to be valid up to forces of several hundred of pN and the extension behaviour of several proteins was described using this model [14, 52].

An extension of the WLC model was developed to account for the enthalpic deformability of the chain segments, in the same fashion as described for the FJC model[53, 54] (Figure 2.11D). In the high force regime, an additional stretching term, the stiffness of the chain Φ is introduced to quantify the increase of the chain extension:

$$F(x) = \frac{k_B T}{l_p}\left(\frac{1}{4\left(1-\frac{x}{Lc}+\frac{F(x)}{\Phi}\right)^2} - \frac{F(x)}{\Phi} - \frac{1}{4} + \frac{x}{L_c}\right) \quad (2.22)$$

2.5. Fast localization of biomolecular interactions

2.5.1. Topography and Recognition Imaging

Since its invention, the AFM has proven its excellent capabilities to resolve structural details of biological samples and to detect molecular recognition processes. These capabilities have been combined into a new technique introduced in 2004 by the group of Hinterdorfer[55, 56], which enables the study of single-molecule interactions while simultaneously recording high-resolution topography images. The technique is now commercially available under the name of Topography and Recognition Imaging (TREC). The principle of the technique is based on a magnetically driven AM-AFM in liquid[57]. As depicted in Figure 2.12, a functionalized AFM probe is oscillated with a magnetic field close

to its resonance frequency while it scans the sample surface. The cantilever´s oscillation amplitude signal is separated into two parts, a lower one containing information on the sample topography and an upper one comprising information on the recognition processes. If a molecular recognition process takes place between the biomolecules on tip and the surface, a reduction of the cantilever oscillation amplitude will take place until the probe moves away from the binding site. By recording the maxima of these parts, topography and recognition maps are reconstructed. If these maps are overlapped, the precise locations of specific molecular binding processes can be identified[58]. The method was demonstrated on receptor-ligand pairs, protein lattices, remodelled chromatin structures, cells and cell membranes[55, 56, 59, 60]. This technique was the first to allow the investigation of binding sites distributions with manometer resolution and under physiological conditions. However, the quantification of the molecular interaction and the extraction of thermodynamic parameters are not trivial tasks due to the complexity of the cantilever dynamics in AM-AFM.

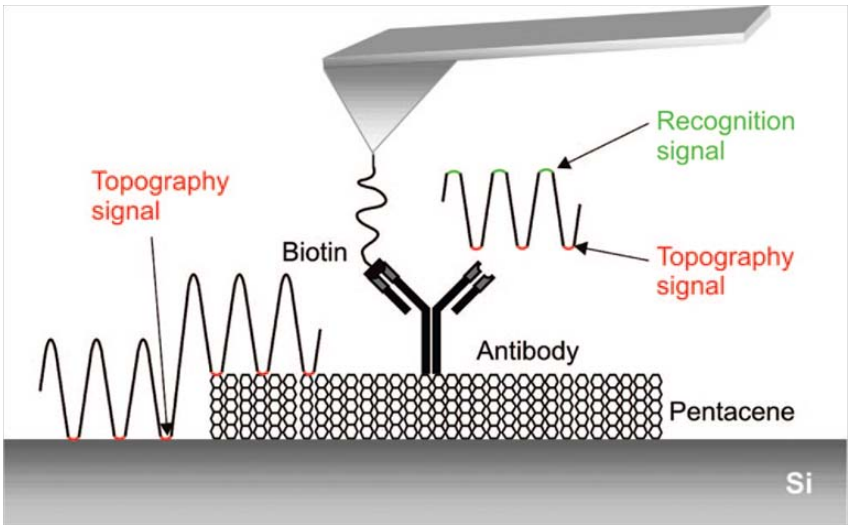

Figure 2.12. Principle of TREC imaging. A magnetically driven cantilever oscillates across the surface. The oscillation signal is split into two parts of which the lower part is used to generate the topography (topography signal, red) and the upper part is used for the recognition image (recognition signal, green). Adapted from Ref. 48.

2.5.2. High-speed force-spectroscopy

Sahin´s group used the torsional harmonic cantilever concept previously developed for high-resolution nanomechanical mapping to demonstrate a rapid interface which allows the detection of single-molecule interactions[61, 62]. T-shaped AFM cantilevers enabled the acquisition of high-speed force-distance curves while imaging the sample in AM-AFM. In this setup, illustrated in Figure 2.13, tip-sample interaction forces are monitored at every single oscillation cycle with sufficient signal-to-noise ratio. While the sample is scanned in the *x*-*y* plane, the T-shaped cantilever is twisted as a result of the tip-sample interaction forces. The twist angle gives the instantaneous force on the tip, while the vertical deflection signal indicates the tip position.

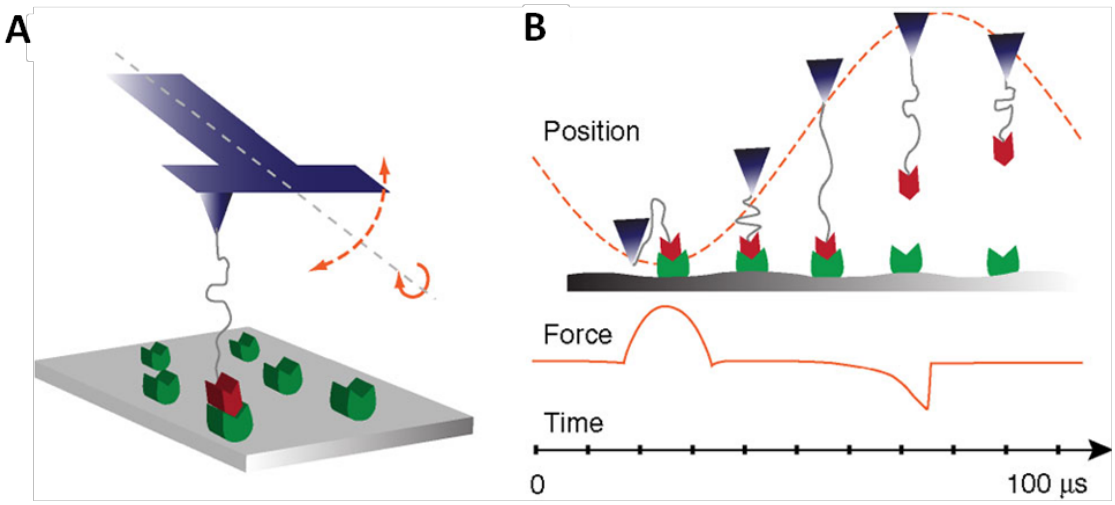

Figure 2.13. Rapid interface for the detection of single-molecule interations. A: A ligand is tethered to a T-shaped AFM cantilever via a flexible polymer spacer. Tip-sample interactions twist the vibrating cantilever. The vertical deflection signal gives the tip position, and the twist angle gives the instantaneous force on the tip. B: The sharp tip vibrates in a sinusoidal trajectory (dashed orange curve) and if a molecular recognition event occurs between the ligand and the receptor, the flexible spacer stretches upon retraction of the tip until the ligand unbinds (solid orange curve). This entire process takes ~100 μs and the molecules are bound for a small fraction of this period. Adapted from Ref. 50.

SMFS measurements on the microsecond timescale were carried out for the first time, along with the acquisition of high-resolution maps of the rupture forces. The biotin-streptavidin complex was investigated at short timescales,

which revealed the existence of an additional energy barrier. At the same time, the 100 μs time resolution brought the experiments as close as an order of magnitude away from molecular dynamics simulations.

The gap between molecular dynamics simulations and force-spectroscopy experiments was recently filled by Rico *et al*. [15]. An adaptation of the high-sped atomic force microscope (HS-AFM) initially developed by Ando[63] made possible the unfolding of a protein over a range of pulling velocities spanning 6 orders of magnitudes (from 0.0097 to 3870 μm/s), encompassing the range of molecular dynamics simulations (>2800 μm/s)[64]. The 1 μs time range allowed the direct comparison of force-spectroscopy measurements and molecular dynamics simulations. The now accessible dynamic range of high-speed force spectroscopy (HS-FS) will probably trigger the development of novel theories and provide new insights into relevant biological processes such as receptor-ligand unbinding, lipid membrane dynamics or cell adhesion.

2.5.3. Force-distance curve-based atomic force microscopy

In contact-mode based force maps, a force curve is recorded in every pixel of the image. These kinds of measurements have certain limitations, such as poor spatial and temporal resolution. Recent developments of the electronics of AFM instruments have overcome these limitations. This has allowed the high-resolution imaging of membrane proteins while mapping their nanomechanical properties[65, 66]. Molecular recognition studies have been carried out in Force-distance (FD) curve-based AFM and this has allowed the detection and localization of receptor-ligand interactions on the cell surface[9, 67]. In this mode, the AFM probe is used to record an array of force curves over the sample (Figure 2.14A). The tip is continuously approached and retracted from the sample and in each such cycle, the sample height is determined and tip-sample interactions are analysed (Figure 2.14B). Quantitative parameters, such as Young's modulus, stiffness, energy dissipation and adhesion, can then be extracted, mapped pixel-by-pixel and directly correlated to the topography. Müller and his co-workers were able to combine high-resolution imaging and quantitative mapping of specific interactions in single native proteins[27]. The

interaction between a Ni^{+}-*N-nitrilotriacetate*-functionalized AFM tip (Ni^{+}-NTA) and *histidine* residues (His_6-tags) on a native protein were detected and quantified at subnanometer resolution. High-resolution images of single proteins adsorbed on gold-coated mica, along with the corresponding adhesion maps quantifying the interaction forces between the tip and the sample were achieved. This recent study opens the possibility to locate and quantify molecular interactions sites on the surface of biological molecules.

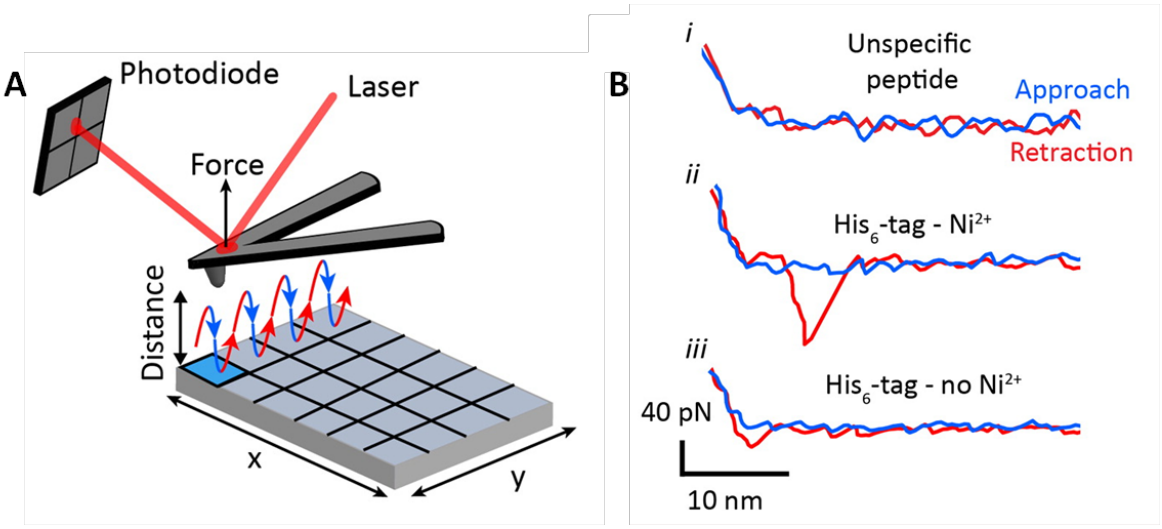

Figure 2.14. Principle of FD-based AFM. A: The cantilever is approached and retracted from the sample in each pixel of the image and the interaction forces are recorded as a function of the tip–sample distance. B: Approach (blue) and retraction (red) force curves recording (i) no interactions , (ii) specific interactions between the tip and the sample, and (iii) unspecific interactions. Adapted from Ref. 27.

2.6. References

1. A. R. Bizzarri and S. Cannistraro, *Dynamic Force Spectroscopy and Biomolecular Recognition*, Taylor & Francis, 2012.
2. D. Morikis and J. D. Lambris, *Trends in Immunology*, 2004, **25**, 700-707.
3. K. Lindorff-Larsen, R. B. Best, M. A. DePristo, C. M. Dobson and M. Vendruscolo, *Nature*, 2005, **433**, 128-132.
4. P. Schuck, *Annual Review of Biophysics and Biomolecular Structure*, 1997, **26**, 541-566.
5. T. Ha, *Nat Meth*, 2014, **11**, 1015-1018.
6. V. T. Moy, E. L. Florin and H. E. Gaub, *Science*, 1994, **266**, 257-259.
7. G. U. Lee, D. A. Kidwell and R. J. Colton, *Langmuir*, 1994, **10**, 354-357.
8. D. Kim and O. Sahin, *Nat Nano*, 2015, **10**, 264-269.
9. V. Dupres, F. D. Menozzi, C. Locht, B. H. Clare, N. L. Abbott, S. Cuenot, C. Bompard, D. Raze and Y. F. Dufrene, *Nat Meth*, 2005, **2**, 515-520.
10. F. Rico and V. T. Moy, *Journal of Molecular Recognition*, 2007, **20**, 495-501.
11. P. Hinterdorfer, W. Baumgartner, H. J. Gruber, K. Schilcher and H. Schindler, *Proceedings of the National Academy of Sciences*, 1996, **93**, 3477-3481.
12. F. Schwesinger, R. Ros, T. Strunz, D. Anselmetti, H. J. Guntherodt, A. Honegger, L. Jermutus, L. Tiefenauer and A. Pluckthun, *Proc Natl Acad Sci U S A*, 2000, **97**, 9972-9977.
13. A. R. Bizzarri and S. Cannistraro, *Nanotechnology*, 2014, **25**, 335102.
14. M. Rief, M. Gautel, F. Oesterhelt, J. M. Fernandez and H. E. Gaub, *Science*, 1997, **276**, 1109-1112.
15. F. Rico, L. Gonzalez, I. Casuso, M. Puig-Vidal and S. Scheuring, *Science*, 2013, **342**, 741-743.
16. M. Carrion-Vazquez, A. F. Oberhauser, S. B. Fowler, P. E. Marszalek, S. E. Broedel, J. Clarke and J. M. Fernandez, *Proceedings of the National Academy of Sciences*, 1999, **96**, 3694-3699.
17. C. Ke, M. Humeniuk, H. S-Gracz and P. E. Marszalek, *Physical Review Letters*, 2007, **99**, 018302.
18. C. Tromas, J. Rojo, J. M. de la Fuente, A. G. Barrientos, R. García and S. Penadés, *Angewandte Chemie International Edition*, 2001, **40**, 3052-3055.
19. T. V. Ratto, K. C. Langry, R. E. Rudd, R. L. Balhorn, M. J. Allen and M. W. McElfresh, *Biophysical journal*, 2004, **86**, 2430-2437.
20. D. Alsteens, P. Van Dijck, P. N. Lipke and Y. F. Dufrene, *Langmuir*, 2013, **29**, 13473-13480.
21. A. V. Taubenberger, D. W. Hutmacher and D. J. Muller, *Tissue Engineering Part B: Reviews*, 2013, **20**, 40-55.
22. K. A. Dill and J. L. MacCallum, *Science*, 2012, **338**, 1042-1046.
23. K. A. Dill, S. B. Ozkan, M. S. Shell and T. R. Weikl, *Annual Review of Biophysics*, 2008, **37**, 289-316.
24. A. Fuhrmann, J. C. Schoening, D. Anselmetti, D. Staiger and R. Ros, *Biophysical journal*, 2009, **96**, 5030-5039.
25. D. Alsteens, M. Pfreundschuh, C. Zhang, P. M. Spoerri, S. R. Coughlin, B. K. Kobilka and D. J. Muller, *Nat Meth*, 2015, **12**, 845-851.
26. A. R. Bizzarri and S. Cannistraro, *Chemical Society reviews*, 2010, **39**, 734-749.
27. M. Pfreundschuh, D. Alsteens, M. Hilbert, M. O. Steinmetz and D. J. Müller, *Nano Lett.*, 2014, **14**, 2957-2964.
28. T. A. Sulchek, R. W. Friddle, K. Langry, E. Y. Lau, H. Albrecht, T. V. Ratto, S. J. DeNardo, M. E. Colvin and A. Noy, *Proc. Natl. Acad. Sci. U. S. A.*, 2005, **102**, 16638-16643.
29. M. Odorico, J.-M. Teulon, T. Bessou, C. Vidaud, L. Bellanger, S.-w. W. Chen, É. Quéméneur, P. Parot and J.-L. Pellequer, *Biophysical journal*, 2007, **93**, 645-654.

30. C. Verbelen, H. J. Gruber and Y. F. Dufrêne, *Journal of Molecular Recognition*, 2007, **20**, 490-494.
31. R. Ros, F. Schwesinger, D. Anselmetti, M. Kubon, R. Schäfer, A. Plückthun and L. Tiefenauer, *Proceedings of the National Academy of Sciences*, 1998, **95**, 7402-7405.
32. L. A. Chtcheglova, A. Haeberli and G. Dietler, *Biopolymers*, 2008, **89**, 292-301.
33. A. S. M. Kamruzzahan, A. Ebner, L. Wildling, F. Kienberger, C. K. Riener, C. D. Hahn, P. D. Pollheimer, P. Winklehner, M. Hölzl, B. Lackner, D. M. Schörkl, P. Hinterdorfer and H. J. Gruber, *Bioconjugate Chemistry*, 2006, **17**, 1473-1481.
34. G. T. Hermanson, in *Bioconjugate Techniques (Third edition)*, ed. G. T. Hermanson, Academic Press, Boston, 2013, DOI: http://dx.doi.org/10.1016/B978-0-12-382239-0.00003-0, pp. 229-258.
35. H. A. Kramers, *Physica*, 1940, **7**, 284-304.
36. P. Hänggi, P. Talkner and M. Borkovec, *Reviews of Modern Physics*, 1990, **62**, 251-341.
37. H. Eyring, *The Journal of Chemical Physics*, 1935, **3**, 107-115.
38. G. I. Bell, *Science*, 1978, **200**, 618-627.
39. E. Evans and K. Ritchie, *Biophysical journal*, 1997, **72**, 1541-1555.
40. R. Merkel, P. Nassoy, A. Leung, K. Ritchie and E. Evans, *Nature*, 1999, **397**, 50-53.
41. E. Evans, K. Ritchie and R. Merkel, *Biophysical journal*, 1995, **68**, 2580-2587.
42. Y. F. Dufrene, D. Martinez-Martin, I. Medalsy, D. Alsteens and D. J. Muller, *Nature Methods*, 2013, **10**, 847-854.
43. C. Friedsam, A. K. Wehle, F. Kühner and H. E. Gaub, *Journal of Physics: Condensed Matter*, 2003, **15**, S1709.
44. F. Oesterhelt, M. Rief and H. E. Gaub, *New Journal of Physics*, 1999, **1**, 6.1-6.5.
45. P. J. Flory, *Statistical mechanics of chain molecules*, Interscience Publishers, 1969.
46. C. Ortiz and G. Hadziioannou, *Macromolecules*, 1999, **32**, 780-787.
47. A. Janshoff, M. Neitzert, Y. Oberdörfer and H. Fuchs, *Angewandte Chemie International Edition*, 2000, **39**, 3212-3237.
48. S. B. Smith, Y. Cui and C. Bustamante, *Science*, 1996, **271**, 795-799.
49. A. V. Dobrynin, J.-M. Y. Carrillo and M. Rubinstein, *Macromolecules*, 2010, **43**, 9181-9190.
50. J. F. Marko and E. D. Siggia, *Macromolecules*, 1995, **28**, 8759-8770.
51. C. Bustamante, J. Marko, E. Siggia and S. Smith, *Science*, 1994, **265**, 1599-1600.
52. A. F. Oberhauser, P. E. Marszalek, H. P. Erickson and J. M. Fernandez, *Nature*, 1998, **393**, 181-185.
53. T. Odijk, *Macromolecules*, 1995, **28**, 7016-7018.
54. M. D. Wang, H. Yin, R. Landick, J. Gelles and S. M. Block, *Biophysical journal*, 1997, **72**, 1335-1346.
55. C. M. Stroh, A. Ebner, M. Geretschläger, G. Freudenthaler, F. Kienberger, A. S. M. Kamruzzahan, S. J. Smith-Gill, H. J. Gruber and P. Hinterdorfer, *Biophysical journal*, 2004, **87**, 1981-1990.
56. C. Stroh, H. Wang, R. Bash, B. Ashcroft, J. Nelson, H. Gruber, D. Lohr, S. M. Lindsay and P. Hinterdorfer, *Proc. Natl. Acad. Sci. U. S. A.*, 2004, **101**, 12503-12507.
57. E. T. Herruzo and R. Garcia, *Applied Physics Letters*, 2007, **91**, 3.
58. J. Preiner, A. Ebner, L. A. Chtcheglova, R. Zhu and P. Hinterdorfer, *Nanotechnology*, 2009, **20**, 215103.
59. J. Preiner, N. S. Losilla, A. Ebner, P. Annibale, F. Biscarini, R. Garcia and P. Hinterdorfer, *Nano Lett.*, 2009, **9**, 571-575.
60. L. A. Chtcheglova, J. Waschke, L. Wildling, D. Drenckhahn and P. Hinterdorfer, *Biophysical journal*, 2007, **93**, L11-L13.
61. M. D. Dong, S. Husale and O. Sahin, *Nature Nanotechnology*, 2009, **4**, 514-517.
62. M. Dong and O. Sahin, *Nat Commun*, 2011, **2**, 247.

63. T. Ando, N. Kodera, E. Takai, D. Maruyama, K. Saito and A. Toda, *Proceedings of the National Academy of Sciences*, 2001, **98**, 12468-12472.
64. E. H. Lee, J. Hsin, M. Sotomayor, G. Comellas and K. Schulten, *Structure*, 2009, **17**, 1295-1306.
65. F. Rico, C. Su and S. Scheuring, *Nano Lett.*, 2011, **11**, 3983-3986.
66. I. Medalsy, U. Hensen and D. J. Muller, *Angewandte Chemie International Edition*, 2011, **50**, 12103-12108.
67. S. Lee, J. Mandic and K. J. Van Vliet, *Proceedings of the National Academy of Sciences*, 2007, **104**, 9609-9614.

Chapter 3

Unbinding forces and energies between a siRNA molecule and a dendrimer measured by force spectroscopy

3.1. Introduction

After being regarded as a promising toolbox for decades, nanotechnology is now a reality and it provides scientists sub-100 nm building blocks for the development of new materials and devices. Nanomedicine encompasses the healthcare applications of nanotechnology, as follows[1]:

- Diagnostics tools and sensors to be used *ex vivo*;
- Innovative imaging and monitoring technologies for diagnostic and sensing applications;
- Novel technologies and biomaterials for drug delivery and tissue engineering.

Nanomedicine formulations are expected to enable less toxic and more effective therapies and diagnostics. Moreover, the use of nanotechnology in the rational design of advanced drug delivery systems could lead to significant improvements in the delivery of therapeutic agents and facilitate their crossing of cellular barriers.

Gene therapy is one of the most important applications of nanomedicine, since it offers new routes for the effective treatment of cancer or neurodegenerative diseases, which are only poorly treatable by conventional methods. Specifically, RNA interference (RNAi) is an endogenous pathway in which small RNA molecules, such as microRNA (miRNA) and synthetic short interfering RNA (siRNA) are able to silence the expression of a gene. By activating this pathway,

siRNA can induce the sequence-specific degradation of target homologous single-stranded RNA[2] and it is able to inactivate the expression of virtually any gene, and the expression of its encoded protein, at almost any stage in development[3] with high specificity and efficiency. The therapeutic potential of siRNA therapeutics is far-reaching and it can now reach targets that were traditionally considered to be “undruggable”. To this day, at least 22 RNAi-based drugs are undergoing clinical trials and many more are being developed[4].

3.1.2. Delivery of siRNA based therapeutics

The RNAi is a fundamental pathway initiated by the presence of double-stranded RNA (dsRNA), which is cleaved by the enzyme Dicer into 21-23 nucleotide (nt) fragments with 2-nt overhangs on their 3´ ends, known as siRNA[5]. Alternatively, a practical shortcut is to directly introduce synthetic siRNA into the cell, thus bypassing Dicer mechanics. This reduces a potentially innate immune interferon response followed by the shutdown of cellular protein expression, which can take place if long dsRNA fragments of more than 30-nt interact with intracellular RNA receptors[6]. As depicted in Figure 3.1, after trespassing the cell membrane and getting into the cell cytoplasm, siRNA fragments are loaded into a protein complex, called RNA-induced silencing complex (RISC)[7]. The siRNA strands are separated into the sense strand (or passenger strand) and the antisense strand (or guide strand). The sense strand is then degraded, while the guide strand remains within the RISC. The activated RISC-guide-strand complex selectively seeks out and cleaves messenger RNA (mRNA) that is complementary to the antisense strand. This results in a selective silencing of gene expression and the blocking of translation mechanisms. The activated RISC–siRNA complex can then be recycled for the destruction of identical mRNA targets[8].

However, siRNA-based therapeutics needs to overcome certain limitations in order for their full potential to be explored. Some of the key challenges of siRNA therapeutics include: (i) the low stability against serum nucleases and rapid clearance from the systemic circulation of unmodified siRNA; (ii) poor cellular

uptake from cell culture media; (iii) the immunogenic profile of siRNA; (iv) the difficulty in crossing cellular membranes and further incorporation in the RNAi machinery; (v) possible unspecific interactions between siRNA and serum proteins or non-target cells[4, 9, 10]. As a result, either chemical modifications or encapsulating materials need to be developed to deliver siRNA to its target.

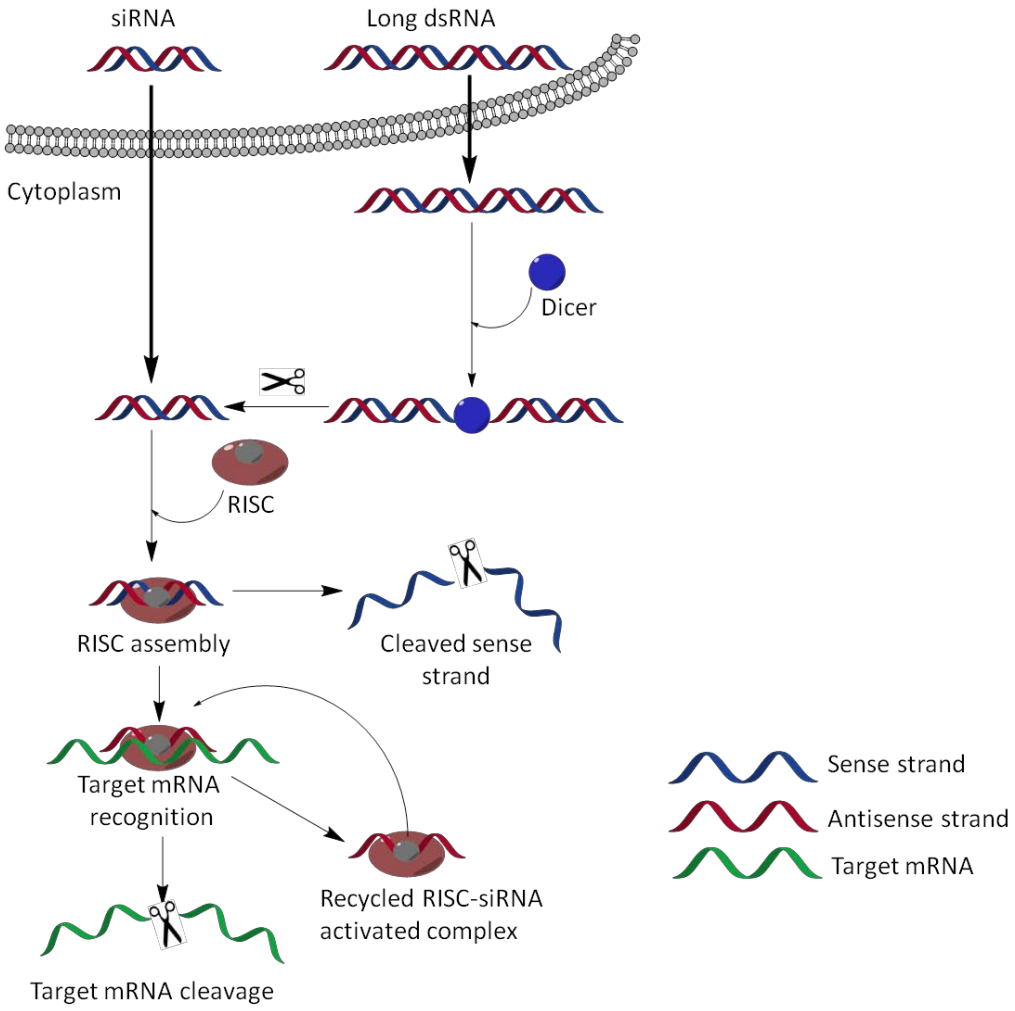

Figure 3.1. The mechanism of RNA interference. After being introduced into the cell cytoplasm, long double-stranded RNA (dsRNA) is cleaved into small interfering RNA (siRNA) by the enzyme Dicer. As an alternative, siRNA can be introduced directly into the cell. The siRNA molecule is then loaded into the RNA-induced silencing complex (RISC). At this point, the sense strand is then cleaved by argonaute 2 (AGO2), while the activated RISC-antisense-strand complex selectively seeks out and cleaves complementary mRNA. This leads to a selective silencing of the target gene. The activated RISC–siRNA complex can then be recycled for the destruction of identical mRNA targets. Adapted from Ref. 8

A number of different materials are currently explored for the *in vivo* siRNA delivery, including antibodies[11], lipids[12], peptides[13], polymers[14], aptamers[15] and small molecules[16]. Among these, the combination of siRNA with nanoparticles (NPs) yields promising systems, which proved to be very efficient for the *in vivo* delivery of siRNA[4, 17-19]. Specifically, NPs based on dendrimers have been successfully used as efficient transfection agents due to their ability of bind and condense nucleic acids into stabilized complexes. Dendrimers are hyperbranched polymers with repetitive structures that have been widely exploited for their potential biological applications including siRNA delivery[20-22]. One of the main advantages of using dendrimer NPs is the full control of their physico-chemical properties through well-established synthesis protocols available for the modification of their functional end groups. Dendrimers bear other unique characteristics, such as biodegradability, multifunctionality, low immunogenicity due to their nanosized dimensions and rheological properties which makes them suitable for efficient transfer to the targeted sites[9, 23, 24]. Polyamidoamine (PAMAM) dendrimers[25, 26] have become the most widely used dendrimer-based vectors for gene transfer since the primary amines located on the surface of these dendrimers provide a high cationic charge density that favors siRNA binding through the phosphate backbone, forming a complex called dendriplex.

However, the parameters that govern the efficiency of a given dendrimer to successfully deliver siRNA inside the cell are still not well understood. A better understanding of the mechanisms which govern the molecular interactions within dendriplexes is required in order to improve efficiency of these systems. In particular, it is important to reveal the interaction forces that bind the dendrimer to the nucleic acid. To this ambitious goal, molecular dynamics simulations have been employed during the last decade, as a tool for the *in silico* exploration of the molecular interactions in siRNA-dendrimer complexes[27-29]. The aforementioned studies have shown that a very small force of interaction precludes the stability of the dendriplex while a strong interaction force prevents the intracellular dissociation of siRNA from the dendrimer and the consequent failure of knocking down the target protein[28].

Despite the fact that the quantitative understanding of the interaction forces and energies between nucleic acids and nanoparticles used in gene delivery systems is of great importance for optimizing the transfection efficiency, only few experimental studies have focused on this matter. Xu *et al.* have investigated the interaction forces between chitosan molecules and siRNA as a function of the media pH, however they were not able to extract any information regarding the energy landscape of the interaction from their study[30].

In this chapter, a single molecule force spectroscopy approach is developed to measure the unbinding forces and free energies between siRNA and PAMAM dendrimers at the single molecule level. The formation of dendriplexes (siRNA-dendrimer complexes) has been quantified in terms of affinity and stability of the formed complex.

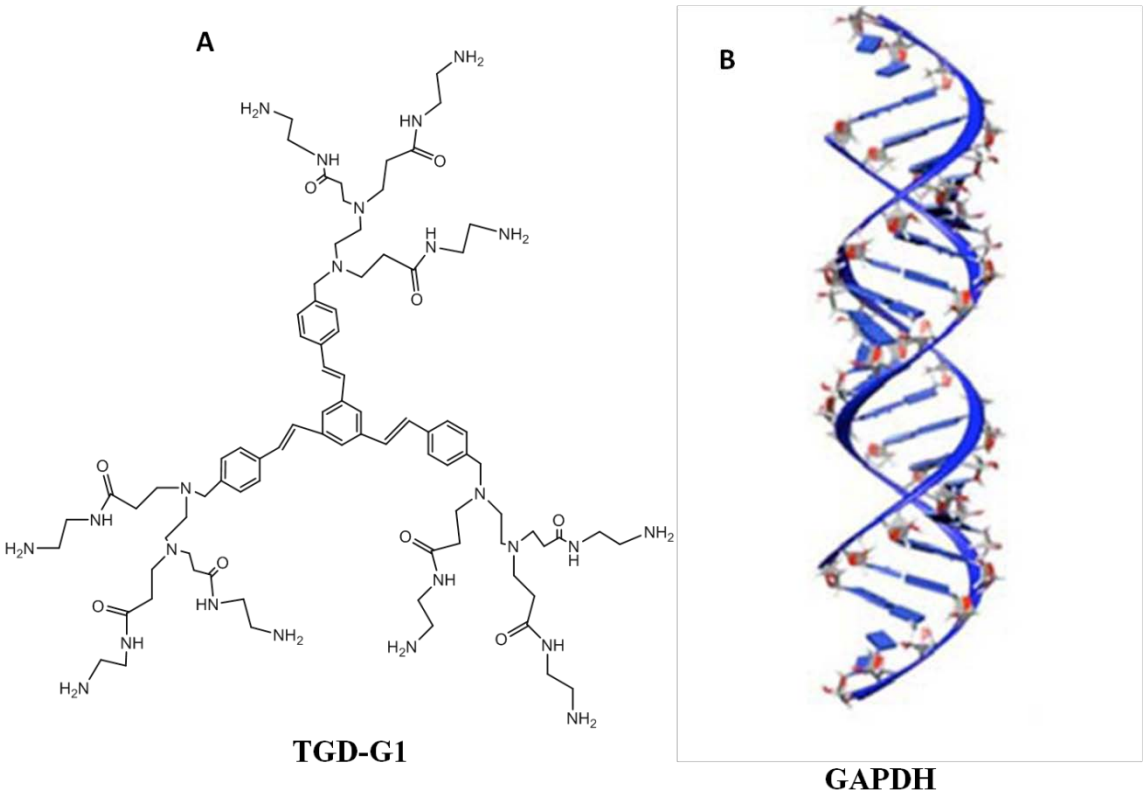

Figure 3.2. A: Chemical structure of the TGD-G1 dendrimers used in the experiments; B: The sequence of GAPDH siRNA and molecular model adapted from Ref.28.

Since largely ramified dendrimers lead to significant toxicity in vivo[31], the highly biocompatible G1 TRANSGENEN PAMAM (TGD-G1 PAMAM) dendrimer was chosen, due to its negligible toxicity and ability to efficiently deliver siRNA and to induce gene silencing in primary neuronal cultures[32, 33]. The chemical structure of the TGD-G1 dendrimer used in the experiments presented here and the sequence of GAPDH siRNA along with its molecular model are shown in Figure 3.2. This dendrimer represents a good model to study the single molecule interaction between dendrimers and siRNA including the binding forces involved in the stabilization of the complex and further siRNA transfection. A better knowledge of this interaction will help design more efficient dendrimers to deliver siRNA to the target cells.

3.2. Experimental methods

3.2.1. Materials and reagents

Phosphate buffered solution (PBS), 4-(2-hydroxyethyl)-1-piperazineethanesulfonic acid (HEPES), hydrogen peroxide 30%, sulphuric acid, 3-aminopropyl-triethoxysilane (APTES), glutaraldehyde 8%, 6-aminohexanethiol, ethanol and dimethyl sulfoxide (DMSO) were purchased from Sigma Aldrich (Spain). The 24-unit ethyleneglycol functionalized with succinimidyl and maleimido ends (NHS-PEG_{24}-Mal) was purchased from Fisher Scientific (Spain). Diethylpyrocarbamate (DEPC) and heparin were obtained from Sigma Aldrich (Spain).

Thiol-siRNA was purchased from Sigma Aldrich (Spain) and its sequence is the following:

Sense: 5´- Thiol-AAG UGG ACA UUG UUG CCA Utt - 3´
Antisense: 5´- Thiol-AUG GCA ACA AUG UCC ACU Utg - 3´

The G1 TGD PAMAM dendrimers combining a conjugated rigid polyphenylenevinylene (PPV) core with flexible polyamidoamine (PAMAM) branches were synthesized as previously described[34] and kindly provided by Prof. Valentin Ceña (Facultad de Medicina, Universidad de Castilla-La Mancha).

3.2.2. Dendrimers sample preparation

After a 30 minute ultrasonic treatment to prevent dendrimer aggregation, 20 μl of a 100 μM dendrimers solution were deposited onto a freshly cleaved piece of mica for 2 minutes. The sample was then rinsed with 10 mM HEPES.

3.2.3. Single molecule force spectroscopy measurements

Single molecule force spectroscopy experiments were performed at room temperature with a Cypher microscope (Asylum Research, Santa Barbara, USA). The experiments were performed in 0.1 M phosphate buffered solution (PBS) at pH 7.4. Triangular silicon nitride cantilevers (MSCT, Bruker, Santa Barbara, USA) with a nominal spring constant of 0.02 N/m and resonant frequency of 7 kHz were used. The tips were functionalized with a single siRNA molecule by following the procedure described in Appendix A.1.3.

Force spectroscopy measurements involve the accurate determination of the cantilever force constant as well as the optical lever sensitivity. The force constant and quality factor were determined by using the thermal noise method[35,36]. The calibrated force constant of the cantilevers was 0.02 ± 0.002 N/m. At the end of each experiment, the optical lever sensitivity was calibrated by acquiring deflection *versus* distance curves on a hard surface (mica). Typically 100 deflection *versus* distance curves were acquired and the sensitivity of the photodiode was calculated as the mean value of the slope of the deflection curve measured in the repulsive region. The force was calculated by using Hooke´s law, $F = -kd$ (*d* is the cantilever deflection, *k* is the cantilever force constant).

Force curves were acquired by approaching and retracting the tip 100 nm from the sample at different velocities (from 100 nm/s to 2.5 μm/s). The maximum

force was maintained below 100 pN to avoid damaging the molecules bound to the tip apex. In each curve, the tip was kept in contact with the sample for 0.5 s to promote the formation of siRNA-dendrimer complexes. For each functionalized tip, we have acquired several force maps, where a force curve was recorded as a function of the (*x*, *y*) coordinate. Those force maps covered 1 μm x 1 μm regions (32 x 32 data points).

3.2.4. Force spectroscopy data analysis

A total of 16800 force distance curves were recorded with 5 functionalized tips and analysed by using customized software. The data processing algorithm was designed using *Spyder* - The Scientific *PYthon* Development EnviRonment. The curves were averaged and the contact point was set by establishing a deflection threshold. The detection of an adhesion force event (either specific or unspecific) was based on the values of the second and third derivatives of the deflection. The event was labelled as an adhesion event whenever the aforementioned derivatives were found to be above 50% with respect to the noise level.

Next, an algorithm was created to discriminate unspecific from specific adhesion events (Figure 3.3.A). The procedure comprised in this algorithm has two main steps: (i) calculation of several parameters for all the detected adhesion events (deviation, slope, unbinding force, and unbinding length); (ii) generation of two-dimensional histograms with these parameters and use of phenomenological observations to select specific unbinding events.

To calculate the deviation parameter, the repulsive part of the retraction force curve is fitted to a straight line (L_{Ref}). Next, a straight line that goes from the adhesion peak minimum force point to a predefined point belonging to L_{Ref} is drawn, L_{event}. The algorithm calculates the deviation between the two straight lines, respectively, L_{Ref} and L_{event} (Figure 3.3.B). The slope parameter is calculated as the slope of the adhesion event near the jump-off point (Figure 3.3.C). The unbinding force (F_{unb}) is defined as the vertical difference between the baseline and the minimum force at retraction, while the unbinding length

(L_{unb}) is defined as the difference between the tip-sample distance where the adhesion event occurs and the contact point (Figure 3.3.D).

Finally, tables containing information on adhesion events for all the experiments are processed. Two types of representations are generated, as follows: (i) common plots showing the number of events with a given unbinding force (1D histogram) and (ii) plots showing the number of events with a given unbinding force and a given value of another parameter, for example, the unbinding length (two-dimensional histograms). In two-dimensional histograms, the *y*-axis represents the unbinding force and the *x*-axis could be the unbinding length, the slope of an adhesion event or the deviation (Figure 3.4).

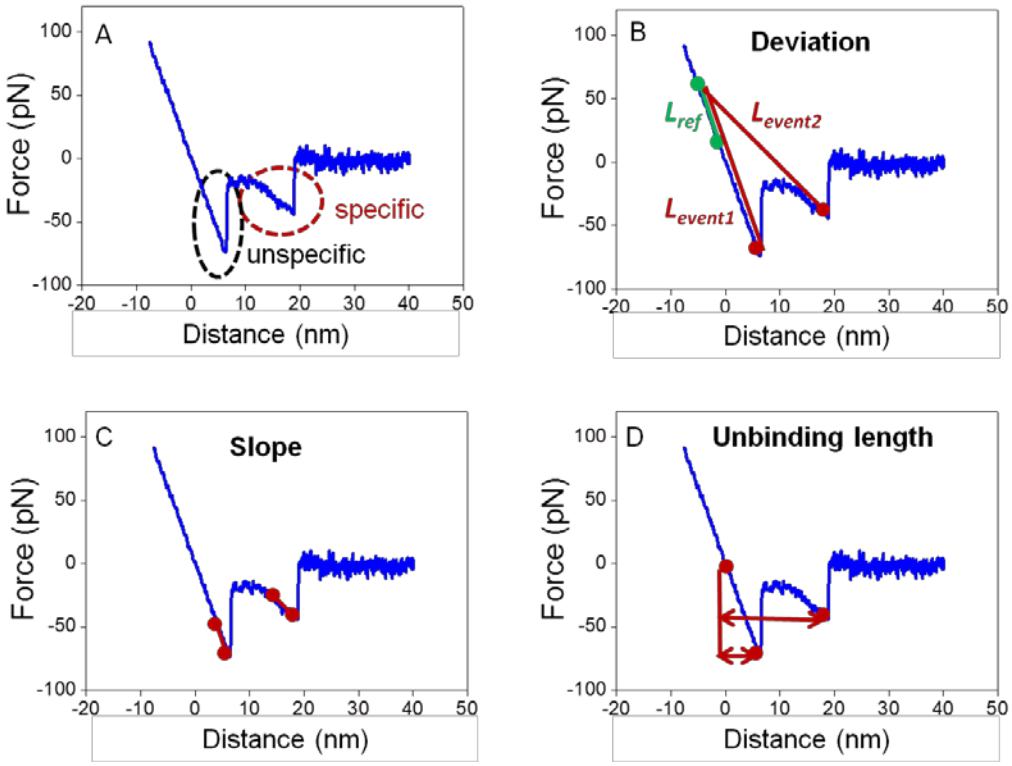

Figure 3.3. A: Evaluation of specific and unspecific adhesion events between siRNA and dendrimers; B: The deviation between the repulsive part of the deflection curve and the straight line that goes from the peak minimum to the contact with the surface is calculated; C: the slope of the adhesion event near the jump-off point is calculated; D: The unbinding length is calculated as the difference between the tip-sample distance where the adhesion event occurs and the contact point.

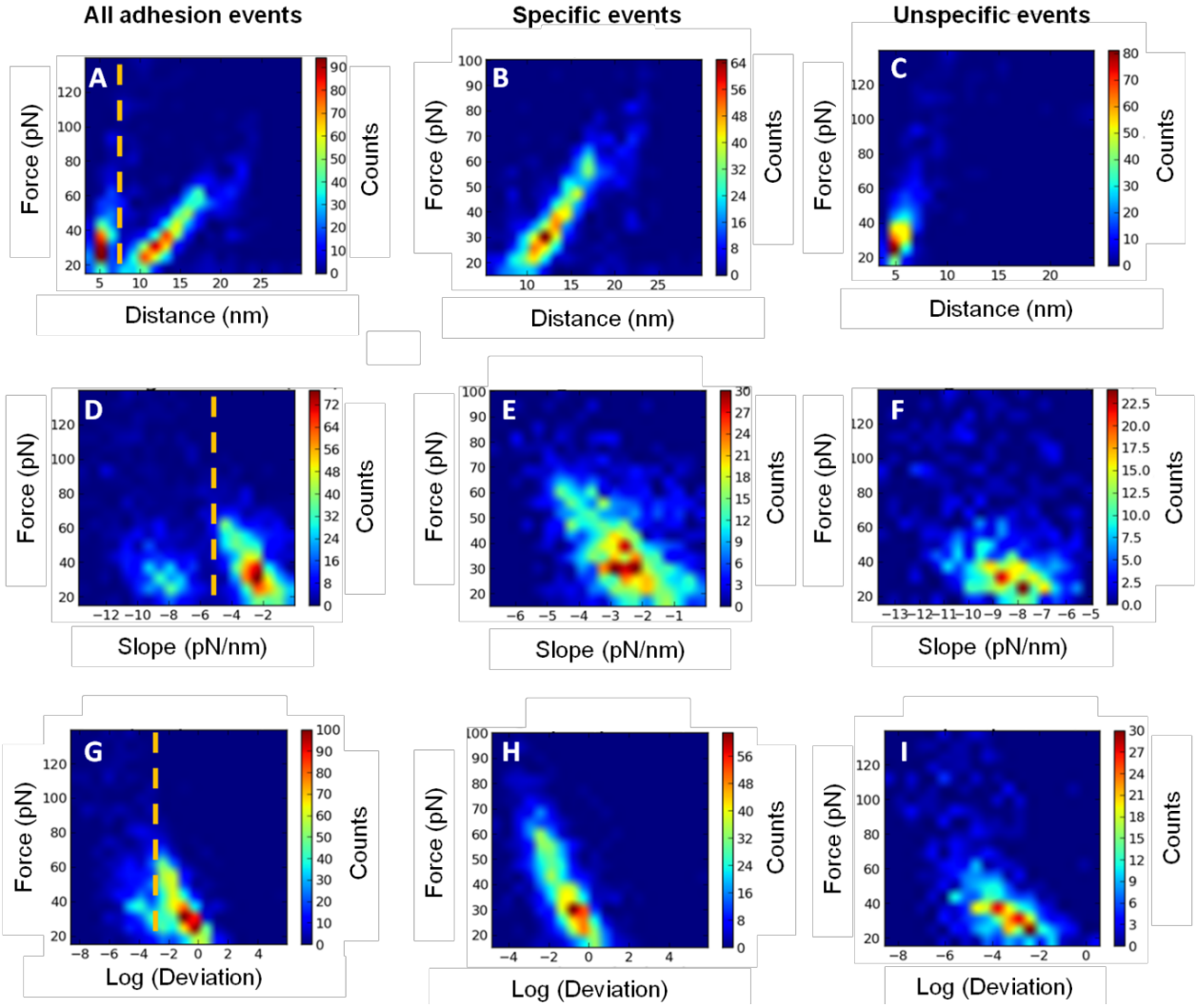

Figure 3.4. Discrimination between specific and unspecific adhesion events. In these two-dimensional histograms, the *y*-axis represents the unbindig force and the *x*-axis is A: unbinding length, D: the slope of an adhesion event or G: the deviation between L_{Ref} and L_{event}. To ascribe one of the spots showing above the average counts values to a specific or unspecific event, we introduce several phenomenological observations. Unspecific adhesion events are usually found near the solid support (retraction curve), here at tip-surface separations below 7 nm; also, the slope of unspecific events is steeper than the one corresponding to a specific interactions, here lower than -5.5 pN/nm; the logarithm of the deviation between L_{Ref} and L_{event} has lower values for unspecific adhesion events, here below -3.1. The application of the above criteria to the two-dimensional histograms enables to remove the spots associated with unspecific interactions (plots C,F,I) from the plots leaving what we call a two-dimensional molecular recognition map (B,E,H).

Two-dimensional histograms show several spots above the average values. To ascribe one of those spots to a specific or unspecific event we introduce several phenomenological observations. Unspecific adhesion events are usually found near the solid support (retraction curve), here at tip-surface separations below 5 nm. In addition, the characteristic calculated slope of unspecific events is steeper than the one corresponding to a specific siRNA-dendrimer interaction.

Also, the deviation between L_{Ref} and L_{event} is higher for specific siRNA-dendrimer adhesion events. The application of the above criteria to the 2D histograms leads to the removal of the spots associated with unspecific interactions from the plots leaving what we call a two-dimensional molecular recognition map. The use of two-dimensional histograms is uncommon in force spectroscopy, although it has been used as an alternative method to present the data[37-39].

3.2.5. siRNA release by polyanion competition

The ability of the complexes to release siRNA in the presence of polyanionic heparin was determined as a measure of complex stability[32]. Complexes were prepared at a dendrimer/siRNA molar ratio of 10 to ensure the complete binding of siRNA by the dendrimer, and then incubated with varying concentrations of heparin sulfate (0.01, 0.02, 0.05, 0.1, 0.2 and 0.5 heparin United States Pharmacopeia units/mL) for 20 min. The solutions were loaded on a 1.2% (w/v) agar gel containing 0.05 mg/ml ethidium bromide. Electrophoresis was performed at 60 mV for 15 min, and the resulting gels were photographed under UV-illumination.

3.2.6. Control experiments

Several rounds of control experiments have been performed to check the specificity of the unbinding events.

First, a heparin competition assay was adapted to our single-molecule force spectroscopy setup. A 60 µl drop of a 0.2 USP heparin units/mL was injected

over the dendrimers monolayer sample and after 30 minutes molecular recognition events were recorded with a siRNA-functionalized tip.

Second, a 20 µl drop of 12 µM free siRNA was injected onto the dendrimers sample surface and incubated for 30 minutes. Next, the molecular recognition experiments were resumed with a siRNA functionalized tip.

Other control experiments involved recording force curves by using unfunctionalized AFM tips on dendrimer monolayers deposited on mica or siRNA-functionalized AFM tips on bare mica substrates.

3.3. Results and discussion

3.3.1. Detection of siRNA-dendrimers interactions

To perform single molecule force spectroscopy measurements, the AFM tip is functionalized with a polyethylene glycol linker (PEG)-siRNA complex. Then, the functionalized tip is brought into contact with a packed dendrimer layer deposited onto the mica substrate (Figure 3.5)

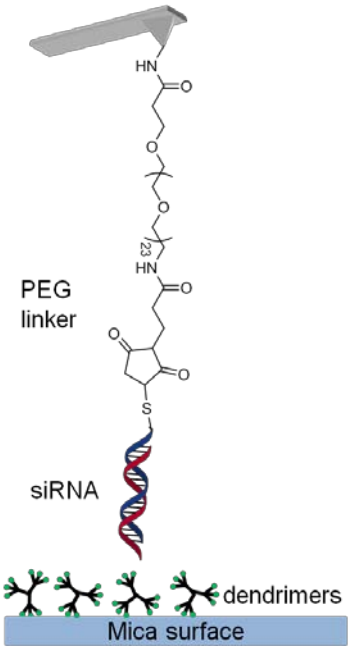

Figure 3.5. Scheme of the tip functionalization with a flexible PEG linker and siRNA and dendrimers physisorbed on the mica substrate.

Figure 3.6A shows several examples of the retraction part of the force versus distance curves obtained during the data acquisition process. The nonlinear stretching of the PEG tether before the cantilever jumps off contact can be observed in all of the curves used in our analysis. The unbinding events were characterized by their unbinding length and unbinding force. Specific and unspecific interactions were identified and discriminated according to the procedure described in section 3.2.4.

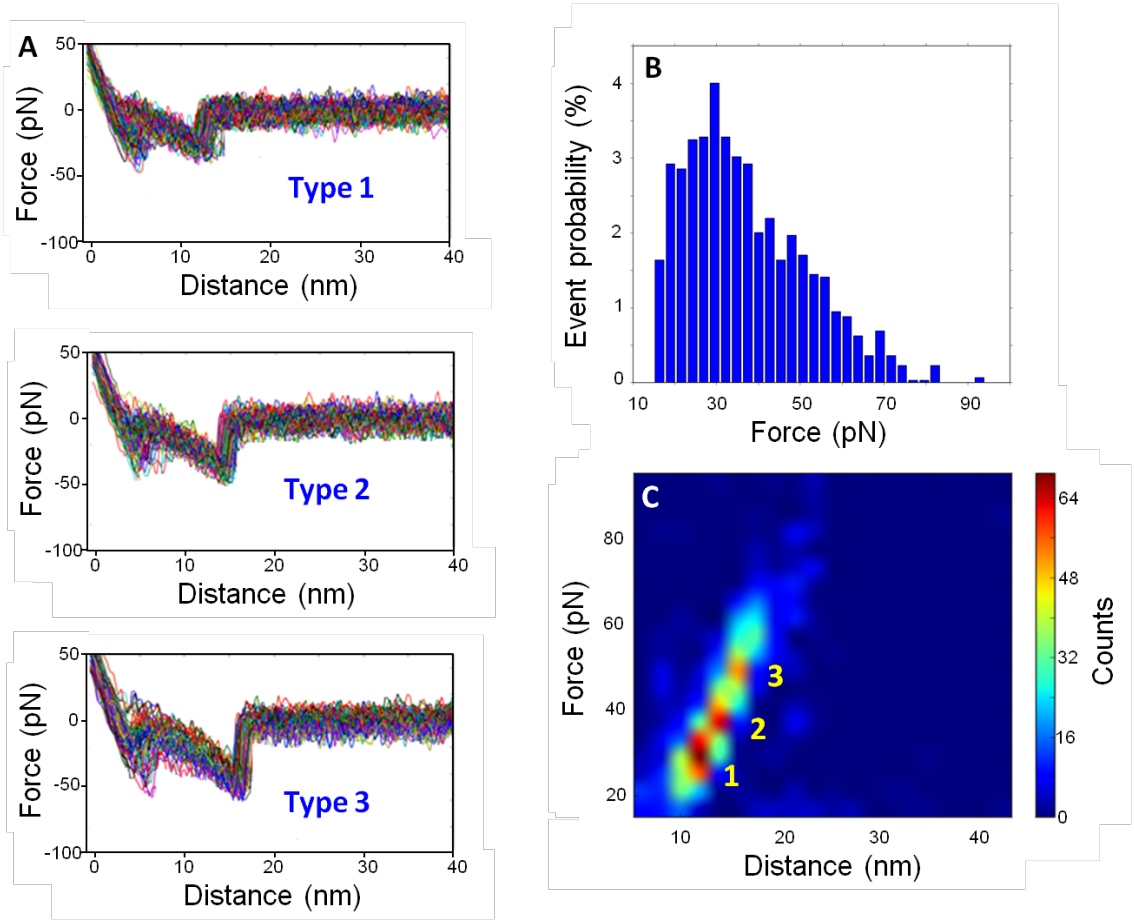

Figure 3.6. Detection of siRNA-dendrimer interactions. A: Cluster of the single force distance plots of regions 1, 2 and 3 of the 2D molecular recognition map; B: Histogram of the specific siRNA-dendrimer interactions. Total number of events, 1341; C: Two dimensional molecular recognition map. The map represents the events with the same force and unbinding distance.

Figure 3.6B depicts the one-dimensional (1D) histogram of the unbinding forces of specific siRNA-dendrimer interactions at a loading rate of 1 nN/s. A total 1341 unbinding events are included in this plot. Unspecific or noisy events occurring at F_{unb} ≤15 pN have been filtered out from this analysis. In this representation,

the most frequent unbinding event is observed at F_{unb} ≈ 28 pN. The positive skew of the histogram is an indication that multiple unbinding events occur . However given the lower probability of this kind of events, it is hard to determine the unbinding forces corresponding to multiple events. A different data representation helps distinguish between single and multiple events. Figure 3.6C shows the two-dimensional (2D) molecular recognition map containing the specific unbinding events with a given unbinding force and unbinding length. The events are plotted in a color-coded scale, where red and blue represent, respectively, the highest and the lowest number of events.

The observed unbinding forces can be grouped into three regions which are characterized, respectively, by maximum values of 28±6 pN, 38±8 pN and 50±9 pN (at a force loading rate of 1 nN/s). In all the cases, the unbinding lengths are determined in the 10-17 nm range. By correlating the unbinding force and unbinding length, we observe that the events corresponding to the lowest force (28 pN) have shorter L_{unb} values (12 nm), while the events observed at higher forces (38 pN and 50 pN) have unbinding lengths, respectively, of 14 nm and 16 nm. The three different force curve signatures shown in Figure 3.6A can be correlated with the regions 1, 2 and 3 of the 2D molecular recognition map. Similar results in terms of unbinding forces and lengths have been obtained with other siRNA-functionalized AFM tips.

The three peaks underline the presence of three different interactions between siRNA and the dendrimers. The persistence length of a double stranded RNA molecule is about 70 nm[41, 42]. This length is several times larger than the nominal siRNA length (5.9 nm), consequently, the siRNA will behave as a rigid rod. The comparison of the nominal length of the siRNA and the dendrimer size indicates that a siRNA molecule could interact simultaneously with several dendrimers.

In Figure 3.7, a model of the possible siRNA-dendrimer complex formation consistent with our observations is depicted. The two asymptotic limits of the unbinding lengths observed experimentally are schematized as follows:

(i) L_{unb}=9 nm. A minimum value of the unbinding length is observed when the interaction area between siRNA and the dendrimers layer occurs at

the free end of RNA (Figure 3.7.A). As the tip is retracted from the surface, the stretching of the polymer linker will represent the major contribution to the unbinding length. In this case, the unbinding length contribution involved in the distance travelled for the detachment of the siRNA molecule from the dendrimer is negligible.

(ii) L_{unb}=16 nm. Figure 3.7.B depicts the condition to obtain the other asymptotic limit. The siRNA molecule is lying flat on the dendrimer layer in a conformation that maximizes the contact area. As the tip is retracted from the surface, the polymeric linker will stretch, but the tip will also have to travel a certain distance to detach the siRNA molecule from the surface. This leads to an unbinding length (L_{unb}=16 nm), which is the sum of the polymer stretching distance and the siRNA detachment distance.

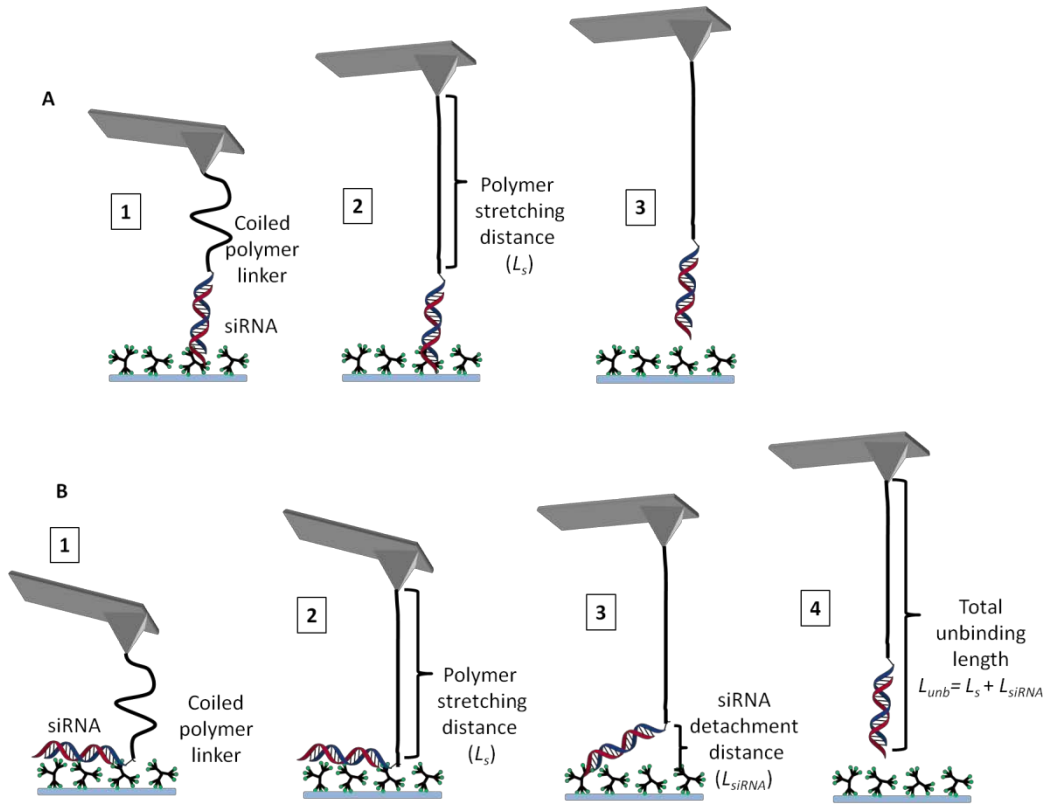

Figure 3.7. Possible siRNA-dendrimer interaction models: the two asymptotic cases. A: The unbinding length is equal to the polymer (PEG) stretching distance. A minimum unbinding length of 9 nm is observed in this case; B: The total unbinding length observed is the sum of polymer (PEG) stretching and siRNA detachment distances. A maximum unbinding length of 16 nm is obtained in this case.

3.3.2. Specificity of the interaction

We have performed four different sets of control experiments to determine the specificity of the measured unbinding events. Figure 3.8 illustrates the typical force curves recorded during the different control experiments. To emphasize the differences between specific and unspecific interactions, we also include a force curve obtained with a siRNA functionalized tip and a dendrimer sample (Figure 3.8A).

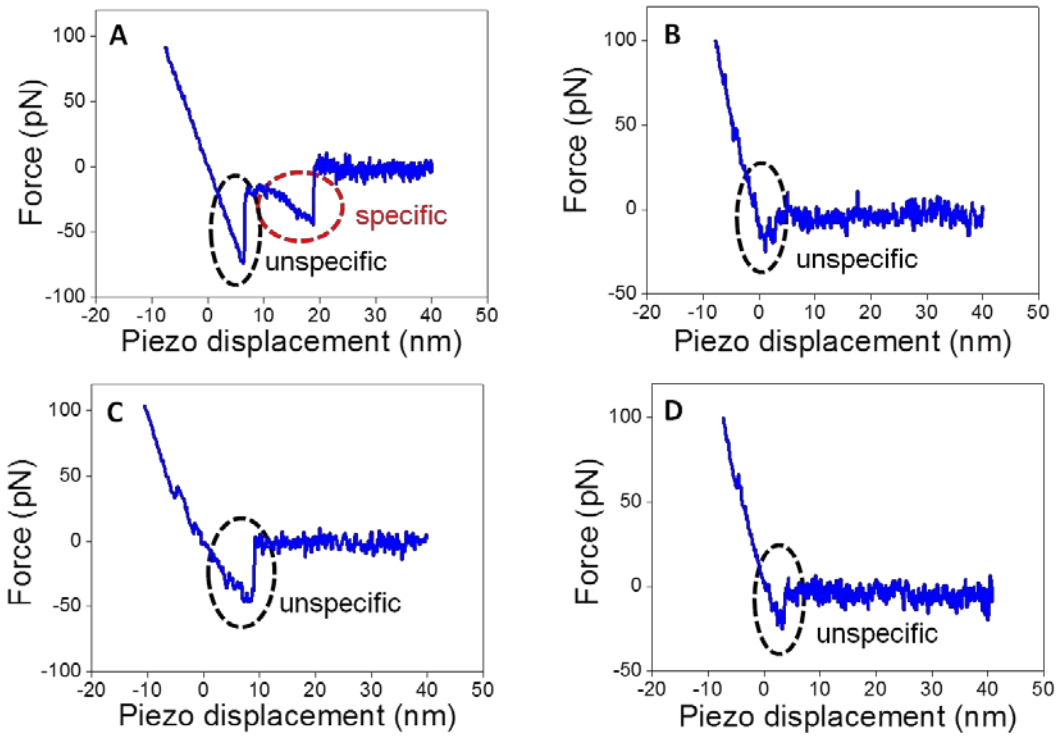

Figure 3.8. Examples of force curves A: Specific siRNA-dendrimer unbinding event. B: Interaction between a siRNA-functionalized AFM tip and the dendrimers monolayer blocked by heparin. C: Interaction between an AFM tip which has not been functionalized with siRNA and dendrimers. D: Interaction between a siRNA-functionalized AFM tip and a freshly cleaved mica sample.

The first two control experiments involved the blocking of the dendrimer´s positively charged regions by injecting either heparin or free siRNA in the environment (Figure 3.8B). In the following control experiments, force curves were recorded either with unfunctionalized AFM tips on the dendrimers

monolayer (Figure 3.8C) or with siRNA-functionalized tips on a bare mica substrate (Figure 3.8D)

Heparin is a highly sulfated glycosaminoglycan that has the highest negative charge density of any known biological molecule[43]. It is expected to block most of dendrimer's surface positive charges that are not bound to the mica substrate. Heparin competition assays were previously performed in order to test the strength of the union between siRNA and dendrimers[28]. Gel electrophorersis shows that 1 μM dendrimer completely binds 100 nM siRNA (dendriplexes) and this is markedly displaced from its binding to the dendrimer by 0.2 United States Pharmacopeia (USP) heparin units/mL (Figure 3.9A). We adapted this assay to our single molecule force spectroscopy setup. Initially, molecular recognition events were recorded between a siRNA-functionalized AFM tip and dendrimers on the surface, then heparin was injected into the system and after 30 minutes molecular recognition events were recorded again.

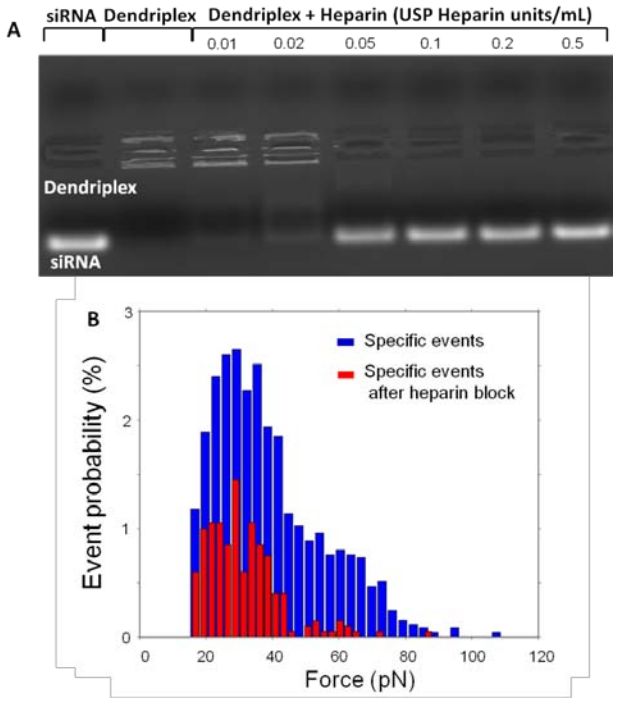

Figure 3.9. A: Gel electrophoresis of dendriplexes incubated with increasing concentrations of heparin. Dendriplexes were formed by incubating a siRNA (100 nM) and dendrimers (1 μM). siRNA was displaced by addingincreasing heparin concentrations (0.01 to 0.5 USP units/mL) to the bulk solution; B: Histograms of siRNA-dendrimers interactions before and after the addition of heparin. Heparin binds the dendrimers and blocks the interaction with the siRNA. The total number of events is, respectively, before and after heparin interactions, 1263 and 209.

Figure 3.9B shows the unbinding force distributions before and after the introduction of heparin. The injection of a competing polyanion (heparin) into the medium leads to a significant reduction of the unbinding events. In the absence of heparin, the probability of finding a force curve with the signature of a specific siRNA-dendrimer event is of 45%. After heparin deposition, the probability is reduced to 11.6%. However, the distribution of the unbinding forces remains unchanged, with the most frequent unbinding events occurring at 28 pN. This is an indication that the remaining events have the same features as the initial ones, which is consistent with some residual activity between siRNA and dendrimers after heparin blocking.

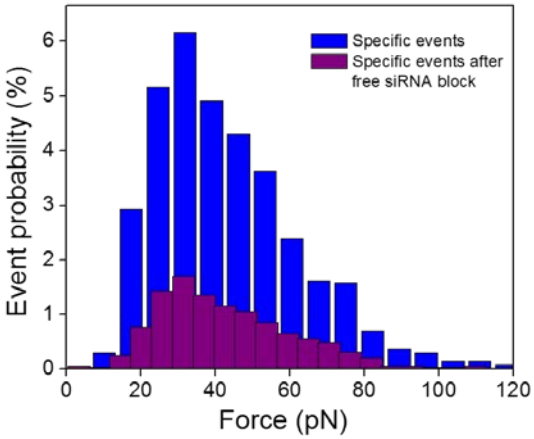

Figure 3.10. Histograms of siRNA-dendrimers unbinding events before and after the injection of free siRNA. The histogram in blue presents specific siRNA-dendrimers unbinding events with a probability of 40%. After the injection of a 12 μM siRNA solution, the dendrimers binding sites are blocked by the presence of free siRNA molecules and the binding probability is reduced to 14%, as displayed in the magenta histogram.

The evolution of the unbinding events frequency was also monitored after the saturation of the dendrimers substrate with free siRNA molecules. Free siRNA molecules with the same nucleotide sequence as the siRNA molecule tethered to the AFM tip were injected onto the dendrimers monolayer. Specifically, a 20 μl drop of a 12 μM siRNA solution was injected into the sample liquid environment and incubated for 30 minutes. Next, the molecular recognition

experiments were resumed with the same siRNA functionalized tip. We observe a reduction of the unbinding event probability from 40% before the injection of free siRNA molecules to 14% after the saturation of the dendrimer substrate with free siRNA (Figure 3.10).

The last two control experiments involved either the use of a non-functionalized AFM tip and dendrimers deposited on mica or of a siRNA-functionalized AFM tip and a bare mica surface. In both cases, the corresponding force curves did not provide a statistically relevant number of unbinding events with the signature used to characterize siRNA-dendrimer specific interactions.

3.3.3. Fit with the FJC model

In order to perform the quantitative analysis of the siRNA-PEG stretching before jump-out to surface (step 4 in Figure 2.3 of Chapter 2.2), the specific unbinding events were fitted with the extended freely jointed chain (FJC) model (Figure 3.11). As previously described in Chapter 2.4.3 of this thesis, the FJC model provides a quantitative description of the behaviour of a polymer under stretching[44, 45]

$$x(F) = L_C\left[\coth\left(\frac{Fl_K}{k_BT}\right) - \frac{k_BT}{Fl_K}\right] \qquad (3.1)$$

where x is the molecular extension under force, F is the applied force, l_K the Kuhn length (l_K= 0.7 nm for the PEG used here[45]), T=298 K, k_B the Boltzmann constant and L_c is the contour length of the polymer.

The experimental nonlinear stretching of the force as a function of piezo-displacement was fitted to Equation 3.1 and the corresponding contour length of the siRNA-PEG complex was extracted. The fit to the FJC model renders a single-mode distribution of the most probable contour length centred at 17±8 nm (Figure 3.12A). This value is very close to the sum of the nominal contour length of the PEG linker used in these experiments 10±5 nm [46, 47] and the 21-base pairs siRNA 5.9 nm (2.8 Å per base pair). Thus the value of the most probable contour length is in good agreement with the length corresponding to

the PEG-linker/siRNA complex. Figure 3.12B shows the 2D molecular recognition map of unbinding forces *versus* contour length of the PEG-linker/siRNA complex. Only single-force events are included in this map. We can observe that there are three different regions in the 2D map, as follows: region 1 with F_{unb} = 28 pN and L_{c1}=15 nm, region 2 with F_{unb}=40 pN and L_{c2} =17 nm and region 3 with F_{unb}=58 pN and L_{c3} =19 nm respectively. The higher-force regions can be linked to multiple unbinding events. As for the contour lengths, we observe that $L_{c1} < L_{c2} < L_{c3}$. This behaviour is at odds with the one observed by Sulchek et al [48] for the stretching of multiple PEG tethers in parallel. Their fit by the FJC model for single and multiple bonds rendered $L_{cmultiple} < L_{csingle}$. On the other hand, it has been estimated that *N*, the largest number of bonds during a tip-sample contact is approximately equal to the ratio of the surface area of the AFM tip spherical cap divided by the area occupied by one molecule[49],

$$N = \frac{2R}{L_c} \qquad (3.2)$$

where *R* is the tip radius and L_c is the contour length of the molecule bound to the tip. In our system the nominal tip radius is *R*=10 nm and the calculated contour length L_c=17 nm, which makes *N*≈1.

This helps draw the conclusion that in the present experiments it would be very difficult to have two or more siRNA molecules interacting simultaneously with the dendrimers and that the unbinding events observed are the result of a single siRNA interacting with several dendrimer molecules at a time.

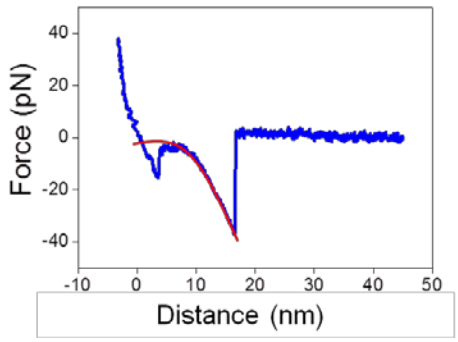

Figure 3.11. Typical unbinding event between siRNA-dendrimer and best fit with the freely-joined chain model.

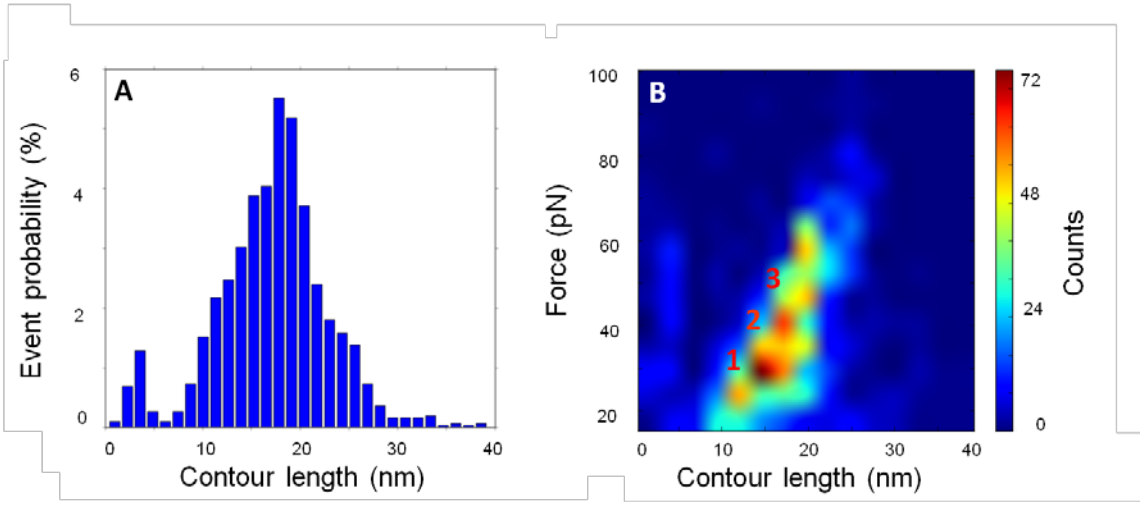

Figure 3.12. A: Histogram of the unbinding events as a function of freely-joined countour length. The maximum happens at 17 nm which matches the nominal length of the PEG (10 nm) and the siRNA (7 nm). Total numbe rof events 1341. B: Two dimensional molecular recognition map of unbinding forces vs. contour length of the siRNA+PEG complex generated by a fit with the freely jointed chain model (FJC).

3.3.4. Dynamic force spectroscopy

To determine the binding parameters of the siRNA-dendrimer complex and to gain insight into the energy landscape of the complex, we have carried out experiments at different loading rates. The kinetic model proposed by Bell [50] and further developed by Evans and Ritchie [51-53] is described in detail in Chapter 2.4.1 of this thesis. Briefly, the Bell-Evans model predicts that the force of a single-energy barrier in the thermally activated regime scales up with the logarithm of the force loading rate,

$$F^*(r) = \frac{k_B T}{x_\beta} \ln\left(\frac{x_\beta r}{k_{off}(0) k_B T}\right) \qquad (3.3)$$

Here F^* is the most probable unbinding force, r is the loading rate, x_β is the position of energy barrier along the reaction coordinate, $k_{off}(0)$ is the dissociation rate of the bond at zero force and $k_B T$ is the thermal energy. As previously shown in Chapter 2.4.2, the use of a polymeric linker to tether the siRNA molecule to the AFM tip makes it necessary to account for the linker

stiffness when calculating the effective force constant of the cantilever-linker system. Hence, the effective loading rate was obtained by multiplying the tip pulling velocity with the effective force constant of the cantilever-PEG system. The effective force constant of the cantilever-PEG is equivalent to the force constant of two springs in series. A practical determination of the effective constant is obtained from the slope of the retraction curve before the jump-off to surface[52-54]. The measured effective force constants were in the range of 3-3.7 pN/nm.

For each loading rate, the most probable unbinding force has been obtained from the maximum of the corresponding unbinding events histogram. Since we observe three different types of force curves in our experiments, we have followed the evolution of the most probable unbinding force with the loading rate for each type of force curve.

Figure 3.13 shows the dependence of the most probable unbinding force *versus* the effective loading rate for the unbinding events corresponding to regions 1, 2 and 3 in Figure 3.6.C. The results are consistent with the prediction of Equation 3.3. The dynamic force spectrum shows a linear behaviour for all regions. We conclude that a single energy barrier characterizes the transition of the dendriplex from the bound to the unbound state.

The position of energy barrier along the reaction coordinate, x_β, was determined from the slope of the linear fit of the unbinding forces versus the loading rate logarithm plot. Next, k_{off} was calculated by extrapolation to zero forces. The characteristic time needed for the spontaneous dissociation of the siRNA-dendrimer complex, τ, is given by the inverse of the kinetic off-rate constant. This parameter can be correlated with the stability of the complex. The dissociation of the siRNA-dendrimer complex under an external force can be described in the frame of the transition state theory[52, 55]. Once k_{off} is estimated using the Bell-Evans model, the measured free energy of the unbinding process ΔG_m can be calculated using the following equation, where h is Planck's constant,

$$\Delta G_m = -k_B T ln \frac{k_{off} h}{k_B T} \qquad (3.4)$$

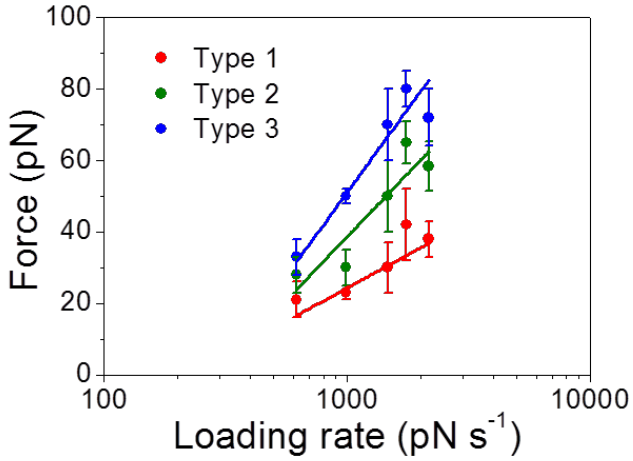

Figure 3.13. Dependence of the unbinding forces with the loading rate and fitting with the Bell-Evans model for the three types of events.

We consider that the siRNA-dendrimer system studied here meets the assumptions of Eyring model due to the small number of bonds involved. The total number of positive charges present on the surface of a G1 TGD PAMAM dendrimer at neutral pH (pH 7.4) is 9 or three charges per branch. The dendrimers form a layer on mica which implies at least one branch (three positive charges) will interact with the negatively charged mica substrate. Therefore, the maximum number of positive charges in the dendrimer available for interacting electrostatically with the negatively charged phosphate groups of the nucleic acid is 6. We also assume that the dissociation of the siRNA-dendrimer complex under force proceeds along a trajectory that resembles the thermodynamically favoured path, so the contribution of the entropic term can be neglected and the free energy change coincides with the change in enthalpy.

It must be noted that the above free energy includes the contribution of the siRNA-dendrimer complex unbinding $\Delta G_{complex}$ as well as of the PEG linker stretching ΔG_{PEG}. Hence, the unbinding free energy linked exclusively to the dissociation process between siRNA and dendrimer can be calculated as follows:

$$\Delta G_{complex} = \Delta G_m - \Delta G_{PEG} \qquad (3.5)$$

The free energy related to the stretching of a 10 nm long PEG linker has been estimated experimentally to be -1.78 kcal/mol[45]. The unbinding free energies for the different siRNA-dendrimer configurations measured here are determined by using Equations (3.4) and (3.5). Table 3.1 summarizes the kinetic parameters- energy barrier bond length, intrinsic unbinding rate, bond lifetime and free energy of the bond for the three types of unbinding events introduced in Figures 3.6.A and 3.6.C.

Table 3.1. *Kinetic parameters of the molecular recognition process for the three types of unbinding events.*

Force (pN)	x_β (nm)	k_{off} (s^{-1})	τ (s)	ΔG_{unb} (eV/kcal mol^{-1})
28	0.25±0.06	0.32±0.13	3.12±1.17	0.709±0.01/16.34±0.23
38	0.14±0.033	0.19±0.09	5.39±2.57	0.722±0.012/16.49±0.28
50	0.14±0.028	0.18±0.07	5.57±2.11	0.724±0.011/16.69±0.25

The length of a hydrogen bond formed between a nitrogen donor and an oxygen acceptor lies between 0.15-0.25 nm, which is in good agreement with the energy barrier bond lengths obtained here. The complexes corresponding to lower unbinding forces (region 1 in Figure 3.6C) are characterized by a barrier bond length of 0.25 nm while the ones giving higher forces (regions 2 and 3 in Figure 3.6C) show a smaller barrier bond length (0.14 nm). The higher lifetime of 5.4 s of the siRNA-dendrimer complexes corresponding to regions 2 and 3 implies a higher stability of these complexes as compared to the ones characterized by smaller unbinding forces. The latter will dissociate faster.

Given the observation above, in this context, the lower force peak depicted in Figure 2D map will correspond to a configuration that minimizes the interaction between the siRNA and the dendrimers (Figure 3.14A). Figure 3.14B shows an

intermediate configuration where the siRNA interacts partially with two dendrimers. The larger force peak (50 pN) implies that the siRNA lies flat on top of several dendrimer molecules (Figure 3.14C). This configuration maximizes the electrostatic attractive interaction between the siRNA and the dendrimers.

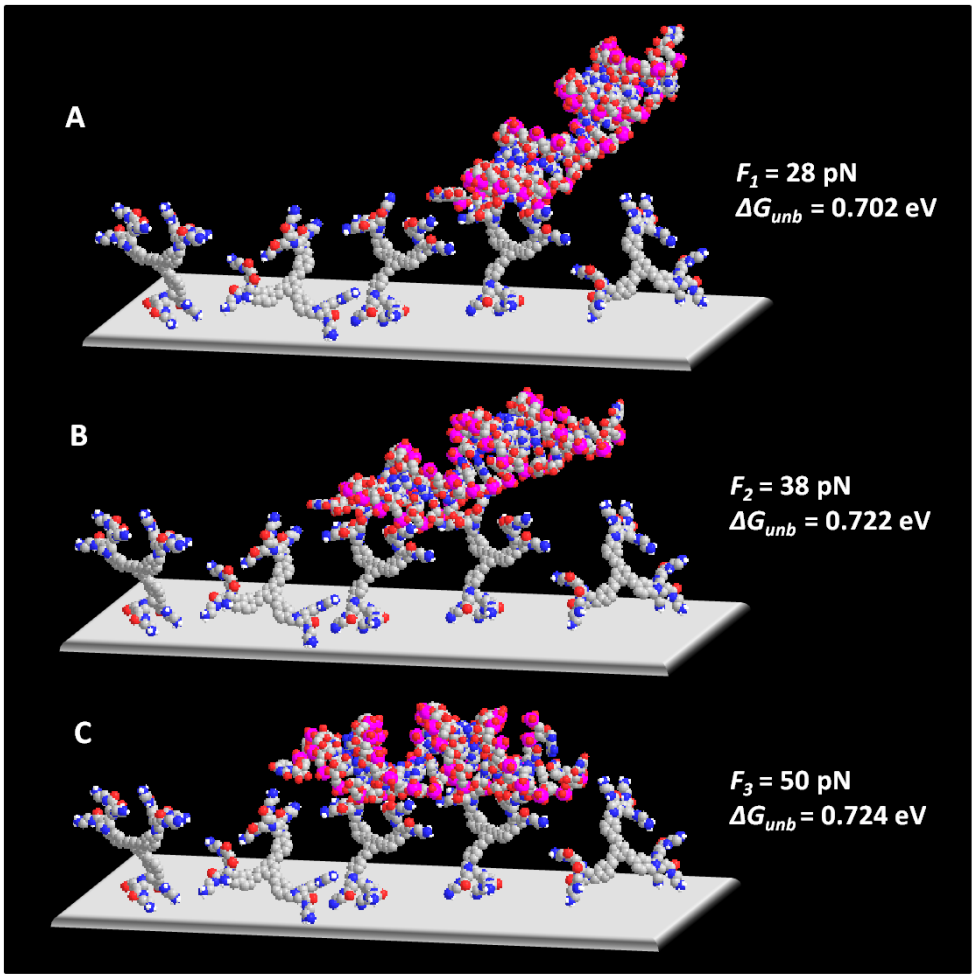

Figure 3.14. Scheme of siRNA-dendrimer configurations in the presence of a mica surface. The while line represents the postion of the mica surface. A: Lower force configuration that minimizes electrostatic the interaction between siRNA and the dendrimers; B: Intermediate configuration; C: Higher force configuration of siRNA lying flat on top of several dendrimer molecules. This configuration maximizes the electrostatic attractive interactions between siRNA and the dendrimers.

Figure 3.15 illustrates the result of a molecular dynamics simulation of the interaction of siRNA and a first-generation dendrimer. The table lists the per-

residue decomposition of the surface attraction between a dendrimer and siRNA. The end groups which do not participate actively to the binding (ΔEint > -5 kcal/mol) are identified in red. The binding energies between the positive residues of the dendrimer and siRNA can be grouped in two clusters, 11.3-13.6 kcal/mol and 5.7-7.6 kcal/mol[28]. The spatial orientation of the residue with respect to the siRNA determines its value binding energy value. The free unbinding energies measured in our experiments (16.34-16.69 kcal/mol) indicate a combination of a higher-energy and a lower energy residue (10.3+6.2=16.5 kcal/mol) as predicted by the simulations. The good agreement between the experimental results and the simulations strengthens the relevance of the simulations. Interestingly, although the unbinding free energies suggest that the number of the electrostatic interactions involved in the dendriplexes formation is similar for all complexes, the spatial conformation of the interacting residues determines the stability of the formed complex.

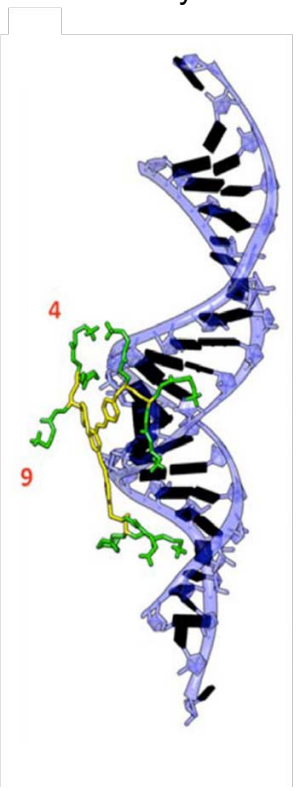

End	ΔE_{int} (kcal/mol)
1	-7.1
2	-7.6
3	-5.7
4	-2.9
5	-11.5
6	-11.3
7	-13.6
8	-6.2
9	-4.4

Figure 3.15. Per-residue decomposition of the surface attraction between TGD-G1 and siRNA. End residues are colored in green, GAPDH strands in blue, while the dendritic scaffold of TGD-G1 is represented in yellow . End groups which do not participate actively to the binding (ΔE_{int} > -5 kcal/mol) are identified in red. Adapted from Ref. [28]

3.4. Conclusions

We have developed a single-molecule force spectroscopy method to measure the unbinding forces and energies between a single siRNA molecule and polyamidoamine dendrimers deposited on a mica surface. We report three types of unbinding events which are characterized, respectively, by forces and free unbinding energies of 28 pN (0.709 eV), 38 pN (0.722 eV) and 50 pN (0.724 eV). The probability of finding specific unbinding events is about 45%. This value reveals a high binding affinity of siRNA towards polyamidoamine dendrimers.

We propose that siRNA interacts either with two of the three amino branches of one dendrimer or with two branches of adjacent dendrimers. The specific binding interaction at 0.724 eV indicates that the siRNA lies flat on top of two dendrimer molecules. This configuration maximizes the electrostatic attractive interactions between siRNA and the dendrimers. The lower peak corresponds to a configuration that minimizes the siRNA-dendrimer interactions. Intermediate configurations are also possible (0.722 eV).

We provide relevant information for future PAMAM-type dendrimer synthesis aimed to transfection procedures in two ways. First, the binding forces between the amino terminal groups located in the PAMAM branches and the phosphate groups in the siRNA molecules should be in the range of 25 to 50 pN for loading rates of about 1 nN/s; this will allow the dissociation of the siRNA from the dendriplex and an efficient transfection, while protecting the dendrimer from RNAse-mediated degradation at the same time. Second, it validates experimentally, for the first time, the theoretical predictions made by molecular modelling on the binding energies between dendrimers and siRNA at the single molecule scale.

3.5. References

1. R. Duncan and R. Gaspar, *Molecular Pharmaceutics*, 2011, **8**, 2101-2141.
2. C. Curtis and A. Nardulli, in *The Nuclear Receptor Superfamily*, ed. I. McEwan, Humana Press, 2009, vol. 505, ch. 11, pp. 187-204.
3. F. Pérez-Martínez, J. Guerra, I. Posadas and V. Ceña, *Pharm Res*, 2011, **28**, 1843-1858.
4. R. Kanasty, J. R. Dorkin, A. Vegas and D. Anderson, *Nature Materials*, 2013, **12**, 967-977.
5. G. J. Hannon, *Nature*, 2002, **418**, 244-251.
6. D. Grimm, K. L. Streetz, C. L. Jopling, T. A. Storm, K. Pandey, C. R. Davis, P. Marion, F. Salazar and M. A. Kay, *Nature*, 2006, **441**, 537-541.
7. T. A. Rand, K. Ginalski, N. V. Grishin and X. Wang, *Proc. Natl. Acad. Sci. U. S. A.*, 2004, **101**, 14385-14389.
8. K. A. Whitehead, R. Langer and D. G. Anderson, *Nat Rev Drug Discov*, 2009, **8**, 129-138.
9. R. A. Petros and J. M. DeSimone, *Nat Rev Drug Discov*, 2010, **9**, 615-627.
10. R. L. Kanasty, K. A. Whitehead, A. J. Vegas and D. G. Anderson, *Mol Ther*, 2012, **20**, 513-524.
11. Y.-d. Yao, T.-m. Sun, S.-y. Huang, S. Dou, L. Lin, J.-n. Chen, J.-b. Ruan, C.-q. Mao, F.-y. Yu, M.-s. Zeng, J.-y. Zang, Q. Liu, F.-x. Su, P. Zhang, J. Lieberman, J. Wang and E. Song, *Science Translational Medicine*, 2012, **4**, 130ra148-130ra148.
12. S. C. Semple, A. Akinc, J. Chen, A. P. Sandhu, B. L. Mui, C. K. Cho, D. W. Y. Sah, D. Stebbing, E. J. Crosley, E. Yaworski, I. M. Hafez, J. R. Dorkin, J. Qin, K. Lam, K. G. Rajeev, K. F. Wong, L. B. Jeffs, L. Nechev, M. L. Eisenhardt, M. Jayaraman, M. Kazem, M. A. Maier, M. Srinivasulu, M. J. Weinstein, Q. Chen, R. Alvarez, S. A. Barros, S. De, S. K. Klimuk, T. Borland, V. Kosovrasti, W. L. Cantley, Y. K. Tam, M. Manoharan, M. A. Ciufolini, M. A. Tracy, A. de Fougerolles, I. MacLachlan, P. R. Cullis, T. D. Madden and M. J. Hope, *Nat Biotech*, 2010, **28**, 172-176.
13. R. H. Mo, J. L. Zaro and W.-C. Shen, *Molecular Pharmaceutics*, 2012, **9**, 299-309.
14. B. Daglar, E. Ozgur, M. E. Corman, L. Uzun and G. B. Demirel, *RSC Advances*, 2014, **4**, 48639-48659.
15. C. P. Neff, J. Zhou, L. Remling, J. Kuruvilla, J. Zhang, H. Li, D. D. Smith, P. Swiderski, J. J. Rossi and R. Akkina, *Science Translational Medicine*, 2011, **3**, 66ra66-66ra66.
16. J. Soutschek, A. Akinc, B. Bramlage, K. Charisse, R. Constien, M. Donoghue, S. Elbashir, A. Geick, P. Hadwiger, J. Harborth, M. John, V. Kesavan, G. Lavine, R. K. Pandey, T. Racie, K. G. Rajeev, I. Rohl, I. Toudjarska, G. Wang, S. Wuschko, D. Bumcrot, V. Koteliansky, S. Limmer, M. Manoharan and H.-P. Vornlocher, *Nature*, 2004, **432**, 173-178.
17. J. E. Dahlman, C. Barnes, O. F. Khan, A. Thiriot, S. Jhunjunwala, T. E. Shaw, Y. Xing, H. B. Sager, G. Sahay, L. Speciner, A. Bader, R. L. Bogorad, H. Yin, T. Racie, Y. Dong, S. Jiang, D. Seedorf, A. Dave, K. Singh Sandhu, M. J. Webber, T. Novobrantseva, V. M. Ruda, K. R. Lytton-JeanAbigail, C. G. Levins, B. Kalish, D. K. Mudge, M. Perez, L. Abezgauz, P. Dutta, L. Smith, K. Charisse, M. W. Kieran, K. Fitzgerald, M. Nahrendorf, D. Danino, R. M. Tuder, U. H. von Andrian, A. Akinc, D. Panigrahy, A. Schroeder, V. Koteliansky, R. Langer and D. G. Anderson, *Nature Nanotechnology*, 2014, **9**, 648-655.
18. M. L. Chen, S. Gao, M. D. Dong, J. Song, C. X. Yang, K. A. Howard, J. Kjems and F. Besenbacher, *ACS Nano*, 2012, **6**, 4835-4844.
19. H. Lee, A. K. R. Lytton-Jean, Y. Chen, K. T. Love, A. I. Park, E. D. Karagiannis, A. Sehgal, W. Querbes, C. S. Zurenko, M. Jayaraman, C. G. Peng, K. Charisse, A. Borodovsky, M. Manoharan, J. S. Donahoe, J. Truelove, M. Nahrendorf, R. Langer and D. G. Anderson, *Nature Nanotechnology*, 2012, **7**, 389-393.

20. A.-M. Caminade, C.-O. Turrin and J.-P. Majoral, *Chemistry – A European Journal*, 2008, **14**, 7422-7432.
21. I. Posadas, F. J. Guerra and V. Ceña, *Nanomedicine*, 2010, **5**, 1219-1236.
22. O. F. Khan, E. W. Zaia, S. Jhunjhunwala, W. Xue, W. Cai, D. S. Yun, C. M. Barnes, J. E. Dahlman, Y. Dong, J. M. Pelet, M. J. Webber, J. K. Tsosie, T. E. Jacks, R. Langer and D. G. Anderson, *Nano Lett.*, 2015, **15**, 3008-3016.
23. E. Abbasi, S. Aval, A. Akbarzadeh, M. Milani, H. Nasrabadi, S. Joo, Y. Hanifehpour, K. Nejati-Koshki and R. Pashaei-Asl, *Nanoscale Research Letters*, 2014, **9**, 247.
24. G. M. Dykes, *Journal of Chemical Technology & Biotechnology*, 2001, **76**, 903-918.
25. D. A. Tomalia, H. Baker, J. Dewald, M. Hall, G. Kallos, S. Martin, J. Roeck, J. Ryder and P. Smith, *Polym J*, 1985, **17**, 117-132.
26. M. K. Mishra, C. A. Beaty, W. G. Lesniak, S. P. Kambhampati, F. Zhang, M. A. Wilson, M. E. Blue, J. C. Troncoso, S. Kannan, M. V. Johnston, W. A. Baumgartner and R. M. Kannan, *ACS Nano*, 2014, **8**, 2134-2147.
27. K. Karatasos, P. Posocco, E. Laurini and S. Pricl, *Macromolecular Bioscience*, 2012, **12**, 225-240.
28. G. M. Pavan, S. Monteagudo, J. Guerra, B. Carrion, V. Ocana, J. Rodriguez-Lopez, A. Danani, F. C. Perez-Martinez and V. Ceña, *Current Medicinal Chemistry*, 2012, **19**, 4929-4941.
29. P. K. Maiti and B. Bagchi, *Nano Lett.*, 2006, **6**, 2478-2485.
30. S. Xu, M. D. Dong, X. Liu, K. A. Howard, J. Kjems and F. Besenbacher, *Biophysical journal*, 2007, **93**, 952-959.
31. S. Sadekar and H. Ghandehari, *Advanced Drug Delivery Reviews*, 2012, **64**, 571-588.
32. I. Posadas, F. C. Pérez-Martínez, J. Guerra, P. Sánchez-Verdú and V. Ceña, *Journal of Neurochemistry*, 2012, **120**, 515-527.
33. M. D. Pérez-Carrión, F. C. Pérez-Martínez, S. Merino, P. Sánchez-Verdú, J. Martínez-Hernández, R. Luján and V. Ceña, *Journal of Neurochemistry*, 2012, **120**, 259-268.
34. A. C. Rodrigo, I. Rivilla, F. C. Pérez-Martínez, S. Monteagudo, V. Ocaña, J. Guerra, J. C. García-Martínez, S. Merino, P. Sánchez-Verdú, V. Ceña and J. Rodríguez-López, *Biomacromolecules*, 2011, **12**, 1205-1213.
35. J. Hutter and J. Bechhoefer, *Review of Scientific Instruments*, 1993, **64**, 1868–1873.
36. H. J. Butt and M. Jaschke, *Nanotechnology*, 1995, **6**, 1.
37. C. Guo, B. Wang, L. Wang and B. Xu, *Chemical Communications*, 2012, **48**, 12222-12224.
38. O. E. Farrance, E. Paci, S. E. Radford and D. J. Brockwell, *ACS Nano*, 2015, **9**, 1315-1324.
39. L. Buscemi, D. Ramonet, F. Klingberg, A. Formey, J. Smith-Clerc, J.-J. Meister and B. Hinz, *Current Biology*, 2011, **21**, 2046-2054.
40. S. Guo, C. Ray, A. Kirkpatrick, N. Lad and B. B. Akhremitchev, *Biophysical journal*, 2008, **95**, 3964-3976.
41. P. Kebbekus, D. E. Draper and P. Hagerman, *Biochemistry*, 1995, **34**, 4354-4357.
42. J. A. Abels, F. Moreno-Herrero, T. van der Heijden, C. Dekker and N. H. Dekker, *Biophysical journal*, 2005, **88**, 2737-2744.
43. D. L. Nelson and M. M. Cox, *Lehninger Principles of Biochemistry*, W.H. Freeman & Company, New York, Fifth Edition edn., 2004.
44. P. J. Flory, *Statistical mechanics of chain molecules*, Interscience Publishers, 1969.
45. F. Oesterhelt, M. Rief and H. E. Gaub, *New Journal of Physics*, 1999, **1**, 6.1-6.5.
46. T. V. Ratto, K. C. Langry, R. E. Rudd, R. L. Balhorn, M. J. Allen and M. W. McElfresh, *Biophysical journal*, 2004, **86**, 2430-2437.
47. C. Ray and B. B. Akhremitchev, *Journal of the American Chemical Society*, 2005, **127**, 14739-14744.

48. T. A. Sulchek, R. W. Friddle, K. Langry, E. Y. Lau, H. Albrecht, T. V. Ratto, S. J. DeNardo, M. E. Colvin and A. Noy, *Proc. Natl. Acad. Sci. U. S. A.*, 2005, **102**, 16638-16643.
49. A. R. Bizzarri and S. Cannistraro, *Dynamic Force Spectroscopy and Biomolecular Recognition*, Taylor & Francis, 2012.
50. G. I. Bell, *Science*, 1978, **200**, 618-627.
51. E. Evans and K. Ritchie, *Biophysical journal*, 1997, **72**, 1541-1555.
52. R. Merkel, P. Nassoy, A. Leung, K. Ritchie and E. Evans, *Nature*, 1999, **397**, 50-53.
53. E. A. Evans and D. A. Calderwood, *Science*, 2007, **316**, 1148-1153.
54. C. Friedsam, A. K. Wehle, F. Kühner and H. E. Gaub, *Journal of Physics: Condensed Matter*, 2003, **15**, S1709.
55. H. Eyring, *The Journal of Chemical Physics*, 1935, **3**, 107-115.

Chapter 4

Single-molecule force spectroscopy applied to immunosensing devices

4.1. Introduction

Immunosensing exploits one of nature's most optimized molecular recognition mechanisms, namely the interaction between an antigen and its specific antibody. Antibodies are capable to recognize their target antigens and bind them with high specificity. Additionally, they can elicit an immune response against the bound antigen by communicating with other components of the immune system and recruiting other cells and molecules[1].

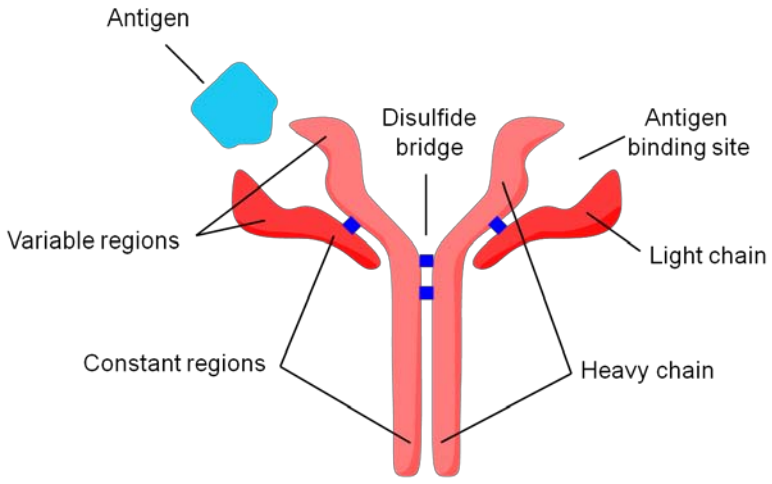

Figure 4.1. Schematic representation of a Y-shaped antibody molecule and its specific antigen. The antibody consists of two heavy chains of 50 kDa and two light chains of 25 kDa. Strong disulfide bonds link the heavy chains to each other and to the light chains. Both heavy and light chains are composed of constant and variable regions.

Immunoglobulin G (IgG) is a glycoprotein complex composed of four peptide chains arranged in a Y-shape. Figure 4.1 depicts the main structural features of an IgG antibody. Its four polypeptide chains (two light chains and two heavy chains) are connected through stable disulfide bonds or hinges. It has two antigen binding frag-

ments (Fab) and one crystallizable fragment (Fc). The antigen binding sites (paratopes), located at the far end of the Fabs, recognize the epitope of an antigen and bind it non-covalently. Both the *lock-and-key*[2] and the *induced fit* mechanisms[3, 4] have been proposed to describe antibody-antigen molecular recognition. The *lock-and-key* hypothesis envisions the antigen as a key which fits exactly into a specific lock, the antibody, while the *induced fit* concept relaxes the requirement for a preexisting specific fit between the antibody and antigen, at the expense of specificity. During the last two decades, a lot of effort was put into understanding the role of conformational changes in molecular recognition processes and it was shown that the ability of an antibody to recognize an antigen is extremely sensitive to the conformational structure of the paratope[5-8]. Further experimental evidence suggests that the flexibility of the interaction is actually a key feature controlling the detection of an antigen[9-11]. This led to the *conformational selection* hypothesis, which postulates that all antibody conformations pre-exist, and the antigen selects the most favored conformation[11]. Therefore, modern studies consider antibodies to be elastic proteins continuously exploring different conformations. This enables them to cross-react with a large number of antigens by establishing elastic nonspecific bonds, which in turn promotes the maturation of the immune response through the ability to recognize new infections[12].

Cytokines refer to a broad category of small secreted proteins, which are generated by immune cells and play a crucial role in cell signaling interactions, such as differentiation, maturation and activation. According to their specific effect and microenvironment, cytokines can be pro-inflammatory, anti-inflammatory or both. Specifically, anti-inflammatory cytokines are involved in the immunoregulatory control of the pro-inflammatory cytokine response. The most important anti-inflammatory cytokines are interleukin IL-1 receptor antagonist, IL-4, IL-10, IL-11 and IL-13. Recently, it has been demonstrated that some cytokines and their receptors may mediate multiple cell signaling pathways connected to the aggressive behavior of cancer, besides the regulation of normal immune responses[13, 14]. In particular, the IL-4 cytokine was pinpointed as a biomarker for colon and prostate cancer, besides its well-established role in pathologies like allergic asthma or spinal cord injury[15-17]. In clinical pharmacology, a biomarker is defined as “a characteristic that is

objectively measured and evaluated as an indicator of normal biological processes, pathogenic processes, or pharmacological responses to a therapeutic intervention"[18]. The early detection of protein biomarkers secreted by tumors is one of the most promising strategies in preventive cancer medicine. This requires the development of ultra-sensitive, cost-effective and reliable biosensing devices, which are able to monitor cancer biomarkers predicted by proteomics. The levels of the over expressed IL-4 cytokine are usually 1000 higher than the physiological ones, which are found in the picomolar range. Therefore, a successful sensor for the detection of IL-4 should be able to bind the cytokine in a specific manner and have a limit of detection in the nanomolar range.

Research for the development of biosensing devices started in the 1970s, but it was not until the tremendous success of biosensors for the diagnosis and management of diabetes mellitus[19] that the amount of available funding helped to develop the field. Today, there is an increasing demand for ultrasensitive, cost-effective and scaled-down biosensors. The accurate detection of biological and chemical agents is of great importance in environmental sciences[20, 21], biomedical research[22, 23], clinical diagnosis[24, 25], as well as anti-bioterrorism applications[26, 27].

Label-free biosensing schemes require the integration of bio-recognition moieties at a solid-liquid interface and their coupling with a transducer. The transduction of the molecular binding event should occur with minimum, if not any, further chemical amplification or development steps. This is particularly relevant for point-of-care applications and in-field deployed sensors. On one hand, both the sensitivity and specificity of a biosensor depend on how the bio-recognition groups are made available to the target, and on the coupling between environment and transducer[28]. On the other hand, novel materials are being developed in order to make the recognition and transduction processes more efficient. Nanomaterials feature extraordinary physicochemical and structural properties[29-31] and quantum dots, nanoparticles, nanowires along with 2D materials have been a great impetus for the advances made in the biosensors field.

The large antibody-antigen binding constant is exploited in Enzyme-Linked ImmunoSorbent Assay (ELISA) to detect the presence of biomarkers in bodily fluids whose concentration can be below picomolar level[1].

Among label-free immunosensors, mechanical and electronic transductions have been demonstrated[32-35]. Mechanical sensors, such as quartz crystal microbalance (QCM)[33] and cantilevers[25], detect changes of mass, binding/unbinding forces and viscoelastic response. They are effective in those regimes where electronic sensing does not provide enough sensitivity. However the interpretation of the device output in terms of specific molecular interactions is not usually straightforward. In the case of an electronic sensor, several phenomena induced by the bio-recognition event might be exploited: local changes of electrostatic potential[36], density of charge carriers, conductivity[37], impedance[38], capacitance[39]. Simplicity of instruments and low cost are factors that make electronic transduction favored for single-shot applications[40]. In fluids, the device sensitivity is optimized by tuning the Debye length scale according to the size of the specific binding pair. The Debye length is adjusted by modulating the ionic strength. However such modulation is not always possible, especially in bodily fluids[41-43].

Quantification, reproducibility and standardization are open issues in label-free immunosensing. They require multi-scale control from nanometer to hundreds of micrometers of the density, orientation and functionality of the recognition moieties on the sensing area of the device. Open questions, that also represent technological challenges, include: how to control the density of active Abs; what fraction of Abs gives rise to specific bio-recognition events; what is the detection limit of the device in terms of number of recognition events; how to make the device more effective, sensitive, and specific.

In this chapter, local and non-local techniques sensitive to antibody-antigen recognition events are combined in a multi-scale approach to quantitatively understand and develop a label-free biosensor. Specifically, a molecular-scale technique, such as single-molecule force spectroscopy (SMFS), is combined with an electrolyte-gated organic field effect transistor (EGOFET) (see Figure 4.2). The EGOFET device was developed in the group of Fabio Biscarini (CNR and University of Modena and Reggio Emilia, Italy). The fabrication and electrical characterization

of the device are described in Appendix B.1. The discussion in this chapter will be mainly focused on the SMFS results.

4.2. Experimental methods

4.2.1. Sample preparation

The glutaraldehyde-based functionalization was performed by immersing the gold gate electrode in a 1 mM solution of 6-aminohexanethiol in ethanol overnight. The activation of the 6-aminohexanethiol self-assembled monolayer was achieved by immersion in a glutaraldehyde solution (2.5% v/v) for 1 h at 5°C. After rinsing with PBS 0.01 M, the functionalized substrate was immersed in a 0.25 mg/ml anti-IL4 solution for 90 minutes.

The protein G-mediated functionalization involved the immersion of the gold substrate in a 5 mg/ml solution of protein G in PBS 0.01 M for 10 minutes. The sample was then rinsed with PBS 0.01 M and immersed in a 0.25 mg/ml anti-IL4 solution for 90 minutes.

4.2.2. Topography measurements

Topography measurements were performed in amplitude modulation AFM by driving mechanically the cantilever[44, 45]. A Multimode AFM fitted with a Nanoscope V controller (Brucer, Santa Barbara) was used for these measurements.
Gold substrates were imaged during the different functionalization steps in both air and PBS 0.01 M medium. Rectangular PPP-NCH cantilevers (Nanoworld AG, Switzerland) with a nominal force constant *k* of 40 N/m and a resonant frequency of 291 kHz were used for air measurements. The free and set point amplitudes were respectively, 8 nm and 6 nm. As for the experiments in PBS 0.01 M environment, rectangular OMCL-RC800PSA cantilevers (Olympus, Japan) with a nominal force constant *k* of 0.4 N/m and a resonant frequency of 33 kHz were used.

The images were analyzed using the WsxM 5.0 software[46] to extract the root-mean-square (*rms*) roughness values for each functionalization step.

4.2.3. Single-molecule force spectroscopy measurements

Single-molecule force spectroscopy experiments were performed in contact mode with a Nanoscope V Multimode AFM (Bruker, Santa Barbara) The experiments were conducted in PBS 0.01 M at 30°C. Triangular silicon nitride OTR-4 cantilevers (Bruker, Santa Barbara) with nominal spring constants *k* of either 0.02 N/m and resonant frequency of 2 kHz or 0.08 N/m and resonant frequency of 8 kHz were used. The protocol described in Appendix A.1.4 was used to functionalize tips the IL-4 cytokine.

The force constant and quality factor were determined as described in Chapter 3.2.3 by using the thermal noise method[47,48].
In single-molecule force spectroscopy experiments the maximum force was maintained below 250 pN to avoid any irreversible damage to the molecules bound to the tip apex. For each functionalized tip, several force maps covering 1 μm x 1 μm regions of the sample (32 x 32 data points) were acquired. To record a typical force curve, the tip was approached and retracted 200 nm from the sample at a speed of 200 nm/s and it was kept in contact with the sample for 0.5 s to facilitate the formation of antibody-antigen complexes.

4.2.4. Control experiments

Several rounds of control experiments have been performed to check the specificity of the unbinding events detected by single-molecule force spectroscopy.

One control experiment involved the acquisition of force curves when using unfunctionalized AFM tips on a monolayer of anti-IL4 antibodies deposited on sample surface. Another control experiment involved the recording of force curves with IL-4 antigen functionalized tips on gold substrates that had no antibodies deposited.

The functionalized tips were also probed against anti-IL4 antibodies immobilized on 6-aminohexanethiol self-assembled monolayer and protein G substrates.

The selectivity of the unbinding events was also assessed in cross-reactivity experiments. The AFM tips functionalized with IL-4 antigen were used on a monolayer of unspecific antibodies (anti-IL6) deposited onto the sample surface.

4.2.5. Force spectroscopy data analysis

A total of 16000 force distance curves were recorded with several functionalized tips on each of the two substrates analyzed (anti-IL4 antibodies on 6-aminohexanethiol self-assembled monolayer and protein G). Data analysis was carried out using the algorithm designed using *Spyder* - The Scientific *PYthon* Development EnviRonment described in Section 3.2.4.

4.3. Results and discussion

4.3.1. Multiscale sensing of antibody-antigen interactions

Here, the analytical target is the IL4 cytokine and the specific recognition moiety is the anti-IL4 monoclonal antibody. As previously described in Chapter 2 of this thesis, SMFS is a powerful technique that has been successfully applied to measure the forces between a wide range of biomolecules, while EGOFETs were shown to transduce signals in neuronal cell populations, sub-nM concentration of neurotransmitters[49] and DNA[50], local pH changes[51], penicillin[52] and biotin-streptavidin hybridization[53].

SMFS measurements have been performed across areas of a real electrode functionalized for the detection of the IL-4 cytokine. In SMFS experiments, the force dependence on the probe-surface distance is recorded (see Chapter 2.3). A force curve exhibits regions where a smooth variation *vs.* the distance is interrupted by abrupt changes. These “jumps” are interpreted as the rupture of single or multiple bonds that were formed because of molecular recognition interactions (Figure 4.2A). The ultra-sensitive SMFS technique is crucial for the quantification of specific IL-4 recognition processes on device-relevant Au surfaces in the limit of strong

electrostatic screening regime. In this chapter, SMFS results will be compared with electrical measurements performed with the EGOFET device.

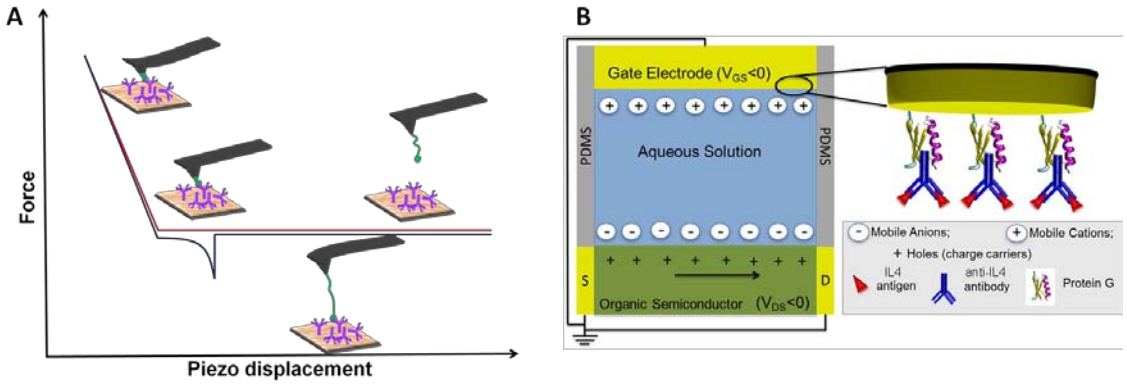

Figure 4.2. Schematic representations of the two techniques used in our multi-scale approach for the detection of antibody-antigen interactions on a real biosensor interface. A: Typical force versus distance curve obtained when an antigen-functionalized AFM cantilever detects a specific antibody-antigen molecular recognition event; B: Schematic EGOFET cross-section along with a sketch of the magnification of the gate/electrolyte interface.

When immersed in an electrolyte solution, the functionalized EGOFET gate electrode binds and detects the biomolecule of interest (Figure 4.2B). A number of local binding events occur at the gate electrode leading to a potential change[54, 55]. This change affects the electrostatic potential at the electrolyte solution/organic semiconductor interface, which couples to the semiconductor channel *via* the capacitance C_{DL} of the Debye-Helmholtz layer. Being C_{DL} on the order of 10-20 μF/cm[56] EGOFET responds to changes of potential as low as 50-100 μV [57]. These correspond approximately to a few recognition events per 100x100 nm^2 area of the device. Considering an active channel area $A=W\cdot L$ given by width W multiplied by length L, EGOFET with A=0.5 mm^2 responds to 10-100 million recognition events occurring on the device.

SMFS on the other hand, is sensitive to a few single antibody-antigen interactions and the value of the measured forces depends on both the loading rate[58, 59] and the relevant electrostatic interactions[60]. Being the latter anisotropic, the orientation of the

recognition moiety on the surface is important. This orientation strongly depends on the protocol adopted to immobilize the recognition group on the surface.

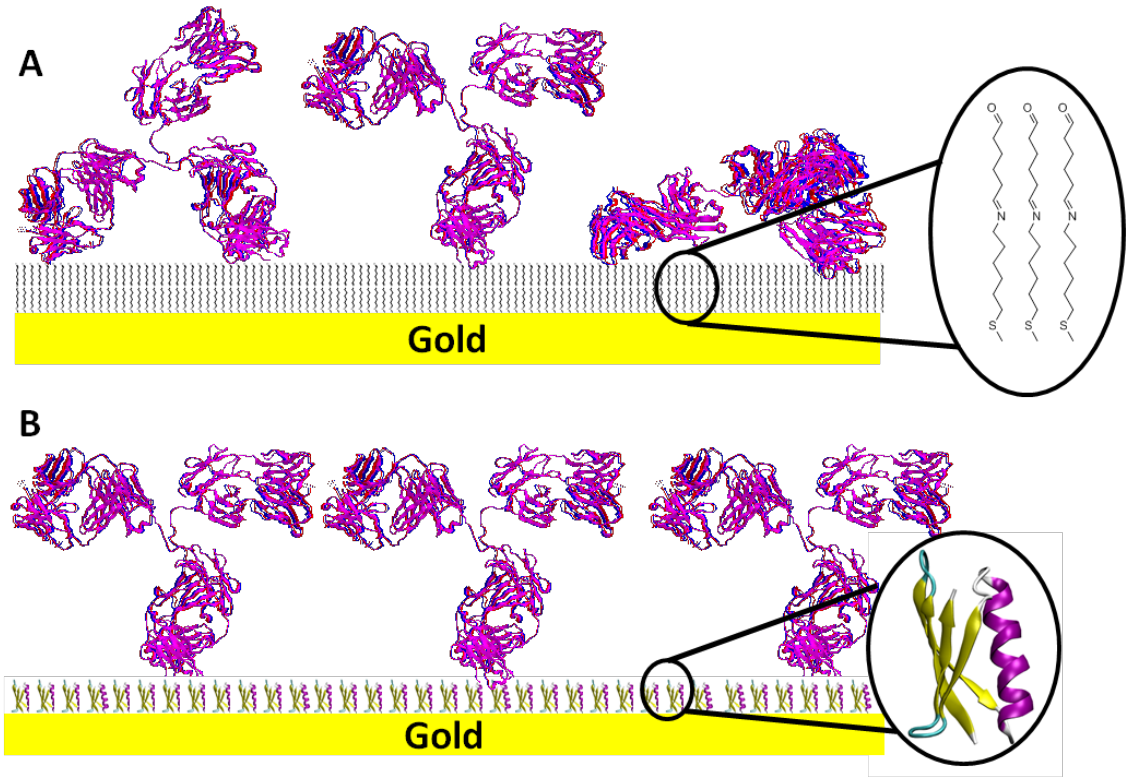

Figure 4.3. Antibodies immobilized on functionalized gold substrates. A: Antibodies on a 6-aminohexanethiol monolayer activated by glutaraldehyde (HSC_6NH_2 functionalization). This functional approach renders a surface with randomly oriented antibodies due to the natural abundance of lysine in the antibodies backbone; B: Antibodies immobilized on a recombinant His-Tagged PG monolayer (PG). Antibodies are oriented by the specific interaction of PG with the fragment crystallizable region (Fc) that forces the antibodies to expose their binding sites to the environment.

In the work described in this chapter, two different substrate functionalization strategies were used to immobilize anti-IL4 antibodies on the EGOFET gate electrode. The first strategy is based on a 6-aminohexanethiol (HSC_6NH_2) monolayer activated by glutaraldehyde[61]. This functional approach guarantees covalent binding between Au and the side chains of the lysine residues in the antibody; however there is no control on the antibody orientation due to the natural abundance of lysine in the antibody backbone (Figure 4.3A). The second strategy exploits the recombinant histidine-tagged protein G (His-Tagged PG), whose N-terminus side is tailored by a 6-histidine chain (6-His-Tag). His-Tags are well known

to bind strongly on polycrystalline Au (Figure 4.3B)[62, 63]. This affinity was already exploited for the fabrication of nanomechanical motors based on the grafting of F1-ATPase on gold substrates[64]. His-Tagged PG forms an oriented layer which promotes antibody immobilization on the Au electrode[65]. Neutron reflectometry, light interferometry and ellipsometry show that antibodies on PG-functionalized ideal surfaces form smooth monolayers[66]. Antibodies are oriented by the specific interaction of PG with the fragment crystallizable region (Fc) that forces the antibody to expose its binding sites to the environment[67, 68].

4.3.2. Evaluation of functionalized gold substrates by tapping mode AFM

The ability of both functionalization protocols to lead to antibodies immobilization onto the gold substrate was evaluated by tapping mode AFM in air and PBS medium. The surface topography of a typical bare gold sample recorded in air is displayed in Figure 4.4A. The sample consists of few tens of nm-diameter gold grains formed by thermal sublimation, with a maximum height of 10 nm and *rms* roughness of 1.1 nm. PG adsorption (Figure 4.4B) yields a smoother surface of reduced height and roughness. Incubation of the sample with the anti-IL4 solution leads to an increase of the maximum height by 3.5 nm and roughness by 0.39 nm (Figure 4.4C). The height difference is in good agreement with the size of IgG antibodies adsorbed with an orientation consistent with the so-called Y configuration previously reported in air[69].

Experiments carried out in PBS show that the *rms* roughness for the different functionalization steps (Figure 4.4D) follows the same trend as in air medium. There is a decrease of the *rms* roughness upon PG deposition, followed by an increase of 0.61 nm as a result of the antibody immobilization.

A similar quantitative analysis of the HSC_6NH_2 functionalized sample height and roughness was not possible due to the high adhesion forces between the tip and the sample.

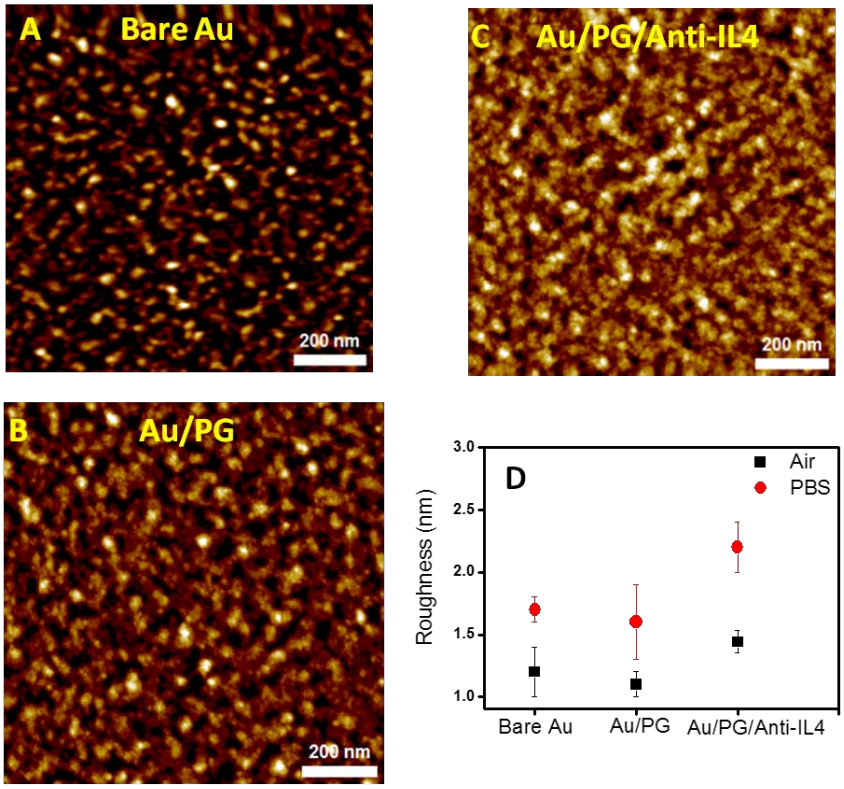

Figure 4.4. A. AFM images of a bare gold substrate in air; B. PG-coated gold in air; C. PG/Anti-IL4-coated gold in air; D. Overlaid *rms* roughness for air and PBS medium.

4.3.3. Detection of IL4 with EGOFET-based immunosensors

The current-voltage characteristics (I-V characteristics) of the immuno-EGOFET were measured in Fabio Biscarini's group. The I-V characteristics of an immune-EGOFET with a gate electrode modified with anti-IL4 immobilized by the HSC_6NH_2 protocol are shown in Figure 4.5A. We observe that the anti-IL4 (red curve) induces an electrical change in the I-V curve with respect to that recorded before anti-IL-4 immobilization (black curve). The Au gate electrode was then incubated in a reference solution of IL-4 at a concentration of 5 nM. This additional exposure does not give rise to further electrical change (blue curve). According to the protocol of Porter *et al.*[70], the biological layer has been electrochemically detached *via* the cleavage of the chemical bond between Au and sulphur of the HSC_6NH_2. The

subsequent increase of the EGOFET performance proves that no deterioration is taking place at the experimental time-scale.

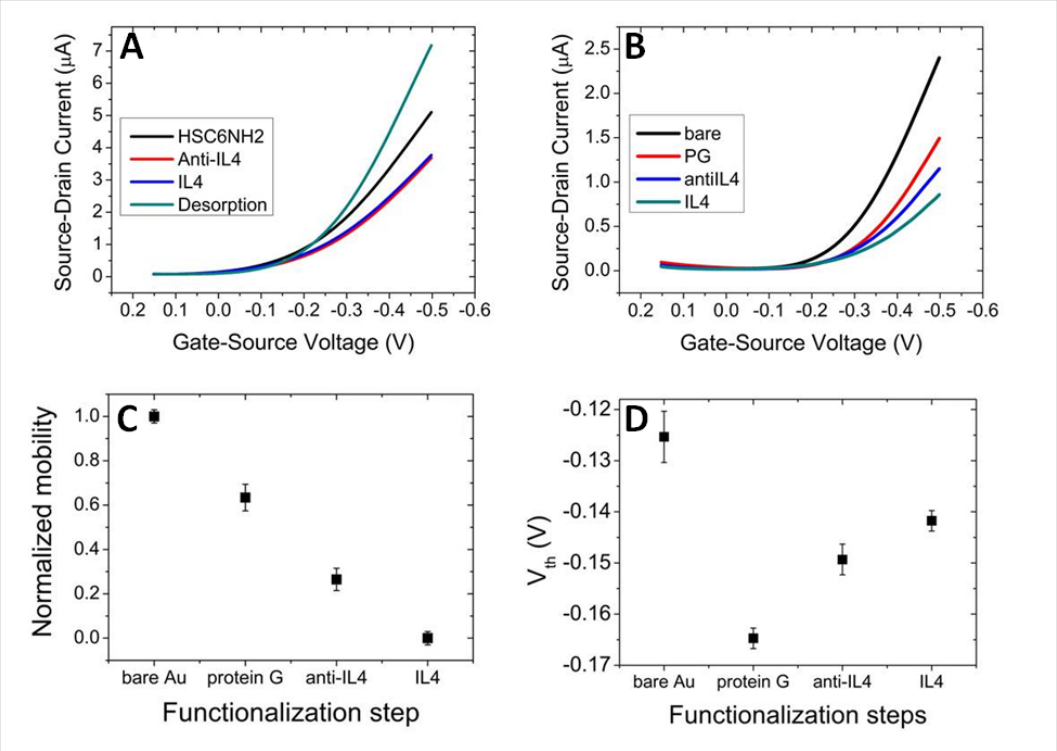

Figure 4.5. I-V transfer characteristics for A: HSC6NH2- and B: PG-based protocols. Normalized mobility ratio C and threshold voltage D trends corresponding to the stepwise functionalization.

The same validation process has been applied to the PG-based protocol (see Figure 4.5B). A significant change in the electrical response is now observed after incubation of the gate electrode in the IL-4 solution. The electrical measurements show that PG functionalized EGOFETs are capable to sense IL4 down to 5 nM concentrations, while the HSC_6NH_2 functionalized device does not give a measurable response. The PG functionalized device shows a mobility loss of 16% and a positive shift in the threshold voltage of approximately 10 mV after exposure to an IL4 solution (see Table 4.1). The absence of significant changes in the electrical properties EGOFETs with gate electrodes modified with the HSC_6NH_2-based functionalization is consistent with a much lower probability of recognition events for randomly oriented anti-IL4.

4.3.4. Detection of single antibody-antigen molecular interactions

After assessing the successful immobilization of anti-IL4 on modified gold substrates, bio-molecular recognition has been studied by means of SMFS using probes functionalized with IL-4 linked to the tip by a flexible heterobifunctional PEG linker. A schematic representation of an AFM tip functionalized with a 10 nm PEG linker and the IL-4 cytokine is depicted in Figure 4.6. The binding forces between the specific probe and anti-IL4 bound to the gold electrode surface were extracted from series of repeated force curves acquired on a 32 x 32 points grid on 1 μm x 1 μm areas of the sample.

Control experiments were performed to confirm the specificity of the detected unbinding events. The first set of controls involved probing the interaction of a bare AFM tip with Au substrates at each functionalization step. In a second controls series, antigen functionalized AFM tips were tests on Au, anti-IL4/HSC6NH2/Au and anti-IL4/PG/Au. Finally, cross-reactivity experiments were carried out by studying the interaction between IL-6 functionalized AFM tips and anti-IL4 substrates.

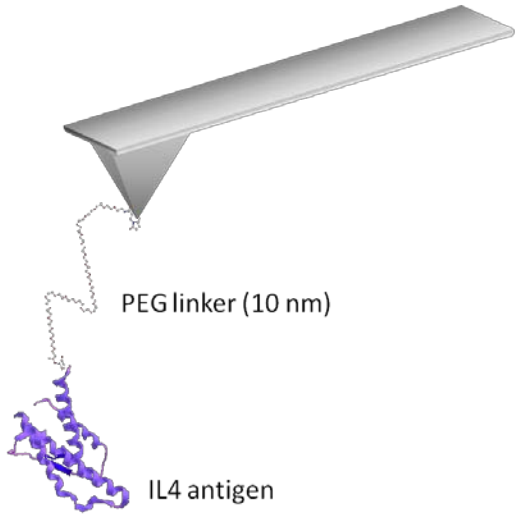

Figure 4.6. Schematic representation of the AFM cantilever functionalized with a 10 nm long PEG linker and an IL4 antigen molecule.

Figures 4.7A-B show the 2D molecular recognition maps containing the number of events with a given unbinding force (F_{unb}) and unbinding length (L_{unb}) for PG- and HSC_6NH_2-functionalized electrodes, respectively. The events are plotted in a colour-coded scale, where red and blue represent, respectively, the highest and the lowest

number of events. These histograms cluster together the curves with similar values of the unbinding forces and unbinding distance. Each point (represented as a hexagon) in the 2D histograms contains the force curves with similar unbinding forces and distances. As an example, Figures 4.7C-D show a representative force curve for one of the purple hexagons in Figures 4.79A and 4.7B. The noisy and adhesive behavior observed in the force curves is related to the fact that the measurements were performed on a real technological surface like polycrystalline gold, instead of prototypical substrates such as mica, which is atomically flat on large areas and more homogenous.

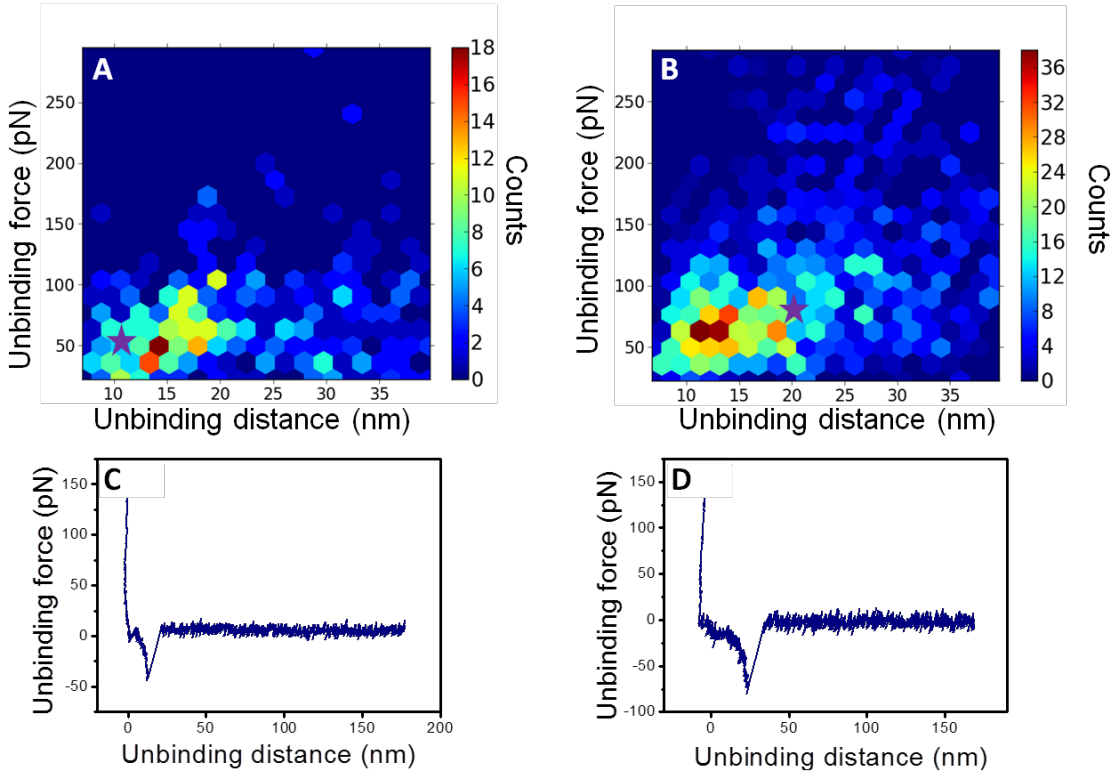

Figure 4.7. Two-dimmensional molecular recognition maps of the unbinding distance and unbinding force for A HSC_6NH_2-based protocol and B PG-based one. C-DTwo representative Force vs distance curves corresponding to the starred hexagons in A and B.

Regarding the unbinding lengths, the highest event probability is found in the 10-20 nm range with a dispersion ranging from 5 to 30 nm for the PG-coated Au surface. The most probable unbinding lengths were found in the 14-20 nm range with dispersion ranging from 7 to 30 nm for the anti-IL4/HSC_6NH_2/Au surface. We infer that for PG/Au electrodes, the unbinding events are more spread out at different

lengths, and their unbinding distance is further away from the surface. This observation is consistent with the presence of a larger fraction of oriented antibodies in a standing Y-shape configuration[6], since in this case we expect unbinding events taking place further away from the surface. Additionally, the Fab fragments of an IgG antibody are linked to the Fc fragment through di-sulphide bonds, resulting in an increased flexibility of these fragments[71]. Consequently, an antibody in Y-shape configuration is less constrained by the substrate, which explains the broader distribution of unbinding events as a function of distance in the case of highly-oriented anti-IL4. The unbinding length distributions of the HSC_6NH_2 mediated anti-IL4 functionalization are not consistent with the observations regarding ordered anti-IL4 monolayers.

4.3.5. Statistical analysis of the unbinding forces

For a better understanding of the antibody-antigen interactions on the electrode surface, a statistical analysis of the large dataset of unbinding forces F_{unb} was performed.

Figure 4.8 shows histograms of the distribution of unbinding forces and their corresponding probabilities for both functionalization strategies. A Gauss fit of the anti-IL4/PG/Au histogram renders a mean value of 71 pN and a standard deviation of 26 pN, while the anti-IL4/HSC_6NH_2/Au histogram is characterized by a mean value of 82 pN and a standard deviation of 33 pN.

Both anti-IL4/PG/Au and anti-IL4/HSC_6NH_2/Au yield apparently skewed histograms of F_{unb}. This is due to the fact that the data sets have been filtered out the unspecific or noisy events occurring at F_{unb} ≤20pN. Moreover, the skewness of the histograms was previously reported as being an indicator of multiple unbinding events taking place between the functionalized tip and the immobilized antibodies[72, 73].

The PG-mediated functionalization renders specific molecular recognition events of lower force and a 3-fold higher event probability as compared to the HSC_6NH_2-mediated one. The higher interaction force obtained for the HSC_6NH_2-mediated functionalization could be linked to a higher strength and stability of the resulting

antibody-antigen complex, but this is inconsistent with the lower binding probability. To deal with these contradictory results, a more thorough statistical analysis of the measured unbinding events was performed (Figure 4.9). This analysis includes the data obtained in control experiments performed on bare gold and with a non-specific antigen, anti-IL6 (crosscheck sample).

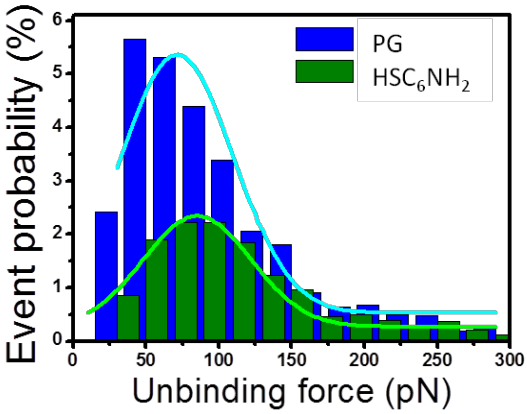

Figure 4.8. Histogram of the unbinding forces distributions and superimposed Gauss fits corresponding to the PG-mediated (blue) and HSC_6NH_2-mediated (green) antibodies immobilization

First, the bin size of each histogram is calculated depending on the number of curves N_{SB} in the data set giving rise to specific binding (*SB*). This number changes from sample to sample and therefore the sizes of histograms in Figure 4.9A are different. Specifically, the number of bins in each histogram is chosen as:

$$N_{bin} = NINT\left(\frac{3.49 \cdot \sigma}{N_{SB}^{1/3}}\right) \qquad (4.1)$$

where NINT is the nearest integer round-off and σ the standard deviation of the data set. The bin size of each histogram is given by

$$\Delta F = \frac{F_{\max} - F_{\min}}{N_{bin}} \qquad (4.2)$$

where F_{max} and F_{min} are the boundary values of the force range measured experimentally.

Next, the value of the histogram is normalized to the Specific Unbinding Probability Density (SUPD) as follows:

$$SUPD(F_k) \approx 100 \frac{N_{SB}}{N_{TOT}} \left(\frac{N_k}{\Delta F \cdot N_{SB}} \right) \quad (4.3)$$

where N_k is the number of curves in the *k-th* bin whose unbinding force F_{unb} falls within $F_k \pm \Delta F/2$. Its integral *vs* F_{unb} across the data set is estimated as the summation on the histogram bins multiplied by ΔF. The summation index runs from 1 to k_{max}, k_{max} being the index corresponding to $F_{kmax}(F_{ub})$.

$$SUP(F_{unb}) = \int_0^{F_{unb}} SUPD(F)dF \approx 100 \left(\sum_{k=1}^{k_{\max}} \frac{N_k}{N_{TOT}} \right) \quad (4.4)$$

The Specific Unbinding Probability is the asymptotic limit of the curves shown in Figure 4.9B.

$$SUP(F_{\max}) = \frac{100 \cdot N_{SB}}{N_{TOT}} \quad (4.5)$$

The skewness (standardized third moment) of each data set is found to be significant as its values largely exceed the corresponding Gaussian distribution estimator $\sqrt{6/N_{SB}}$ [74]. The three data sets exhibit a mean force value $\left\langle F_{ub}^* \right\rangle (\pm \sigma)$ equal to 98(±55) pN, 109(±59) pN and 80(±39) pN for PG, HSC_6NH_2, and crosscheck samples respectively. These values were inserted as parameters in Eq. 4.6, which describes a chi-square distribution normalized to the overall probability to detect a specific unbinding event[75, 76].

$$SUPD(F_{ub}) = 100 \cdot \frac{N_{SB}}{N_{tot}} \cdot \chi^2 \left(F_{ub} \right) = 100 \cdot \frac{N_{SB}}{N_{tot}} \frac{1}{2^p \Gamma(p)} \left(\frac{\sqrt{p} \cdot F_{ub}}{\sigma} \right)^{p-1} \exp\left(-\frac{\sqrt{p} \cdot F_{ub}}{\sigma} \right) \quad (4.6)$$

Here the parameters are: $p = \left(\frac{\left\langle F_{ub}^* \right\rangle}{\sigma} \right)^2$ and $\Gamma(p)$ the gamma function. The trends of SUPD, depicted as continuous curves overlapping the histograms in Figure 4.11A, show a conformational adherence within the force range from 20 pN to 300 pN[77-80].

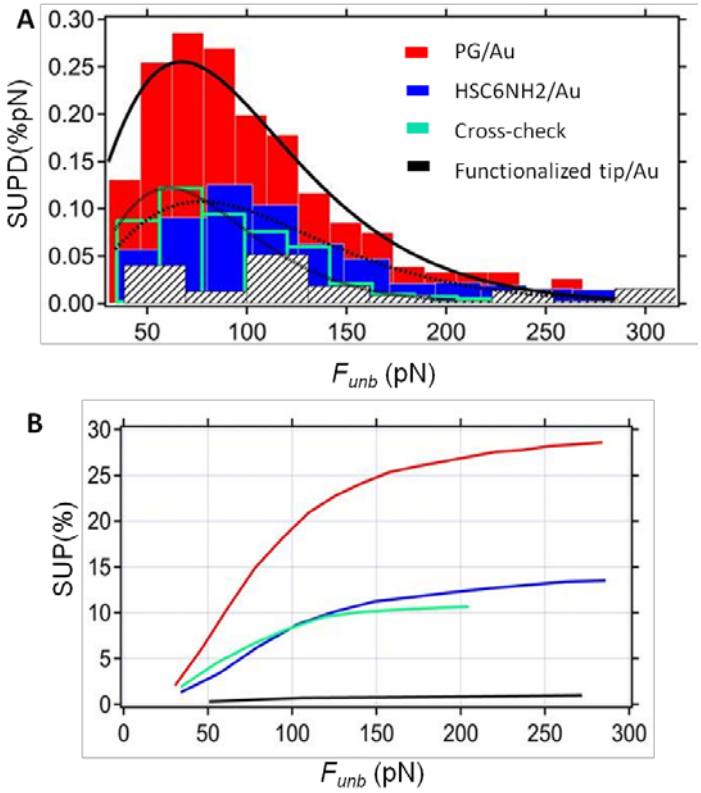

Figure 4.9. A. Histograms of SUPD as a function of the unbinding force. Red, blue, empty and white-black patterned bars stand for PG, HSC_6NH_2, cross-check and bare Au respectively. Solid, dashed and dotted lines are the best χ-square fits corresponding to PG, HSC_6NH_2 and cross-check; B. SUP *vs.* F_{unb} plots are shown for each protocol.

The results of the statistical analysis in Figure 4.9A show that the SUPD curves for both PG and HSC_6NH_2 functionalized samples present the same tendency and can be overlapped by vertical rescaling. On the other hand, they are substantially different from crosscheck sample curve, which has a similar shape but whose peak is displaced towards lower force values. As discussed in the introductory Section 4.1 of this chapter, antibodies are expected to be able to interact in a nonspecific manner with different antigens by exploring different conformations and establishing elastic bonds (see *conformational selection* hypothesis). Therefore, the lower unbinding forces corresponding to the crosscheck sample are in good agreement with the *conformational selection* hypothesis describing antibody-antigen molecular recognition processes.

The SUPD curves in figure 4.9A corresponding to PG and HSC_6NH_2 functionalized samples are radically different from the control sample (bare Au) curve, which does not exhibit an apparent skewness.

By examining the SUP curves, we find that anti-IL4/PG/Au induces a three-fold higher frequency of specific binding events than the anti-IL4/HSC_6NH_2/Au sample (Figure 4.9B). These values can be interpreted as the result of the effective coverage of functional antibodies on the respective surfaces, *viz.* PG yields a 30% coverage of active antibodies for IL4 recognition, whereas HSC_6NH_2 only 10%.

Interestingly, the SUP of HSC_6NH_2 is comparable to that of the crosscheck sample, although it appears that the latter contributes to lower force events. The distribution related to bare gold shows a different trend, and the SUP is much lower than all the other distributions. This means that IL4 poorly interact with un-functionalized Au, as expected.

4.3.6. Dynamic force spectroscopy

In order to gain insights into the energy landscape of the bound complexes, we carried out experiments at different retraction velocities. The Bell-Evans model has been extensively discussed in Chapter 2.4.1. According to this model, the force of a single-energy barrier in the thermally activated regime scales up with the logarithm of the loading rate[58, 59]:

$$F^*(r) = \frac{k_B T}{x_\beta} \ln\left(\frac{x_\beta r}{k_{off}(0) k_B T} \right) \qquad (4.7)$$

Here F^* is the most probable unbinding force, r is the loading rate, x_β is the position of energy barrier along the reaction coordinate, $k_{off}(0)$ is the dissociation rate of the bond at zero force and k_BT is the thermal energy. The loading rate is the product between the retract velocity and the spring constant. To account for the contribution of the PEG linker spring constant to the overall spring constant of the system, the loading rate was extracted from the slope of the force curve before unbinding occurs (see Chapter 2.4.2). The retract velocity was varied from 100 nm/s to 1 μm/s and cantilevers of 0.02 N/m and 0.08 N/m were used.

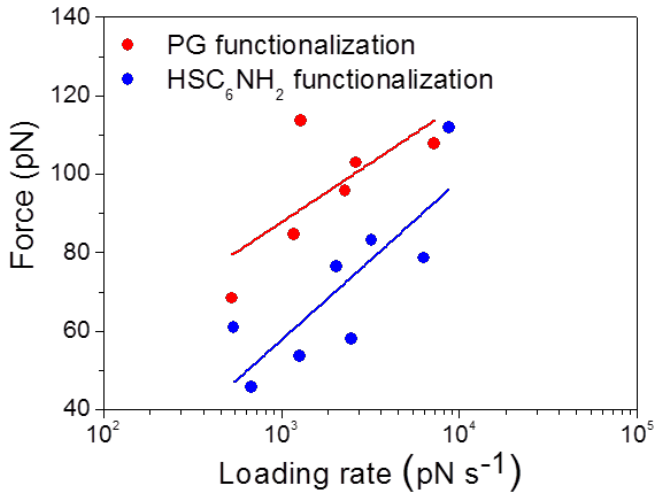

4.10. Most probable unbinding forces *versus* loading rates for PG and HSC_6NH_2 protocols and corresponding Bell-Evans fits with Equation 4.7.

The plot in Figure 4.10 displays the linear increase of the most probable unbinding force with the logarithm of the loading rate for the two antibody immobilization protocols. This characteristic behavior for a thermally activated dissociation process under an applied load has been previously observed for other antibody-antigen complexes[81].

To determine the kinetic parameters of the molecular recognition process, the position of energy barrier along the reaction coordinate x_β was extracted from the slope of linear fit of the unbinding forces *vs.* loading rate logarithm plot (see Equation 4.7). Next, the kinetic off-rate constant of dissociation at zero force k_{off} was calculated by extrapolation to zero forces. Antibody-antigen complexes have limited lifetimes, which are shortened by thermal activation under an applied force. The characteristic time needed for the spontaneous dissociation, τ, is given by the inverse of the kinetic off-rate constant and can be correlated with the specificity of the recognition process as well as the stability of the complex.

The associated values for the Bell-Evans model parameters are reported in Table 4.1. The value of the k_{off} $=4\cdot10^{-3}$ s^{-1}, corresponding to τ=206 s for PG-based functionalization, is in good agreement with the values observed in literature for specific antigen-antibody pairing characterized by single-molecule force spectroscopy[77, 79, 82]. For the HSC_6NH_2-functionalization, we obtain k_{off} =0.209 s^{-1}, corresponding to a lifetime τ=4.78 s. The almost two orders of magnitude ratio of the k_{off} indicates that the antigen fits more steadily the antibody when the latter is

immobilized onto the PG substrate, as compared to the HSC_6NH_2-functionalization[83, 84]. This yields the increased binding affinity between IL4/anti-IL4 when PG is used for the antibody immobilization. As far as the potential barrier width between the bound complex and the transition state, x_β, is concerned, the values for both functionalization approaches fall in the range usually found for specific interactions between partners with a rather high conformational stability[85]. We observe that the IL4/anti-IL4 complex formed *via* PG immobilization with a lifetime of the complex of 206 s shows higher stability as compared to the one formed onto the SAM-functionalized surface, which will dissociate faster at a complex lifetime of 4.78 s.

In the frame of the transition state theory[59, 86] (see Chapter 2.4.1), once k_{off} is calculated, the measured free energy of the unbinding process ΔG_m can be estimated using the following equation, where *h* is Planck's constant:

$$\Delta G_m = -k_B T \ln \frac{k_{off} \cdot h}{k_B T} \quad (4.8)$$

The total free energy of the antibody-antigen complex has been estimated for the two gold functionalization approaches, obtaining values of -21.74 kcal/mol for the PG mediated functionalization and -19.59 kcal/mol for the HSC_6NH_2-functionalization. One should take into account the fact that this free energy includes some contribution from the unbinding process of the antibody-antigen complex, as well as from the stretching of the PEG linker. Therefore, the free energy related exclusively to the unbinding process of the IL4/anti-IL4 complex $\Delta G_{complex}$ can be calculated from this expression:

$$\Delta G_{complex} = \Delta G_m - \Delta G_{PEG} \quad (4.9)$$

The free energy related to the stretching of a 10 nm long PEG linker has been estimated experimentally to be -1.75 kcal/mol[87], so the unbinding free energy corresponding to the antibody-antigen pairs are 20.07±0.95 kcal/mol for the PG-based functionalization and 17.92±0.48 kcal/mol for the HSC6NH2 functionalization. Similar values for the unbinding energies of antibody-antigen complexes were previously reported[10, 88]. These values of the unbinding free energy could be related to the breaking of several hydrogen bonds and one or two salt bridges that are responsible of the antibody-antigen recognition.

The exploration of the energy landscape of the antibody-antigen pair studied here by SMFS provides important information for further optimization of surface immobilization strategies in immunosensing. The antibody-antigen complexes formed when the antibodies are immobilized on PG have a higher free unbinding energy as compared to the HSC_6NH_2 functionalization. By correlating the higher binding probability of the antibodies on PG substrates with the findings on the dissociation free energy, one can hypothesize that the surface attachment strategy (high-affinity immobilization *vs* covalent binding) can potentially alter the binding sites conformation. Similar findings were reported in a SPR biosensing setup[89]. This could be linked to a higher heterogeneity of the surface environment and binding sites distribution, as well as to steric constraints imposed by the covalent immobilization. The immobilization of the antibodies based on the affinity of the Fc fragment for PG renders an ordered monolayer where molecules have higher flexibility. This allows for a higher conformational freedom of the Fab fragments, which results in a more stable antibody-antigen complex.

Table 4.1

Experiment	x_β (Å)	k_{off} (s^{-1})	τ (s)	$\Delta G_{complex}$ (kcal/mol)	μ (% loss)	ΔV_{th} (mV)
IL4 on Protein G	3.2 (±0.2)	0.004 (±0.002)	206 (±103)	20.07 (±0.95)	16	≈10
IL4 on HSC6NH2	2.4 (±0.1)	0.209 (±0.073)	4.78 (±1.6)	17.92 (±0.48)	-	-

4.4. Conclusions

The use of two completely different techniques in terms of spatial and temporal scales, such as single-molecule force spectroscopy and electrical measurements by means of organic transistors, allowed a direct correlation between them in the study of specific interactions of an antibody-antigen pair (anti-IL4 and IL-4). For this purpose, two strategies of surface functionalization have been assessed, one based on the use of amino-terminated self-assembled monolayers and another one by means of His-Tagged Protein G. Single force spectroscopy measurements detected a larger probability (30%) of unbinding events for the PG-based strategy with respect to HSC_6NH_2-based one (10%).

Furthermore, by using single-molecule force spectroscopy the average lifetime of the antibody-antigen complex for the two different strategies was estimated. It was shown that the complexes formed on the anti-IL4/PG/Au interface have a significantly higher lifetime (τ = 206(±103) s), than the ones formed on anti-IL4/HSC_6NH_2/Au (τ = 4.78(±1.6) s). These experimental evidences clearly prove how PG yields a more ordered antibodies layer, hence a higher coverage of active antibodies towards IL-4. The direct implementation of these Au electrodes in EGOFET architecture confirms different sensitivities as a function of the functionalization strategies. As a result, EGOFET successfully sensed IL-4 down to a concentration of 5 nM when the gate electrode was functionalized with PG, whereas EGOFETs functionalized by HSC_6NH_2 failed to detect any interactions at the same antigen concentration.

Finally, this comparative study meets the challenging task of correlating a mechanical nanoscale metrology like single-molecule force spectroscopy, which probes individual or a few antibody-antigen pairings, with the electrical response of an electrolyte-gated field effect transistor that involves a wide number of recognition events.

4.5. References

1. B. K. Van Weemen and A. H. W. M. Schuurs, *FEBS Letters*, 1971, **15**, 232-236.
2. A. Amit, R. Mariuzza, S. Phillips and R. Poljak, *Science*, 1986, **233**, 747-753.
3. R. Stanfield, T. Fieser, R. Lerner and I. Wilson, *Science*, 1990, **248**, 712-719.
4. J. Rini, U. Schulze-Gahmen and I. Wilson, *Science*, 1992, **255**, 959-965.
5. W. Wang, W. Ye, Q. Yu, C. Jiang, J. Zhang, R. Luo and H.-F. Chen, *The Journal of Physical Chemistry B*, 2013, **117**, 4912-4923.
6. Z. Xiubo, Y. Mohammed, P. Fang and R. L. Jian, in *Proteins at Interfaces III State of the Art*, American Chemical Society, 2012, vol. 1120, ch. 25, pp. 543-574.
7. N. Willem, A. H. Thomas and L. B. John, in *Proteins at Interfaces III State of the Art*, American Chemical Society, 2012, vol. 1120, ch. 1, pp. 1-34.
8. L. C. James, P. Roversi and D. S. Tawfik, *Science*, 2003, **299**, 1362-1367.
9. R. Jimenez, G. Salazar, J. Yin, T. Joo and F. E. Romesberg, *Proc. Natl. Acad. Sci. U. S. A.*, 2004, **101**, 3803-3808.
10. A. Alemany, N. Sanvicens, S. d. Lorenzo, M. P. Marco and F. Ritort, *Nano Lett.*, 2013, **13**, 5197-5202.
11. D. D. Boehr, R. Nussinov and P. E. Wright, *Nat Chem Biol*, 2009, **5**, 789-796.
12. R. Medzhitov and C. A. Janeway, *Science*, 2002, **296**, 298-300.
13. A. Suzuki, P. Leland, B. H. Joshi and R. K. Puri, *Cytokine*, 2015, **75**, 79-88.
14. V. Gocheva, H.-W. Wang, B. B. Gadea, T. Shree, K. E. Hunter, A. L. Garfall, T. Berman and J. A. Joyce, *Genes & Development*, 2010, **24**, 241-255.
15. B. H. Joshi, P. Leland, S. Lababidi, F. Varrichio and R. K. Puri, *Cancer Medicine*, 2014, **3**, 1615-1628.
16. O. Prokopchuk, Y. Liu, D. Henne-Bruns and M. Kornmann, *Br J Cancer*, 2005, **92**, 921-928.
17. M. Todaro, Y. Lombardo, M. G. Francipane, M. P. Alea, P. Cammareri, F. Iovino, A. B. Di Stefano, C. Di Bernardo, A. Agrusa, G. Condorelli, H. Walczak and G. Stassi, *Cell Death Differ*, 2008, **15**, 762-772.
18. G. Biomarkers Definitions Working, *Clinical Pharmacology & Therapeutics*, 2001, **69**, 89-95.
19. A. P. F. Turner and J. C. Pickup, *Biosensors*, 1985, **1**, 85-115.
20. L. Su, W. Jia, C. Hou and Y. Lei, *Biosensors and Bioelectronics*, 2011, **26**, 1788-1799.
21. J. Kirsch, C. Siltanen, Q. Zhou, A. Revzin and A. Simonian, *Chemical Society reviews*, 2013, **42**, 8733-8768.
22. K. Saha, S. S. Agasti, C. Kim, X. Li and V. M. Rotello, *Chemical Reviews*, 2012, **112**, 2739-2779.
23. J. Tamayo, P. M. Kosaka, J. J. Ruz, A. San Paulo and M. Calleja, *Chemical Society reviews*, 2013, **42**, 1287-1311.
24. B. V. Chikkaveeraiah, A. A. Bhirde, N. Y. Morgan, H. S. Eden and X. Chen, *ACS Nano*, 2012, **6**, 6546-6561.
25. P. M. Kosaka, PiniV, J. J. Ruz, R. A. da Silva, M. U. González, RamosD, CallejaM and TamayoJ, *Nat Nano*, 2014, **9**, 1047-1053.
26. P. R. Sajanlal and T. Pradeep, *Nanoscale*, 2012, **4**, 3427-3437.
27. M. Euler, Y. Wang, D. Heidenreich, P. Patel, O. Strohmeier, S. Hakenberg, M. Niedrig, F. T. Hufert and M. Weidmann, *Journal of Clinical Microbiology*, 2013, **51**, 1110-1117.
28. S. Casalini, A. C. Dumitru, F. Leonardi, C. A. Bortolotti, E. T. Herruzo, A. Campana, R. F. de Oliveira, T. Cramer, R. Garcia and F. Biscarini, *ACS Nano*, 2015, **9**, 5051-5062.
29. G. T. Hermanson, in *Bioconjugate Techniques (Third edition)*, ed. G. T. Hermanson, Academic Press, Boston, 2013, DOI: http://dx.doi.org/10.1016/B978-0-12-382239-0.00016-9, pp. 741-755.
30. Y. Liu, X. Dong and P. Chen, *Chemical Society reviews*, 2012, **41**, 2283-2307.

31. R. Mas-Balleste, C. Gomez-Navarro, J. Gomez-Herrero and F. Zamora, *Nanoscale*, 2011, **3**, 20-30.
32. B. Hock, *Analytica Chimica Acta*, 1997, **347**, 177-186.
33. S. Kurosawa, J.-W. Park, H. Aizawa, S.-I. Wakida, H. Tao and K. Ishihara, *Biosensors and Bioelectronics*, 2006, **22**, 473-481.
34. R. Raiteri, M. Grattarola, H.-J. Butt and P. Skládal, *Sensors and Actuators B: Chemical*, 2001, **79**, 115-126.
35. I. Abdulhalim, M. Zourob and A. Lakhtakia, *Electromagnetics*, 2008, **28**, 214-242.
36. C.-S. Lee, S. Kim and M. Kim, *Sensors*, 2009, **9**, 7111.
37. K. Liang, W. Mu, M. Huang, Z. Yu and Q. Lai, *Electroanalysis*, 2006, **18**, 1505-1510.
38. Z. Li, Y. Fu, W. Fang and Y. Li, *Sensors*, 2015, **15**, 19212.
39. H. C. W. Hays, P. A. Millner and M. I. Prodromidis, *Sensors and Actuators B: Chemical*, 2006, **114**, 1064-1070.
40. Y. Wan, Y. Su, X. Zhu, G. Liu and C. Fan, *Biosensors and Bioelectronics*, 2013, **47**, 1-11.
41. P. Casal, X. Wen, S. Gupta, T. Nicholson, Y. Wang, A. Theiss, B. Bhushan, L. Brillson, W. Lu and S. C. Lee, *Philosophical Transactions of the Royal Society of London A: Mathematical, Physical and Engineering Sciences*, 2012, **370**, 2474-2488.
42. G. Palazzo, D. De Tullio, M. Magliulo, A. Mallardi, F. Intranuovo, M. Y. Mulla, P. Favia, I. Vikholm-Lundin and L. Torsi, *Advanced Materials*, 2015, **27**, 911-916.
43. A. D. Sheehan, J. Quinn, S. Daly, P. Dillon and R. O'Kennedy, *Analytical Letters*, 2003, **36**, 511-537.
44. E. T. Herruzo and R. Garcia, *Applied Physics Letters*, 2007, **91**, 3.
45. A. San Paulo and R. García, *Physical Review B*, 1999, **60**, 4961-4967.
46. I. Horcas, R. Fernández, J. M. Gómez-Rodríguez, J. Colchero, J. Gómez-Herrero and A. M. Baro, *Review of Scientific Instruments*, 2007, **78**, 013705.
47. J. Hutter and J. Bechhoefer, *Review of Scientific Instruments*, 1993, **64**, 1868–1873.
48. H. J. Butt and M. Jaschke, *Nanotechnology*, 1995, **6**, 1.
49. S. Casalini, F. Leonardi, T. Cramer and F. Biscarini, *Organic Electronics*, 2013, **14**, 156-163.
50. L. Kergoat, B. Piro, M. Berggren, M.-C. Pham, A. Yassar and G. Horowitz, *Organic Electronics*, 2012, **13**, 1-6.
51. F. Buth, D. Kumar, M. Stutzmann and J. A. Garrido, *Applied Physics Letters*, 2011, **98**, 153302.
52. F. Buth, A. Donner, M. Sachsenhauser, M. Stutzmann and J. A. Garrido, *Advanced Materials*, 2012, **24**, 4511-4517.
53. M. Magliulo, A. Mallardi, M. Y. Mulla, S. Cotrone, B. R. Pistillo, P. Favia, I. Vikholm-Lundin, G. Palazzo and L. Torsi, *Advanced Materials*, 2013, **25**, 2090-2094.
54. A. Campana, T. Cramer, D. T. Simon, M. Berggren and F. Biscarini, *Advanced Materials*, 2014, **26**, 3874-3878.
55. D. Khodagholy, T. Doublet, P. Quilichini, M. Gurfinkel, P. Leleux, A. Ghestem, E. Ismailova, T. Hervé, S. Sanaur, C. Bernard and G. G. Malliaras, *Nat Commun*, 2013, **4**, 1575.
56. T. Cramer, A. Kyndiah, M. Murgia, F. Leonardi, S. Casalini and F. Biscarini, *Applied Physics Letters*, 2012, **100**, 143302.
57. T. Cramer, A. Campana, F. Leonardi, S. Casalini, A. Kyndiah, M. Murgia and F. Biscarini, *Journal of Materials Chemistry B*, 2013, **1**, 3728-3741.
58. R. Merkel, P. Nassoy, A. Leung, K. Ritchie and E. Evans, *Nature*, 1999, **397**, 50-53.
59. E. Evans and K. Ritchie, *Biophysical journal*, 1997, **72**, 1541-1555.
60. I. D. Medalsy and D. J. Müller, *ACS Nano*, 2013, **7**, 2642-2650.
61. L. Betancor, F. López-Gallego, A. Hidalgo, N. Alonso-Morales, G. D.-O. C. Mateo, R. Fernández-Lafuente and J. M. Guisán, *Enzyme and Microbial Technology*, 2006, **39**, 877-882.
62. Z. Yang and Y.-P. Zhao, *Engineering Analysis with Boundary Elements*, 2007, **31**, 402-409.
63. D. Kim and A. E. Herr, *Biomicrofluidics*, 2013, **7**, 041501.
64. G. Bachand and C. Montemagno, *Biomed Microdevices*, 2000, **2**, 179-184.

65. J. E. Baio, F. Cheng, D. M. Ratner, P. S. Stayton and D. G. Castner, *Journal of biomedical materials research. Part A*, 2011, **97**, 1-7.
66. A. K. Trilling, J. Beekwilder and H. Zuilhof, *Analyst*, 2013, **138**, 1619-1627.
67. Y. M. Bae, B.-K. Oh, W. Lee, W. H. Lee and J.-W. Choi, *Biosensors and Bioelectronics*, 2005, **21**, 103-110.
68. H. Y. Song, X. Zhou, J. Hobley and X. Su, *Langmuir*, 2012, **28**, 997-1004.
69. A. San Paulo and R. García, *Biophysical journal*, 2000, **78**, 1599-1605.
70. M. M. Walczak, D. D. Popenoe, R. S. Deinhammer, B. D. Lamp, C. Chung and M. D. Porter, *Langmuir*, 1991, **7**, 2687-2693.
71. S. Ido, H. Kimiya, K. Kobayashi, H. Kominami, K. Matsushige and H. Yamada, *Nat Mater*, 2014, **13**, 264-270.
72. T. A. Sulchek, R. W. Friddle, K. Langry, E. Y. Lau, H. Albrecht, T. V. Ratto, S. J. DeNardo, M. E. Colvin and A. Noy, *Proc. Natl. Acad. Sci. U. S. A.*, 2005, **102**, 16638-16643.
73. S. Allen, J. Davies, M. C. Davies, A. C. Dawkes, C. J. Roberts, S. J. Tendler and P. M. Williams, *The Biochemical journal*, 1999, **341 (Pt 1)**, 173-178.
74. W. H. Press, S. A. Teukolsky, W. T. Vetterling and B. P. Flannery, *Numerical Recipes 3rd Edition: The Art of Scientific Computing*, 2007.
75. F. Biscarini, R. Zamboni, P. Samorí, P. Ostoja and C. Taliani, *Physical Review B*, 1995, **52**, 14868-14877.
76. M. Abramowitz and I. A. Stegun, *Handbook of Mathematical Functions with Formulas, Graphs, and Mathematical Tables*, 1972.
77. F. Schwesinger, R. Ros, T. Strunz, D. Anselmetti, H. J. Guntherodt, A. Honegger, L. Jermutus, L. Tiefenauer and A. Pluckthun, *Proc Natl Acad Sci U S A*, 2000, **97**, 9972-9977.
78. K. L. Brogan, J. H. Shin and M. H. Schoenfisch, *Langmuir*, 2004, **20**, 9729-9735.
79. A. Berquand, N. Xia, D. G. Castner, B. H. Clare, N. L. Abbott, V. Dupres, Y. Adriaensen and Y. F. Dufrene, *Langmuir*, 2005, **21**, 5517-5523.
80. F. Kienberger, G. Kada, H. Mueller and P. Hinterdorfer, *Journal of molecular biology*, 2005, **347**, 597-606.
81. A. R. Bizzarri and S. Cannistraro, *Nanotechnology*, 2014, **25**, 335102.
82. A. R. Bizzarri and S. Cannistraro, *Chemical Society reviews*, 2010, **39**, 734-749.
83. B. Bonanni, A. S. Kamruzzahan, A. R. Bizzarri, C. Rankl, H. J. Gruber, P. Hinterdorfer and S. Cannistraro, *Biophysical journal*, 2005, **89**, 2783-2791.
84. B. Bonanni, A. R. Bizzarri and S. Cannistraro, *The journal of physical chemistry. B*, 2006, **110**, 14574-14580.
85. A. R. Bizzarri and S. Cannistraro, *Dynamic Force Spectroscopy and Biomolecular Recognition*, Taylor & Francis, 2012.
86. H. Eyring, *The Journal of Chemical Physics*, 1935, **3**, 107-115.
87. F. Oesterhelt, M. Rief and H. E. Gaub, *New Journal of Physics*, 1999, **1**, 6.1-6.5.
88. R. Ros, F. Schwesinger, D. Anselmetti, M. Kubon, R. Schäfer, A. Plückthun and L. Tiefenauer, *Proceedings of the National Academy of Sciences*, 1998, **95**, 7402-7405.
89. H. Zhao, I. I. Gorshkova, G. L. Fu and P. Schuck, *Methods*, 2013, **59**, 328-335.

Chapter 5

Vertical adsorption orientations and immunological recognition of antibodies on graphene

5.1. Graphene as a biosensing platform

Graphene refers to single or few graphite layers and it is a two-dimensional carbon allotrope displaying planar sp^2 bonding. The discovery of electrically isolated graphene in 2004[1] provoked extraordinary excitement in the nanomaterials field[2, 3]. The excitement even reached the European Commission, which launched "The Graphene Flagship" in 2013, a 1.3 billion euro initiative meant to smooth the transitioning path of graphene from the laboratory to the marketplace.

What makes graphene a very promising sensor material are its remarkable properties. Graphene is a very robust and highly tunable material, with unique physicochemical properties (theoretical surface area of 2630 m^2/g for suspended graphene), high mechanical strength and excellent electric and thermal conductivities[2, 4-7].

A key point in the fabrication graphene-based devices is the fabrication method. Mechanical exfoliation from highly oriented pyrolytic graphite (HOPG) is one of the most widely used methods in laboratories all over the world. This method renders small-sized (< 100 μm) pristine graphene flakes (Figure 5.1), which are mostly suitable for proof-of-concept experiments and fundamental studies. Other methods that have been employed for the production of higher surfaces of graphene are nanoimprinting, thermal decomposition of silicon carbide (SiC) in ultra high vacuum (UHV), chemical vapor deposition (CVD) growth on transition metal substrates or substrate-free CVD. The latter aims the mass-production of graphene surfaces for electronics applications. The thermal reduction of graphite oxide (GO) is also a method that can yield large graphene

areas at reduced production costs. Despite its economical advantages, graphene obtained by GO reduction has a high number of structural defects and functional groups, which limits its applications.

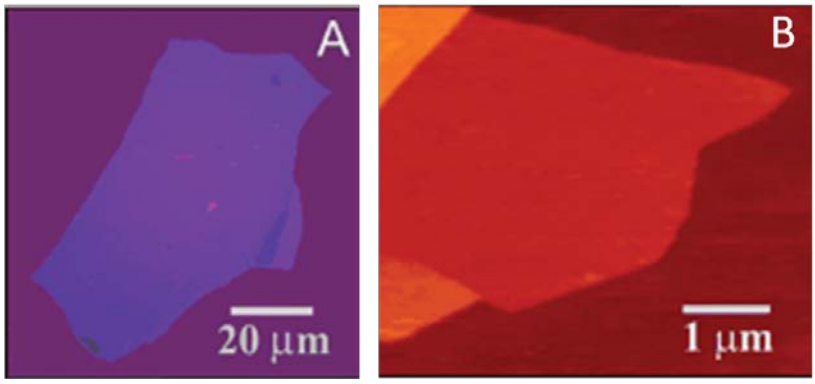

Figure 5.1. A: Photograph (in normal white light) of a relatively large multilayer graphene flake with thickness ~3 nm on top of an oxidized Si wafer. B: AFM image of a single-layer graphene obtained by mechanical cleavage of graphite. Adapted from Ref.1.

Graphene physical sensors for photons[8], mass[9], strain[10] and magnetic field[11] were demonstrated during the last decade. Graphene would also be an ideal substrate for biomedical applications and it has already been considered for the development of biosensors, medical implants and drug delivery systems[12, 13].
The study of protein interaction with graphene surfaces is a subject of fundamental and technological interest. Proteins constitute the largest and most widely employed class of biomolecules for surface functionalization. Biosensors applications strongly rely on protein adsorption and a key requirement for biosensing devices is that the protein must remain bioactive upon deposition. Protein adsorption also represents an interesting and important fundamental problem because it is the result of the interplay among protein-surface interactions, hydration forces, and the protein ability to change conformation as controlled by its internal strength. In the past years, many experimental studies have addressed the understanding and controlling of protein-surface interactions[14]. Nevertheless, due to the inherent difficulties to probe events either *in situ* or at an atomistic level, protein adsorption is not well understood

yet. As a result, the design of most devices dependent on protein-surface interaction is still based on trial and error approaches.

Different biomedical applications[15, 16] such as immunoassays[17, 18] and biosensors[19] would benefit from a better understanding of the Immunoglobulin G (IgG) adsorption to solid surfaces. IgG is the most abundant of the five classes of antibodies produced by the body and provides the majority of antibody-based immune response[20]. The main structural features of IgG antibodies have been described in Chapter 4.1. The ability of IgG antibodies to bind a specific antigen, which characterizes their bioactivity, is extremely sensitive to conformational changes in the structure of the paratope[14, 21]. Many experimental methods for controlling the antibody adsorption orientation have been thoroughly investigated in order to improve the sensitivity of current immunoassays. This has proved to be a highly non trivial task since for all the surfaces studied so far[21-24], including mica, quartz, silica and pentacene, antibodies adsorb preferentially in configurations where the Fabs are not easily accessible and, consequently, except in the recent study of 2D crystals built from IgG domains (fragments)[25], the IgG activity towards the antigen is diminished.

Given the increased thrust in the development of graphene-based biosensor devices, its biocompatibility and biosafety[26] need to be carefully addressed. To assess the suitability of graphene as a support surface for a new generation of biosensors and, in particular, immunosensors, it is crucial to have extensive knowledge and control on how antibodies adsorb on the material (e.g. orientation and bioactivity). Previous work has shown that, independently of the ionic strength and pH, antibodies show a high affinity for hydrophobic surfaces[27]. Therefore, being graphene hydrophobic, one expects it to be able to immobilize IgGs. While a high adsorption affinity is a required feature to develop IgG-based biosensors, a strong adsorption could lead to an undesired protein unfolding or to a loss of its bioactivity[28].

An ideal immunosensing surface should prevent any major unfolding of the immobilized antibodies and should also leave the Fabs pointing towards the solution to increase the response of the device. From an experimental perspective, it is very challenging to determine both the actual adsorption orientation of a given antibody as well as the degree of adsorption-induced unfolding on IgG. The high lateral resolution of atomic force microscopy and its ability to image individual molecules on different environments makes AFM an ideal technique for this task. Force microscopy studies of antibody deposition and adsorption have been performed in air and liquid on different surfaces such as mica[25, 29, 30], pentacene[24] or biological membranes[31]. High-resolution images have revealed some of the dominant adsorption configurations but they can only provide very limited information about the different factors that lead to the observed morphologies. Accurate atomistic simulations of IgG in the protein native liquid environment are a great tool, which can provide more knowledge on the adsorption orientations of antibodies on different substrates. This makes atomistic simulations the perfect complement to AFM experiments of IgG adsorption.

The overall protein adsorption process is composed of three main stages: diffusion of the protein from the bulk solution into the interface region, dehydration of the protein/surface interface, and, finally, deformation and attachment of the protein onto the surface.

Previous combined studies, focused on the adsorption of small peptides[32, 33], have validated the use of simulation methods –such as molecular dynamics (MD), steered-molecular-dynamics (SMD), and the associated classical force fields–, to gain direct, quantitative information about the competing mechanisms involved in the adsorption of small protein fragments. These calculations use an accurate atomistic description of the solvent, including explicitly water molecules in the simulations. Extending this approach to large proteins like the IgG, with more than 20000 atoms and a molecular weight of 150 kDa, is a very challenging task, due to the sheer size of the calculations and the long simulation times needed to describe the diffusion and dehydration stages[34]. Previous theoretical studies of protein adsorption on graphene or alike hydrophobic surfaces where water is considered explicitly have been restricted

to short peptide-chains[32, 35] or small proteins like BMP-2 (26 kDa)[36]. Larger proteins like bovine serum albumin (BSA) (66 kDa) have been addressed using an implicit solvent approach[37, 38]. All of these studies have found an almost complete loss of the secondary structure, suggesting that the IgG would unfold and lose its bioactivity once it is adsorbed over graphene. However, this evidence has to be taken with caution. Sun et al.[39] have found differences in the adsorption behavior with the solvent model used. Furthermore, earlier results for the unfolding of moderately large proteins like lysozyme (14.3 kDa, 125 aminoacids) coming from implicit solvent studies[38] have been questioned by more recent simulations using explicit water models[34, 40]. From a more fundamental perspective, it is not clear if the free energy balance, which results in the unfolding of the small peptides on hydrophobic surfaces, holds in the case of a large protein.

In this chapter, the adsorption of IgG antibodies on graphene was studied by a combination of AFM observations and large-scale molecular dynamics simulations. The details of the molecular dynamics simulations performed by the group of Ruben Perez at the Universidad Autonoma de Madrid can be found in Appendix B.2. The discussion included in this thesis will mostly focus on the description of the data obtained from AFM experiments and the comparison between the experimental and theoretical results.

5.2. Experimental methods

5.2.1. Antibodies adsorption on graphene

Graphene layers were generated by repeatedly cleaving HOPG with adhesive tape. The graphene flakes adhered to the tape were transferred to mica by a applying a gentle mechanical contact between the tape and a freshly cleaved piece of mica[41].

For high resolution imaging of individual antibodies, a 1 mg/ml anti-IL4 stock solution (Biovision, Spain) was diluted to a concentration of 0.5 μg/ml and

deposited onto the graphene substrate for 20 s. The sample was then rinsed with ultrapure water.

Single molecule force spectroscopy experiments were performed both on individual antibodies and on antibodies monolayer samples. To obtain a monolayer, the anti-IL4 stock solution (1 mg/ml) was diluted to a concentration of 50 μg/ml and deposited for 10 minutes onto the graphene substrate. The sample was rinsed with PBS 0.01 M pH 7.4.

5.2.2. High-resolution images of individual antibodies on graphene

Either a Cypher AFM (Asylum Research-Oxford Instruments, Santa Barbara) or a Multimode V AFM (Bruker, Santa Barbara) were operated in amplitude modulation[29, 42] to image individual antibodies attached to the graphene substrate.

The antibodies immobilized on graphene were imaged in air and ultrapure water. High-resolution imaging experiments in air were performed with supersharp SSS-NCL cantilevers (Nanosensors, Switzerland), which have a nominal force constant k of 35 N/m and resonant frequency ω of 310 kHz. The free and set point amplitudes were respectively, 8 nm and 7 nm. As for the experiments in water medium, biolever fast BL-AC10DS-A2 cantilevers, (Olympus, Japan) having a force constant k of 100 pN/nm, resonant frequency ω of 307.60 kHz and quality factor of 1.4 were used. The free and set point amplitudes were 3.8 nm and 2.8 nm.

The analysis of the high-resolution images was carried out using the WSxM 5.0 software[43].

5.2.3. Single molecule force spectroscopy measurements

Triangular silicon nitride cantilevers (OTR4, Bruker, Santa Barbara) functionalized with recombinant murine IL-4 (Deltaclon, Spain), a specific antigen for the anti-IL4 antibody following were used to probe the antibody-antigen interaction on graphene substrates. The tip functionalization procedure used here is described in Appendix A.1.4.

Force mapping experiments were performed at room temperature with a Nanowizard III microscope (JPK Instruments, Germany). Triangular silicon nitride cantilevers with a nominal spring constant of 0.02 N/m and resonant frequency of 2 kHz were used. The force constant and quality factor were determined as described in Chapter 3.2.3 by using the thermal noise method[44 45].

The maximum force was maintained below 250 pN to avoid any irreversible damage to the molecules bound to the tip apex. For each functionalized tip, several force maps covering 1 μm x 1 μm regions of the sample (32 x 32 data points) were acquired. In each force curve, the tip was approached and retracted 100 nm from the sample at a speed of 200 nm/s and it was kept in contact with the sample for 0.5 s to facilitate the formation of antibody-antigen complexes.

A total of 12000 force distance curves were recorded with several functionalized tips. The data analysis was carried out using the algorithm designed using *Spyder* - The Scientific *PYthon* Development EnviRonment described in Section 3.2.4.

For simultaneous topography and molecular recognition experiments, the Nanowizard III microscope was operated in closed-loop Quantitative Imaging (QI) mode. In QI mode, a force *versus* distance curve is acquired at each pixel of the image, while maintaining the x and y positions constant. The Antigen-functionalized tips were used to record *1* μm x 1 μm images of 400 x 400 points. Best high resolution AFM topography images and adhesion maps were obtained at imaging forces below 150 pN, tip velocity of 9.4 µm/s and 153 points per force *versus* distance curve.

5.2.4. Control experiments

The specificity of the unbinding events was assessed by performing three types of control experiments. In the first one, the AFM tips functionalized with IL4 antigen were used on a monolayer of unspecific antibodies (anti-IL6) deposited onto the graphene sample surface. Another control experiment involved the acquisition of force curves when using unfunctionalized AFM tips on a

monolayer of anti-IL4 antibodies deposited on graphene. The last control experiment involved the recording of force curves with IL4 antigen functionalized tips on a bare graphene substrate.

5.3. Results and discussion

5.3.1. Antibodies adsorption orientations on graphene

Four different molecular orientations for the antibodies adsorbed to the graphene substrate have been identified and named in previous studies[21, 27], as follows: *Flat-on* (all the three fragments adsorbed to the support), *End-on* (only the Fc adsorbed), *Sideway-on* (one Fab and the Fc adsorbed) and *Head-on* (both Fabs adsorbed).

In the molecular dynamics simulations, steered molecular dynamics was used to apply a gentle force on the IgG hydrophobic backbone (see Appendix B2, Figure B3). This speeds up the slowest step of the adsorption process, namely the protein diffusion from the solution into the interface region. The protein is brought closer to the substrate, intensifying the dehydration while keeping the internal structure intact. The protocol applied for the simulation of each orientation is the following: Firstly, the IgG (Protein Data Bank ID: 1IGT) is positioned in one of the four orientations at a distance of 10 Å from a 20 × 20 nm^2 three-layer graphene slab with A-B-A stacking, and the system is solvated with TIP3P water molecules (150000-250000 depending on the orientation). Then, the system is heated at 300 K, the IgG freely adsorbs during 10 ns, the enhanced adsorption is applied for 2 ns, and finally, the system is left to equilibrate for another 140 ns.

In our experimental approach, a 60 μl drop of a 0.5 μg/ml IgG antibodies solution is deposited on the graphene substrate for 20 s. The sample is then rinsed with ultrapure water and imaged either in air or water medium.

The first two columns of Figure 5.2 present the top and side view of the final adsorption configuration for each of the four characteristic orientations of the

antibodies after 152 ns of MD simulation. By using the adsorption protocol described before, 150 ns MD simulations are long enough to capture all of the relevant protein rearrangements involved in the adsorption process, and to reach the final stable equilibrium configuration for each IgG orientation. MD simulations show that in graphene, vertical orientations like *End-on* and *Sideway-on*, exposing the active Fab domains, seem to be stable adsorption configurations, at variance with previous findings on hydrophilic surfaces[22, 27].

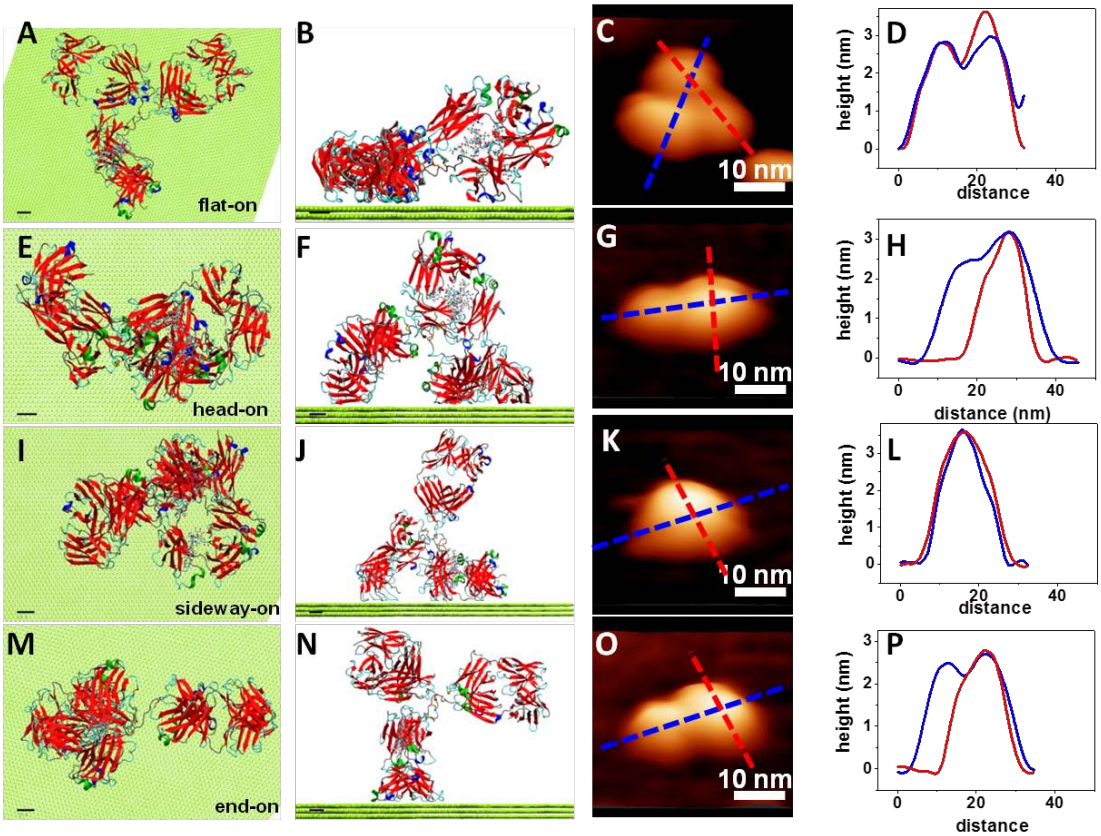

Figure 5.2. Stable adsorption configurations of IgG on graphene in water. From left to right, the first two columns correspond to the structures for the four different orientations after 152 ns of MD simulations, while the other two display AM-AFM images that reveal these characteristic adsorption configurations. Panels A,E,I and M (B,F,J,N) show the corresponding top (side) views. Scale bars in MD images are 1 nm. Panels C,G,K and O show the topogaphic AFM images of the four orientations adopted by the IgG antibodies adsorbed on graphene. Panels D,H,L and P display the corresponding cross-sections along the lines marked in the images. The assignment of each AFM image to a given orientation is further supported by the good agreement between inter-domain distances measured from MD final structures and AFM images (see Figure 5.4 and Table 5.1).

Additionally, in contrast with the strong (complete) denaturation previously found for protein fragments[32, 40, 46], small proteins like BMP-2[36] and larger proteins treated with implicit solvent methods[37, 38] the structure of the IgG is preserved during the adsorption process. Furthermore, in all of the orientations, the adsorbed residues have an even distribution of hydrophobic/hydrophilic residues. We do not observe any movement of residues belonging to the hydrophobic core/regions of the protein towards the surface as observed on smaller protein fragments[34].

High-resolution AM-AFM images of individual anti-IL4 antibodies deposited on graphene in water medium are shown in the third column of Figure 5.2 (panels C, G, K, O). The corresponding cross-sections along the lines marked on the images are displayed in panels D, H, L and P of the same figure.

A qualitative comparison of the AFM and MD results shows a good agreement between experiments and simulations. The images reveal the four characteristic orientations of IgG on graphene described by the MD simulations. The lateral and vertical resolutions of the images allow us to make a direct connection between protein configurations in theory and experiment. Moreover, the time scales of AFM (100 ms) and MD (100 ns) experiments are separated by six orders of magnitude, which further proves the long-term stability of the structures found in the MD simulations.

In particular, the *Head-on* and *End-on* orientations may look similar in the topography image, but their cross-sections show different features. The *Head-on* orientation shows two protrusions of different heights, a lower one that corresponds to an adsorbed Fab fragment and a higher one corresponding to a Fab lying over the Fc fragment (blue line in Figure 5.2H). On the other hand, for the *End-on* orientation two protrusions of roughly similar height are visible, as confirmed by the blue line in the cross-section profile in panel P. We have assigned these two protrusions to the Fab fragments exposed to the environment. The 8 nm separation between the two fragments was confirmed by the molecular dynamics simulations (see Table 5.1).

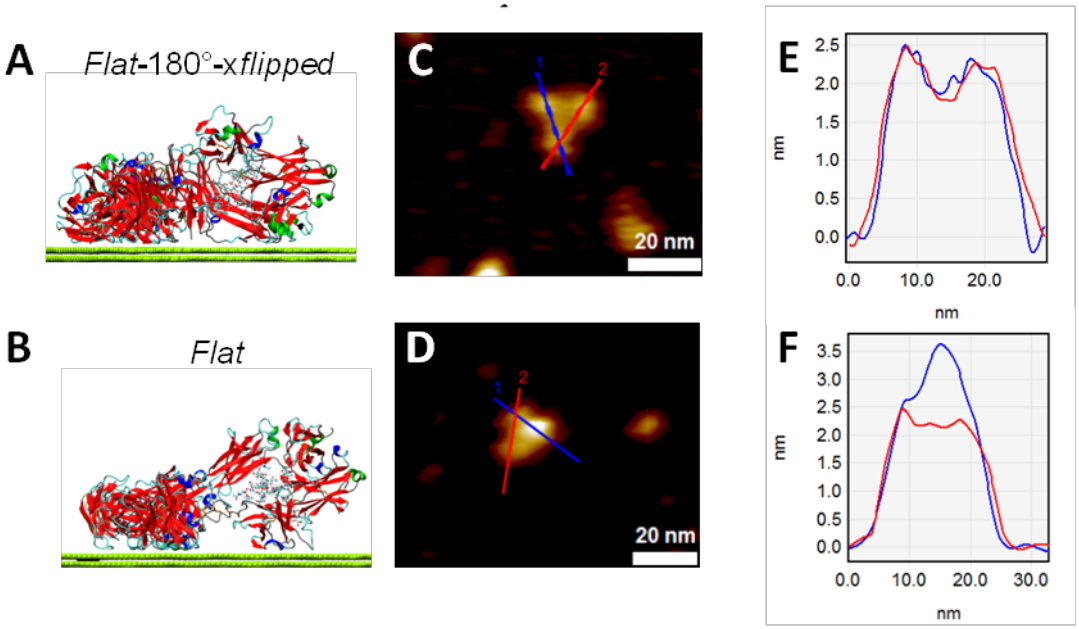

Figure 5.3. Comparison of the final adsorption configuration of the *Flat* and *Flat*-180°x-fliped orientations. A,B: Side view of the IgG adsorbed after a 150 ns MD simulation. C,D: AFM topographic images of the antibodies in the *Flat*-180°x-fliped and *Flat* orientations; E,F: Height profiles along the red and blue lines represented in the corresponding topography image.

Particularly, for the *Head-on* orientation, the adsorbed left-hand-side Fab was resolved. AFM experiments are able to discriminate between two configurations where the antibody lies flat on the surface. The *Flat*-180°-x*flipped* orientation (Figure 5.3) is a specular reflection of the *Flat* configuration displayed in Figure 5.2. In spite of the apparent equivalence between the two structures, MD simulations show differences in their final adsorption structures. The Fc fragment is less strongly adsorbed in the *Flat* configuration. This fact, together with the torsional restrain imposed by the different adsorption of the Fab fragments, lifts the Fc domain upwards. The height profiles in Figure 5.3 confirm these differences in the adsorption configuration.

The inter-domain distances have been measured and compared in the AFM and MD simulations images and the results are presented in Figure 5.4 and Table 5.1. The points of maximum height were chosen to calculate the inter-domain distances in both the AFM and MD simulations images. Only orientations where the AFM height profile showed two peaks were included in this analysis. This quantitative analysis shows that the measured inter-domain

distances, extracted from AFM topography cross-sections (right panels in Figure 5.4) are in agreement with the MD simulations results. Due tip-antibody convolution effects, the overall size of the antibody is larger than the nominal value. However, this distortion does not affect the inter-domain distances. These distances are also in agreement with previous findings of the IgG antibody structure[47].

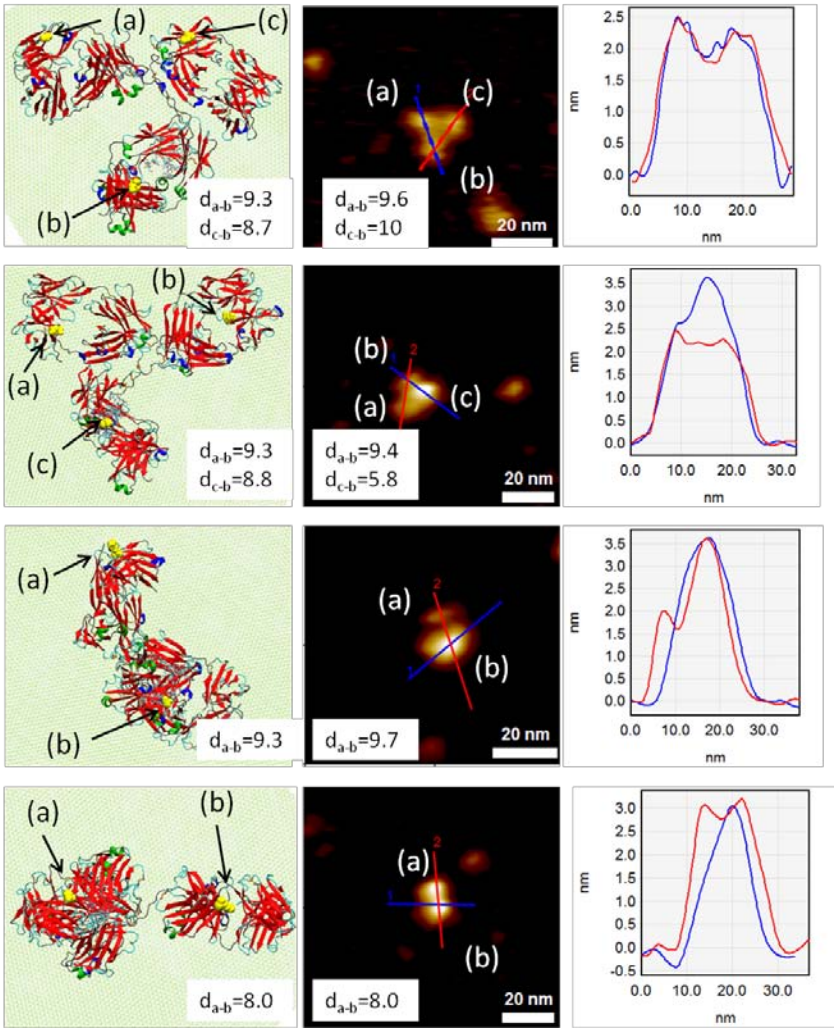

Figure 5.4. Comparison of the inter-domain distances as measured by MD simulations (left panel) and AFM (middle panel) and corresponding cross-sections (right panel). Only orientations whose AFM height profile had two peaks have been compared. The points (a,b and c) selected on the MD simulations images correspond to maximum height sites in the experimental data.

Table 5.1. *Comparison of the inter-domain distances (in nm) as measured by AFM and by MD simulations.*

	AFM		MD	
Orientation	**Fab1-Fab2 (nm)**	**Fab-Fc (nm)**	**Fab1-Fab2 (nm)**	**Fab-Fc (nm)**
Flat	9.4	5.8	9.3	8.8
Flat-180x-flipped	9.6	10.0	9.3	8.7
Sideway	-	9.7	-	9.3
End	8.0	-	8.0	-

The height analysis of the antibodies adsorbed on graphene reveals some differences between experiments and theory. The experimental values are in the 3 to 3.5 nm range (right panels in Figures 5.2 and 5.4). For the *Flat* orientation, the maximum height value is also lower than the nominal height of the molecule ($\lesssim$ 6 nm). This is a common discrepancy observed in AFM experiments in both air and liquid medium. The mismatch is due to the elastic deformation of the antibodies produced by the force applied by the AFM probe during imaging. Numerical simulations[48] indicate that, for the operational values used here to image the proteins, the peak force is in the 400 pN range which implies deformations of about 2 nm for a system with an effective Young modulus of 30 MPa. The deformation is enhanced for vertical orientations since they are softer along the direction perpendicular to the plane, due to the smaller effective z-atomic-density along these orientations.

5.3.2. Statistical distribution of adsorption orientations of antibodies on graphene

To gain insight into the statistical distribution of adsorption orientations of the IgG antibody over graphene, a further analysis of the AFM images obtained in

water and air environment was performed. The antibodies orientations have been classified in three large groups: flat, vertical and non-resolved. The flat group includes images that show the characteristic Y-shape of *Flat-on* orientation. They are easily recognizable by the presence of three lobes in the AFM image. The vertical group comprises antibodies in *Head-on*, *Sideway-on* and *End-on* orientations, which are characterized by the presence of one or two lobes plus a protrusion. The non-resolved group comprises biomolecules that show a geometry that did not match any of the orientations given by the MD simulations. This happens when two antibodies are very close to each other or when the subunits were not properly resolved by the AFM.

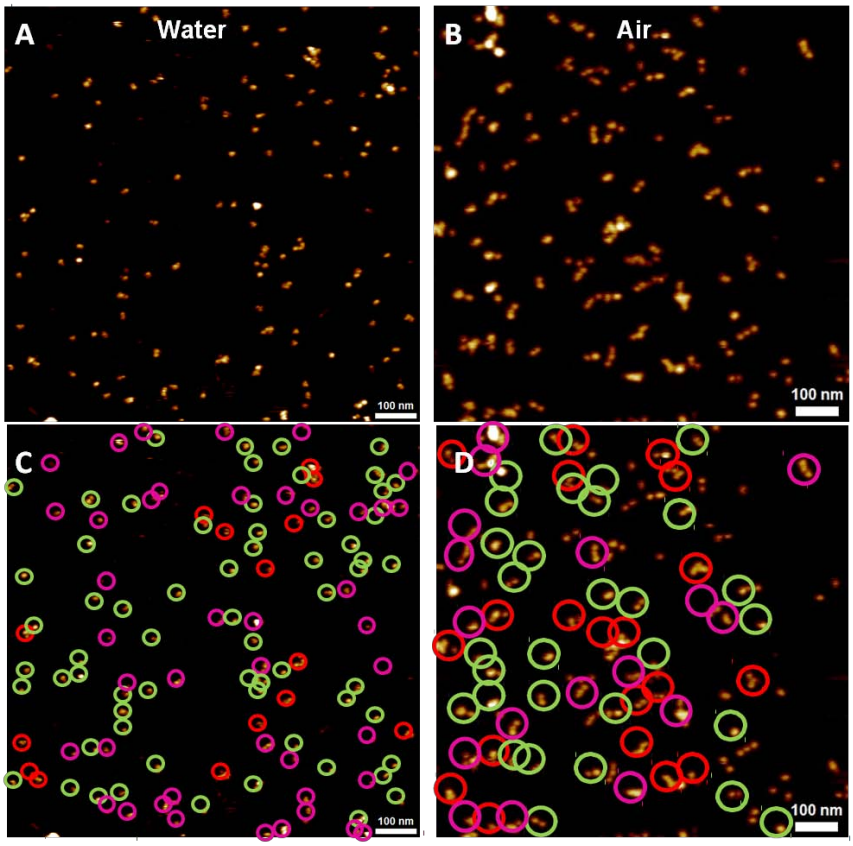

Figure 5.5. A,B: AFM topographic images of the IgG adsorbed over graphene in water and in air, respectively. C,D: A manual identification of each of the orientations found in the image on top. The unresolved is represented with a magenta circle, the vertical orientations are represented with a green circle and the *Flat* orientation is represented with a red circle.

Several 500×500 nm^2 and 1 μm x 1 μm images of antibodies on graphene were analyzed and categorized according to the aforementioned orientations. Figures 5.5 and 5.6 are illustrative examples of the images used to quantify the adsorption orientations distribution.

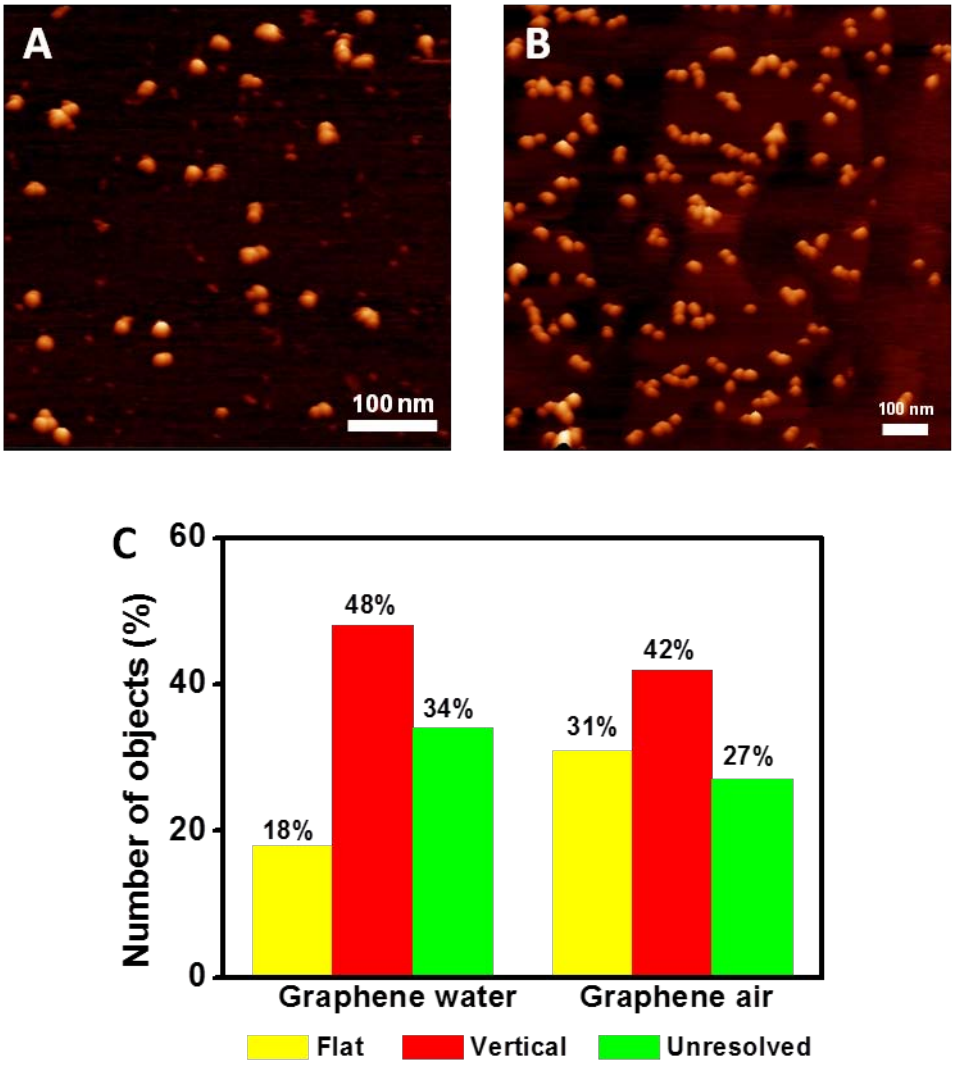

Figure 5.6. A: AM-AFM topographic image of the IgG adsorbed on graphene (water). B: AM-AFM topographic image of the IgG adsorbed on graphene (air). C: Histogram of antibodies adsorbed along a Flat orientation (i.e. Flat-on and Flat-180°-xflipped), a vertical orientation (i.e. Head, Sideway, and End) and unresolved orientations. The total number of counts in water is 145 and in air is 385.

Our findings are depicted in Figure 5.6C. The histogram shows that IgG antibodies adsorb mostly on vertical orientations (i.e. *Head-on*, *Sideway-on*, *End-on*). This is in contrast with the results obtained on the hydrophilic surfaces like mica (see Figure 1.6 of this thesis), silica and quartz studied so far[21, 22, 27]. Although the relevant findings on the adsorption orientations are the ones in liquid medium, experiments performed in air were also included in our analysis (Figure 5.6B) to see whether or not the dehydration process could introduce some changes in the dominant orientations. Although there are differences in the relative percentages of the *Flat-on* and unresolved orientations, our results in air clearly show that just as in water medium, the vertical orientation is the dominant one.

SMD simulations were performed for the IgG desorption process in order to understand the origin of the statistical distribution obtained in the AFM experiments. According to the Jarzynski equality the free energy difference between two equilibrium states can be obtained by an exponential average of the work needed to take the system from one state to the other (i.e. from adsorbed to desorbed IgG) via any desired non-equilibrium process[49]. The average has to be done over multiple initial configurations/coordinates sampled from the initial equilibrium state. This method, previously used to measure the adsorption energy of a peptide onto different hydrophobic surfaces[33], provides results in excellent agreement with those obtained from single-molecule force spectroscopy studies. SMD was performed by applying a constant force to the same 30 carbon atoms used for the enhanced adsorption step (see Appendix B2 and Figure B3).

The adsorption free energies obtained for the orientations *Flat, Head, Sideway* and *End* are 685, 503, 359 and 325 kcal/mol, respectively. A linear dependence with a ratio of 0.28±0.016 kcal/molÅ^2 was found for the energies *versus* contact areas for all orientations. This is in good agreement with previous studies of complexes interacting mostly through London dispersion forces[50]. Therefore, it reinforces the argument that the forces governing the adsorption of large proteins like the IgG arise mostly from van der Waals (vdW) interactions, while hydrophobic forces seem to play a very minor role.

These large adsorption energies provide the clue for the observation of the different adsorption orientations. All of them have adsorption energies that are much higher than the total IgG unfolding energy barrier of $\sim 165 - 265$ kcal/mol[51]. If enough thermal energy were available, it would be energetically less costly for the IgG to unfold than to desorb. As both theory and experiments undoubtedly show that the IgG retains its secondary structure when adsorbed over graphene, it follows that this is not the case. In order to change its adsorption orientation, the IgG must first desorb (partially or totally) from the surface. Given that the thermal energy available is smaller than the high energy barriers required for this process to occur, once the IgG gets adsorbed along a given orientation, it will not naturally desorb nor change its orientation. As discussed above, the similarity between air and water AFM measurements, shows that entropic thermal fluctuations, enhanced in the water measurements, are not large enough to affect the final adsorption state and change this scenario. The picture that emerges for the adsorption process is the following: Initially, the IgG is freely drifting in the solvent until it reaches the surface along any of the 6 possible molecular orientations (*Flat, Head, Sideway, End*, and the two other equivalent orientations, i.e. *Flat*-180°x-fliped and *Sideway*-180°x-fliped). Then, already in close contact with the surface, it starts to adsorb along its particular landing orientation. Once the adsorption process starts, given its speed and the high adsorption energies, the antibody gets anchored to the surface along the landing orientation. As a result, the final adsorption orientation is determined by the essentially random landing orientation, i.e. each of the six orientations have an equal probability of being found over the graphene surface. The statistics obtained from AFM the experiments support this description. If the unresolved orientations are not taken into account, we observe 27% of the antibodies adsorb on a *Flat* orientation in water (i.e., *Flat* and *Flat*-180°x-fliped), which is in good agreement with the probability of (2/6) × 100 = 33.3% predicted for randomly landing on this orientation.

5.3.3. Immunological response of antibodies adsorbed on graphene

The immunological activity of the deposited antibodies has been assessed by SFS. The experiments involve the measurement of the rupture forces existing between an antigen (IL4 cytokine) attached to the AFM tip and IgG antibodies (anti-IL4)[52] immobilized on the graphene substrate (Figure 5.7). As previously discussed in Chapter 4, anti-IL4 is an IgG-type antibody and it has a high affinity for the IL4 cytokine.

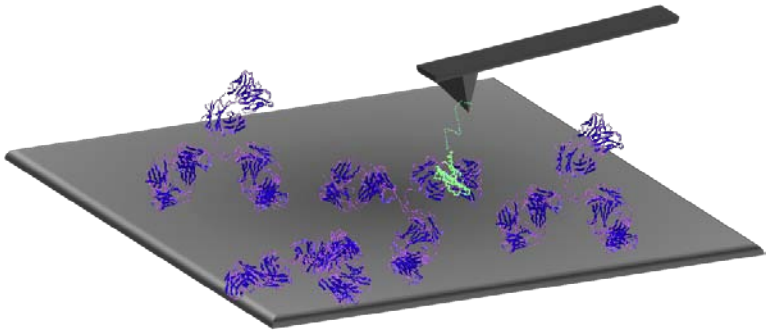

Figure 5.6. Schematics of IL4 cytokine (antigen) attached to the AFM tip (light green) and the anti-IL4 antibodies immobilized on the graphene substrate.

A rigorous validation of the immunological response by SFS requires a statistical analysis of thousands of force curves. The binding forces between the tip-bound antigen and the antibodies adsorbed on graphene were extracted from series of repeated force curves acquired on a 32 x 32 points grid on 1 μm x 1 μm areas of the sample.

Figure 5.8A shows the 1D histogram of the unbinding forces of specific antibody-antigen interactions at a loading rate of 2.5 nN/s. A total 879 unbinding events are included in this plot and they represent 14% of the total number of recorded force curves. Unspecific or noisy events occurring at $F_{unb} \leq 20$ pN have been filtered out from this analysis. In this representation, the most frequent unbinding event is observed at $F_{unb} \approx 89 \pm 30$ pN.(as obtained with a

Gauss fit). Similar results were previously obtained with the same antibody-antigen pair immobilized on a gold substrate (see Chapter 4.3.4).

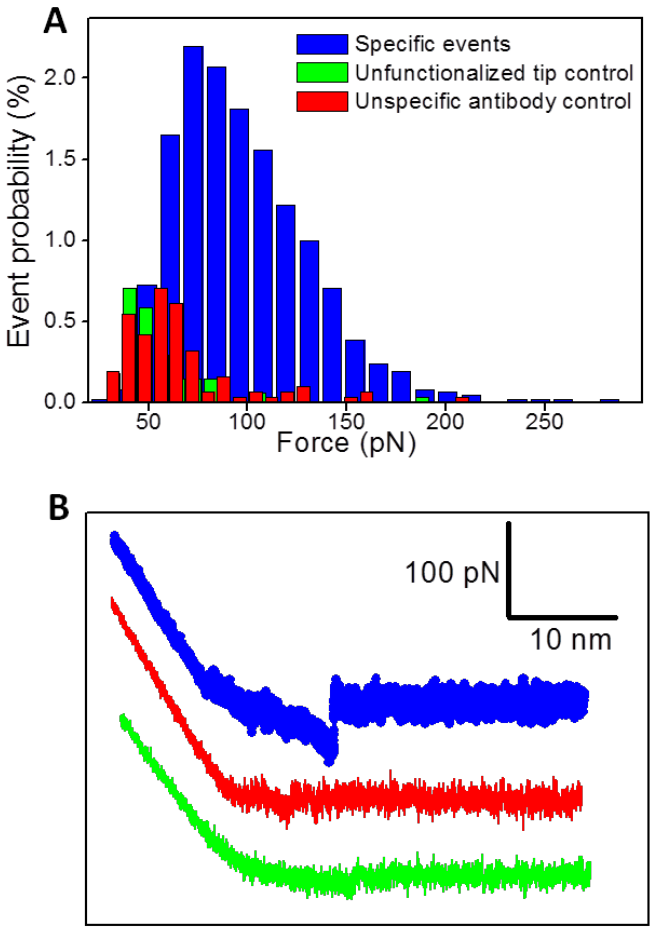

Figure 5.8. A: Histogram of rupture forces the immunological detection and two control experiments on graphene. B: Typical force *vs* distance curves , as follows: blue for specific antibody-antigen recognition events, red for interaction between IL4 antigen and anti-IL6 antibody, green for interaction between an unfunctionalized AFM tip and the graphene substrate.

To investigate if the detected unbinding events were indeed specific, we have performed three different sets of control experiments. In the first control experiment we measured the interaction between the IL4 antigen on the tip and a non-specific antibody (anti-IL6) on the graphene substrate. In other control experiments, we recorded force curves in the absence of an antigen on the AFM tip (unfunctionalized tip) or of an antibody on the graphene surface (bare graphene). No adhesion events were recorded when the antigen-functionalized

AFM tip was brought into contact with a bare graphene surface. As shown in figure 5.8A, the interaction forces corresponding to the unspecific antibody and unfunctionalized tip control are centered at 50 pN and 30 pN, respectively, as compared with 89 pN for the specific events. Moreover, their corresponding event probabilities are 3.4% for the unspecific antibody control and 2.3% for the unfunctionalized tip control, which is significantly lower than the 14% probability found for the specific events.

Figure 5.8B shows typical force *vs.* distance curves obtained while performing control experiments. Force curves corresponding to specific antibody-antigen recognition events are also displayed for comparison. The red curve is typical for the interaction between the IL4 antigen and anti-IL6 antibody, while the green curve corresponds to the interaction between an unfunctionalized AFM tip and the graphene substrate. We can then conclude that we have indeed quantified specific antibody-antigen unbinding events.

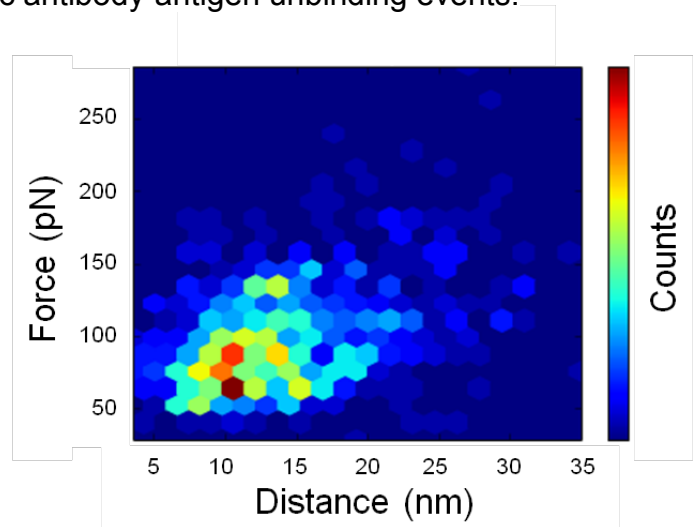

Figure 5.9. Two-dimensional molecular recognition map of the IL-4 and anti-IL-4 interaction on graphene. The map plots the rupture forces with the corresponding unbinding distances. The most frequent molecular recognition events were observed at unbinding distances of 10-15 nm and unbinding forces of 60-90 pN.

In Figure 5.9, a two dimensional molecular recognition map[52, 54] obtained on graphene is depicted. The map shows that the most probable rupture force between IL4 and anti-IL4 is observed at 75 pN, while multiple unbinding events could be occurring at 130 pN. The characteristic unbinding length for specific biorecognition events is of 11 nm. This is in good correlation with the expected

stretching of the 10 nm long PEG linker before the tip jumps off to surface[55, 56]. These findings support the idea that antibodies deposited on graphene retain their biological activity.

5.3.4. Simultaneous topography and molecular recognition on graphene

Once we were able to prove that specific antibody-antigen interactions could be detected on the graphene substrate, we went a step further and in a second approach we combined high resolution imaging with quantitative mapping of specific localized interactions between antibody-antigen pairs[57, 58]. The atomic force microscope was used to record force-distance curves over a heterogeneous sample of individual antibodies immobilized on the graphene substrate. Force-distance curves were recorded in every pixel over 1 μm x 1 μm areas divided in 400 x 400 pixels at a tip velocity of 9 µm/s. The topography image was then correlated with the adhesion map containing specific antibody-antigen interactions and unspecific graphene-antigen interactions. Figure 5.10A shows the topography image of IgG antibodies distributed on graphene, while in figure 5.10B the corresponding force curves obtained on the four antibodies marked in 5.10A are depicted. To illustrate the specific character of the interactions between the antibody and its specific antigen, two force curves obtained on two locations where the AFM image does not show any antibody are also plotted.

The unbinding forces found in these experiments range between 120-150 pN at a loading rate of 110 nN/s. This is in good correlation with previous data obtained while performing antibody-antigen unbinding experiments at similar loading rates[55].

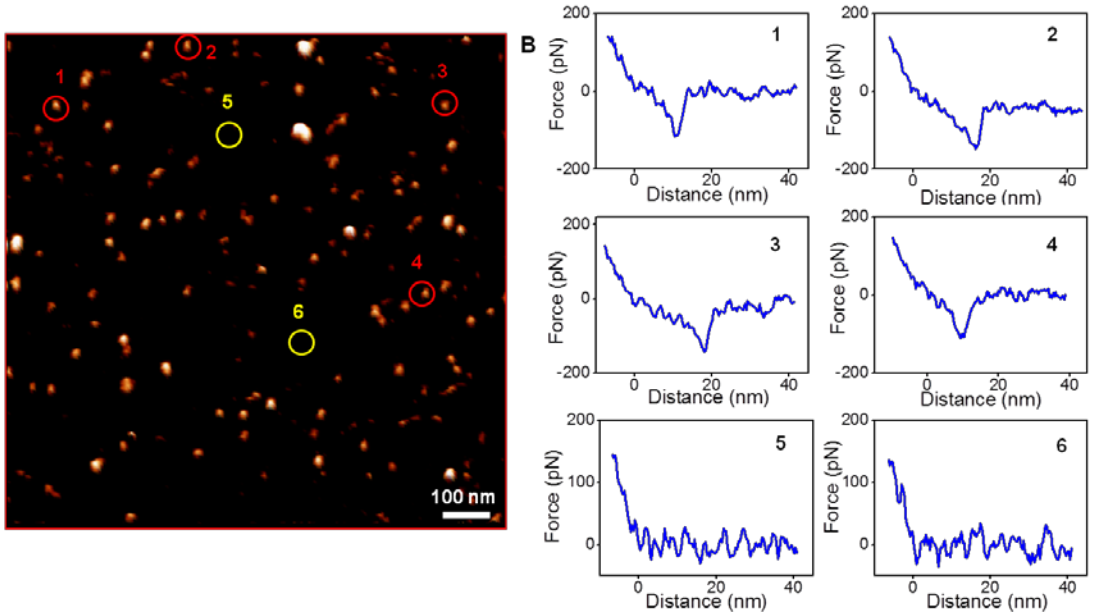

Figure 5.10. Single molecule force spectroscopy on graphene. A: Topography and adhesion force AFM image of anti-IL4 antibodies on graphene. A force *versus* distance curve is acquired at each pixel of the image, while maintaining the *x* and *y* positions constant. The circles indicate the positions of the force curves illustrated in B. B: Force *versus* distance curves measured in the positions marked in A. Curves 1-4 correspond to positions where antibodies are located in the AFM image while 5-6 correspond to locations with no antibodies. The topography image and the force curves were obtained by applying forces below 150 pN.

5.4. Conclusions

In summary, high-resolution AFM imaging and single-molecule force spectroscopy, combined with MD simulations, reveal the adsorption conformations and immunological activity of antibodies on graphene, taken as a hydrophobic surface model.

The experimental and theoretical results presented in this chapter conclusively demonstrate that the IgG antibodies are strongly adsorbed on graphene, do not unfold upon adsorption, and retain their secondary structure. Most of the antibodies adsorb, even at small IgG-surface coverage densities, in vertical orientations that expose both Fab-binding sites for the specific binding to

antigens. This is a particularly relevant result since on all passive adsorption surfaces studied so far, IgG adsorb preferentially in Flat orientations, where the Fab domains are not easily accessible and therefore the antibody may lose some of its bioactivity once it is adsorbed. Force spectroscopy measurements demonstrate the immunological response of the deposited antibodies by selectively interaction with their specific antigens. This confirms that the antibodies deposited on graphene retain their immunological activity.

All of these features, preservation of the secondary structure, strong protein anchoring, vertical adsorption orientations, and immunological recognition are key properties to develop very sensitive graphene-based immunological biosensors.

5.5. References

1. K. S. Novoselov, A. K. Geim, S. V. Morozov, D. Jiang, Y. Zhang, S. V. Dubonos, I. V. Grigorieva and A. A. Firsov, *Science*, 2004, **306**, 666-669.
2. A. K. Geim and K. S. Novoselov, *Nat Mater*, 2007, **6**, 183-191.
3. C. N. R. Rao, A. K. Sood, K. S. Subrahmanyam and A. Govindaraj, *Angewandte Chemie International Edition*, 2009, **48**, 7752-7777.
4. S. Park and R. S. Ruoff, *Nat Nano*, 2009, **4**, 217-224.
5. A. A. Balandin, S. Ghosh, W. Bao, I. Calizo, D. Teweldebrhan, F. Miao and C. N. Lau, *Nano Lett.*, 2008, **8**, 902-907.
6. R. F. Service, *Science*, 2009, **324**, 875-877.
7. C. Lee, X. Wei, J. W. Kysar and J. Hone, *Science*, 2008, **321**, 385-388.
8. F. Xia, T. Mueller, R. Golizadeh-Mojarad, M. Freitag, Y.-m. Lin, J. Tsang, V. Perebeinos and P. Avouris, *Nano Lett.*, 2009, **9**, 1039-1044.
9. B. Arash, Q. Wang and W. H. Duan, *Physics Letters A*, 2011, **375**, 2411-2415.
10. Y. Wang, R. Yang, Z. Shi, L. Zhang, D. Shi, E. Wang and G. Zhang, *ACS Nano*, 2011, **5**, 3645-3650.
11. S. Pisana, P. M. Braganca, E. E. Marinero and B. A. Gurney, *Magnetics, IEEE Transactions on*, 2010, **46**, 1910-1913.
12. Y. Liu, X. Dong and P. Chen, *Chemical Society reviews*, 2012, **41**, 2283-2307.
13. Y. Zhang, T. R. Nayak, H. Hong and W. Cai, *Nanoscale*, 2012, **4**, 3833-3842.
14. N. Willem, A. H. Thomas and L. B. John, in *Proteins at Interfaces III State of the Art*, American Chemical Society, 2012, vol. 1120, ch. 1, pp. 1-34.
15. W. R. Sanhai, J. H. Sakamoto, R. Canady and M. Ferrari, *Nat Nano*, 2008, **3**, 242-244.
16. A. E. Nel, L. Madler, D. Velegol, T. Xia, E. M. V. Hoek, P. Somasundaran, F. Klaessig, V. Castranova and M. Thompson, *Nat Mater*, 2009, **8**, 543-557.
17. J. Tate and G. Ward, *Clin Biochem Rev*, 2004, **25**, 105-120.
18. W. J. Payne, D. L. Marshall, R. K. Shockley and W. J. Martin, *Clinical Microbiology Reviews*, 1988, **1**, 313-329.
19. J. Tamayo, P. M. Kosaka, J. J. Ruz, A. San Paulo and M. Calleja, *Chemical Society reviews*, 2013, **42**, 1287-1311.
20. G. B. Pier, J. B. Lyczak and L. M. Wetzler, *Immunology, infection, and immunity*, ASM Press, Washington, D.C. , 2004.
21. Z. Xiubo, Y. Mohammed, P. Fang and R. L. Jian, in *Proteins at Interfaces III State of the Art*, American Chemical Society, 2012, vol. 1120, ch. 25, pp. 543-574.
22. N. Tajima, M. Takai and K. Ishihara, *Analytical Chemistry*, 2011, **83**, 1969-1976.
23. H. Xu, J. R. Lu and D. E. Williams, *The Journal of Physical Chemistry B*, 2006, **110**, 1907-1914.
24. J. Preiner, N. S. Losilla, A. Ebner, P. Annibale, F. Biscarini, R. Garcia and P. Hinterdorfer, *Nano Lett.*, 2009, **9**, 571-575.
25. S. Ido, H. Kimiya, K. Kobayashi, H. Kominami, K. Matsushige and H. Yamada, *Nat Mater*, 2014, **13**, 264-270.
26. M. Xu, T. Liang, M. Shi and H. Chen, *Chemical Reviews*, 2013, **113**, 3766-3798.
27. D.-G. Christine, in *Proteins at Interfaces III State of the Art*, American Chemical Society, 2012, vol. 1120, ch. 21, pp. 453-469.
28. T. Alava, J. A. Mann, C. Théodore, J. J. Benitez, W. R. Dichtel, J. M. Parpia and H. G. Craighead, *Analytical Chemistry*, 2013, **85**, 2754-2759.
29. A. San Paulo and R. García, *Physical Review B*, 1999, **60**, 4961-4967.

30. D. Martinez-Martin, E. T. Herruzo, C. Dietz, J. Gomez-Herrero and R. Garcia, *Physical Review Letters*, 2011, **106**, 198101.
31. F. Kienberger, H. Mueller, V. Pastushenko and P. Hinterdorfer, *EMBO reports*, 2004, **5**, 579-583.
32. J. Katoch, S. N. Kim, Z. Kuang, B. L. Farmer, R. R. Naik, S. A. Tatulian and M. Ishigami, *Nano Lett.*, 2012, **12**, 2342-2346.
33. D. Horinek, A. Serr, M. Geisler, T. Pirzer, U. Slotta, S. Q. Lud, J. A. Garrido, T. Scheibel, T. Hugel and R. R. Netz, *Proceedings of the National Academy of Sciences*, 2008, **105**, 2842-2847.
34. T. Wei, M. A. Carignano and I. Szleifer, *Langmuir*, 2011, **27**, 12074-12081.
35. L. Ou, Y. Luo and G. Wei, *The journal of physical chemistry. B*, 2011, **115**, 9813-9822.
36. C. Mücksch and H. M. Urbassek, *PLoS One*, 2013, **8**, e64883.
37. C. Mücksch and H. M. Urbassek, *Langmuir*, 2011, **27**, 12938-12943.
38. G. Raffaini and F. Ganazzoli, *Langmuir*, 2010, **26**, 5679-5689.
39. Y. Sun, B. N. Dominy and R. A. Latour, *Journal of Computational Chemistry*, 2007, **28**, 1883-1892.
40. T. Wei, M. A. Carignano and I. Szleifer, *The Journal of Physical Chemistry B*, 2012, **116**, 10189-10194.
41. R. Mas-Balleste, C. Gomez-Navarro, J. Gomez-Herrero and F. Zamora, *Nanoscale*, 2011, **3**, 20-30.
42. E. T. Herruzo and R. Garcia, *Applied Physics Letters*, 2007, **91**, 3.
43. I. Horcas, R. Fernández, J. M. Gómez-Rodríguez, J. Colchero, J. Gómez-Herrero and A. M. Baro, *Review of Scientific Instruments*, 2007, **78**, 013705.
44. J. Hutter and J. Bechhoefer, *Review of Scientific Instruments*, 1993, **64**, 1868–1873.
45. H. J. Butt and M. Jaschke, *Nanotechnology*, 1995, **6**, 1.
46. C.-c. Chiu, G. R. Dieckmann and S. O. Nielsen, *The Journal of Physical Chemistry B*, 2008, **112**, 16326-16333.
47. L. J. Harris, S. B. Larson, K. W. Hasel and A. McPherson, *Biochemistry*, 1997, **36**, 1581-1597.
48. H. V. Guzman, P. D. Garcia and R. Garcia, *Beilstein Journal of Nanotechnology*, 2015, **6**, 369-379.
49. C. Jarzynski, *Physical Review Letters*, 1997, **78**, 2690-2693.
50. P. Jurecka, J. Sponer, J. Cerny and P. Hobza, *Physical Chemistry Chemical Physics*, 2006, **8**, 1985-1993.
51. A. W. P. Vermeer, W. Norde and A. van Amerongen, *Biophysical journal*, **79**, 2150-2154.
52. S. Casalini, A. C. Dumitru, F. Leonardi, C. A. Bortolotti, E. T. Herruzo, A. Campana, R. F. de Oliveira, T. Cramer, R. Garcia and F. Biscarini, *ACS Nano*, 2015, **9**, 5051-5062.
53. E. Evans and P. M. Williams, eds., *Physics of Bio-Molecules and Cells*, Springer and EDP Sciences, Heidelberg, 2002.
54. A. C. Dumitru, E. T. Herruzo, E. Rausell, V. Cena and R. Garcia, *Nanoscale*, 2015, **7**, 20267-20276.
55. A. R. Bizzarri and S. Cannistraro, *Nanotechnology*, 2014, **25**, 335102.
56. A. S. M. Kamruzzahan, A. Ebner, L. Wildling, F. Kienberger, C. K. Riener, C. D. Hahn, P. D. Pollheimer, P. Winklehner, M. Hölzl, B. Lackner, D. M. Schörkl, P. Hinterdorfer and H. J. Gruber, *Bioconjugate Chemistry*, 2006, **17**, 1473-1481.
57. M. Pfreundschuh, D. Alsteens, M. Hilbert, M. O. Steinmetz and D. J. Müller, *Nano Lett.*, 2014, **14**, 2957-2964.
58. D. Alsteens, M. Pfreundschuh, C. Zhang, P. M. Spoerri, S. R. Coughlin, B. K. Kobilka and D. J. Muller, *Nat Meth*, 2015, **12**, 845-851.

Chapter 6

In-situ nanomechanical characterization of the early stages of swelling and degradation of a biodegradable polymer

6.1. Introduction

Poly(lactic-*co*-glycolic) acid (PLGA) is a biocompatible and biodegradable [1-4] polymer which has been widely used for biomedical applications such as drug release particles and films, sutures, artificial skin grafts, substrate for cell proliferation and implants [5-9].

One of the key features of this polymer is the fact that it undergoes hydrolytic degradation[10, 11] of the ester backbone in aqueous medium and the resulting products (lactic and glycolic acid) are metabolized and eliminated (Figure 6.1). Once the polymer is introduced into the aqueous medium, hydrolysis of the ester linkages generates acids. The acids then act as catalysts in the hydrolysis of more ester bonds, in an autocatalytic process.

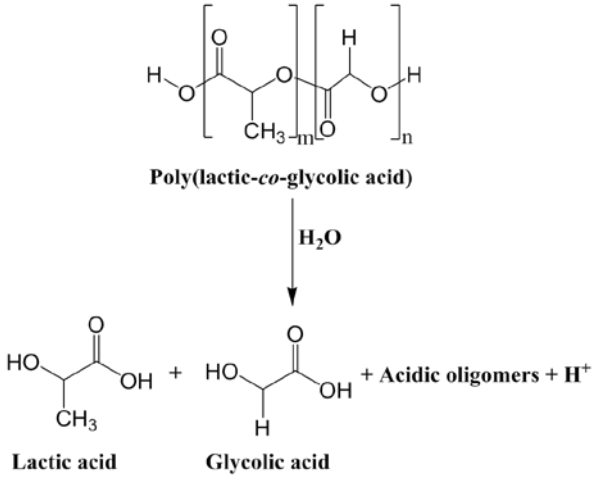

Figure 6.1. Chemical structure of Poly(lactic-co-glycolic acid) and the products of its hydrolytic degradation. In a PLGA copolymer *m* and *n* refer to the amounts of lactide and glycolide monomer units.

The applications of PLGA depend strongly on the dynamics of scaffold degradation. Efforts have been made to understand and control the mechanism of PLGA degradation in relation with the structure and morphology, chemical architecture, processing method of the material and also the medium in which the polymer is placed[12-14].

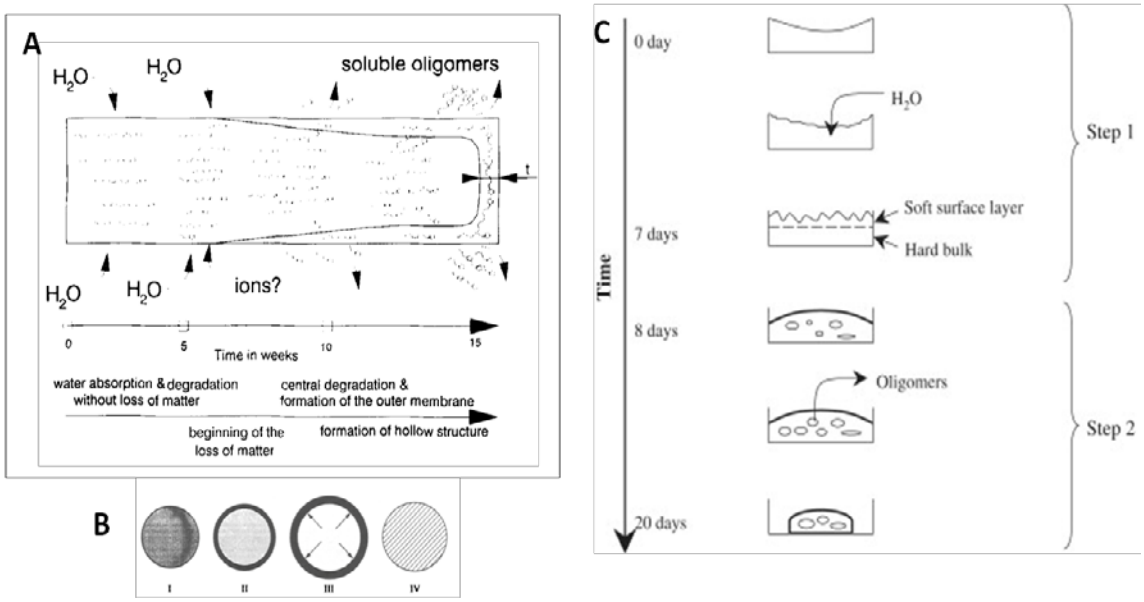

Figure 6.2. Proposed degradation mechanisms of PLGA. A: Size-dependent heterogeneous degradation model proposed in Ref. 11; B: Heterogeneous degradation of PLGA microspheres with a fast degrading core (adapted from Ref. 13); C: Two-step degradation of PLGA films observed in Ref. 15.

Since the behavior of the polymer in a degradation medium depends on various characteristics of the material, one could define the degradation of PLGA copolymers as a collective process, which involves bulk and surface erosion as well as bulk and surface diffusion. The extent of these processes and their prevalence strongly depend on lactic-glycolic acid content, size of the device, degradation medium, temperature, porosity, and molecular weight. For instance, Vert et al.[11] have found that large PLGA based devices have a higher degradation rate in the core than on the surface and proposed a heterogeneous degradation model (Figure 6.2A). Park and al. [13] have studied microspheres and found a faster degrading core as compared to the surface layer, as

depicted in Figure 6.2B, while a more recent study by Vey and al. [15] proposes a two step degradation mechanism for PLGA films (Figure 6.2C).

However, the dynamics of PLGA degradation and the factors which influence it are not fully understood, consequently, it is hard to predict the degradation process in vitro and in vivo.

Understanding the correlation between nanoscale and macroscale materials properties is a key issue to improve the performance of material and devices[16-18]. Several techniques previously employed to study the changes that biodegradable scaffolds undergo upon degradation cannot be used *in situ* or in a liquid environment[15, 19, 20]. Moreover, most of the methods are designed for the evaluation of bulk properties and polymer samples.

Atomic force microscopy and spectroscopy methods provide high-resolution approaches to characterize the topography and mechanical response of soft-matter interfaces in air and buffer[21-25].

In this chapter, a high-resolution nanomechanical characterization of the early stages of swelling and degradation of a PLGA 75:25 copolymer in phosphate buffer saline (PBS) is presented. Force microscopy and spectroscopy methods have been used to follow the *in-situ* evolution of nanoscale PLGA patterns fabricated by focused ion beam lithography.

6.2. Experimental methods

6.2.1. PLGA patterned surfaces

Silicon substrates have been cleaned with 2-propanol, acetone and distilled water by ultrasonic treatment for 5 minutes each. The substrates were then immersed in a H_2O_2:NH_4OH:H_2O (1:1:2) mixture and four ultrasound cycles of 10 minutes have been performed. After the cleaning procedure, substrates were immersed in a solution containing 11 μl

APTES and 50 mL ethanol for 45 minutes. Finally, the substrates were rinsed with ethanol, water and N_2 dried. PLGA 75:25 (M_W=66000-107000 g/mol) was dissolved in chloroform (2 % wt) and spin coated at 5400 rpm for 120 s onto the APTES-functionalized silicon substrate. The solvent was allowed to evaporate at room temperature for 24 hours before any further processing of the samples.

An IonLiNE (Ion beam Lithography, Nanofabrication and Engineering Workstation RAITH GmbH, Germany) focused ion beam apparatus was used to obtain the patterned surfaces onto silicon. The aperture used was of 70 μm, the intensity of the Ga^+ ions was 132 pA and the dose 20000 $\mu C/cm^2$ in 10 loops. The size of the patterned area was 25 μm x 25 μm.

6.2.2. AFM analysis

The experiments were performed with a Multimode atomic force microscope fitted with a Nanoscope V controller (Bruker, Santa Barbara). The images were obtained in the amplitude modulation AFM mode (repulsive regime)[26] by driving mechanically the cantilever [27]. The free amplitude A_0 was 20 nm and the setpoint amplitude A_{sp} was 13 nm. At day 0 the PLGA samples were characterized (topography and mechanical response) in air and afterwards they were immersed in PBS buffer. During 14 days, the samples were analyzed in PBS on a daily basis to follow the changes in morphology and mechanical properties.

6.2.2.1. Topography analysis of the PLGA patterns

Images and force curves were recorded in both air and PBS environment. Rectangular PPP-NCH (Nanosensors, Switzerland) cantilevers with a nominal force constant k= 40 N/m and a resonant frequency of 291 kHz were used for air measurements.

For the experiments performed in PBS buffer, rectangular PPP-FM (Nanosensors, Switzerland) cantilevers with a nominal force constant k= 2.8 N/m and resonant frequency of 75 kHz were employed. The

microscope is equipped with a liquid cell where approximately 60 μl of PBS at pH 7.4 are introduced in order to carry out the measurements.

6.2.2.2. Nanomechanical spectroscopy

Nanomechanical spectroscopy refers to the determination of mechanical properties such as the Young modulus with nanoscale spatial resolution from AFM observables[24, 28-30]. The nanomechanical measurements involve the accurate determination of the cantilever force constant as well as the optical lever sensitivity. The force constant and quality factor are determined by using the thermal noise method [31]. In order to calibrate the optical lever sensitivity we have acquired deflection versus distance curves on a hard surface (muscovite mica). Typically 100 deflection versus distance curves were acquired and the sensitivity of the photodiode is calculated from the mean value of the slope of the above mentioned curve in the repulsive region.

The force curves were obtained in contact mode by approaching and retracting the tip towards the sample 300 nm at 1 Hz. Each curve has 1024 points. Once the deflection versus piezo-displacement curves are obtained, the curves are converted into force *versus* tip-sample separation curves by applying Hooke´s law; $F = -kd$ (d is the cantilever deflection, k is the cantilever force constant). Finally, the indentation δ is calculated by taking the difference between the piezo-displacement z_p of the piezo-scanner and the deflection[29]. Typical indentation levels were maintained below 10 nm (which corresponds to roughly 10% of the thickness of the PLGA patterns) to minimize the contribution of the substrate to the mechanical response of the material.

The Young modulus was derived using the Sneddon model for a paraboloid probe [32] where F is the applied load, R the curvature radius of the probe apex, E the effective Young modulus of the material, v the Poisson ratio (0.3 for polymeric materials),

$$F = \frac{4}{3}\frac{E}{(1-\nu^2)}R^{1/2}\delta^{3/2} \quad (6.1)$$

The Young modulus is computed from the slope of Equation 6.1. Figure 6.3 shows a typical force curve where the fitting area used to calculate the Young modulus is highlighted in green.

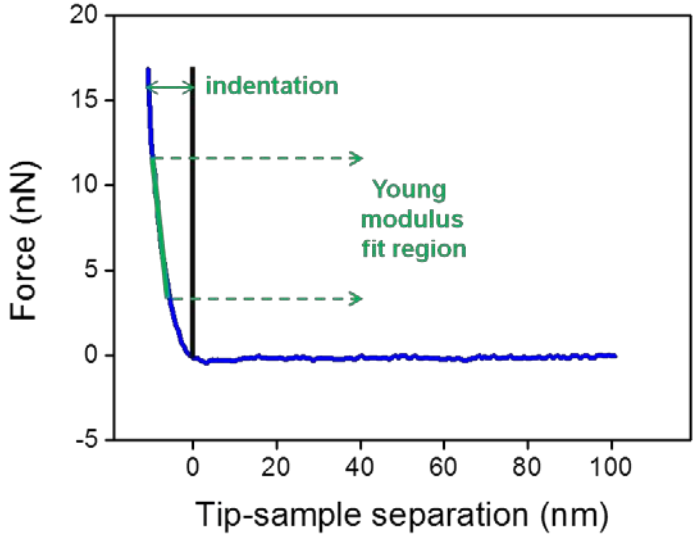

Figure 6.3. Typical force versus distance curve obtained on PLGA. The indentation is calculated as the difference between the displacement of the piezo-scanner and the deflection. The section of the curve used to fit Equation 6.1 and obtain the Young modulus is highlighted in green.

6.3. Results

To follow, measure and understand the changes experienced by the PLGA upon immersion in PBS we have performed two types of measurements. First, we use the AFM to map the topographical changes at the nanoscale as a function of the immersion time in buffer environment. Second, we measure changes of the elastic response (Young modulus) of the scaffold. The measurements are performed over 14 days. This period was chosen in view of potential applications of the PLGA as scaffold to attach cells, since many cell types have maturation and proliferation periods of 7 to 14 days[33].

6.3.1. Topography and nanomechanical properties of PLGA the samples before incubation in PBS

The samples were analyzed in air at room temperature prior to the immersion in PBS buffer. An array of PLGA rectangular structures separated by 2.5 μm was fabricated on silicon by using focused ion beam lithography (Figure 6.4A). Each PLGA pattern has an area of 1.5 μm x 1 μm and a height of 100 nm (Figure 6.4B). A cross-section of a single PLGA pattern in shown in Figure 6.4C. The peak at the edges of the pattern is a result of the lithography process.

This kind of pattern facilitates the measurement of the surface topography, the volume changes and the mechanical response of the same region with a spatial accuracy in the sub-100 nm range. The measurements included here represent averages over 8 different PLGA patterns.

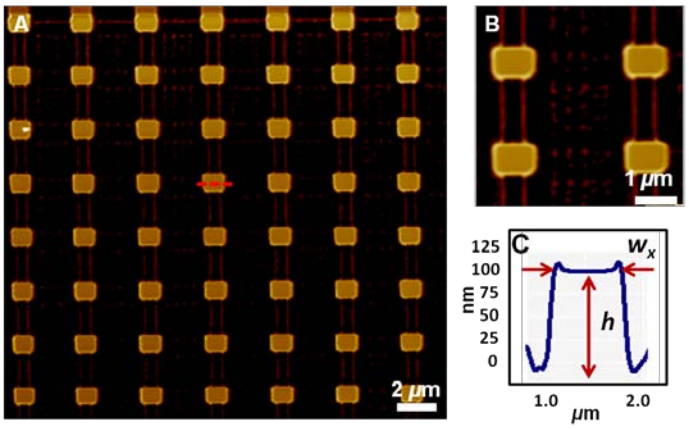

Figure 6.4. AFM topography images of PLGA nanopatterns on a silicon substrate. A. 25 μm x 25 μm area of PLGA patterns on silicon. B. Zoom of four PLGA patterns. C. Cross-section of a PLGA pattern.

6.3.2. Topography evolution of PLGA structures in PBS

Patterned PLGA samples have been immersed in PBS buffer of pH 7.4 at room temperature. The samples have been analyzed on a daily basis for

14 days in PBS. At the end of each day the buffer solution was refreshed. The evolution of the width and height of the same PLGA structure is presented in Figure 6.5. The time evolution graphs show two distinctive regions. First, both height and width show an oscillating behavior that ends at day 8. After that, the two decrease with the immersion time. The pattern doubles its width after the first day of immersion. In addition, during the whole period studied here, the width of the PLGA structure was wider than the original value. The changes in height are in the 5-15% range with respect to the dry pattern. The alternating increase/decrease behavior has also been observed in macroscopic PLGA samples [20, 34]. The data shows higher variations in width as compared to height.

Figure 6.6 shows the evolution of the volume with the immersion time. The volume is calculated as the product between the following pattern parameters: width in the x and y axis w_x, w_y and height h. We observe that the volume reproduces the same behavior shown above, this is, the volume shows a sharp increase during the first 24 hours of immersion, which is followed by a relatively slow decrease (day 2 to day 4), then it increases over the following 4 days and from then on the volume decreases.

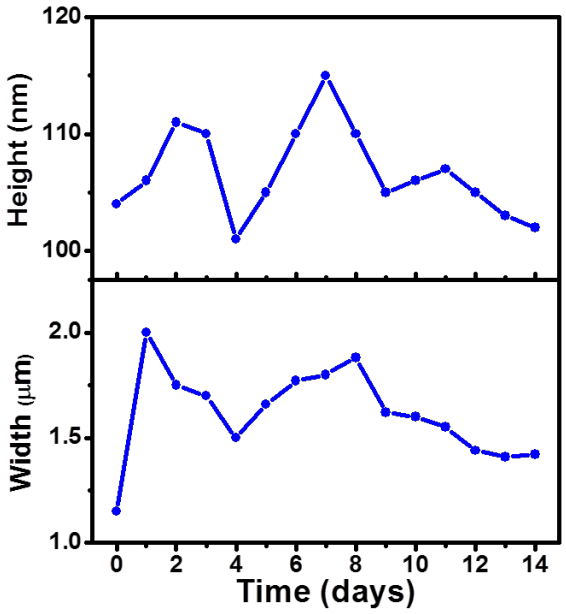

Figure 6.5. Evolution of the height and width of a single PLGA pattern as a function of the days immersed in PBS. The values represent an average over 8 different patterns.

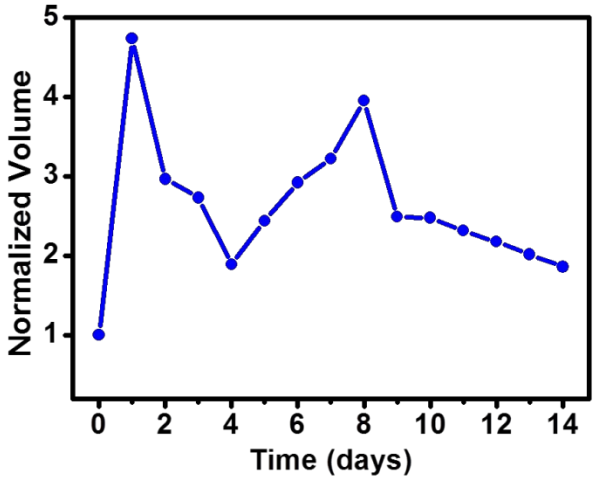

Figure 6.6. Evolution of the volume of the PLGA patterns upon immersion in PBS. The values are normalized with respect to the initial value of the volume in air (V_{air} is 0.097 μm^2) and they represent an average over 8 different patterns.

To better visualize the volume evolution, the volume has been normalized to its initial (dry) volume. At the end of the 14 days in PBS, the pattern shape was conserved although the volume shows a 2-fold increase. The volume changes of the PLGA structure at its peak value represents a 4-fold increase.

.

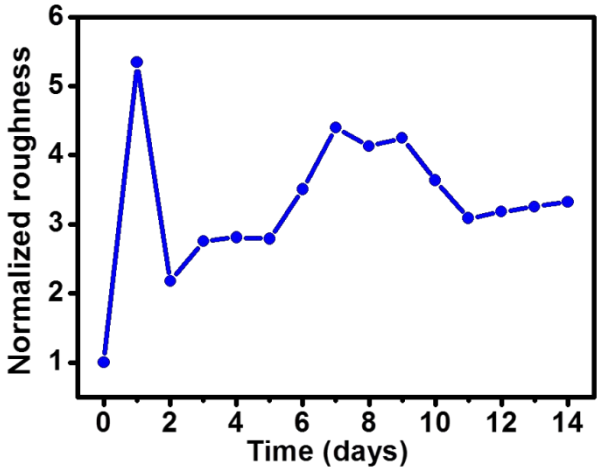

Figure 6.7. Normalized roughness of the surface of PLGA patterns as a function of immersion time in PBS. Roughness values *(rms*) have been normalized with respect to the *rms* value obtained in air before immersion in PBS (rms_{air} is 0.52 nm).

We have also measured the surface roughness over the top section of the PLGA structures (approximately 1 μm^2) (Figure 6.7). The overall behavior reproduces the oscillating behavior noted above. A sharp increase after the 1st immersion day is followed by a quick decrease during the 2nd day. This is followed by an overall increase that peaks between days 6 and 8. After that the roughness decreases for two additional days and then there is a small increase. We note that immersion in PBS, with independence of the number of immersion days, increases the roughness with respect to the dry sample. After the first day the roughness (*rms* value) has a 5-fold increase. At the end of the period studied here the *rms* shows a 3-fold increase with respect to the dry PLGA surface

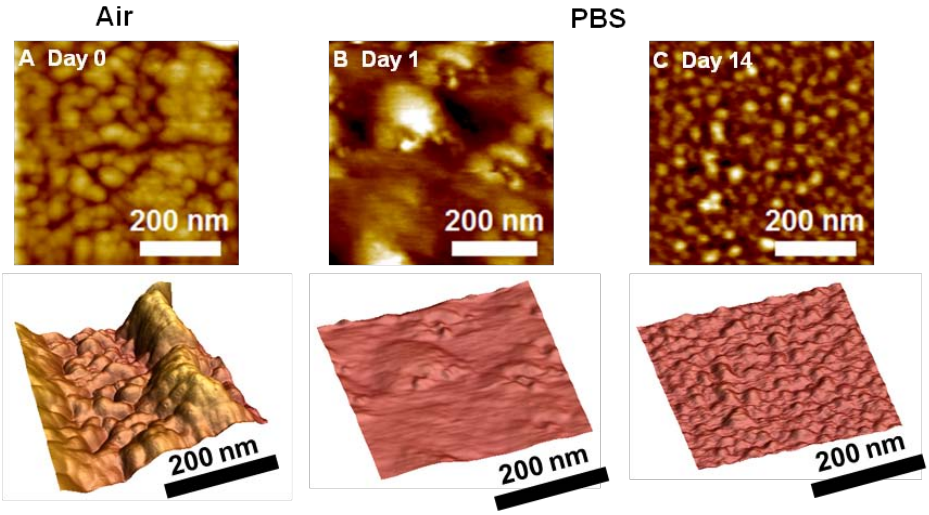

Figure 6.8. High resolution topography images of a PLGA nanopattern's top surface. 3-d images are shown for a better visualization of the erosion process. A: Pattern topography as imaged in air medium before starting the degradation experiment; B: Image of the PLGA pattern surface taken in PBS buffer after 1 day of incubation; C: Surface topography of a PLGA pattern measured in PBS buffer on day 14 of immersion.

We have studied the evolution of the surface topography of the PLGA pattern by performing amplitude modulation AFM measurements in the repulsive regime. Figure 6.8 depicts the surface topography of the same pattern before and during immersion in PBS. Prior to PBS immersion the pattern shows considerable height changes (Fig. 6.8A). Those height

variations across the pattern surface are significantly reduced after immersion in PBS (Fig. 6.8B and C).

6.3.3. Nanomechanical analysis of the PLGA patterns

The nanomechanical analysis of the PLGA structures has been carried out both before immersion in PBS and also every day during 14 days (Figure 6.9). The values of the Young modulus are normalized with the value obtained in air at day 0. Initially (air) the Young modulus is about 2.4 GPa. An important drop of the Young modulus down to around 200 MPa is observed when the sample is immersed in PBS. The steady decrease continues until around day 7, when it reaches 17 MPa. From this point on, the Young modulus decreases and small fluctuations are observed between days 11 and 14.

The decrease of the Young modulus is marked by the presence of two regions with higher slopes (red arrows in Figure 6.9), one during the 1st day of immersion and the other between days 6 and 7. Those days coincide with the times when the morphological features of the patterns show a fast increase.

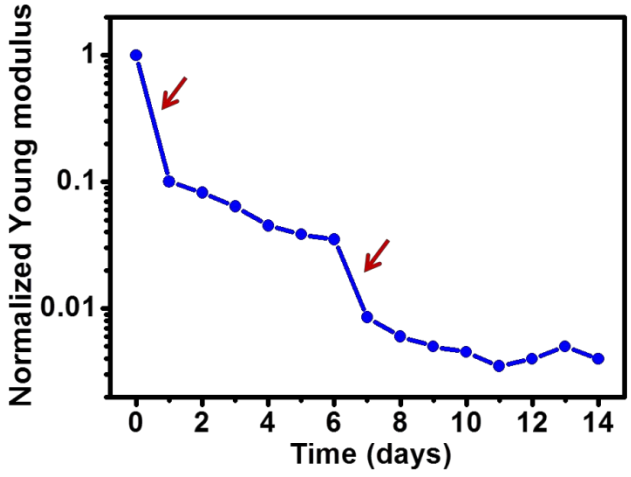

Figure 6.9. Evolution of the Young modulus of the PLGA patterns as a function of the immersion time in PBS. The values are normalized with respect to the initial value of the Young modulus in air (E_0 is 2.4 GPa) and represent an average over 8 different patterns.

6.4. Discussion

The experimental data show oscillations in the volume and roughness which are not present in the Young modulus evolution (Fig. 6.10). The Young modulus decreases from the first day of immersion. However, the highest decrease of the Young modulus coincides or is very close to the days when the volume reaches the local maxima.

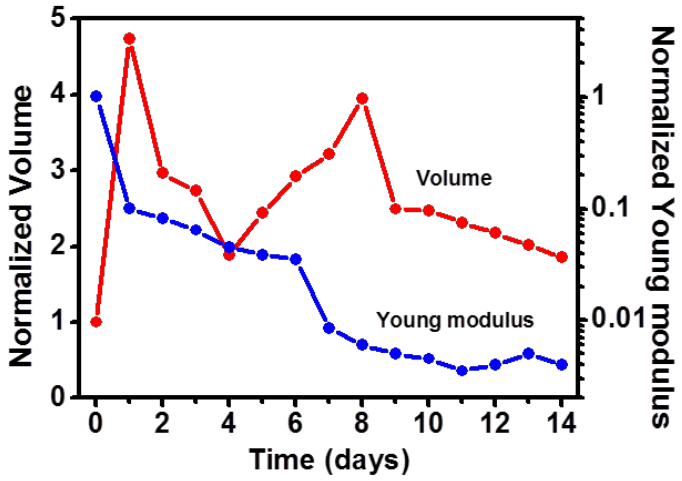

Figure 6.10. Young modulus and volume evolution upon immersion in PBS.

A theoretical model was developed in Francesco Zerbetto's group (University of Bologna) to explain the volume changes observed on the PLGA patterns during the first week. The numerical method used to develop the polymer-swelling model is presented in Appendix B.4 of this thesis.

Figure 6.11 shows the comparison between theory and experimental data. The model describes the width expansion as a function of time by introducing three regimes. Initially, the solvent diffuses into the polymer from the external interfaces. The diffusion coefficient depends on the solvent concentration. The solvent uptake is slow in the unsolvated polymer domain, and it becomes faster in the regions where the polymer has been already solvated. The solvation favors the rearrangement of polymer chains, which in turn leads to a quick increase in volume (1D diffusion). The presence of solvent molecules triggers internal stresses in the polymer which give rise to the uncoiling and rearrangement of large

segments of polymer chains. This regime involves a volume shrinking (relaxation). Once the stresses are removed by viscous flow, further solvent uptake is possible which leads to a second swelling (3D diffusion).

This swelling-deswelling process is accompanied by a decrease of the Young modulus. The sharp decrease of *E* in the first 24 hours is correlated with the initial swelling process due the uptake of solvent molecules. The moderate decrease of *E* observed between day 1 and day 6 is also consistent with the model involving uncoiling of the polymer chains and subsequent filling of the polymer voids. The release of the polymer stresses favors the uptake of solvent molecules which causes swelling which in turns produces a relatively sharp decrease of the Young modulus.

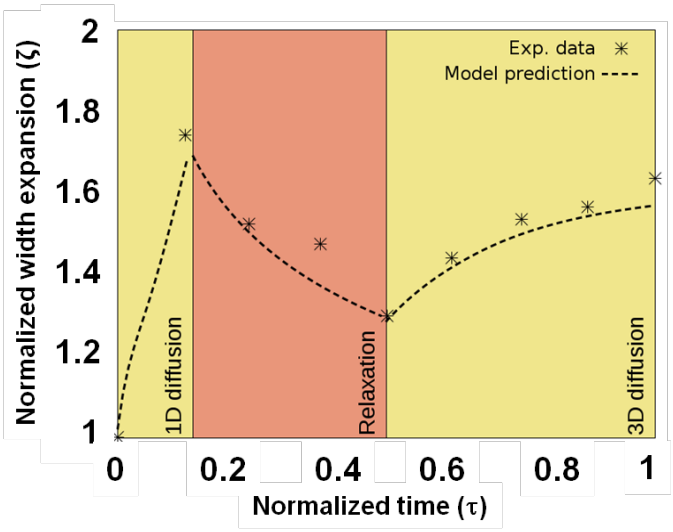

Figure 6.11. Normalized width expansion of the PLGA as a function of time. Three regimes of the polymer volume changes are highlighted: (1) Initial swelling, (2) Relaxation, (3) Final swelling. Experimental results are in agreement with the solution of the model, which is plotted as a dashed line.

Certainly, PLGA degradation both due to erosion (Fig. 6.8) and bulk degradation is happening since day 1. However, those processes, in particular bulk degradation does not seem to dominate the evolution during this period of time (from day 0 to day 7). The degradation of PLGA

is caused by the hydrolysis of the ester bonds inside the polymeric matrix in the presence of water molecules, with the formation of acidic oligomers and finally monomers (Figure 6.1). However, the hydrolysis of the ester links is slower than water diffusion through the material[14]. The initial increase of the volume is induced by water molecules penetrating the polymeric matrix.

The small variation in volume of the PLGA patterns along with the decrease tendency of the height observed from day 8 onwards can be interpreted as a result of pore formation inside the polymer matrix and a slow release of oligomers resulted from the hydrolysis of ester bonds. This leads to a small-scaled mass loss, which is reflected by a 5% drop in height at day 14 in PBS as compared to the one at day 1. The reported mass loss for 75:25 PLGA copolymers in the first two weeks of degradation is between 10 and 20% [15, 35]. Interestingly, as mentioned in a recent study on hydrogel particles swelling, [34] the process takes place anisotropically and inhomogeneously. We observe that PLGA structures swell more in length and width than in height (Figure 6.5). This is due to the fact that they are bound to the stiff silicon substrate, which is acting as a constraint on the vertical axis.

In situ measurements of the surface topography at the nanoscale during degradation provide information about the erosion process that takes place at the interface between the PLGA scaffold and the liquid environment. The initial surface displaying significant variations in height is transformed into an eroded area with numerous protrusions and gaps (Figure 6.8). Our findings regarding the surface roughness are similar to the ones of Semler and al. [36]. They have also observed a decrease of the number of regions containing rapid and drastic variations as a result of degradation.

The initial measurements in air show that the material has a relatively high Young modulus of about 2.4 GPa. This value is in agreement with bulk measurements reported elsewhere [37]. Once the sample is immersed in PBS, a sharp decrease of the mechanical properties is observed along

with the swelling of the material. By looking at Figure 6.10, we observe that there is a competition between swelling and degradation. From day 1 to 8, significant fluctuations of the volume lead to the conclusion that swelling is the major factor generating the decrease of the Young modulus. In addition, the reported decrease of the molecular weight of PLGA copolymers upon immersion in PBS[15, 20] generates lower molecular weight compounds, which are more flexible due to the weakening of the intermolecular bonds inside the polymer chain. As a result, the polymeric matrix is not as tightly packet as in the initial dry state, so this is also a factor which leads to the softening of the material. A comparison of mechanical response versus molecular weight of poly-lactic and poly-glycolic based polymers also shows that there is a strong dependence between mechanical properties and molecular weight[38]. Small fluctuations in the Young modulus take place between days 9-14, but the decrease tendency is preserved.

6.5. Conclusions

We report a high spatial resolution and nanomechanical spectroscopy mapping of the early-stages of the evolution of PLGA structures upon immersion in a biological buffer. The evolution of the morphological properties, size and surface roughness and mechanical properties (Young modulus) shows four stages. The first stage is characterized by a fast swelling. It also involves a sharp decrease of the Young modulus. The sudden increase in volume and roughness observed in the first 24 hours and the observed decrease in Young modulus are due to a diffusion process where the diffusion coefficient D depends on the solvent concentration C. The solvent uptake is favoured in the already solvated polymer chains leading to a fast increase of the free volume.

The second stage involves is a relaxation process that implies a rearrangement of the polymers chains. The PLGA patterns decrease in

size to reach a local minimum in the volume. The relatively slow volume decrease in this regime is associated with the polymer response to the stress caused by the presence of the solution. The Young modulus keeps decreasing but at a slower rate.

After the stress is dissipated by the viscous flow of the polymer, the polymer is ready to accept more solvent and a second swelling occurs (third stage). Here the Young modulus also shows a sharper decrease rate. After this stage, the volume shows a steady decrease which is interpreted as the start of the full degradation of the PLGA. The Young modulus shows a tendency to decrease but it is less evident than in the previous stages. At the end of observation process the Young module has decreased by almost three-orders of magnitude from an initial value of 2.4 GPa to 9 MPa.

The observed results are a consequence of three different processes, coupled diffusion-swelling, degradation and erosion. The coupled diffusion-swelling process lasts about 1 week. The presence of a second peak in the volume and roughness indicates a competition between swelling and hydrolytic degradation of the ester bonds, the latter a thermally activated process that happens at a slower rate than water adsorption.

The significant fluctuations of the surface roughness together with the decrease of the Young modulus could have implications on cells adherence and proliferation.

6.6. References

1. J. M. Anderson and M. S. Shive, *Advanced Drug Delivery Reviews*, 1997, **28**, 5-24.
2. K. Yamaguchi and J. M. Anderson, *Journal of Controlled Release*, 1993, **24**, 81-93.
3. S. E. Gautier, M. Oudega, M. Fragoso, P. Chapon, G. W. Plant, M. B. Bunge and J.-M. Parel, *Journal of Biomedical Materials Research*, 1998, **42**, 642-654.
4. A. A. Ignatius and L. E. Claes, *Biomaterials*, 1996, **17**, 831-839.
5. C. J. Ke, T. Y. Su, H. L. Chen, H. L. Liu, W. L. Chiang, P. C. Chu, Y. N. Xia and H. W. Sung, *Angewandte Chemie-International Edition*, 2011, **50**, 8086-8089.
6. M. L. Chen, S. Gao, M. D. Dong, J. Song, C. X. Yang, K. A. Howard, J. Kjems and F. Besenbacher, *ACS Nano*, 2012, **6**, 4835-4844.
7. A. Mathew, T. Fukuda, Y. Nagaoka, T. Hasumura, H. Morimoto, Y. Yoshida, T. Maekawa, K. Venugopal and D. S. Kumar, *PLoS One*, 2012, **7**, 10.
8. N. Hild, O. D. Schneider, D. Mohn, N. A. Luechinger, F. M. Koehler, S. Hofmann, J. R. Vetsch, B. W. Thimm, R. Muller and W. J. Stark, *Nanoscale*, 2011, **3**, 401-409.
9. G.-J. Wang, Y.-C. Lin and S.-h. Hsu, *Biomed Microdevices*, 2010, **12**, 841-848.
10. X. S. Wu and N. Wang, *Journal of Biomaterials Science, Polymer Edition*, 2001, **12**, 21-34.
11. I. Grizzi, H. Garreau, S. Li and M. Vert, *Biomaterials*, 1995, **16**, 305-311.
12. E. Vey, C. Roger, L. Meehan, J. Booth, M. Claybourn, A. F. Miller and A. Saiani, *Polymer Degradation and Stability*, 2008, **93**, 1869-1876.
13. T. G. Park, *Biomaterials*, 1995, **16**, 1123-1130.
14. A. Göpferich, *Biomaterials*, 1996, **17**, 103-114.
15. E. Vey, C. Rodger, L. Meehan, J. Booth, M. Claybourn, A. F. Miller and A. Saiani, *Polymer Degradation and Stability*, 2012, **97**, 358-365.
16. H. Assender, V. Bliznyuk and K. Porfyrakis, *Science*, 2002, **297**, 973-976.
17. J. G. Goetz, S. Minguet, I. Navarro-LÈrida, J. J. Lazcano, R. Samaniego, E. Calvo, M. Tello, T. Osteso-Ib·Òez, T. Pellinen, A. Echarri, A. Cerezo, A. J. P. Klein-Szanto, R. Garcia, P. J. Keely, P. S·nchez-Mateos, E. Cukierman and M. A. Del†Pozo, *Cell*, 2011, **146**, 148-163.
18. M. Chyasnavichyus, S. L. Young and V. V. Tsukruk, *Langmuir*, 2014, **30**, 10566–10582.
19. E. Pamula and E. Menaszek, *J Mater Sci: Mater Med*, 2008, **19**, 2063-2070.
20. J. K. Perron, H. E. Naguib, J. Daka, A. Chawla and R. Wilkins, *Journal of Biomedical Materials Research Part B: Applied Biomaterials*, 2009, **91B**, 876-886.
21. Y. F. Dufrene, D. Martinez-Martin, I. Medalsy, D. Alsteens and D. J. Muller, *Nature Methods*, 2013, **10**, 847-854.
22. A. Ikai, in *Nano/Micro Biotechnology*, eds. I. Endo and T. Nagamune, Springer Berlin Heidelberg, 2010, vol. 119, ch. 41, pp. 47-61.
23. E. T. Herruzo, A. P. Perrino and R. Garcia, *Nature Communications*, 2014, **5**, 3126-3204.
24. D. Martinez-Martin, E. T. Herruzo, C. Dietz, J. Gomez-Herrero and R. Garcia, *Physical Review Letters*, 2011, **106**, 198101.
25. M. Chen, S. R. Nielsen, T. Uyar, S. Zhang, A. Zafar, M. Dong and F. Besenbacher, *Journal of Materials Chemistry C*, 2013, **1**, 850-855.
26. R. Garcia and A. San Paulo, *Physical Review B*, 1999, **60**, 4961-4967.
27. E. T. Herruzo and R. Garcia, *Applied Physics Letters*, 2007, **91**, 143113.
28. M. D. Dong, S. Husale and O. Sahin, *Nature Nanotechnology*, 2009, **4**, 514-517.
29. H.-J. Butt, B. Cappella and M. Kappl, *Surface Science Reports*, 2005, **59**, 1-152.
30. S. Zhang, H. Aslan, F. Besenbacher and M. Dong, *Chemical Society reviews*, 2014, **43**, 7412-7429.

31. H. J. Butt and M. Jaschke, *Nanotechnology*, 1995, **6**, 1.
32. I. N. Sneddon, *International Journal of Engineering Science*, 1965, **3**, 47-57.
33. C. Gualandi, M. Govoni, L. Foroni, S. Valente, M. Bianchi, E. Giordano, G. Pasquinelli, F. Biscarini and M. L. Focarete, *European Polymer Journal*, 2012, **48**, 2008-2018.
34. M. Caldorera-Moore, M. K. Kang, Z. Moore, V. Singh, S. V. Sreenivasan, L. Shi, R. Huang and K. Roy, *Soft Matter*, 2011, **7**, 2879-2887.
35. N. Samadi, A. Abbadessa, A. Di Stefano, C. F. van Nostrum, T. Vermonden, S. Rahimian, E. A. Teunissen, M. J. van Steenbergen, M. Amidi and W. E. Hennink, *Journal of Controlled Release*, 2013, **172**, 436-443.
36. E. J. Semler, J. S. Tjia and P. V. Moghe, *Biotechnology Progress*, 1997, **13**, 630-634.
37. E. Pamula, J. Kokoszka, K. Cholewa-Kowalska, M. Laczka, L. Kantor, L. Niedzwiedzki, G. Reilly, J. Filipowska, W. Madej, M. Kolodziejczyk, G. Tylko and A. Osyczka, *Ann Biomed Eng*, 2011, **39**, 2114-2129.
38. E. Vidović, D. Klee and H. Höcker, *Journal of Applied Polymer Science*, 2013, **130**, 3682-3688.

Chapter 7

Interfacing polymers and tissues: Quantitative local assessment of the Foreign Body Reaction of Mononuclear Phagocytes to Polymeric Materials

7.1. Introduction

7.1.1. Foreign body reaction

Synthetic biomaterials are widely used to fabricate medical devices regulating, replacing or restoring impaired functions of the body. These applications are expected to grow with the advent of advanced therapies based on loco-regional treatments or stem-cell grafts for tissue regeneration [1 2].

Interfacing neural tissue with solid state electronics in a minimally invasive manner is a fundamental requirement for the clinical translation of neural prosthetic devices aimed to monitor, replace or regenerate neurological functions lost as a consequence of an injury or pathology. However, the implantation of any material or medical device into a host tissue is likely to trigger an adverse foreign body reaction (FBR) [2-4], which is a cascade of events strongly intertwined with the interactions between cells and materials or substances not recognized as “self” [5] (Figure 7.1).

The FBR is generally characterized by the *recruitment*, *adhesion*, *migration* and *activation* of immune cells at the implantation site. The implantation of any material/device determines, in fact, an initial blood vessels and tissue disruption with consequent leakage of plasma fluid and local *recruitment* of blood borne immune cells (e.g. monocytes/macrophages, mast cells, neutrophils). Consequently, implanted materials/devices are subjected to an immediate

nonspecific adsorption of proteins (called biofouling) that favors the *adhesion* of neutrophils and blood-derived monocytes[6]. Upon extravasation, monocytes differentiate into macrophages that *migrate* towards the tissue/implant interface and secrete pro-inflammatory cytokines [e.g. tumor necrosis factor-α (TNF-α), interleukin-1β (IL-1β), and IL-6], chemokines [e.g. monocyte chemotactic protein 1 **(**MCP-1 or CCL2), fraktalin, IL-8] and growth factors [e.g. macrophage-colony stimulating factor (M-CSF)] to recruit additional immune cells and fibroblasts. Because most implants are large, individual macrophages cannot phagocytose them and eventually they fuse to form large multinucleated foreign body giant cells (FBGCs) aiming to embrace the implant and start a wound healing process[2]. During this phase, macrophages release reactive oxygen intermediates (ROIs), nitric oxide (NO), degrading enzymes and acids, thus leading to the possible damage of the medical device. Furthermore, recruited fibroblasts and mast cells produce collagen-based extracellular matrix that wraps the implanted material/device in a fibrotic capsule that insulates the device impeding any interaction with the surrounding tissue. In the specific context of the central nervous system (CNS), the FBR also leads to the activation of microglia (the resident macrophages) and astrocytes. These cells contribute to the maintenance of tissue homeostasis in physiological conditions while functioning as a first-line of defense upon injury or perturbations of the local environment. Importantly, microglia/astrocyte activation increases local inflammation, thus resulting in scar formation and damage of neuronal circuitries[7].

The origin of FBR is not completely understood, though it is now clear that elasticity/plasticity[8], surface texture, wettability and surface tension[9-11] can affect its occurrence. Surface engineering of biomaterial surfaces using either micro-patterning techniques or chemical modifications has been successfully validated to reduce/tune the FBR [2, 12]. Alternatively, materials/devices can be designed in order to actively release anti-inflammatory drugs (e.g. dexamethasone)[13], which can act by reducing both the inflammation derived from the implantation procedure itself and/or by limiting the onset of the FBR[14]. Although various *in vitro* models of FBR have been proposed, a wide correlation study investigating

the properties of the materials and their interaction with CNS immune competent cells (i.e. macrophages, microglia and astrocytes) is missing, hence highly demanded. Furthermore, the ideal anti-inflammatory drug to be delivered in the CNS has not been identified yet.

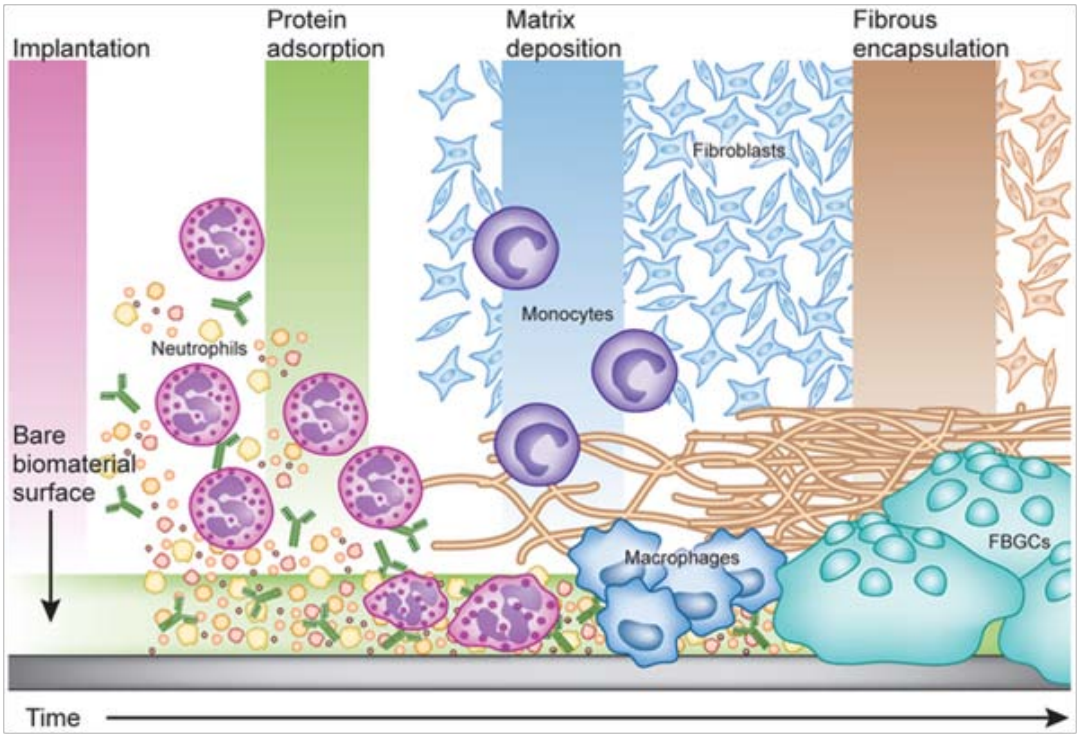

Figure 7.1. The FBR process initiates immediately upon implant contact with host fluids (e.g., blood, lymph, wound fluids) by spontaneous uncontrolled adsorption of host proteins to the implant surface. The resulting implant-tissue interface is coated with diverse protein species in various conformations and adsorbed states. Host cells responsible for normal wound healing encounter this unusual adsorbed-protein layer. Within hours, neutrophils enter the implant tissue site and react by producing cytokines, chemokines, reactive oxygen species and other enzymes. In the next several days, these neutrophil products recruit tissue-resident macrophages and undifferentiated monocytes to the wound site, concomitant with the exit of neutrophils. Macrophages respond to the implant by producing their own set of signaling molecules, which attract fibroblasts. Fibroblasts produce excess collagen. Their presence correlates with formation of foreign-body giant cells (FBGCs), whose role in the foreign-body response is poorly understood. With time, a dense collagenous fibrotic capsule is created around the implant, isolating it physically and physiologically from the host tissue. Adapted from Ref.4.

Cell/material adhesion is a multiscale phenomenon, hence there is a lag in accessing the cell/material interaction from the single cell down to the molecular level. Most studies are based on phenomenological or semi-quantitative cell adhesion assays *in vitro*[15]. The established methodologies foresee the detection of relevant biomarkers expressed by cells of the immune system, together with the evaluation of cell morphological parameters. *In-vitro* assays imply a lengthy response, large variances of the observables, and difficult standardization of the protocols. Advancing the methodology from the heuristic level to a robust quantitative characterization in a shorter timescale is important both for materials screening, as well as to evaluate the synergic effects of drugs and chemotrophic factors that may prevent or delay the onset of cell adhesion.

7.1.2. Single-cell force spectroscopy

7.1.2.1. Introduction

Cell adhesion is a key factor to be taken into account when designing new medical devices and implants. Cells have the capability to respond to the physico-chemical properties of their surrounding environment by regulating several fundamental cellular processes, such as proliferation, migration, survival and differentiation[16]. Cell adhesion can be investigated employing a wide array of qualitative and quantitative assays, however most studies usually provide only qualitative or at best semi-quantitative information.

Historically, washing assays proved to be a useful and versatile technique for the estimation of the cell adhesion to a substrate. The method involves the incubation of the cells on a substrate of interest, followed by rinsing with a solute (usually physiological buffer) to remove weekly attached or no adhered cells. The adhesion is measured as the ratio between the number of remaining cells to the number of the cells initially present on the substrate surface. The lack of standardization of this type of assay lead to the development of more elaborated hydrodynamic assays, such as spinning disc devices[17] or flow

chambers[18]. Nevertheless, shear forces are practically unknown in these kinds of assays, since they depend on several parameters such as cell shape, size and attachment to the substrate. Additionally, only average cell adhesion characteristics can be extracted by means of hydrodynamic assays. This means that subpopulations resulting from cells heterogeneity or different functional states cannot be revealed. In biomaterials research, a popular qualitative method is to correlate the cell adhesion strength with morphological characteristics of the cell (e.g. cell shape, area, elongation).

Single-cell methods developed during the last decades provide a quantitative and controlled approach to measure the strength of cell adhesion. Some examples of single-cell assays are magnetic[19, 20] and optical tweezers[21], micropipettes[22] and atomic force microscopy[23]. AFM-based single-cell force spectroscopy (SCFS) stands out as a versatile technique, which enables the quantification of cell adhesion in a wide range of forces, from 10 pN to 10^6 pN. [24-26]. Recent developments in AFM instrumentation enabled the use of SCFS as a valuable tool for the quantification of cell-cell and cell-substrate adhesion forces.[24, 26-30]

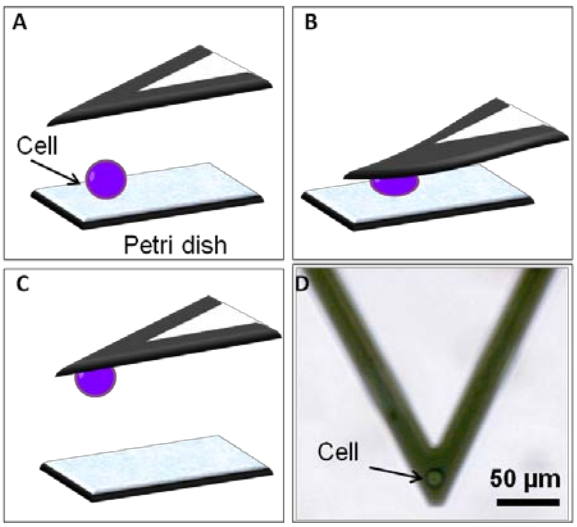

Figure 7.2. Attaching a cell to the AFM cantilever. A: The functionalized AFM cantilever is placed above the cell to be attached; B: The cantilever is pressed onto a cell by applying a contact force of few nN for several seconds; C: Next, the cantilever is pulled away from the sample surface and the cell is allowed a resting time of several minutes before starting the adhesion measurements; D: Optical phase contrast image of a tip-less cantilever with a mononuclear phagocyte cell attached to it. Adapted from Ref. 23.

In a single-cell force spectroscopy experiment, single suspended cells are injected into the AFM liquid cell. As depicted in Figure 7.2 A-C, a functionalized tip-less AFM cantilever is lowered on top of a single cell and pressed onto it to attach it. The cantilever is then pulled away and the cell is allowed a recovery time of several minutes to allow a firm attachment to the cantilever surface. The cell can then be used to measure the adhesion with different substrates. To do so, cell and substrate are brought into contact for a previously set contact time and the cantilever is raised to detach the cell. In these measurements, the force dependence on the probe-surface distance, termed force curve, is recorded.

A phase contrast optical image of a cell bound to a tipless AFM cantilever is displayed in figure 5.2D. The inverted optical microscope coupled to the AFM is a key element, which enables a permanent control of the cell morphology and attachment to the cantilever.

Figure 7.3 shows a typical force *versus* distance curve obtained by performing SCFS experiments. The difference between the minimum point of the adhesion part of the force versus distance curve and the baseline is called adhesion force (F_{adh}). The force *versus* distance curve obtained in single-cell adhesion experiments can be divided into 4 regions. In the first one, the sharp increase of the adhesion force corresponds to the elastic stretching of the entire cell. In this region several individual receptor-ligand unbinding events occur as well. In the second region, as the strain on the cell increases, sequential de-adhesion steps can be observed, with a force loading slope that is close to an elastic behaviour. The third region is characterized by a force loading slope close to zero. In this region of long plateaus of constant force, large membrane tethers are detached from the surface. Finally, in the last region all cell elements are completely detached from the sample surface.

7.1.2.2. Cell attachment to the AFM cantilever

To perform SCFS measurements, the AFM cantilever needs to be functionalized prior to the cell attachment step. An overview of the most commonly used cell attachment strategies is presented in Table 7.1. Cell immobilization strategies

usually exploit the high binding affinity between receptor-ligand pairs or protein-extracellular matrix interactions. Some of the most common cantilever functionalization methods include coating with Concavalin A, extracellular matrix proteins (collagen, fibronectin) or biotintylation of cell surface proteins followed by the immobilization on streptavidin functionalized cantilevers[28]. A fundamental aspect to be taken into account when choosing the cantilever functionalization strategy is whether the protein coating will affect the functioning of the studied cell type. For example, Concavalin A is known to change the functional state of mononuclear phagocytes and lymphocytes[31, 32]. Recently, protein-based conventional cell immobilization methods were replaced by underpressure immobilization with fluidic force microscopy (FluidFM). In this approach, specially designed cantilevers with integrated microchannels connected to an external fluidic circuit are used to attach the cell by applying a defined underpressure through the microfluidic-channelled probe.

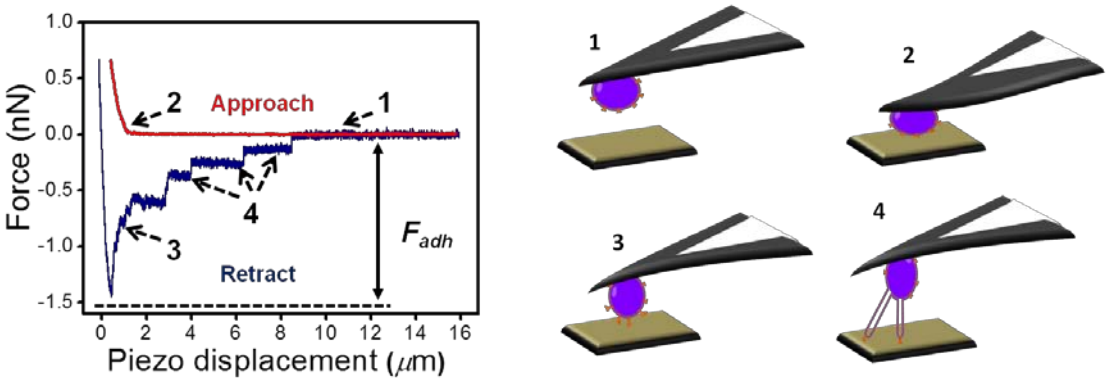

Figure 7.3. A: Representative force curve from a cell adhesion force spectroscopy experiment. The force curve shows four regions: in Step 1 the cell is approached to the polymeric material and pressed onto it until a setpoint is reached (Step 2). Step 3 represents the pulling of the whole cell surface and the unbinding of cell membrane proteins. The plateaus in Step 4 are due the detachment from the surface of micrometer-long membrane tethers. Adapted from Ref.23.

Table 7.1. *Overview of cell attachment strategies to the AFM cantilever. Adapted from Ref. 28.*

Functionalization strategy	**Attachment principle**	**Observations**
Lectins (Concavalin A, wheat germ agglutinin)	Binding of carbohydrate groups on the cell surface	Concavalin A is the most commonly used functionalization method for eukaryotic cells; Unsuitable for lymphocytes and macrophages due to activation; Binding can cause changes in cell stiffness.
Streptavidin	Binding of biotinylated cells	Cell surface biotinylation may affect cell surface receptors functioning
BD CellTak	Polyphenolic proteins extracted from marine mussel	
Extracellular matrix proteins (fibronectin, collagen)	Binding to cell adhesion receptors on the cell surface	Binding via extracellular matrix receptors can modulate the adhesive properties of the cell (e.g. by receptor cross-talk of redistribution of adhesion receptors)
Pressure-controlled cell capture	Cell immobilization by applying an underpressure through cantilever microfluidic channels	Allows sequential capture of multiple cells using the same cantilever; Requires additional specialized equipment.

In this chapter, a quantitative method was developed to assess the *in vitro* foreign body reaction of mononuclear phagocytes to polymers relevant in implants for prosthetics, advanced therapies and regenerative medicine. The study described here proposes an approach that combines single-cell force spectroscopy with the immunogenic profiling and morphological analysis of mononuclear phagocytes. This multi-scale approach involves the quantification of cell adhesion at two different time scales: 0-60 s for SCFS and 1-24 h for the immunogenic and morphological analysis. While the analysis of the cells shape, area, number and filopodia provides indirect and qualitative data on how cells adhere to different substrates, SCFS is a technique that can quantify cell adhesion strength with high sensitivity and has the capability of studying the dynamics of cell adhesion processes. Furthermore, in SCFS there is no need for previous fluorescent labeling of the samples and the data analysis is not as time consuming and operator dependent as in the case of the morphological analysis.

Two biocompatible polymeric materials were chosen as prototypical materials for biomedical applications, as follows: poly-dimethylsiloxane (PDMS) - a non-biodegradable polymer - and poly-(lactic-*co*-glycolic acid) (PLGA) - a biodegradable polymer [33] [34]. Cells are usually seeded on polystyrene (PS) Petri dishes; therefore this material is used as the control interface for mechanical and topographical properties. PLGA and PDMS are both relevant materials for the development of biomedical applications. Recently, PDMS neural implants with mechanical properties that match the native tissue were demonstrated[33], while in another study PLGA and PDMS were integrated in an *in vivo* demonstration of of implantable, multifunctional silicon sensors for the brain[35]. PDMS has the advantage of being a versatile material, whose mechanical properties can be adjusted according to the implantation site, however it is not biodegradable, which means that when used in regenerative medicine applications, a second intervention will be necessary to explant the PDMS device. Conversely, PLGA is particularly interesting due to its use as a substrate in bioresorbable implants, whose operation time scale is tailored to a few months, for the advanced treatment of pathologies of the nervous system. The PLGA degradation mechanism is discussed in detail in Chapter 6 of this thesis.

A Minocycline dose-dependent study was performed and the immunogenic profiling and morphological analysis provided indirect evidence that 50 □M Minocycline was the concentration which had a major effect on cell activation, migration and adhesion. This hypothesis was further tested with SCFS and we found that the adhesion force is lower when cells are treated with Minocycline.

The results presented in this chapter are part of a collaborative work with the groups of Stefano Pluchino (University of Cambridge, UK) and Fabio Biscarini (CNR and University of Modena Reggio Emilia, Italy). The discussion will focus mainly on the AFM results, while the details regarding the other techniques used to develop the work are described in Appendix B3.

7.2. Experimental methods

7.2.1. Amplitude modulation AFM imaging

The topography of the PLGA and PDMS samples used in this work was measured in air environment with a Nanowizard III AFM (JPK Instruments, Germany) in amplitude modulation AFM by driving mechanically the cantilever[36, 37]. Rectangular PPP-NCH (Nanosensors, Switzerland) cantilevers with a nominal force constant k= 40 N m^{-1} and a resonant frequency of 291 kHz were employed in these measurements. The free and set point amplitudes were respectively, 17 nm and 11 nm. The images were then processed with the JPK Data Processing Software and the roughness value was extracted (root-mean square, *rms*).

7.2.2. Nanomechanical spectroscopy

The cantilever force constant and optical lever sensitivity were determined as described in Chapter 3.2.3.

Nanomechanical measurements (see Chapter 6.2.2.2) were carried out in several 4 μm^2 regions of the samples. Force *versus* distance curves were obtained in contact mode by approaching and retracting the tip towards the sample 150 nm at 200 nm/s. Each curve has 2050 points. Once the deflection versus piezo-displacement curves were obtained, the curves were converted into force *versus* indentation curves by applying Hooke´s law; $F = -kd$ (d is the cantilever deflection, k is the cantilever force constant). Finally, the indentation δ is calculated by taking the difference between the piezo-displacement z_p of the piezo-scanner, the initial contact distance z_0, and the deflection[38]. Typical indentation levels were maintained below 10% of the sample thickness to minimize the contribution of the substrate to the mechanical response of the material.

The Young modulus was derived using the Sneddon model for a paraboloid probe [39] (Equation 7.1) where F is the applied load, R the

curvature radius of the probe apex, *E* the effective Young modulus of the material, *v* the Poisson ratio (0.3 for polymeric materials),

$$F = \frac{4}{3}\frac{E}{(1-\nu^2)}R^{1/2}\delta^{3/2} \quad (7.1)$$

The approach part of the force *versus* indentation curves was fitted to Equation 7.1 and the Young modulus was extracted.

7.2.3. Cell culture for SCFS experiments

Differentiated bone marrow-derived mononuclear phagocytes (BMDM) cells (see Appendix B.3.2) were maintained in Dulbecco's Modified Eagle's Medium (DMEM) High Glucose medium supplemented with 10% fetal bovine serum (FBS) (v/v), 10% macrophage colony-stimulating factor (M-CSF) (v/v) and 1% Penicillin/Streptomycin (v/v). Cells were grown up to 80% confluence and maintained at 37°C and 5% humidified CO_2. Cells were detached using a scraper, centrifuged at 1300 rpm for 10 minutes and re-suspended into serum-free High Glucose DMEM (measurement medium).

7.2.4. Minocycline administration

Minocycline hydrochloride (Sigma-Aldrich) was dissolved in DMEM at an initial concentration of 5 mM, it underwent an ultrasound treatment and was then sterilized through a 0.2 *μ*m filter. Minocycline was administered at final concentrations ranging from 0.5 *μ*M to 50 *μ*M. Because of its short half-life, the same amount of Minocycline was added every 12 hours to maintain the drug concentration constant.

To quantify the effect of Minocycline on cell adhesion, we measured the response of both treated and untreated cells. To limit cell variability and heterogeneity issues, for each measurement, a batch of mononuclear phagocyte cells was divided into treated and untreated samples. The two

samples were then measured the same day and at the same point of their growth cycle. Untreated cells were used as described above. As for the treated cells, Minocycline was added to the cell culture medium to a final concentration of 50 μM every 12h, prior to SCFS experiments.

7.2.5. Single-cell force spectroscopy measurements

Cell adhesion measurements were conducted using a Nanowizard III AFM (JPK Instruments, Germany) mounted on top of an inverted optical microscope (Axiovert A1, Zeiss, Germany). The optical sensitivity and force constant of the tipless cantilevers were calibrated before starting the cell adhesion measurements as described in Chapter 3.2.3. The calibrated force constant of the cantilevers was found to be in the 0.05 to 0.07 N/m range.

For adhesion force measurements, tipless AFM microcantilevers were functionalized with fetal bovine serum (FBS) by following the protocol in Appendix A.1.5. Next, 60 μL of mononuclear phagocytes cells suspension were gently injected into the AFM liquid cell containing 2 ml serum-free DMEM medium. To attach a single cell to the FBS-functionalized cantilever, the sensor was lowered towards the Petri dish at a speed of 5 μm/s and pressed onto a cell by applying a contact force of 3 nN for 5 s. Then the cantilever was pulled 50 μm away from the sample surface. A resting period of 10 minutes was introduced before the adhesion measurements. The microcantielver with the cell attached to it was then approached towards the relevant material surface at a speed of 5 μm/s until reaching a contact force of 0.3-0.5 nN. The cantilever height was maintained constant for a set time of 10 and 30 s (for the comparison between cell adhesion on PLGA and PDMS) and 5, 10, 30 and 60 s for the quantification of the Minocycline effect on cell adhesion. After each force cycle, the cell was allowed a recovery time larger than the contact time.

7.3. Results and discussion

7.3.1. AFM topography and roughness measurements

PDMS and PLGA films of, respectively, 100 *µ*m and 5 *µ*m thicknesses were used in all analyses. PS tissue-culture plates were used as controls. The materials preparation experimental procedure is presented in Appendix B.3.1. The morphologies of PS, PLGA and PDMS surfaces obtained by AFM are shown in Figure 7.4A. All surfaces exhibit a smooth morphology with a saturated root-mean-square (*rms*) roughness <4 nm (Figure 7.4B). PLGA and is the smoothest among the six materials, with *rms* roughness values below 1 nm. The *rms* roughness values obtained for PDMS and PS are respectively, 2.5 nm and 2.9 nm. Particularly, the surface topography analysis of PLGA revealed the presence of cavities with diameters ranging from 50-300 nm and depths of 30-70 nm.

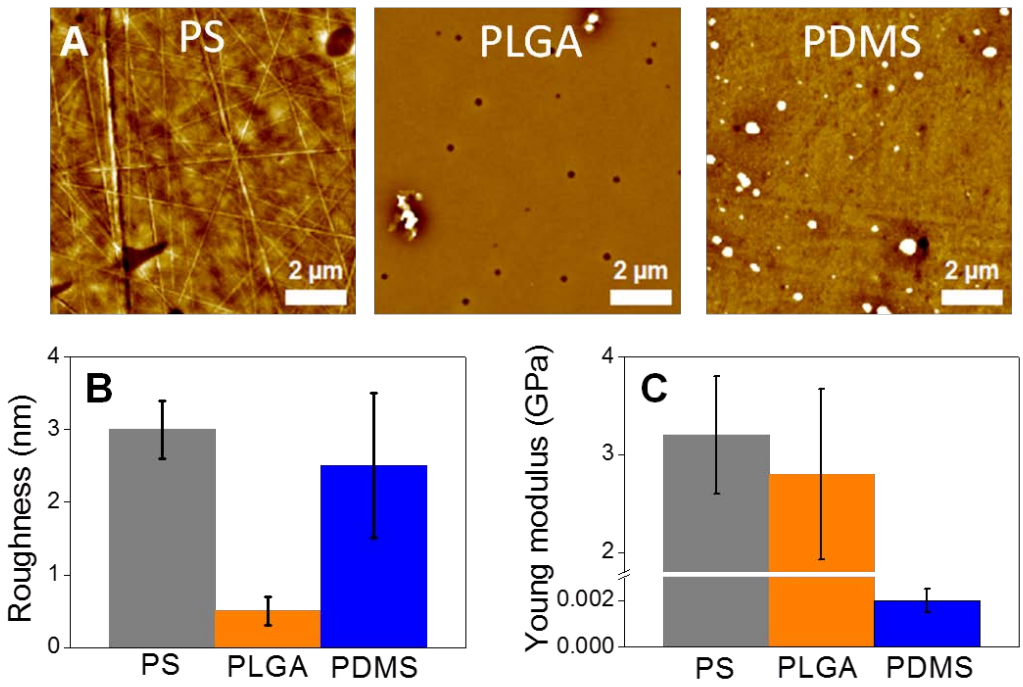

Figure 7.4. A: Amplitude modulation AFM images of PS, PLGA, and PDMS. B: Root-mean-square (*rms*) roughness values obtained from AFM images of the different surfaces as from A. C: Young modulus values of the materials in A.

7.3.2. Nanomechanical analysis

The nanomechanical properties of PS, PLGA and PDMS displayed in Figure 7.4C were measured by AFM-based nanomechanical spectroscopy. PLGA has a Young modulus of 2.7 GPa and bears some similarity with PS, which is slightly stiffer at 3.2 GPa. At variance with PLGA and PS, PDMS, is a more deformable material displaying a Young modulus three orders of magnitude lower, respectively 2.5 MPa.

7.3.3. Evaluation of mononuclear phagocytes interaction with polymeric substrates by optical microscopy

To evaluate the medium-term interaction of MPs with substrates, the number and morphology of adhering cells was quantified (see Appendix B.3.) MPs exhibit different morphologies: small and rounded when plated on PDMS, large and spread when plated on PLGA and PS (Figure 7.5A). Significant differences are observed in the number of cells adhering to the studied materials, with PDMS showing the lowest and PLGA the highest numbers of adhering MPs both after 1 hour (*data not shown*) and 24 hours *in vitro* (Figure 7.5B), respectively. As the fraction of proliferating cells was only about 1-2% (over total plated), we confirm that the above difference depends on the different adhesive response of MPs, and not on the proliferation rates, consistently with previous observations on organic thin films. [40]

The MPs morphology was evaluated by estimating the average projected area of the cells (Figure 7.5C) and their elongation factor (Figure 7.5D), a parameter that has been previously associated with the functional state of MPs. [12] Cell adhesion and migration are also accompanied by the formation of filopodia, thin spike-like cytoplasmic outgrowth containing bundles of parallel actin filaments that act as *fingers* probing the microenvironment in adhering/migrating cells. [41] PLGA promoted extensive formation of filopodia, while PDMS showed an opposite effect leading to smooth cell contours (Figure 7.5E).

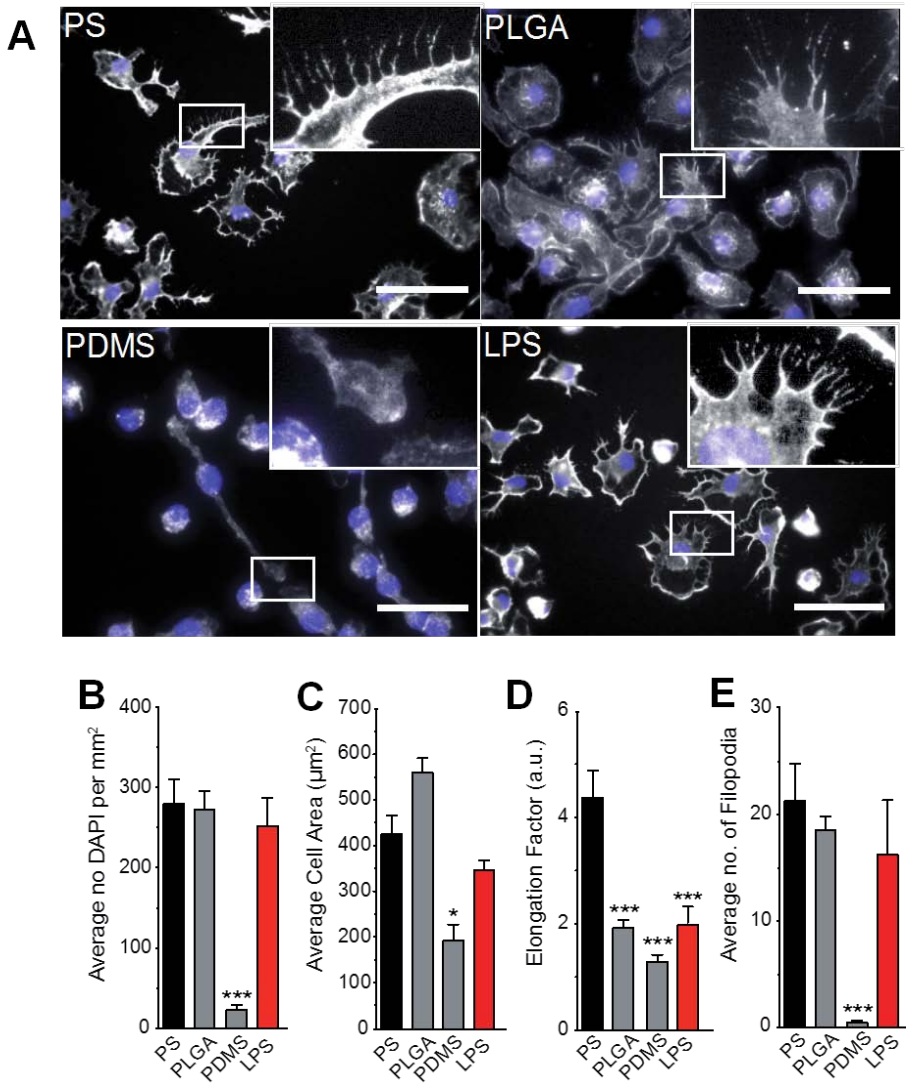

Figure 7.5. A: Immunofluorescence images of MPs adhering to PS and polymer films *in vitro* 24 hours after plating (scale bar: 50 µm). Insets evidence the development of filopodia. Cytoskeleton is labelled with Phalloidin (grey) and nuclei are labelled with DAPI (blue). Quantification of morphological features of MPs adhered to different substrates: B: number of adherent cells, C: average cell area, D: elongation factor and E: number of filopodia. LPS-activated MPs were used as positive controls (red bars).

7.3.4. Cell adhesion forces on PLGA and PDMS

To elucidate the interactions occurring between MPs and polymer films we performed SCFS measurements in a serum-free setting. In our approach the cantilever is amino-functionalized and coated with fetal bovine serum. Then a

single MP is adhered to the end of the cantilever, with the aim of measuring the force as a function of the probe-surface distance (force curve). As previously mentioned in Section 7.1.2.1 of this chapter, the analysis of force curves recorded while detaching a single MP from the substrate suggests a complex interaction characterized by (1) a sharp increase of the adhesion force corresponding to the elastic stretching of the entire cell; (2) a sequence of de-adhesion steps attributed to the unbinding of cell membrane proteins from the surface; (3) a region of plateaus of constant force extending around 1000 nm distance due to the detachment from the surface of micrometer-long membrane tethers; (4) a complete detachment of the cell from the surface (Figure 7.6A).

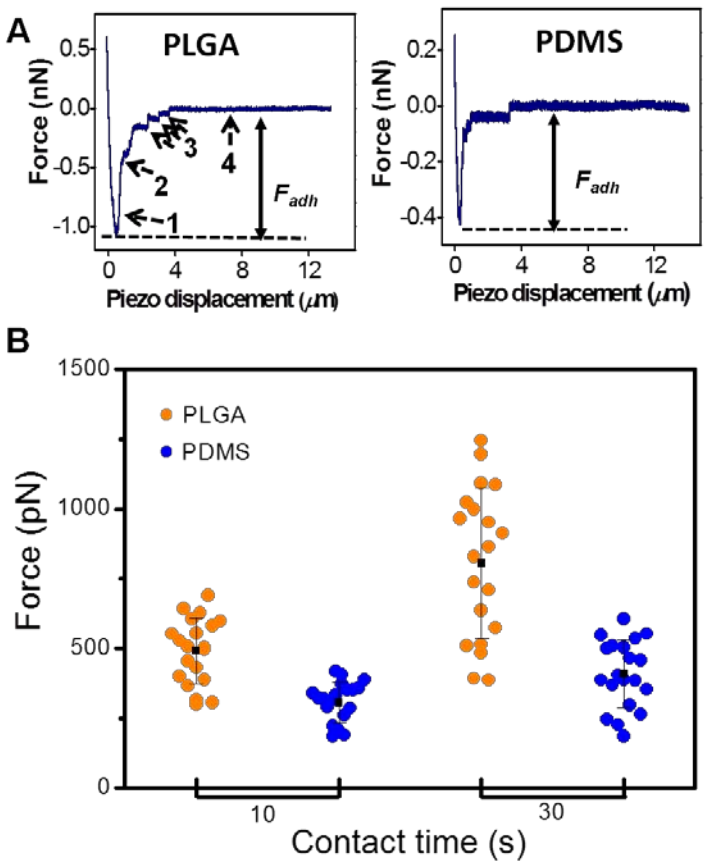

Figure 7.6. A: Typical force curve (retraction or unloading part) from representative SCFS experiments on PLGA and PDMS. B: Quantification of adhesion force (pN) on PLGA (orange dots) and PDMS (blue dots) samples, at two different contact times (10 and 30 s). At least 20 cells were tested in alternating measurements for each material. The adhesion force increases with the contact time on both interfaces.

To compare the strength of adhesion on PLGA and PDMS, we also measure the adhesion forces of MPs for contact times of 10 and 30 s (Figure 7.6B). The data set includes 20 cells and each measurement involves acquisition and average of 10 force curves per each contact time. For both materials the adhesion force increases with contact time, although the tendency is more marked for PLGA. We measured >1.5-fold higher adhesion forces on PLGA (492 $\pm$ 118 pN at 10s and 805 $\pm$ 269 pN at 30s) than PDMS (306 $\pm$ 73. pN at 10s and 409 $\pm$ 121 pN at 30s). We also observe a larger standard deviation on PLGA than on PDMS. The variation coefficients (ratio of standard deviation to mean) on PDMS and PLGA are comparable (0.23 at 10 s, 0.3 at 30 s). This indicates that the force curves measured between MPs and PDMS result from similar interactions and the greater mean and dispersion in the case of PLGA arise from an increasing number of the adhesion proteins in the extracellular membrane expressed by the MP interacting with PLGA. This could be a consequence of three-dimensional surface of PLGA, which displays protrusions of 30-70 nm in depth and 0.1-0.3 μm in diameter.

We observe a direct correlation between MPs adhesion, the elastic modulus of the substrate and the topography features. Hence, our SCFS and optical microscopy analyses findings hint that a soft and smooth material like PDMS will be less immunogenic than PLGA.

7.3.5. Quantification of the Minocycline effect on mononuclear phagocytes adhesion

One of the possible strategies to overcome foreign body reaction consists in the release of drugs with anti-inflammatory properties. Minocycline is a Food and Drug Administration (FDA) approved drug known to have central nervous system anti-inflammatory properties, via inactivation of microglial cells[42]. Interestingly Minocycline has also been proved to have neurorestorative[43] as well as neuroprotective properties[44]. Recently, Minocycline which was shown to supress Interleukin-6 receptors and prevent the migration, invasion and

adhesion capacity of ovarian cancer cells[45, 46]. To the best of our knowledge the efficacy of Minocycline in reducing FBR has never been tested before. Based on the above observations, and the relevance of PLGA for the fabrication of bioresorbable implants, we test the effects of Minocycline on the adhesion of MPs on PLGA.

MPs were seeded on PLGA and treated for 24h with two different doses (10 *μ*M and 50 *μ*M) of Minocycline. We analyzed the possible effect of Minocycline on the adhesion of MPs to PLGA by quantifying at the number of filopodia after 24h of contact. As shown in Figures 7.7 and 7.8**,** 50 *μ*M Minocycline is effective in reducing the formation of filopodia of MPs seeded on PLGA, while 10 *μ*M Minocycline had little effect.

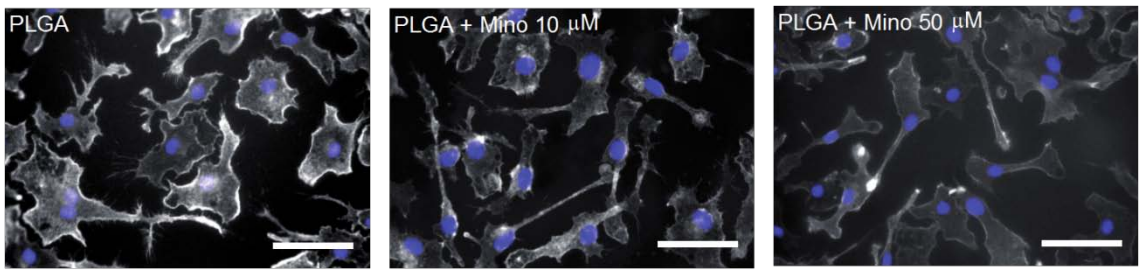

Figure 7.7. Immunofluorescence images of MPs adhering to PLGA without Minocycline (left), 10 µM Minocycline (center), and 50 µM Minocycline (right) after 24 hours in vitro. Cytoskeleton is labeled with Phalloidin (grey) and nuclei are labeled with DAPI (blue). Scale bar: 50 µm.

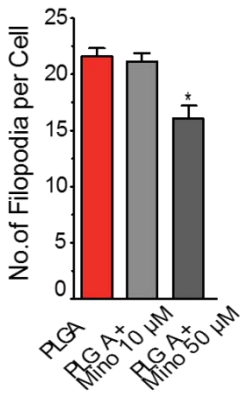

7.8. Quantification of filopodia formation 24 hours after plating on PLGA and PLGA + Minocycline.

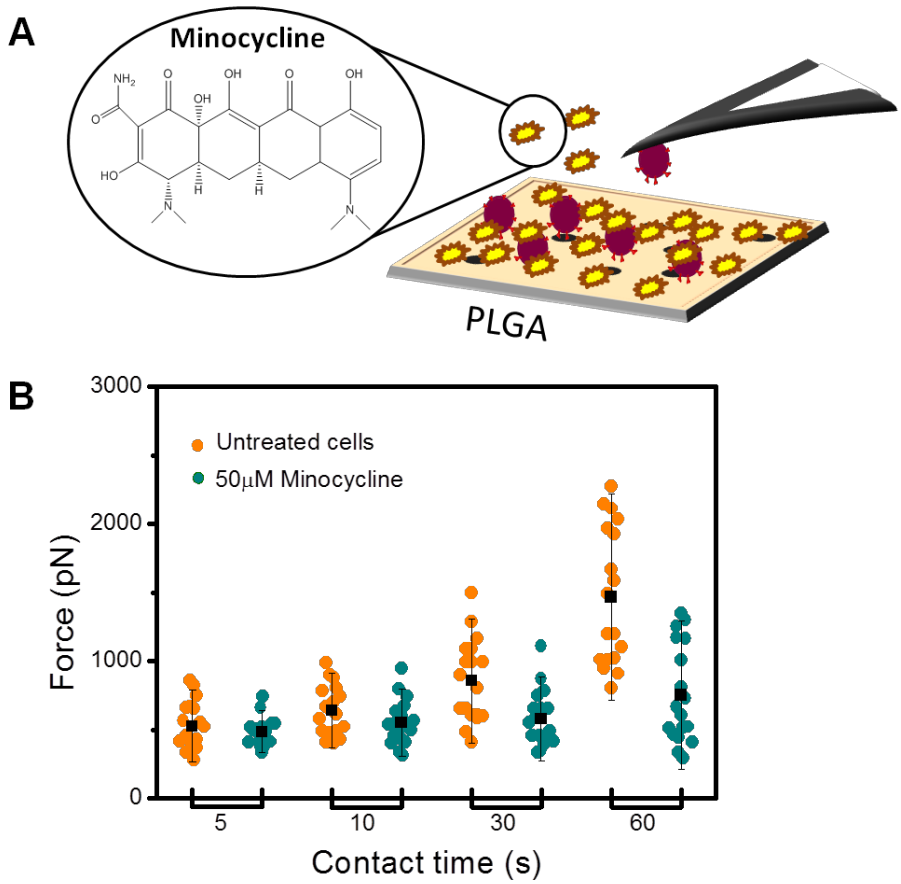

Figure 7.9. A: Schematic of SCFS experiment with Minocycline-treated cells. The administration of Minocycline was done every 12 hours prior to SCFS measurements. B: SCFS-based quantification of adhesion force to PLGA: control (orange) *vs*. Minocycline-treated (green) MPs at 5, 10, 30 and 60 seconds after contact

In order to have a quantitative evaluation of the influence of Minocycline on the adhesion of MPs to PLGA, we applied SCFS to study the adhesion forces of both treated (every 12 h prior to the measurement) and untreated cells. To avoid data variability due to cell heterogeneity issues, both treated and untreated cells included in this analysis belonged to the same batch and were seeded and measured the same day. A schematic of the Minocycline SCFS experimental setup is depicted in Figure 7.9A. Minocycline-treated MPs were analyzed by SCFS at increasing contact times of 5, 10, 30 and 60 s on PLGA. The data set includes $n \geq 17$ cells and $n \geq 3$ force curves per contact time. Figure 7.9B shows the adhesion force as a function of the contact time for untreated and

Minocycline-treated cells. The mean value of the adhesion force at 5 s seems not to be influenced by the Minocycline treatment. However, significant differences are recorded for longer contact times. The adhesion force of untreated cells shows a three-fold increase with time (527 ± 174 pN at 5s and 1469 ± 502 pN at 60 s), while the mean value of Minocycline-treated cells remains almost constant in the 5-30 s range (486± 101 pN at 5 s and 578 ± 204 at 30s) with an increase at 60 s (754 ± 360 pN) which is not statistically significant. These results suggest that Minocycline effectively decreases the adhesion force between MPs and PLGA. Importantly, Minocycline did not affect MPs viability at any concentration tested. The finer mechanism behind the action of Minocycline is not accessible to our comparative experiment, and further studies are required. The outcome is that, albeit PLGA is clearly immunogenic, the FBR against PLGA can be reduced by the local supply of Minocycline.

7.4. Conclusions

A single-cell force spectroscopy method was implemented to study foreign body reaction and correlate it with the immunogenic profiles of mononuclear phagocytes. In the single-cell force spectroscopy experiments a single mononuclear phagocyte, linked at the end of an AFM cantilever was used to probe the adhesion forces between the cell and the polymer surface. The time evolution (1-60 s) of the adhesion force between the phagocyte and the polymer surface before and after the treatment with an immunosuppressive drug was studied. Specifically, Minocycline, a Federal Drug Administration (FDA)-approved third generation tetracycline with anti-inflammatory effects was used. The data presented here shows that the adhesion force values measured at the single cell level correlate to the immunogenic profiles obtained by analysis of morphology of the mononuclear phagocytes in culture medium.

In this multi-scale study, the existence of a correlation between the adhesion force of mononuclear phagocytes to synthetic polymer surfaces and their activation towards FBR *in vitro* was demonstrated. In particular, the large mean value and spread of the adhesion force is related to the pro-inflammatory response of the phagocytes. The action of an anti-inflammatory drug such as Minocycline on the MPs yields a decrease of their adhesive force, and hence inhibits the FBR induced by PLGA. Our evidence hints to the molecular basis of FBR, and clearly indicates that adhesion is a potential target to minimize the FBR against materials that are immunogenic *a priori*. SCFS coupled with mechanical, morphology and biomarkers analyses provides an effective tool to screen the immunogenic potential of materials and assess *in vitro* the efficacy of chemical or pharmacological treatments.

Numerous studies suggest that mechanical properties of the adhesion substrate have a strong influence on cell migration, adhesion and differentiation. These studies show that cells actively probe and respond to mechanical cues through differential signaling from integrin based molecular complexes[47]. A further step in elucidating the mechanism by which mononuclear phagocytes are activated towards FBR would be the study mechanotransduction on single-cell adhesion.

SCFS measurements could provide valuable information on the molecular mechanism by which Minocycline inhibits the immunogenic response of a material. In our present study, response recorded in the force distance curves in SCFS experiments includes the contribution of many different cell surface receptors. For a thorough analysis of the different receptors involved in the adhesion process, force distance curves can be recorded in the absence and presence of specific blocking agents. By correlating these results, the contribution of specific receptors to the adhesion process can be evaluated

7.5. References

1. S. N. Jayasinghe, *Biomatter*, 2013, **3**.
2. J. M. Anderson, A. Rodriguez and D. T. Chang, *Semin Immunol*, 2008, **20**, 86-100.
3. D. T. Luttikhuizen, M. C. Harmsen and M. J. Van Luyn, *Tissue engineering*, 2006, **12**, 1955-1970.
4. D. W. Grainger, *Nat Biotech*, 2013, **31**, 507-509.
5. C. Mazza and B. Malissen, in *How the Immune System Recognizes Self and Nonself: Immunoreceptors and Their Signaling*, ed. D. Kitamura, Springer Japan, Tokyo, 2008, DOI: 10.1007/978-4-431-73884-8_5, pp. 133-171.
6. C. J. Wilson, R. E. Clegg, D. I. Leavesley and M. J. Pearcy, *Tissue engineering*, 2005, **11**, 1-18.
7. M. Aschner, *Neurotoxicology*, 1998, **19**, 7-17; discussion 37-18.
8. P. Moshayedi, G. Ng, J. C. F. Kwok, G. S. H. Yeo, C. E. Bryant, J. W. Fawcett, K. Franze and J. Guck, *Biomaterials*, 2014, **35**, 3919-3925.
9. E. F. Irwin, K. Saha, M. Rosenbluth, L. J. Gamble, D. G. Castner and K. E. Healy, *Journal of Biomaterials Science, Polymer Edition*, 2008, **19**, 1363-1382.
10. R. J. Schutte, L. Xie, B. Klitzman and W. M. Reichert, *Biomaterials*, 2009, **30**, 160-168.
11. T. O. Collier, J. M. Anderson, W. G. Brodbeck, T. Barber and K. E. Healy, *Journal of Biomedical Materials Research Part A*, 2004, **69A**, 644-650.
12. F. Y. McWhorter, T. Wang, P. Nguyen, T. Chung and W. F. Liu, *Proc Natl Acad Sci U S A*, 2013, **110**, 17253-17258.
13. D. A. Joyce, A. Kloda and J. H. Steer, *Immunology and cell biology*, 1997, **75**, 345-350.
14. N. M. Vacanti, H. Cheng, P. S. Hill, J. D. T. Guerreiro, T. T. Dang, M. Ma, S. Watson, N. S. Hwang, R. Langer and D. G. Anderson, *Biomacromolecules*, 2012, **13**, 3031-3038.
15. J. S. Hayes, E. M. Czekanska and R. G. Richards, *Adv Biochem Eng Biotechnol*, 2012, **126**, 1-31.
16. A. L. Berrier and K. M. Yamada, *Journal of Cellular Physiology*, 2007, **213**, 565-573.
17. A. J. García, P. Ducheyne and D. Boettiger, *Biomaterials*, 1997, **18**, 1091-1098.
18. D. F. Kucik, in *Current Protocols in Cell Biology*, John Wiley & Sons, Inc., 2001, DOI: 10.1002/0471143030.cb0906s43.
19. P. Kollmannsberger and B. Fabry, *Review of Scientific Instruments*, 2007, **78**, 114301.
20. N. Walter, C. Selhuber, H. Kessler and J. P. Spatz, *Nano Lett.*, 2006, **6**, 398-402.
21. M. Andersson, A. Madgavkar, M. Stjerndahl, Y. Wu, W. Tan, R. Duran, S. Niehren, K. Mustafa, K. Arvidson and A. Wennerberg, *Review of Scientific Instruments*, 2007, **78**, 074302.
22. K. Sung, L. Sung, M. Crimmins, S. Burakoff and S. Chien, *Science*, 1986, **234**, 1405-1408.
23. J. Helenius, C. P. Heisenberg, H. E. Gaub and D. J. Muller, *J Cell Sci*, 2008, **121**, 1785-1791.
24. M. Benoit, D. Gabriel, G. Gerisch and H. E. Gaub, *Nat Cell Biol*, 2000, **2**, 313-317.
25. Y. F. Dufrene, D. Martinez-Martin, I. Medalsy, D. Alsteens and D. J. Muller, *Nat Meth*, 2013, **10**, 847-854.
26. J. Beckmann, R. Schubert, R. Chiquet-Ehrismann and D. J. Müller, *Nano Lett.*, 2013, **13**, 2937-2946.
27. E. A. Evans and D. A. Calderwood, *Science*, 2007, **316**, 1148-1153.
28. A. V. Taubenberger, D. W. Hutmacher and D. J. Muller, *Tissue Eng Part B Rev*, 2014, **20**, 40-55.

29. L. Dao, C. Gonnermann and C. M. Franz, *Journal of Molecular Recognition*, 2013, **26**, 578-589.
30. D. Alsteens, P. Van Dijck, P. N. Lipke and Y. F. Dufrene, *Langmuir*, 2013, **29**, 13473-13480.
31. V. Kesherwani and A. Sodhi, *Nitric Oxide*, 2007, **16**, 294-305.
32. K. G. Sundqvist, P. Otteskog, L. Wanger, R. Thorstensson and G. Utter, *Experimental Cell Research*, 1980, **130**, 327-337.
33. I. R. Minev, P. Musienko, A. Hirsch, Q. Barraud, N. Wenger, E. M. Moraud, J. Gandar, M. Capogrosso, T. Milekovic, L. Asboth, R. F. Torres, N. Vachicouras, Q. Liu, N. Pavlova, S. Duis, A. Larmagnac, J. Voros, S. Micera, Z. Suo, G. Courtine and S. P. Lacour, *Science*, 2015, **347**, 159-163.
34. A. Campana, T. Cramer, D. T. Simon, M. Berggren and F. Biscarini, *Adv Mater*, 2014, **26**, 3874-3878.
35. S.-K. Kang, R. K. J. Murphy, S.-W. Hwang, S. M. Lee, D. V. Harburg, N. A. Krueger, J. Shin, P. Gamble, H. Cheng, S. Yu, Z. Liu, J. G. McCall, M. Stephen, H. Ying, J. Kim, G. Park, R. C. Webb, C. H. Lee, S. Chung, D. S. Wie, A. D. Gujar, B. Vemulapalli, A. H. Kim, K.-M. Lee, J. Cheng, Y. Huang, S. H. Lee, P. V. Braun, W. Z. Ray and J. A. Rogers, *Nature*, 2016, **advance online publication**.
36. A. San Paulo and R. García, *Physical Review B*, 1999, **60**, 4961-4967.
37. E. T. Herruzo and R. Garcia, *Applied Physics Letters*, 2007, **91**, 3.
38. H.-J. Butt, B. Cappella and M. Kappl, *Surface Science Reports*, 2005, **59**, 1-152.
39. I. N. Sneddon, *International Journal of Engineering Science*, 1965, **3**, 47-57.
40. I. Tonazzini, E. Bystrenova, B. Chelli, P. Greco, P. Stoliar, A. Calo, A. Lazar, F. Borgatti, P. D'Angelo, C. Martini and F. Biscarini, *Biophys J*, 2010, **98**, 2804-2812.
41. P. K. Mattila and P. Lappalainen, *Nat Rev Mol Cell Biol*, 2008, **9**, 446-454.
42. F. Giuliani, W. Hader and V. W. Yong, *Journal of Leukocyte Biology*, 2005, **78**, 135-143.
43. R. L. Rennaker, J. Miller, H. Tang and D. A. Wilson, *Journal of Neural Engineering*, 2007, **4**, L1.
44. J. M. Plane, Y. Shen, D. E. Pleasure and W. Deng, *Archives of Neurology*, 2010, **67**, 1442-1448.
45. P. Ataie-Kachoie, D. L. Morris and M. H. Pourgholami, *PLoS One*, 2013, **8**, e60817.
46. F. Regen, I. Heuser, I. Herzog and J. Hellmann-Regen, *Urology*, **83**, 509.e501-509.e506.
47. B. Geiger, J. P. Spatz and A. D. Bershadsky, *Nat Rev Mol Cell Biol*, 2009, **10**, 21-33.

Conclusions

1. Different tip-functionalization procedures have been designed in order to measure the interactions between an antibody and its specific antigen, the components of a siRNA delivery system (siRNA and a dendrimer) or cells and polymeric materials. The chemical sequence of the functionalization process involves three main steps: (i) chemical functionalization of the AFM tip in order to make it readily available for reactions with a heterobifunctional linker, (ii) attachment of the ligand bearing a complementary functionality to one of the two ends of the heterobifunctional linker and (iii) tethering of the ligand-linker complex to the AFM tip. When using a single cell as probe, the cantilever functionalization should exploit either the high binding affinities of cell membrane receptors and their cognate ligands or electrostatic interactions between the extracellular matrix and proteins.

2. A method to discriminate between specific molecular recognition events and unspecific adhesion events in single-molecule force spectroscopy experiments was developed. Semi-automated software was developed using *Spyder - The Scientific PYthon Development EnviRonment* platform and the results are plotted as two-dimensional molecular recognition histograms. This greatly simplifies the analysis of the large amount of data obtained in single molecule force spectroscopy experiments. The method was further applied in all SMFS studies carried out in this thesis.

3. Single-molecule force spectroscopy was used to study the dissociation kinetics of a siRNA delivery system. The unbinding forces and energies between a single siRNA molecule and a polyamidoamine dendrimers deposited on a mica surface were measured. We found a high binding affinity of siRNA towards polyamidoamine dendrimers, with a binding probability of 45%. The data analysis method implemented in this thesis allowed the identification of three types of unbinding events, which are characterized by rupture forces and unbinding energies of 28 pN (0.709 eV),

38 pN (0.722 eV) and 50 pN (0.724 eV) at a loading rate of 1 nN/s. The distribution of the measured unbinding forces and distances suggests that siRNA interacts either with two of the three amino branches of one dendrimer or with two branches of adjacent dendrimers. The most frequent binding interaction, with an unbinding free energy of 0.724 eV indicates that siRNA lies flat on top of two dendrimer molecules. This configuration maximizes the electrostatic attractive interactions between siRNA and the dendrimers. The lower rupture force corresponds to a configuration that minimizes the siRNA-dendrimer interactions, while intermediate configurations are also possible (0.722 eV).

4. The information provided by single-molecule force spectroscopy is highly relevant for the design of future dendrimer-based siRNA delivery systems. According to our findings, the binding forces between the amino terminal groups located in the PAMAM branches and the phosphate groups in the siRNA molecules should be in the range of 25 to 50 pN for loading rates of about 1 nN/s. Such a binding strength will allow the siRNA dissociation from the dendriplex and an efficient transfection, while protecting the dendrimer from RNAse-mediated degradation at the same time. Our experimental data validates for the first time, the theoretical predictions made by molecular modelling on the binding energies between dendrimers and siRNA at the single molecule scale.

5. The combination of single molecule force spectroscopy with electrical measurements by means of organic transistors allowed the rationalization of the response of an electrolyte-gated field effect transistor device. The detection of 5 nM of an anti-inflammatory cytokine, IL-4, with an EGOFET device was achieved. Two surface functionalization strategies were evaluated both by single-molecule force spectroscopy and electrical measurements: one based on the use of amino-terminated self-assembled monolayers and another one by means of His-Tagged Protein G.

6. Single force spectroscopy measurements detected a larger probability (30%) of unbinding events for the Protein G-based strategy with respect to 6-

aminohexanethiol-based one (10%). Furthermore, single force spectroscopy showed that the complexes formed on the Protein-G functionalized interface have a significantly higher lifetime (τ = 206 ± 103 s), than the ones formed on the 6-aminohexanethiol surface (τ = 4.78 ±1.6 s). Our measurements at the single molecule level prove how Protein G yields a more ordered antibodies layer, hence a higher coverage of active antibodies towards IL-4. The direct implementation of these Au electrodes in EGOFET architecture confirms different sensitivities as a function of the functionalization strategies. This comparative study meets the challenging task of correlating a mechanical nanoscale metrology that probes individual or a few antibody-antigen pairings with the electrical EGOFET response that involves a wide number of recognition events.

7. An extended single-molecule study, involving the combination of high resolution AFM, single molecule force spectroscopy and molecular dynamics simulations, revealed that immunoglobulin G antibodies adsorbed on graphene maintain their secondary structure and immunological activity. The experimental and theoretical results were in good agreement and showed that IgG antibodies adsorb strongly on graphene, do not unfold upon adsorption, and retain their secondary structure. We observed that most of the antibodies adsorb, even at small IgG-surface coverage densities, in vertical orientations that expose both Fab-binding sites for the specific binding to antigens.

8. The selective interaction of IgG antibodies deposited on graphene with their specific antigens was measured by single molecule force spectroscopy. Our experiments confirmed that IgG antibodies immobilized on graphene retain their immunological activity. All of these features, preservation of the secondary structure, strong protein anchoring, vertical adsorption orientations, and immunological recognition are key properties to develop very sensitive graphene-based immunological biosensors.

9. Nanomechanical spectroscopy mapping was implemented for the *in situ* study of the early stages of the evolution of biodegradable polymeric

structures upon immersion in a biological buffer. We quantified the evolution of the morphological and mechanical properties of PLGA micropillars and found the degradation process to be characterized by four stages. A fast swelling accompanied by a sharp decrease of the Young modulus mark the first stage. By correlating the experimental results with a theoretical polymer swelling model, we hypothesize that a solvent diffusion process is taking place, where the diffusion coefficient *D* depends on the solvent concentration *C*. The solvent uptake is favoured in the already solvated polymer chains leading to a fast increase of the free volume. In the second stage, a relaxation process characterized by the rearrangement of the polymers chains is observed. The PLGA patterns decrease in size to reach a local minimum in the volume. The relatively slow volume decrease in this regime is associated with the polymer response to the stress caused by the presence of the solution. The Young modulus keeps decreasing but at a slower rate. After the stress is dissipated by the viscous flow of the polymer, the polymer is ready to accept more solvent and a second swelling occurs (third stage). Here the Young modulus also shows a sharper decrease rate. After this stage, the volume shows a steady decrease, which is interpreted, as the start of the full degradation of the PLGA. The Young modulus shows a tendency to decrease but it is less evident than in the previous stages. At the end of observation process the Young modulus has decreased by almost three-orders of magnitude from an initial value of 2.4 GPa to 9 MPa.

10. The observed results while studying PLGA degradation are a consequence of three different processes, coupled diffusion-swelling, degradation and erosion. The coupled diffusion-swelling process lasts about 1 week. The presence of a second peak in the volume and roughness indicates a competition between swelling and hydrolytic degradation of the ester bonds, the latter a thermally activated process that happens at a slower rate than water adsorption. The significant fluctuations of the surface roughness together with the decrease of the Young modulus could have implications on cells adherence and proliferation.

11. Single-cell force spectroscopy was implemented to study foreign body reaction towards polymeric materials used in regenerative medicine, such as PDMS and PLGA. SCFS was combined with the immunogenic profiling of mononuclear phagocytes and the characterization of material properties at the nanoscale. We observed that adhesion force values measured at the single cell level correlate to the immunogenic profiles obtained by analysis of morphology of the mononuclear phagocytes in culture medium. In our study, we found a relationship between the adhesion force of mononuclear phagocytes to synthetic polymer surfaces and their activation towards FBR *in vitro*.

12. The time evolution at short time scales (1-60 s) of the adhesion force between a mononuclear phagocyte and the polymer surface before and after the treatment with an immunosuppressive drug was studied. Specifically, Minocycline, a Federal Drug Administration (FDA)-approved third generation tetracycline with anti-inflammatory effects was used. The action of an anti-inflammatory drug such as Minocycline on the MPs yields a decrease of their adhesive force, and hence inhibits the FBR induced by PLGA. Our evidence hints to the molecular basis of FBR, and clearly indicates that adhesion is a potential target to minimize the FBR against materials that are immunogenic *a priori*. SCFS coupled with mechanical, morphology and biomarkers analyses provides an effective tool to screen the immunogenic potential of materials and assess *in vitro* the efficacy of chemical or pharmacological treatments.

Conclusiones

1. Se diseñaron distintos procedimientos para la funcionalización de la punta de AFM con el objetivo de medir varios tipos de interacciones, como anticuerpo-antígeno, interacciones entre los componentes de un sistema para la entrega celular de acido ribonucleico pequeño de interferencia (siRNA) o bien para medir la adhesión entre células y materiales poliméricos. La secuencia química del proceso de funcionalización tiene tres pasos principales: (i) la funcionalización química de la punta para facilitar la reacción con un enlazador bifuncional, (ii) la reacción de un ligando con una funcionalidad del enlazador bifuncional y (iii) el anclaje del complejo enlazador-ligando a la punta de AFM. Cuando se usa una célula para funcionalizar la micropalanca, se debe de explotar la alta afinidad entre los receptores membranares y sus correspondientes ligandos o las interacciones electrostáticas entre la matriz celular y proteínas.

2. En esta tesis se desarrolló un método para discriminar entre eventos específicos de reconocimiento molecular y eventos no específicos en experimentos de microscopia de fuerza a nivel de moléculas individuales. En particular, se desarrolló un software semiautomático con la plataforma *Spyder - The Scientific PYthon Development EnviRonment* para analizar los datos y representarlos en histogramas bidimensionales de reconocimiento molecular. Este procedimiento simplifica el análisis de datos obtenidos en experimentos de espectroscopia de fuerza, ya que se conoce que la cantidad de datos generada en este tipo de medidas hace el análisis manual una tarea casi imposible. El método se utilizó para analizar todos los datos de SMFS presentados en esta tesis.

3. Se realizaron experimentos de espectroscopia de fuerza a nivel de moléculas individuales para estudiar la cinética de disociación de un

sistema de entrega de material genético capaz de realizar transcripción genética. Se midieron las energías y las fuerzas de disociación de un complejo formado por una sola molécula de acido ribonucleico pequeño de interferencia y dendrímeros de poliamidoamina (PAMAM) depositados sobre una superficie de mica. Se encontró una alta afinidad de unión de siRNA hacia el dendrímero de poliamidoamina, con una probabilidad de unión del 45%. El método de análisis de datos implementado en esta tesis permitió la identificación de tres tipos de eventos de disociación, que se caracterizan por las fuerzas de ruptura y energías de disociación de 28 pN (0.709 eV), 38 pN (0.722 eV) y 50 pN (0.724 eV) a una carga de 1 nN/s. La distribución de fuerzas y distancias de disociación medidas sugiere que el siRNA interactúa, ya sea, con dos de los tres grupos amino de un dendrímero o con dos grupos amino perteneciendo a dendrímeros adyacentes. La interacción de unión más frecuente, con una energía libre de disociación de 0.724 eV, indica que el siRNA yace en forma plana sobre la parte superior de dos moléculas de dendrímero. Esta configuración maximiza las interacciones atractivas electrostáticas entre el siRNA y los dendrímeros. La fuerza de ruptura inferior corresponde a una configuración que reduce al mínimo las interacciones siRNA-dendrímero, mientras que las configuraciones intermedias también son posibles (0.722 eV).

4. La información proporcionada por la espectroscopia de fuerza a nivel de moléculas individuales es altamente relevante para el diseño de futuros sistemas de entrega de siRNA basados en dendrímeros. Por lo tanto, las fuerzas de unión entre los grupos amino terminales situados en las ramificaciones del dendrímero y los grupos fosfato en las moléculas de siRNA deben estar en el rango de 25 a 50 pN para una carga de aproximadamente 1 nN/s. Tal fuerza de unión permitirá la disociación del siRNA del dendrimero y una eficiente transfección, mientras que al mismo tiempo se sigue protegiendo el dendrímero de la degradación mediada por la ARNasa. Los datos experimentales validan por primera vez, las

predicciones teóricas del modelo molecular de energías de enlace entre dendrímeros y siRNA a la escala de una sola molécula.

5. La combinación de espectroscopia de fuerza a nivel de moléculas individuales con medidas eléctricas por medio de transistores orgánicos permite la racionalización de la respuesta de un transistor de efecto de campo con puerta electrolítica (EGOFET). Se logró la detección de 5 nM de una citocina anti-inflamatoria, IL-4, con un dispositivo de EGOFET. Se evaluaron dos estrategias de funcionalización de la superficie, tanto por espectroscopia de fuerza a nivel de moléculas individuales, como mediante medidas eléctricas: una basada en el uso de monocapas autoensambladas de aminos terminales (HSC_6NH_2) y otra mediante proteína G con etiquetas polihistidina (PG).

6. Las medidas de espectroscopia de fuerza detectaron una probabilidad mayor (30%) de eventos de disociación para la estrategia basada en PG con respecto a la de HSC_6NH_2 (10%). Por otra parte, la espectroscopia de fuerza mostró que los complejos formados en la interfaz funcionalizada con proteína-G tienen un tiempo de vida significativamente mayor (τ = 206 ± 103 s), que los que forman en la superficie del HSC_6NH_2 (τ = 4,78 ± 1,6 s). Nuestras mediciones a nivel de una sola molécula demuestran cómo la funcionalización con PG produce una capa de anticuerpos más ordenada y de allí, una mayor cobertura de anticuerpos activos hacia IL-4. La aplicación directa de estos electrodos de oro en la arquitectura de los EGOFET, confirma diferentes sensibilidades en función de las estrategias de funcionalización. Este estudio comparativo reúne la difícil tarea de correlacionar un método de metrología mecánica a nanoescala, que detecta uniones anticuerpo-antígeno individuales o de unas pocas moleculas, con la respuesta eléctrica del EGOFET, que implica un gran número de eventos de reconocimiento.

7. Un extenso estudio de espectroscopia de fuerza, que implica la combinación de AFM de alta resolución y simulaciones de dinámica molecular, reveló que los anticuerpos de inmunoglobulina G (IgG) adsorbidos sobre grafeno mantienen su estructura secundaria y la actividad inmunológica. Hay una buena correlación entre los datos experimentales y teóricos, que demuestran que los anticuerpos IgG se adsorben fuertemente en el grafeno y que no se produce desenrollamiento de los anticuerpos adsorbidos, conservandose su estructura secundaria. Hemos observado que la mayoría de los anticuerpos se adsorben, incluso a pequeñas densidades de IgG en la superficie, en orientaciones verticales que exponen ambos sitios de asociación de las regiones de unión Fab del anticuerpo para la unión específica al antígeno.

8. Los experimentos de espectroscopia de fuerza molecular demostraron además que los anticuerpos depositados son bioactivos, midiendo la interacción selectiva con sus antígenos específicos. Esto confirma que los anticuerpos depositados sobre grafeno conservan su actividad inmunológica. Todas estas características, la preservación de la estructura secundaria, el fuerte anclaje de proteínas, las orientaciones verticales de adsorción, y el reconocimiento inmunológico, son propiedades clave para desarrollar biosensores inmunológicos muy sensibles basados en el grafeno.

9. Se implementó la espectroscopia de fuerzas en modo de mapas nanomecánicas para el estudio *in situ* de la evolución de estructuras poliméricas biodegradables en las primeras etapas tras su inmersión en un tampón biológico. Se cuantificó la evolución de las propiedades morfológicas y mecánicas de micropilares de PLGA y encontramos que el proceso de degradación se caracteriza por cuatro etapas. Una

hinchazón rápida acompañada por una fuerte disminución del módulo de Young marca la primera etapa. Correlacionando los resultados experimentales con el modelo teórico del proceso de hinchazón del polímero, se postula, que en esta etapa, un proceso de difusión del disolvente está tomando lugar, donde el coeficiente de difusión D depende de la concentración de disolvente C. La absorción de disolvente se ve favorecida en las cadenas de polímero ya solventadas, lo que conduce a un rápido aumento del volumen libre. En la segunda etapa, se observa un proceso de relajación que se caracteriza por la reordenación de las cadenas poliméricas. Los patrones de PLGA disminuyen de tamaño para llegar a un mínimo local en el volumen. La lenta disminución del volumen en este proceso se asocia con la respuesta del polímero al estrés causado por la presencia de la solución. El módulo de Young sigue disminuyendo, pero a un ritmo más lento. Después de que el estrés se disipa por el flujo viscoso del polímero, el polímero está preparado para aceptar más disolvente y producir una segunda hinchazón (tercera etapa). Aquí, el módulo de Young también muestra una tasa de descenso más aguda. Después de esta etapa, el volumen muestra una disminución constante, lo que se interpreta como el inicio de la degradación completa del PLGA. El módulo de Young muestra una tendencia a disminuir, pero es menos evidente que en las etapas anteriores. Al final del proceso de observación, el módulo de Young se ha reducido en casi tres órdenes de magnitud desde su valor inicial de 2,4 GPa a 9 MPa.

10. Los resultados observados durante el estudio de la degradación del PLGA son una consecuencia de tres procesos diferentes, difusión-hinchazón, degradación y erosión. El proceso de difusión-hinchazón dura alrededor de 1 semana. La presencia de un segundo pico en el volumen y la rugosidad, indican una competencia entre la hinchazón y

la degradación hidrolítica de los enlaces éster. El último es un proceso activado térmicamente que ocurre a un ritmo más lento que la adsorción de agua. Las fluctuaciones significativas de la rugosidad de la superficie, junto con la disminución del módulo de Young podrían tener implicaciones en la adhesión y proliferación celular.

11. Se implementaron medidas de espectroscopia de fuerza a nivel de una célula individual (SCFS) para estudiar la reacción de un cuerpo extraño (FBR) hacia dos materiales poliméricos utilizados en la medicina regenerativa, tales como PDMS y PLGA. Los estudios de SCFS se combinaron con los perfiles inmunógenicos de fagocitos mononucleares y la caracterización de las propiedades de los materiales a nanoescala. Se observó que los valores de fuerza de adhesión medidos a nivel de células individuales se correlacionan con los perfiles inmunógenos obtenidos mediante el análisis de la morfología de los fagocitos mononucleares en medio de cultivo. En nuestro estudio encontramos una correlación entre la fuerza de adhesión de los fagocitos mononucleares (MP) a las superficies de polímero sintético, y su activación hacia el FBR *in vitro*.

12. Se midió la evolución de la fuerza de adhesión entre un fagocito mononuclear y la superficie del polímero, antes y después del tratamiento con un fármaco inmunodepresor, a escalas de tiempo cortas de 1-60 s. El fármaco inmunodepresor utilizado fue la minociclina, un fármaco de tercera generación de la familia de tetraciclinas aprobado por la Agencia Federal de Fármacos de EEUU (FDA), y que tienen acción anti-inflamatoria. La acción de un fármaco anti-inflamatorio como la minociclina sobre los MP, produce una disminución de su fuerza de adhesión, y por lo tanto inhibe la FBR inducida por el PLGA. Nuestras evidencias apuntan hacia la base molecular de FBR, indicando claramente que la adhesión es un objetivo potencial para reducir al mínimo la FBR contra los materiales que son inmunogénicos *a priori*. Los experimentos de SCFS junto con el análisis de propiedades

mecánicas, morfológicas y de biomarcadores proporcionan una herramienta eficaz para la detección del potencial inmunogénico de materiales, y para la evaluación *in vitro* de la eficacia de los tratamientos farmacológicos o químicos.

Appendix A

A.1. AFM tips functionalization protocols

A.1.1. Aminofunctionalization

Silicon nitride cantilevers are first cleaned thoroughly by immersion in a piranha solution (4 volumes of an aqueous solution of 70% sulphuric acid with 1 volume of a solution of 30% hydrogen peroxide) for 30 minutes. The cantilevers are then rinsed with ultrapure water and dipped into a solution of APTES:water:ethanol (volume ratio 5:5:90) for 45 minutes. The shelf life of APTES at room temperature is short and it should be replaced on a monthly basis. Finally, the cantilevers are rinsed with ethanol, water and dried with N_2. They can be stored in a glass dish for a few days at room temperature.

A.1.2. Tips functionalization with PEG-biotin

The functionalization is carried out in a Teflon reaction chamber, which can be obtained by drilling a circular hole with a perfectly flat bottom into a small Teflon block (1 cm diameter and 2 cm high). A suitable Teflon disk is required to cover the chamber.

First, 1 mg of Biotin-PEG-NHS is dissolved in 0.5 ml trichlorometane. The solution is transferred to the teflon reaction chamber and 30 μl triethylamine are added. Aminofunctionalized AFM cantilevers are immersed into the Teflon chamber. The chamber is covered and the cantilevers are incubated for 2 hours. Finally, the cantilevers are washed with trichloromethane 3 times to remove unreacted reagents and N_2 dried.

To prepare the avidin monolayer sample, a 1 mg/ml stock solution was dissolved in 1 mM NaCl to obtain a 0.1 mg/ml working solution. Next, a 60 μl drop of the 0.1 mg/ml avidin solution is deposited on a freshly cleaved mica

sheet for 15 minutes. The sample is rinsed 10 times with 1 mM NaCl and 3 times with 0.01 M PBS.

A.1.3. Tips functionalization with siRNA

A 250 mM heterobifunctional NHS-PEG_{24}-Mal linker stock solution is dissolved in PBS to a concentration of 1mM. APTES-functionalized AFM cantilevers are immersed into the PEG linker solution for 30 minutes at room temperature.

Finally, the AFM cantilevers functionalized with the PEG linker are immersed into a 2.5 μM thiol-siRNA solution for 12 hours at 4°C [1]. The tips are then rinsed with 10 mM HEPES and stored at 4°C in a glass dish until further use.

A.1.4. Tips functionalization with a protein

A sulfhydryl addition kit containing the following reactants: SATA (*N*-succinimidyl-S-acetylthioacetate), hydroxylamine·HCl, conjugation buffer stock (10X) and dimethylformamide from Thermo Fisher (Spain, Ref. 23460) is used.

First, free sulfhydryl groups are added to the protein. To this end, the protein is incubated with a10-fold molar excess of 8.65 mM SATA solution in DMF for 30 minutes at room temperature. To de-protect the latent sulfhydryl groups 2.5 µl of a 50 mg/mL Hydroxylamine·HCl in Conjugation Buffer Stock (10X) solution is added to the SATA-modified antigen solution. The solution is then incubated for two hours at room temperature. The de-protected sulfhydryl protein is then added to an equilibrated desalting column to remove non-reacted reagents. The maleimide conjugation buffer (1X) is added to the desalting column and 1 ml fractions are collected. The absorbance of each fraction is measured at 280 nm to locate the protein. Fractions containing most of the protein are then reacted with a 10-fold molar excess of PEG linker and incubated at 4°C overnight.

In the last step, amino-functionalized AFM tips are immersed in the PEG-antigen solution for two hours at room temperature. Finally, the tips are rinsed with 0.01 M PBS and stored at 4°C in a glass dish until further usage.

A.1.5. AFM cantilevers functionalization for single-cell force spectroscopy measurements

All reagents used for the cantilevers functionalization were purchased from Sigma Aldrich (Spain). Tipless cantilevers (NPO-10, Bruker, USA) were first amino-functionalized as described in Section A.1.1. Next, the amino-functionalized cantilevers were coated with FBS by immersion in 10% FBS at 4°C overnight, rinsed ten times in 0.01 M PBS (pH 7.4) and stored at 4°C in a glass Petri dish.

A.2. Biotin-avidin interaction study

A.2.1. Introduction and motivation

A test experiment was designed in order to evaluate the tip functionalization protocols used in this thesis. For this purpose, the interaction between biotin and avidin was studied with single-molecule force spectroscopy. The protocol in section A.1.2 of this appendix was used to carry out the tip functionalization and sample preparation.

The experiment has several particularities, which enabled us to assess our SMFS capabilities. First, it involves the study of the interaction between two biomolecular partners with a high affinity towards each other. Biotin is a very specific ligand of the tetrameric avidin protein. The dissociation constant of the system is $K_D \approx 10^{-15}$ M, which makes it one of the strongest receptor-ligand systems known so far[2]. The affinity is reduced when free biotin is linked to a PEG chain, however the dissociation time is still of the order of days.[3]

Second, the biotin-avidin system is one of the most widely studied in SMFS, which means that there is an important amount of literature data to compare our experimental results with.[4-6]

AFM tips were functionalized with PEG linkers bearing two functionalities: biotin at one end and NHS ester at the other (Figure A.1A). The NHS ester end is used to tether the PEG linker to the AFM tip, while the biotin end remains available for the interaction with avidin on the sample.

Two sets of AFM tips were functionalized with Biotin-PEG-NHS having either 18 or 27 ethylene glycol units (purchased from JKU Linz). The structure of the two Biotin-PEG-NHS molecules used in this work is depicted in Figures A.1B-C. The PEG18 molecule has a nominal length of 6 nm, while the PEG27 molecule is 9 nm long. This makes for a total length of 10 nm for the Biotin-PEG18-NHS complex and 14 nm long for Biotin-PEG27-NHS.

Once the tip is functionalized with biotin, avidin is immobilized on a freshly cleaved mica sheet by electrostatic adsorption at neutral pH. Avidin adsorption is particularly strong and fast at low ionic strength, so low concentrations of NaCl (1 mM) should be used to form the avidin monolayer.

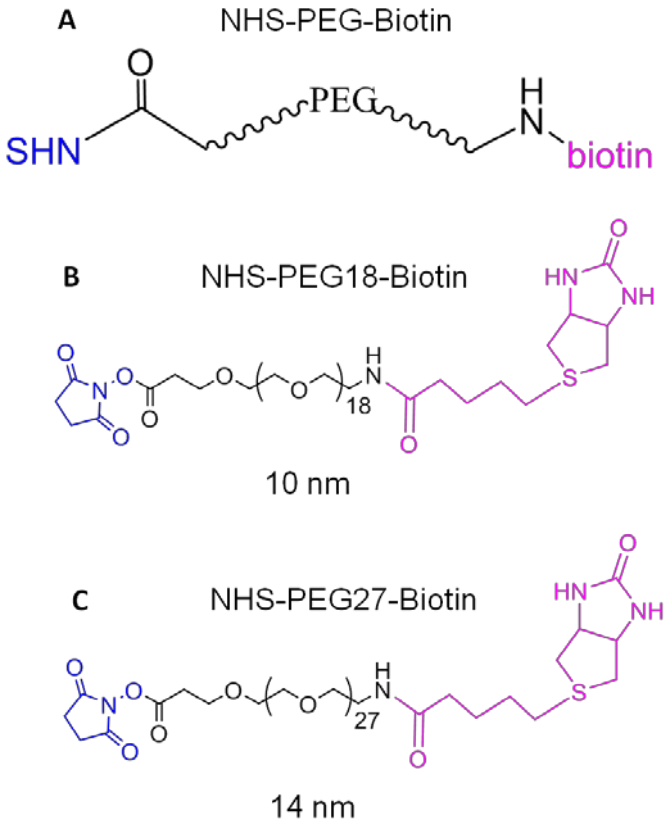

Figure A.1: Structure of the linkers used to tether biotin residues to the amino-functionalized AFM tip. A: generic Biotin-PEG-NHS linker. B: Biotin-PEG18-NHS linker. C: Biotin-PEG27-NHS linker.

A.2.2. Experimental setup

Single molecule force spectroscopy experiments were performed in contact mode either with a Nanowizard III (JPK, Germany) or a Cypher (Asylum Research, Santa Barbara) microscope. The experiments were conducted in PBS 0.01 M with triangular silicon nitride MCST cantilevers (Bruker, Santa Barbara) with a nominal spring constant *k* of 0.02 N/m and resonant frequency of 2 kHz. The force constant and quality factor were determined as described in Chapter 3.2.3 by using the thermal noise method[7,8].

For the data acquisition, the maximum force was maintained below 250 pN to avoid any irreversible damage to the molecules bound to the tip apex. Several force maps covering 1 μm x 1 μm regions of the sample (32 x 32 data points) were acquired for each functionalized tip. To record a typical force curve, the tip was approached and retracted 100 nm from the sample at a speed of 400 nm/s and it was kept in contact with the sample for 0.5 s to facilitate the formation of antibody-antigen complexes. The loading rate was calculated as the slope of the force versus time curve before the unbinding jump to surface event.
A total of 1500 force curves were recorded with each AFM tip and they were analyzed with a customized software described in Chapter 3.2.4.

A.2.3. Results and discussion

Biotin-avidin single-molecule interactions were measured using AFM tips functionalized with PEG-Biotin complexes of different nominal lengths (see Figures A.1B-C). The results are depicted in Figure A.2, where two dimensional molecular recognition maps were used to display the results. In Figure B.2A, the results corresponding to the PEG18-Biotin linker are presented, while Figure B.2B shows the results for the PEG27-Biotin linker. We observe that both functionalizations render molecular recognition events of similar unbinding force, as follows: 35±5 pN for PEG18-Biotin and 38±8 pN for PEG27-Biotin. These unbinding forces observed here, at a loading rate of 1 nN/s are in good agreement with previous studies of the biotin-avidin system at the same loading

rate[5, 6, 9]. By looking at the unbinding distances, we observe that they are in the expected range. Specifically, we found unbinding distances of 10±2 nm and 14±3 nm for the PEG18-Biotin and PEG27-Biotin linker functionalization, respectively.

The binding probability is 5% for the PEG18-Biotin functionalization, as compared to 8% for the PEG27-Biotin functionalization. This could be related to the higher orientational freedom of the PEG27-bound biotin, as compared to the biotin molecule linked to the shorter PEG18 tether.

The experiments performed with the PEG18-Biotin and PEG27-Biotin linkers provided clear-cut data, which proves that our functionalization strategy and data analysis protocols are sound and reliable.

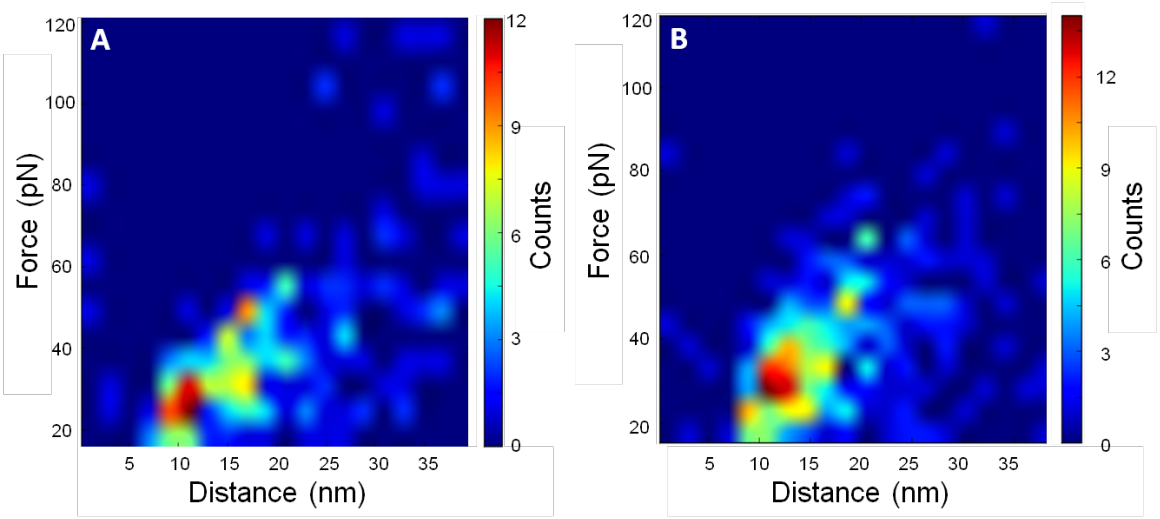

Figure 2. Two dimensional molecular recognition maps of biotin-avidin unbinding forces and distances. A: Tip functionalized with a 6 nm long PEG18-Biotin linker. B: Tip functionalized with a 9 nm long PEG27-Biotin linker. The most probable unbinding force for both functionalization strategis is ≈ 35pN at a loading rate of 1 nN/s. The unbinding distances are 10 nm and 14 nm for the PEG18-Biotin and PEG27-Biotin linker functionalization, respectively.

A.3. Reducing the number of unspecific and multiple interactions

The number and distribution of specific binding events in single molecule force spectroscopy (SMFS) experiments depends on the density and orientation of the molecules immobilized on the sample surface. However, experimental limitations in current state of the art SMFS make it difficult to draw a linear relationship between the number of active biological molecules on the sample and the number of the specific unbinding events. Specifically, the data interpretation is hampered by the presence of both unspecific and multiple simultaneous unbinding events. An efficient way to reduce the number of multiple unbinding events is by limiting the number of interactions between the tip and the sample. This can be achieved by using an extension of a statistical method proposed by Evans and Williams based on a Poissonian analysis of rupture forces[10].

By relating the fraction of specific adhesion events within a total sample of force measurements to a Poisson distribution, for a large number of recorded force curves, the probability of finding *n* bonds with a mean *N* is given by:

$$P(n,N) = e^{-N}\frac{N^n}{n!} \qquad \text{(A.1)}$$

Let the total number of recorded events N_{tot} be the sum of the specific adhesion events N_{adh} and unspecific events N_{unsp}:

$$N_{tot} = N_{adh} + N_{unsp} \qquad \text{(A.2)}$$

We consider the total number of specific adhesion events as the sum of all single N_1 and multiple N_i specific events:

$$N_{adh} = N_1 + \sum_{i=2}^{\infty} N_i \qquad \text{(A.3)}$$

The sum of all probabilities for which an adhesion event occurs ($n \neq 0$) gives the fraction of all possible adhesion events for any bond valence.

$$\sum_{n=1}^{\infty} e^{-N} \frac{N^n}{n!} = 1 - e^{-N} = \frac{N_{adh}}{N_{tot}} \quad \text{(A.4)}$$

So the mean number of bonds per contact is related to the fraction of adhesion events by:

$$N = \ln\left(\frac{N_{tot}}{N_{tot} - N_{adh}} \right) \quad \text{(A.5)}$$

With this solution for *N*, we can solve Eq.1 for $P(n=1, N)$ to find the fraction of single events out of the total number of recorded samples:

$$\frac{N_1}{N_{tot}} = \left(1 - \frac{N_{adh}}{N_{tot}} \right) \ln\left(\frac{N_{tot}}{N_{tot} - N_{adh}} \right) \quad \text{(A.6)}$$

The fraction of single bonds out of the number of successful adhesion events is $P(n=1, N) / \left(\frac{N_{adh}}{N_{tot}} \right)$

$$\frac{N_1}{N_{adh}} = \left(\left(\frac{N_{adh}}{N_{tot}} \right)^{-1} - 1 \right) \ln\left(\frac{N_{tot}}{N_{tot} - N_{adh}} \right) \quad \text{(A.7)}$$

Our purpose is to record a high proportion of single adhesion events, so let the number of single adhesion events N_1 be 90% of the total number of specific adhesion events N_{adh}:

$$\frac{N_1}{N_{adh}} = 0.9 \qquad \text{(A.8)}$$

We can now extract the corresponding ratio of adhesion events frequency from Eq.A.7:

$$\frac{N_{adh}}{N_{tot}} = 0.18 \qquad \text{(A.9)}$$

Therefore, in order for the majority (90%) of the specific unbinding events detected in our SMFS experiments to be single events, the number of specific events should account for 18% of the total number of recorded events. In

practice, this is accomplished by adjusting the experimental parameters (i.e. by selecting an AFM cantilever with a very sharp tip, limiting the contact time, low density of ligands on the AFM tip etc).

A.4. References

1. A. Fuhrmann, J. C. Schoening, D. Anselmetti, D. Staiger and R. Ros, *Biophysical journal*, 2009, **96**, 5030-5039.
2. N. Michael Green, in *Methods in Enzymology*, eds. W. Meir and A. B. Edward, Academic Press, 1990, vol. Volume 184, pp. 51-67.
3. K. Kaiser, M. Marek, T. Haselgrübler, H. Schindler and H. J. Gruber, *Bioconjugate Chemistry*, 1997, **8**, 545-551.
4. V. T. Moy, E. L. Florin and H. E. Gaub, *Science*, 1994, **266**, 257-259.
5. R. Merkel, P. Nassoy, A. Leung, K. Ritchie and E. Evans, *Nature*, 1999, **397**, 50-53.
6. F. Rico and V. T. Moy, *Journal of Molecular Recognition*, 2007, **20**, 495-501.
7. J. Hutter and J. Bechhoefer, *Review of Scientific Instruments*, 1993, **64**, 1868–1873.
8. H. J. Butt and M. Jaschke, *Nanotechnology*, 1995, **6**, 1.
9. R. De Paris, T. Strunz, K. Oroszlan, H.-J. Güntherodt and M. Hegner, *Single Molecules*, 2000, **1**, 285-290.
10. E. Evans and P. M. Williams, eds., *Physics of Bio-Molecules and Cells*, Springer and EDP Sciences, Heidelberg, 2002.

Appendix B

Contributions of collaborators

B.1. EGOFET fabrication and electrical characterization

The work presented in this section is related to the findings presented in Chapter 4 of this thesis and it was carried out by Stefano Casalini, Francesca Leonardi, Carlo Bortolotti, Alessandra Campana and Tobias Cramer in Fabio Biscarini's group at the University of Modena and Reggio Emilia and CNR, Italy.

B.1.1. EGOFET fabrication

Electrolyte-gated organic field-effect transistor (EGOFET) devices were prepared onto gold-coated glass slides purchased from Phasis (Switzerland). The substrates are made of quartz glass (1 mm thick) and a gold layer of 50 nm plus few nm of titanium as adhesive layer. Each test-pattern bears 4 transistors, whose channel length is 15 μm and channel width equal to 27 mm. The fabrication was carried out by laser ablation with a short-pulsed Nd:YAG infrared (IR)-laser supplied by a laser scan marker (Scriba Nanotecnologie, Italy). The IR-Laser pulse frequency and intensity were optimized in order to find the best compromise between the removal of the Au layer and roughening of the underlying quartz. Typical operation was performed at a laser power of 8300 W, a pulse of 10 ns and a frequency of 15500 Hz. The laser focus is moved over the surface at a scan-rate of 2000 μm/s. Details are described elsewhere[1].

The pentacene deposition was performed by thermal sublimation in ultra-high vacuum with base pressure of 5×10^{-8} mbar at a rate of 7.5 Å min^{-1} at room temperature. The pentacene was 15 nm thick (~10 monolayers, ML)[2].

B.1.2. Gate functionalization

6-aminohexanethiol (HSC_6NH_2) and glutaraldehyde were purchased from Sigma-Aldrich and used without further purification. Recombinant protein G (PG), monoclonal anti-murine IL-4 (anti-IL4) and recombinant murine IL-4 (a specific antigen for the anti-IL4 antibody, IL4) were produced by Biovision (San Francisco, USA). His-Tagged recombinant protein G lacks the albumin and cell membrane binding domains.

The gate electrode is a polycrystalline Au wire (diameter equal to 1 mm). First, this electrode underwent a standard cleaning procedure[2]: (i) immersion in a concentrated H_2SO_4 at 100°C for 1h; (ii) 20 cycles of electro-polishing by sweeping the potential from 0V to 1.5 V in H_2SO_4 (1 M).

The glutaraldehyde-based functionalization was performed by immersing the gold gate electrode in a 1 mM solution of 6-aminohexanethiol in ethanol overnight. The activation of the 6-aminohexanethiol self-assembled monolayer was achieved by immersion in a glutaraldehyde solution (2.5% v/v) for 1 h at 5°C. After rinsing with PBS 0.01 M, the functionalized substrate was immersed in a 0.25 mg/ml anti-IL4 solution for 90 minutes.

The protein G-mediated functionalization involved the immersion of the gold substrate in a 5 mg/ml solution of protein G in PBS 0.01 M for 10 minutes. The sample was then rinsed with PBS 0.01 M and immersed in a 0.25 mg/ml anti-IL4 solution for 90 minutes.

To establish the minimum detection level of IL4 in test solutions, the antibody-coated electrode was immersed in a buffer solution (10 mM PBS, pH 7.4) and a 5 nM IL-4 solution was injected.

B.1.3. Electrical measurements

All the electrical measurements were performed with home-built EGOFETs operated in a buffer solution (100 mM of PBS at pH≈7.4) mimicking the physiological conditions. The buffer solution was confined on top of the electronic transducer by means of a PDMS pool.

Source, drain and gate electrodes were connected to a Keithley 2612 Source Meter. The electrical response was acquired by means of a probe station. All the electrical measurements were carried out in ambient atmosphere. The I-V transfer characteristics were performed by sweeping the gate-source voltage (V_{GS}) from +0.2 V to -0.5 V while leaving the drain-source voltage constant at -0.5V (saturation regime) for the reference device. I-V output characteristics were measured by sweeping drain-source voltage (V_{DS}) from 0 V to -0.5 V and V_{GS} from 0 V to -0.5 V with step of 0.1 V. The V_{GS} scan rate was 20 mV/s and 80 mV/s for transfer and output characteristics respectively.

Electrochemical measurements were performed by a three-electrodes cell connected to a potentiostat/galvanostat μ-Autolab type III (Metrohm Italiana, Italy), using a polycrystalline Au wire as working electrode, functionalized with the above-mentioned protocols; a Pt sheet and Ag/AgCl were used as counter and reference electrodes respectively.

The impedance response was fitted by Randles circuit, which is an equivalent circuit composed by an electrolyte solution resistance, R_S, a charge transfer resistance, R_{CT}, a Debye-Helmhotz capacitance, C_{dl} and a Warburg element, W.

B.1.4. Evaluation of functionalized gold substrates by electrochemical measurements

The result of Au functionalization was first assessed by cyclic voltammetry and impedance spectroscopy (see Figure B.1) by monitoring the changes in the faradaic response of the ferricyanide redox probe, $[Fe(CN)_6]^{3-/4-}$. In the case of HSC_6NH_2-functionalized Au electrodes, cyclic voltammetry displays an increase of the peak-to-peak distance from 60 mV to >250 mV upon changing the pH of the solution from neutral to basic values (Figure B.1A). This indicates a dramatic slowing down of the electron transfer, not observed on bare Au, that is consistent with the presence of the amino-terminated self-assembled monolayer (SAM) on the electrode surface[3].

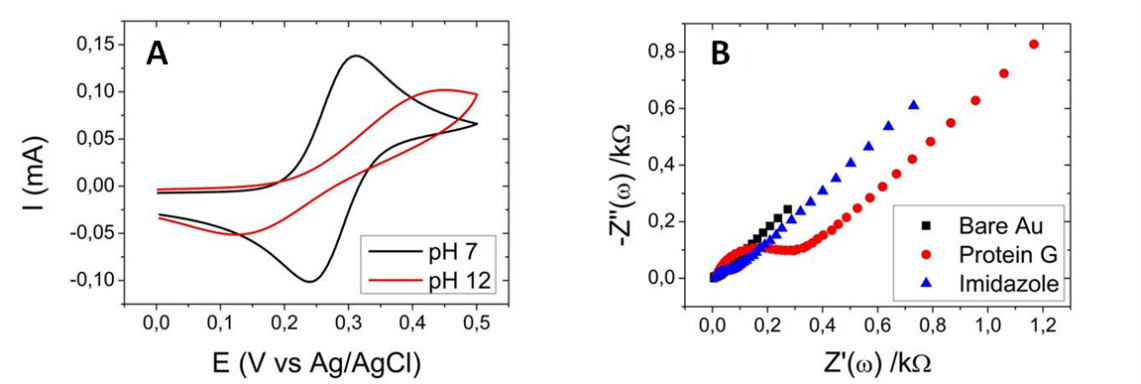

Figure B.1. A: Cyclic voltammograms of the ferricyanide signal at neutral and basic pH at a polycrystalline gold electrode functionalized with HSC_6NH_2. B: Impedance spectroscopy for bare Au (black filled squares), PG adsorption (red filled circles) and PG elution mediated by imidazole exposure (blue filled triangles).

We monitored PG adsorption onto polycrystalline Au electrodes by means of impedance spectroscopy (Figure B.1B). The data fitted with Randles circuit (see Experimental Methods Section) show that the capacitance (C_{DL}) decreases from 11.3(±0.2) μF to 2.1(±0.1) μF and the charge-transfer resistance (R_{CT}) increases from 12.8(±0.2) Ω to 270(±3) Ω. This indicates that PG is adsorbed onto Au electrode. The orientation of the adsorbed PG is assessed by measuring the impedance changes upon incubation of the PG-functionalized electrode in a 400 mM imidazole solution for 30 min. We observe a capacitance increase to 2.7(±0.1) µF, along with a dramatic decrease of R_{CT} down to 63(±0.1) Ω. These changes evidence partial desorption of His-Tagged PG from the gold electrode, thus proving that His-Tag mediates the PG assembly on Au.

Both strategies are effective for immobilizing anti-IL4 on the surface as apparent from Figure B.2 and Table B.1. For both electrode functionalizations, we observe a significant increase of the charge transfer resistance R_{CT} upon incubation in anti-IL4 solution. The capacitance change is consistent with the Ab adsorption for the HSC_6NH_2-functionalized electrode. The capacitance exhibits no significant change in the case of PG-functionalized electrode.

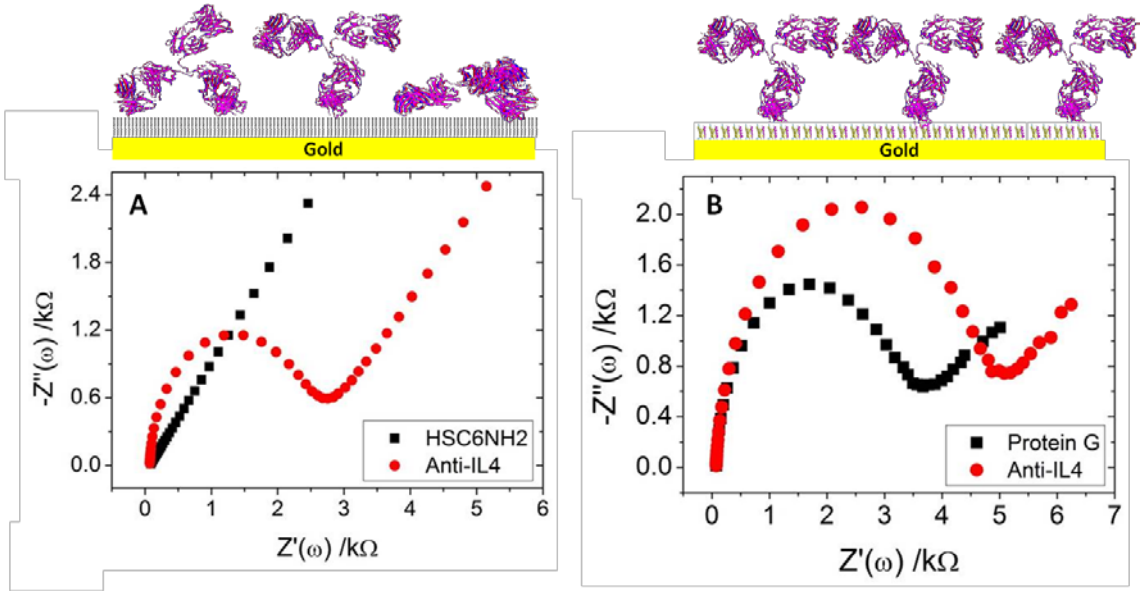

Figure B.2. Nyquist plots of A: HSC6NH2- and B: PG-mediated treatment. On the upper part of these plots, a cartoon of the two functionalization strategies is shown.

***Table B.1**. C_{DL} and R_{CT} values are listed for the two functionalization protocols.*

Electrode modifiers	**C_{DL} (μF)**	**R_{CT} (kΩ)**
HSC_6NH_2	1.3 (±0.1)	0.7(±0.1)
HSC_6NH_2 + Anti-IL4	0.56 (±0.07)	2.3(±0.1)
PG	1.14(±0.02)	3.1(±0.1)
PG + Anti-IL4	1.22(±0.02)	4.3(±0.1)

B.2. Molecular dynamics simulations of Immunoglobulin G adsorption on graphene

The molecular dynamics and steered molecular dynamics simulations were performed in by Guilherme Vilhena in Ruben Perez's group at the Universidad Autonoma de Madrid. This section was included to complement the information presented in Chapter 5 of this thesis.

The protein structure of the Immunoglobulin G (IgG), composed by 1316 amino acids and 2 glycan heteropolymer chains, was obtained from the protein data bank (PDBID: 1IGT[5]). The overall protonation state corresponds to a pH of 7.6 and a zero net charge. The IgG was then placed on top of a 20 × 20 nm^2 three-layer graphene slab with A-B-A stacking. The bottom layer of the slab has been kept fixed during the simulations. The system was solvated with a cubic box of TIP3P water molecules[6] with a 10 Å buffer of solvent between the solvent and the furthest dimension in each direction. In total, we have 12946 atoms in the protein, 47019 in the slab representing the substrate, and, depending on the IgG orientation, from 385257 to 709248 atoms in the water solvent. The protein and the oligosaccharide were modeled by the AMBER's ff99SB[7] and Glycam04[8] force fields respectively. The choice of these force-fields was motivated by a previous work, in which they reported[9] that these force fields successfully sample the conformational space that an antibody explores in aqueous solution. The carbon atoms of the three-layered graphene were modeled by the OPLS aromatic carbon force field present on AMBER's generalized AMBER force field. These force fields are known to accurately reproduce graphene/graphite mechanical and hydration properties[10].

All the simulations were performed using AMBER software suite[11]. In particular, the MD simulations were carried out using AMBER's PMEMD with NVIDIA GPU acceleration[12]. Production MD simulations were carried out at a constant temperature of 300 K ensured by a Langevin thermostat. A constant pressure of 1 atm was enforced during the thermalization state. Given the higher

computational cost of a NPT simulation, and also that it is reasonable to assume that the system pressure should remain unaltered during the adsorption process, during the production runs (the ones following thermalization) we have kept the volume fixed. The time step for integrating the equations of motion was set to 2 fs and the SHAKE algorithm was used in all of the simulations. The Particle-Mesh-Ewald summation was used to calculate long range electrostatic interaction. The cutoff for the Van-der-Waals interaction was set to 10Å. All simulations were carried out on 6 GPUs per orientation, summing up a total of more than one million hours of CPU time.

Steered-molecular-dynamics (SMD) simulations were used at two different stages: initially to enhance the protein adsorption (in the time interval 10-12 ns), and at the end in order to compute desorption free energies. In both cases these were the SMD parameters: the group of atoms to which the force is applied, the velocity of the SMD, and the spring constant of the applied force. The convergence of the above parameters required the following: not to produce any structural rearrangement on the IgG, and to yield a stabilization (with null variation) of the desorption free-energy curve once the protein is far from the surface. The set of parameters that satisfied all these requirements were: all the 30 S-bounded cysteine alpha carbons represented in Figure B.3 and a spring constant of 50 kcal/molÅ^{-1}.

The desorption free energies of the *Flat* and *Sideway* IgG orientations were obtained via an exponential average (i.e. using the Jarzynski equality[13]) of the work curves obtained in 15 independent SMDs with starting configurations sampled every 2 ns from the last 30 ns of simulation. The desorption free energies of the *Head* and *End* orientations were obtained via a single work curve obtained by performing a single SMD with the initial atomic coordinates extracted from the 150th ns of the simulation.

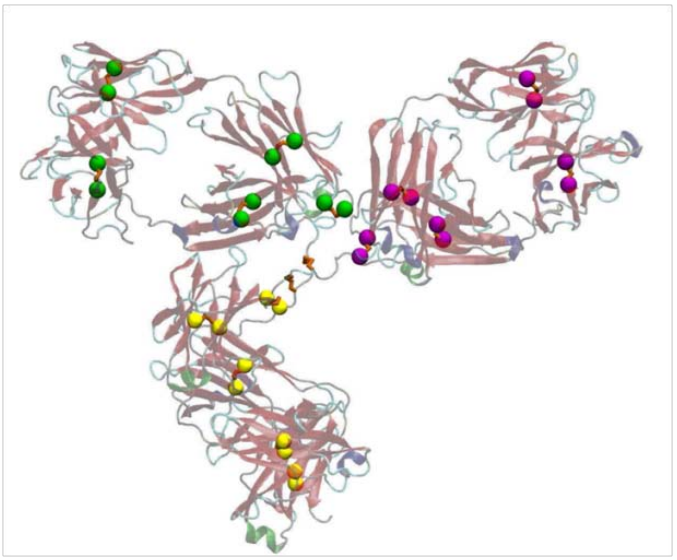

Figure B.3. Representation of the hydrophobic backbone used in the steered-molecular dynamics simulations. The IgG is represented with its secondary structure using a transparent texture. The highlighted atoms are the atoms over which the forces were applied. The atoms in green and purple belong to the Fabs and the atoms in yellow belong to the Fc region. Note that these atoms are the alpha-carbons of cysteines. This choice is motivated by two reasons: (i) these atoms are evenly distributed along the IgG. (ii) Since they belong to cysteines forming very strong S-bonds, they are very resilient to any kind of force applied. In this way we ensure an even force distribution along the protein without affecting its internal structure.

B.3. Foreign Body Reaction of Mononuclear Phagocytes to Polymer Scaffolds

This section is intended to provide additional details on the experimental methods used by our collaborators to obtain the data discussed in Chapter 7 of this thesis. The PLGA and PDMS materials described here were obtained by Giulia Foschi in Fabio Biscarini's group at the University of Modena and Reggio Emilia and CNR, Italy. All molecular biology studies on macrophage cells were carried out by Matteo Donega and Elena Giusto in Stefano Pluchino's group at the University of Cambridge, UK.

B.3.1. Materials preparation

PLGA (molecular weight: 66000 - 107000) composed by a 75:25 ratio of D,L-lactide and glycolide units was purchased from Sigma-Aldrich (P1941) and used as received. PLGA films were prepared by solution casting method. PLGA is dissolved in dichloromethane upon stirring for about 40 minutes at room temperature, to obtain a 1% wt solution. A volume of 100 µL of this solution is then cast onto a cleaned glass slide (Thermo Scientific) into a square frame (Sigma, S1815, Secure Slip™ glass coverslip silicone 1.2 cm x 1.2 cm) to obtain a thin layer of the solution with defined geometry and thickness. The solvent is allowed to evaporate at 55°C for 5 hours in an oven, and then the frame is removed. The resulting transparent film is disinfected in 99% ethanol for 15 minutes and dried in air before using it. We measured a film thickness of about 5 µm.

PDMS (Sylgard 184, Dow Corning) was mixed in a 10:1 (w/w) ratio of silicone and curing agent and placed in a vacuum chamber. The PDMS films (100 µm-thick) have been obtained by spin coating (spin speed 500 rpm, acceleration 500 rpm/s and duration time 3 minutes) and post-baking in an oven at 120°C for 1 hour.

B.3.2. Macrophages isolation and differentiation

All the procedures were performed accordingly to the principles of laboratory animal care approved by the UK Home Office animals (scientific procedures) act 1986. Bone marrow-derived monocytes were isolated from adult C57BL/6 male mice (Jax®)[14].

Briefly, mice were euthanized followed by neck dislocation. Femurs and tibias were collected, cleaned of the muscles and flushed using 25-gauge needles mounted on 10 ml syringes filled with DMEM High Glucose medium (Life Technologies). A hypotonic solution (NH_4Cl 0.8%, pH 7.5) was used to lyse and remove red cells from the cell suspension. To obtain bone marrow-derived macrophages (MPs), monocytes were filtered through a 0.2 µm cell strainer and plated with high glucose DMEM supplemented with 10% fetal bovine serum (FBS, Gibco Life Technologies), Penicillin-Streptomycin (Life Technologies) and 20% L929 (Sigma-Aldrich) conditioned medium as a source of macrophage colony stimulating factor (mCSF) for 6 to 8 days at 37°C, 5% CO_2. Upon differentiation, MPs were detached with cold phosphate buffer saline (PBS) and plated with fresh complete medium (with only 10% of L929 conditioned-medium) on PS or on different materials at a density of 27.000 cells/cm^2, unless differently specified, for the different time points needed.

B.3.3. Immunocytochemistry

MPs were fixed with pre-warmed 2% PFA and 2% sucrose in PBS for 5-10 min at RT and subsequently washed 3 times with PBS and conserved at 4°C with 0.005% PBS sodium azide. Fixed cells were then incubated 30' at RT with 555 conjugated Phalloidin (Life Technologies) diluted 1:100 in blocking solution (PBS + 10% Normal Goat Serum). MPs were washed three times in 1X PBS and incubated for 3 min with 4',6-diamidino-2-phenylindole (DAPI, 1:10.000 in 1X PBS) at room temperature in the dark. Finally, cells were washed twice with PBS, once with distilled water and mounted on glass microscope slides with mounting medium (DAKO). Slides were stored at 4 or -20°C.

B.3.4. Microscopy and image analysis

Fluorescent images were acquired using a Leica DMI 4000B inverted widefield fluorescence microscope equipped with a Leica DFC3000 G camera or a Leica SPE DMI4000B scanning laser confocal microscope. Appropriate Macros created with Fiji software were used for subsequent analyses. Quantifications were performed on 6 images acquired in 6 random fields for each sample/coverslip and the relative percentage of antigen-positive cells quantified

over the total number of DAPI-stained nuclei in the imaged field. Mean Fluorescence Intensity (MFI), normalized over the stained area using a threshold restriction method, has been used to evaluate relative expression of proteins.

For cell morphology analysis the long axis and short axis of each cell were manually traced and measured with Fiji software, as already described. The long axis was defined as the longest length of the cell, and the short axis was defined as the length across the nucleus in a direction perpendicular to the long axis. The ratio of the two axes was determined to be the elongation factor. The number of filopodia and the elongation factor were measured from 50 cells per experiment, selecting 5 isolated cells (not in close contact with other cells) per field.

B.3.5. Migration assay

MPs were seeded at high density (350.000 cells/cm^2) on 6 mm glass coverslips and kept in complete medium for 48h. Afterwards, glass coverslips were carefully broken into smaller pieces using a sterile forceps. The glass pieces showing a confluent distribution of MPs were selected and flipped-over the top of the different materials, with the cells facing the surface of organic substrates. After 24h of contact, 6 random images at the border of each coverslip were acquired with a Leica LEITZ DMIRB inverted microscope equipped with a Nikon digital camera DXM1200F. The number of cells migrating in each field was normalized over the length (μm) of the glass perimeter in that field. The number of cells migrating onto the substrate was expressed as number of cells/10 μm diameter). We also measured the maximum distance of migration, expressed as the distance (μm) between the farthest migrated cell and the coverslip edge. Analyses were performed using Fiji software.

B.3.6. Statistical analysis

Statistical analyses were performed using GraphPad Prism 5.0 software. One-Way analysis of variance (ANOVA) followed by Bonferroni's post hoc test correction was used for multiple group comparison, unless otherwise stated.

B.4. Polymer swelling model

The polymer swelling model described here was developed by Marco Dallavalle in Francesco Zerbetto's group at the University of Bologna. The numerical approach below was used to explain the experimental observations on PLGA swelling and degradation presented in Chapter 6 of this thesis.

In order to model closely the experimental data we applied a numerical approach. The backbone of the model is based on Peppas et al.'s work [15]. The model explicitly describes swelling. It is able to portray a range of diffusional behaviours, from Fickian to Case II[16, 17]. Non-ideal concentration effects on the diffusion coefficient can be included. The model is solved numerically using finite element methodology[18].At the basis of the model is Fick's law:

$$\frac{\delta C}{\delta \tau} = \frac{\delta}{\delta \xi}\left(D \frac{\delta C}{\delta \xi} \right) \text{(B.1)}$$

where:

$$C = \frac{C_w}{C_{w,e}} \text{(B.2)}$$

Here, C is the normalized concentration of the solvent, C_w the local (non-equilibrium) concentration of solvent and $C_{w,e}$ the equilibrium concentration of the solvent. The spatial coordinate, x is normalized with respect to the polymer dry thickness, L_0 (4) and the penetrant diffusion coefficient D normalizes the time scale (Equation 6.5);

$$\xi = \frac{x}{L_0} \text{(B.3)}$$

$$\tau = \frac{Dt}{L_0^2} \text{(B.4)}$$

The coefficient D is described by Fujita-type exponential $D(C)=\exp[-\beta(1-C)]$, where β is a parameter that defines the concentration dependence of D. The layers are allowed to expand as a function of the amount of

solvent. The material swelling is described by the three equations. Initially the swelling follows

$$\Delta\xi_{1,i} = \frac{\Delta\xi_0}{(1 - v_e C_i)} \quad (B.5)$$

with i=1, 2...20, being the index of the 20 spatial domains in which the polymer is sub-divided for computational purposes; u_e is a material constant. Equation 6 describes swelling at early times, specifically for the first time region. In the second time region the polymer relaxes as:

$$\Delta\xi_i = \alpha\tau^b \quad (B.6)$$

with α=1.12 and b=0.21. While for longer times we consider

$$\Delta\xi_{3,i} = \left[\frac{\Delta\xi_0^3}{(1 - v_e C_i)}\right]^{1/3} \quad (B.7)$$

with the material constant v_e=0.76.

Full details about the numerical solution are found in reference [19].

B.5. References

1. A. Campana, T. Cramer, P. Greco, G. Foschi, M. Murgia and F. Biscarini, *Applied Physics Letters*, 2013, **103**, 073302.
2. S. Casalini, A. Shehu, S. Destri, W. Porzio, M. C. Pasini, F. Vignali, F. Borgatti, C. Albonetti, F. Leonardi and F. Biscarini, *Organic Electronics*, 2012, **13**, 789-795.
3. M. L. Wallwork, D. A. Smith, J. Zhang, J. Kirkham and C. Robinson, *Langmuir*, 2001, **17**, 1126-1131.
4. M. M. Walczak, D. D. Popenoe, R. S. Deinhammer, B. D. Lamp, C. Chung and M. D. Porter, *Langmuir*, 1991, **7**, 2687-2693.
5. L. J. Harris, S. B. Larson, K. W. Hasel and A. McPherson, *Biochemistry*, 1997, **36**, 1581-1597.
6. W. L. Jorgensen, J. Chandrasekhar, J. D. Madura, R. W. Impey and M. L. Klein, *The Journal of Chemical Physics*, 1983, **79**, 926-935.
7. K. Lindorff-Larsen, S. Piana, K. Palmo, P. Maragakis, J. L. Klepeis, R. O. Dror and D. E. Shaw, *Proteins*, 2010, **78**, 1950-1958.
8. K. N. Kirschner, A. B. Yongye, S. M. Tschampel, J. González-Outeiriño, C. R. Daniels, B. L. Foley and R. J. Woods, *Journal of Computational Chemistry*, 2008, **29**, 622-655.
9. C.-c. Chiu, G. R. Dieckmann and S. O. Nielsen, *The Journal of Physical Chemistry B*, 2008, **112**, 16326-16333.
10. C. Mücksch and H. M. Urbassek, *PLoS One*, 2013, **8**, e64883.
11. AMBER, http://ambermd.org/).
12. R. Salomon-Ferrer, A. W. Götz, D. Poole, S. Le Grand and R. C. Walker, *Journal of Chemical Theory and Computation*, 2013, **9**, 3878-3888.
13. C. Jarzynski, *Physical Review Letters*, 1997, **78**, 2690-2693.
14. V. A. Deshmukh, V. Tardif, C. A. Lyssiotis, C. C. Green, B. Kerman, H. J. Kim, K. Padmanabhan, J. G. Swoboda, I. Ahmad, T. Kondo, F. H. Gage, A. N. Theofilopoulos, B. R. Lawson, P. G. Schultz and L. L. Lairson, *Nature*, 2013, **502**, 327-332.
15. R. W. Korsmeyer and N. A. Peppas, *Journal of Controlled Release*, 1984, **1**, 89-98.
16. T. Alfrey, E. F. Gurnee and W. G. Lloyd, *Journal of Polymer Science Part C: Polymer Symposia*, 1966, **12**, 249-261.
17. J. S. Vrentas, C. M. Jarzebski and J. L. Duda, *AIChE Journal*, 1975, **21**, 894-901.
18. www.comsol.com.
19. A. C. Dumitru, F. M. Espinosa, R. Garcia, G. Foschi, S. Tortorella, F. Valle, M. Dallavalle, F. Zerbetto and F. Biscarini, *Nanoscale*, 2015, **7**, 5403-5410.

Publications list

Articles related to the present doctoral thesis:

1. **A.C. Dumitru**, E.T. Herruzo, E.Rausell, V. Ceña, R.Garcia, *Unbinding forces and energies between a siRNA molecule and a dendrimer measured by force spectroscopy,* **Nanoscale**, 2015, **7**, 20267-20276.

2. **A.C. Dumitru**, F.M. Espinosa, R. Garcia, G. Foschi, S. Tortorella, F. Valle, M. Dallavalle, F. Zerbetto and F. Biscarini, *In-situ nanomechanical characterization of the early stages of swelling and degradation of a biodegradable polymer,* **Nanoscale**, 2015, **7**, 5403-5410

3. S. Casalini, **A. C. Dumitru**, F. Leonardi, C.A. Bortolotti, E.T. Herruzo, A. Campana, R.F. de Oliveira, T. Cramer, R. Garcia and F. Biscarini, *Multiscale Sensing of Antibody-Antigen Interactions by Organic Transistors and Single-Molecule Force Spectroscopy,* **ACS Nano**, 2015, 9, 5051-5062

4. J.G. Vilhena, **A.C. Dumitru**, E.T. Herruzo, J.I.Mendieta-Moreno,R.Garcia, P.A.Serena, R.Perez, *Vertical adsorption orientations and immunological recognition of antibodies on graphene (submitted*)

5. E. Giusto, M. Donegà, **A.C. Dumitru**, G. Foschi, M. Bianchi, A. Russo, S. Casalini, T. Leonardi, F. Biscarini, R.Garcia, S.Pluchino, *Assessing the Foreign Body Reaction of Mononuclear Phagocytes to Polymer Scaffolds by Single Cell Force Spectroscopy: a Multiscale Comparative Study* (*submitted*)